Doctoral theses at NTNU, 2023:240

Jonas Tjemsland

Probing dark matter with astroparticles

Doctoral thesis

NTNU
Norwegian University of Science and Technology
Thesis for the Degree of
Philosophiae Doctor
Faculty of Natural Sciences
Department of Physics

NTNU
Norwegian University of
Science and Technology

Jonas Tjemsland

Probing dark matter with astroparticles

Thesis for the Degree of Philosophiae Doctor

Trondheim, August 2023

Norwegian University of Science and Technology
Faculty of Natural Sciences
Department of Physics

NTNU
Norwegian University of
Science and Technology

NTNU
Norwegian University of Science and Technology

Thesis for the Degree of Philosophiae Doctor

Faculty of Natural Sciences
Department of Physics

ISBN 978-82-326-7180-9 (printed ver.)
ISBN 978-82-326-7179-3 (electronic ver.)
ISSN 1503-8181 (printed ver.)
ISSN 2703-8084 (online ver.)

Doctoral theses at NTNU, 2023:240

Printed by NTNU Grafisk senter

Abstract

There is an enormous amount of evidence for the existence of dark matter, from scales ranging from the faintest dwarf galaxies to the Universe as a whole. However, its nature remains a mystery. This thesis is a part of the community effort to reveal the properties of dark matter, focusing on how one can use gamma-rays and cosmic rays to indirectly probe its nature. Three main topics have been studied: cosmic ray antinuclei, photon-axion oscillations and millicharged particles.

Cosmic ray antinuclei, such as antideuterons and antihelions, are ideal detection channels for new and exotic physics—including dark matter annihilations or decays—due to low astrophysical backgrounds. At the same time, their composite structure and small binding energies make them excellent probes for particle correlations and density fluctuations in collider experiments, shedding light on the hadronization process or even the QCD phase diagram. In order to correctly interpret experimental data, a solid understanding of the antinucleus formation process is needed. The main focus in this thesis has therefore been to improve the theoretical description of the formation of (anti)deuteron and (anti)helion in small interacting systems, such as e^+e^-, pp and pN collisions, and in particular, dark matter annihilations and decays. The main outcome has been a new and improved coalescence model, which takes into account both the size of the formation region and nucleon momentum correlations.

Axions and axion-like particles (ALPs) are interesting dark matter candidates despite their small masses. These particles are characterized by their two-photon coupling, which leads to so-called photon-ALP oscillations when photons propagate through a magnetic field. Parts of this thesis have been dedicated to study the distinctive signatures that these oscillations will imprint in the energy spectrum of high-energy photons from astrophysical sources. In particular, the detection of oscillatory features, or "ALP wiggles", in the photon spectra has been extensively studied.

Despite intensive searches, none of the traditional dark matter candidates have been found yet. This has lead to an increased interest in alternative candidates, such as hidden sectors. If the hidden sector is connected to the Standard Model with a massive dark photon as a mediator, the dark matter may have a small charge. This case is known as millicharged dark matter. Two topics related to millicharged particles have been studied: the production of light exotic particles by meson decays in air showers, and the impact of millicharged dark matter on the evolution of the turbulence in the Milky Way.

Populærvitenskapelig sammendrag

Hele 85 % av massen i universet består av såkalt mørk materie. Vi vet ikke hva det er, men vi er rimelig sikre på at det eksisterer. Bevisene er mange: spiralgalakser roterer merkelig, galaksehoper har for høy bevegelsesenergi, og ikke minst, vi trenger det for å beskrive hvordan de små tetthetsforskjellene i den kosmiske bakgrunnsstøyen har utviklet seg til galaksene og galaksehopene vi ser i dag. Likevel beskriver alle disse bare hvordan den mørke materien virker på vanlig materie gjennom gravitasjonskraften. Vi vet fremdeles lite om den mørke materiens sanne natur.

Standardmodellen innen partikkelfysikken har vært enormt vellykket—kanskje mest kjent er dens prediksjon av elektronets magnetiske moment til en presisjon på 10^{-10}(!)—og det kunne tilsynelatende se ut til at alle brikkene var falt på plass etter at Higgs-bosonet ble observert ved CERN i 2011; endelig hadde man funnet partikkelen som gir og forklarer massen til kvarkene, de ladde leptonene og vekselvirkningskvantene. Til tross for dette har Standardmodellen fremdeles en del teoretiske mangler som tyder på at den ikke er komplett. For eksempel vet vi ikke hvorfor massen til Higgs-bosonet er mye mindre enn Planck-massen, hvorfor nøytrinoene har masse eller hvorfor nøytronet ikke har et elektrisk dipolmoment. Kanskje enda viktigere: ingen av partiklene i Standardmodellen kan forklare mørk materie. Til det trenger vi ny og spennende fysikk!

Denne avhandlingen har fokusert på hvordan man kan lære mer om mørk materie ved å observere kosmisk stråling her på Jorda, og er således en liten del av en fellesskapsinnsats for å belyse den mørke materien. Avhandlingen har i all hovedsak tatt for seg tre temaer: kosmiske antinukleuser, foton-axion oscillasjon, og milliladde partikler.

Preface

This thesis is submitted in partial fulfillment of the requirements for the degree Philosophiae Doctor (PhD) at the Norwegian University of Science and Technology (NTNU). The research at which this thesis is based was carried out in the Astrophysics and Theoretical Physics group at the Department of Physics under the supervision of Prof. Michael Kachelrieß.

The overall topic of this thesis is *astroparticle physics* and *dark matter (DM)*. For me, astroparticle physics is a perfect culmination of astrophysics, particle physics and cosmology, and the search for DM highlights their connectedness. It is therefore fitting that the thesis has the open title "Probing dark matter with astroparticles". A major reason why I love working in the (broad) field of astroparticle physics and DM is that while the existence of DM and the search for new physics drive my curiosity and motivation, the results and methodologies can be applied to other fields. For example, a large portion of my PhD work has been dedicated to study the formation of (anti)deuteron and (anti)helion in small interacting systems. Even though the main motivation for this was to better understand their production in exotic processes, such as DM annihilations or decays in the Milky Way, it has proven to be useful for experimental groups to understand their production in accelerator studies.

There are many who deserve my thanks for making this thesis possible, all of whom cannot be listed here. First and foremost, I must congratulate Michael Kachelrieß for being an excellent supervisor. You answer all my requests and questions like a physics guru, and have always time for a chat, a coffee and a discussion. I have appreciated your honesty, which has improved my scientific skills. Thank you for your supervision, critique and collaboration over the past five years! Furthermore, I would like to express my sincere thanks to Sergey Ostapchenko for outstanding discussions and collaborations, Manuel Meyer for hospitality during my research stay in Hamburg, and Bidisha Sen and Michael Kachelrieß for comments on this manuscript. Last and most important, I would like to extend my gratitude to my wife and son, because of whom I will formally finish my PhD ahead of time.

Structure of the thesis

The papers written during my PhD have all been, to some degree, motivated by indirect detection of DM. The papers can crudely be split into three sub-categories: antinuclei (Papers I, II, IV, V, VII, IX, X, XII, XIII, XVII, XVIII), photon-ALP oscillation (Papers

VIII, XI, XIV, XV, XVI) and millicharged particles (Papers III, VI). Since the three topics ostensibly may seem unrelated, the first part of this thesis is dedicated to give a brief and general overview of DM, with a focus on weakly interacting massive particles (WIMPs) and axion-like particles (ALPs). The main goal of this part is to highlight the importance of the papers and put them into perspective. My hope is that this will clarify the coherency of the work.

In the second part, most of the papers are presented in their entirety. In the introduction for this part, I will provide a description of the goals and outcomes of the papers, presenting them as a coherent work. In addition, I include a short editorial comment on the concrete motivation for why the work was undertaken for each paper, thus emphasizing the value of the individual papers.

Jonas Tjemsland
July 18, 2023
Trondheim, Norway

The pursuit of knowledge is a lifelong journey,
but the destination is not a degree or a diploma,
but rather a deeper understanding of the world and our place in it.
– ChatGPT (2023)

Contents

Abbreviations

2HDM Two Higgs Doublet Model 19

ALP axion-like particle vi, 3, 32, 33, 35–37, 39, 51, 52, 150, 200

BBN Big Bang nucleosynthesis 6, 10, 16

CMB cosmic microwave background 5, 9, 10, 13, 16, 39

CTA Cherenkov Telescope Array 36

DM dark matter v, vi, 3, 5–13, 15–27, 33, 35–37, 39, 51, 52, 68, 96, 146

EBL extragalactic background light 37

FIMP Feebly Interacting Massive Particle 18

FRW Friedman-Robertson-Walker 33

LSP lightest supersymmetric particle 18

MC Monte Carlo 24, 176

MOND modified Newtonian dynamics 12, 13

MSSM Minimal Supersymmetric Standard Model 18, 19, 39

NFW Navarro-Frenk-White 8

NTNU Norwegian University of Science and Technology v

PBH primordial black hole 3, 6, 12

QCD quantum chromodynamics 19, 29, 30, 33–35

SD spin-dependent 22

SI spin-independent 22

SM Standard Model 3, 6, 7, 10, 11, 15, 16, 18–20, 23, 25, 31, 32, 39, 52

SUSY supersymmetry 18, 39

WIMP weakly interacting massive particle vi, 3, 7, 10, 11, 15–18, 20, 23–25, 33, 39, 51, 52, 68

List of papers

I. Kachelrieß, M., Ostapchenko, S. & Tjemsland, J. "Alternative coalescence model for deuteron, tritium, helium-3 and their antinuclei". *Eur. Phys. J. A* **56,** 4. arXiv: 1905.01192 [hep-ph] (2020)

II. Kachelrieß, M., Ostapchenko, S. & Tjemsland, J. "Revisiting cosmic ray antinuclei fluxes with a new coalescence model". *JCAP* **08,** 048. arXiv: 2002.10481 [hep-ph] (2020)

III. Kachelrieß, M. & Tjemsland, J. "Reacceleration of charged dark matter". *JCAP* **10,** 001. arXiv: 2006.10479 [astro-ph.HE] (2020)

IV. Kachelrieß, M., Ostapchenko, S. & Tjemsland, J. "On nuclear coalescence in small interacting systems". *Eur. Phys. J. A* **57,** 167. arXiv: 2012.04352 [hep-ph] (2021)

V. Tjemsland, J. "Formation of light (anti)nuclei". *PoS* **TOOLS2020,** 006. arXiv: 2012.12252 [hep-ph] (2021)

VI. Kachelrieß, M. & Tjemsland, J. "Meson production in air showers and the search for light exotic particles". *Astropart. Phys.* **132,** 102622. arXiv: 2104.06811 [hep-ph] (2021)

VII. Kachelrieß, M., Ostapchenko, S. & Tjemsland, J. "Comment on "Dark Matter Annihilation Can Produce a Detectable Antihelium Flux through $\bar{\Lambda}_b$ Decays"". arXiv: 2105.00799 [hep-ph] (May 2021)

VIII. Kachelrieß, M. & Tjemsland, J. "On the origin and the detection of characteristic axion wiggles in photon spectra". *JCAP* **01,** 025. arXiv: 2111.08303 [astro-ph.HE] (2022)

IX. Kachelrieß, M., Ostapchenko, S. & Tjemsland, J. "AAfrag 2.01: interpolation routines for Monte Carlo results on secondary production including light antinuclei in hadronic interactions". *Comput. Phys. Commun.* **287,** 108698. arXiv: 2206.00998 [hep-ph] (2023)

X. Kachelrieß, M., Ostapchenko, S. & Tjemsland, J. "The effect of non-equal emission times and space-time correlations on (anti-) nuclei production". *Submitted to Phys. Rev. C.* arXiv: 2303.08437 [hep-ph] (Mar. 2023)

XI. Kachelrieß, M. & Tjemsland, J. "Detecting ALP wiggles at TeV energies". *Sumbitted to JCAP.* arXiv: 2305.03604 [hep-ph] (May 2023)

Papers not attached to the thesis

XII. Kachelrieß, M., Ostapchenko, S. & Tjemsland, J. "Formation models for cosmic ray antinuclei". *PoS* **ICRC2021,** 558 (2021)

XIII. Kachelrieß, M., Ostapchenko, S. & Tjemsland, J. "Nuclear coalescence and collective behaviour in small interacting systems". *PoS* **EPS-HEP2021,** 318 (2022)

XIV. Kachelrieß, M. & Tjemsland, J. "Photon-ALP oscillations with ELMAG". *PoS* **CompTools2021,** 002 (2022)

XV. Kachelrieß, M. & Tjemsland, J. "Photon-ALP oscillations at CTA energies". *Accepted for publication in SciPost Phys. Proc.* **IDM2022** (Oct. 2022)

XVI. Kachelrieß, M. & Tjemsland, J. "Photon-ALP oscillations at TeV energies". *PoS* **ICHEP2022,** 1166 (Oct. 2022)

XVII. Kachelrieß, M., Ostapchenko, S. & Tjemsland, J. "Nuclear coalescence, collective behaviour and emission volume in small interacting systems". *PoS* **ICHEP2022,** 1165 (2022)

Contributions to papers not included in the thesis

XVIII. von Doetinchem, P. *et al.* "Cosmic-ray antinuclei as messengers of new physics: status and outlook for the new decade". *JCAP* **08,** 035. arXiv: 2002.04163 [astro-ph.HE] (2020)

The search for dark matter

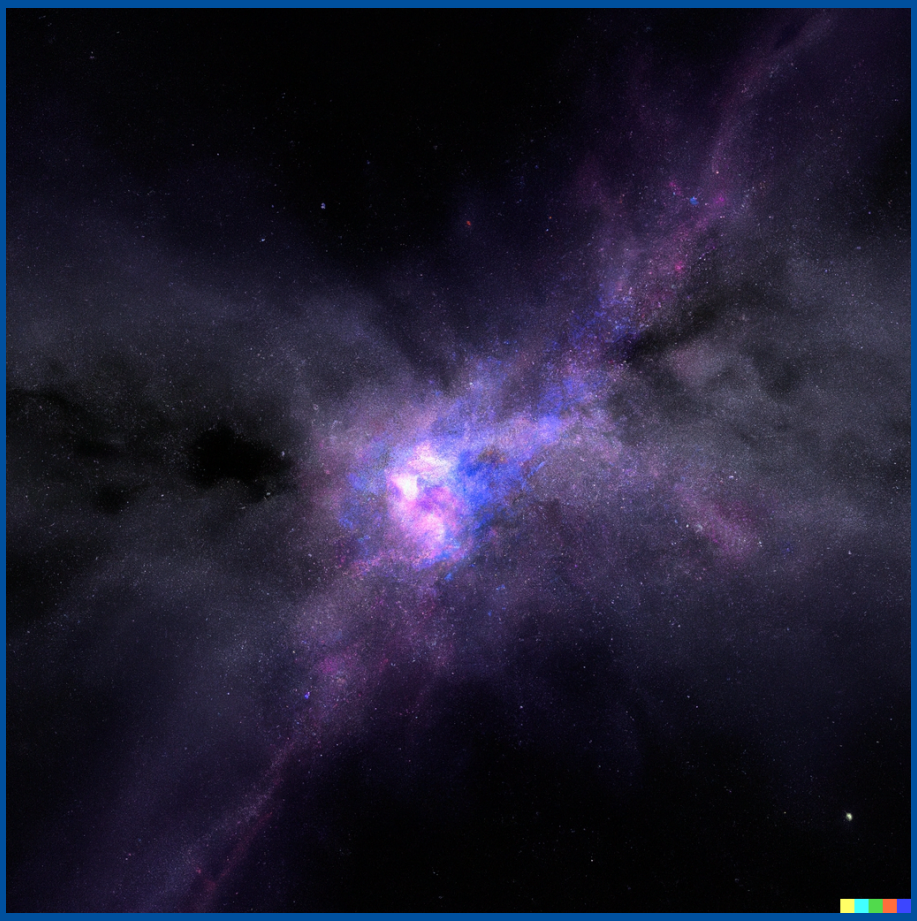

"Weakly interacting massive particle as a dark matter candidate" by Dall·E (2023)

1 Introduction

There is an enormous amount of evidence for the existence of dark matter (DM) on scales ranging from the faintest dwarf galaxies to the Universe as a whole: Measured Galaxy rotation curves seem to require an additional collisionless matter distribution. Measurements of the velocity dispersion of galaxies within galaxy clusters and gravitational lensing uncover a mass well beyond the mass inferred by X-ray observations and stellar count estimates. Most importantly, explaining structure formation requires the presence of a dominant DM component. The existence of DM is thus well established in the modern cosmological paradigm: It accounts for 84.4 % of the matter content in the Universe, or 26.4 % of the critical density [1]. However, the current evidences for DM rely on its gravitational interaction with ordinary matter, and despite immense effort over the years and its plentiful abundance, its nature has yet to be revealed.

It is usually assumed that the DM consists of particles. Although the Standard Model (SM) of particle physics has been immensely successful—predicting the electron magnetic moment to more than 10 significant digits compared to experiments [2]—it has several fundamental theoretical shortcomings signaling its incompleteness. Among these are the hierarchy problem, the strong CP problem and the neutrino mass problem. In addition, there are experimental hints, such as the $g-2$ and W mass anomalies. Importantly, the SM fails to provide a viable DM candidate. There exists, however, a plethora of possible candidates, including weakly interacting massive particles (WIMPs), axions and axion-like particles (ALPs), sterile neutrinos, or even primordial black holes (PBHs). Understanding their phenomenological consequences may help to guide the experimental effort to unravel the nature of DM.

In this part of the thesis, a general introduction to the topic of DM will be given, with a focus on WIMPs and axions. These are particularly well-motivated DM candidates as WIMPs may solve the hierarchy problem while the axion solves the strong CP problem. Furthermore, they are naturally produced with the right abundances in the early Universe. The main purpose of this discussion is to provide a motivation for, and an overall coherency of, the papers attached to this thesis.

2 Dark matter

The existence of DM is well established. However, since all current evidence rely on its gravitational interaction with ordinary matter, no one knows what it *actually* is. This chapter will give a general introduction into DM. Why does one know that it exists? What can it consist of?

2.1 The pre-history

The most cited pioneer in the field of DM is arguably Swiss astronomer F. Zwicky, who in 1933, used the virial theorem to deduce the mass of the Coma Cluster [3]. By comparing it to the luminous mass, he concluded that DM has to be present in a much greater amount than the luminous matter. This is oftentimes cited as the first experimental proof of DM, as well as the introduction to the notion "dark matter". However, the calculations had assumptions that were questioned by his peers at the time, and the observation did not yield any information about the nature of the missing mass. Therefore, it was not until the 1970s that the existence of DM garnered interest in the astrophysics community. At this time, there was a revolution in the measurements of galaxy rotation curves[1]: In 1970, V. Rubin and K. Ford performed an optical study of the rotation curve of M31 [4], which they extended to ten spiral galaxies in 1978 [5]. They noticed that the velocity remained constant to as far out as one could observe, which contradicts the Newtonian expectation, $v(r) \sim 1/r$. A simple explanation, which is the common consensus today, is the existence of an additional unobserved spherically symmetric mass distribution of DM with $\rho(r) \sim 1/r^2$ at large r. This is known as the dark halo. Today, the most conclusive evidence for the existence of DM is credited to the exceptional conformity between the measured cosmic microwave background (CMB) anisotropies and the prediction by the standard model of cosmology, ΛCDM, which was initially developed by J. Peebles. Peebles received the Nobel Prize in 2019 for his contributions to theoretical discoveries in cosmology.

The history of DM is, however, more rich and nuanced than the standard textbook representation portrayed above, as adequately described in, e.g., the review of DM history by G. Bertone and D. Hooper [6]. For example, as early as in 1904, Lord Kelvin attempted a dynamical estimate for the amount of DM in the Milky Way using the theory of gases [7]. Inspired by Kelvin in 1906, H. Poincaré estimated the amount of matter in the Milky Way

[1] That is, a measurement of the velocity of the stars around the galactic center as a function of the distance from the center, $v(r)$.

using the velocity dispersion of the stars, and found that *"since his number is comparable to that which the telescope gives, then there is no dark matter, or at least not so much as there is of shining matter"* [8]. Although this conclusion was in disfavor of DM, it is evident that astronomers have considered the possibility of the existence of a large amount of unobservable matter for a long time. Conclusive statements about the existence of a dark halo were not made until the 1970s [6], after the improvements in the measurements of galaxy rotation curves lead by K. Ford and V. Rubin. However, even if the work by V. Rubin and K. Ford lead to a groundbreaking improvement in the quality of rotation curves, their light curves extended to shorter radii than radio measurements, and their results could not be used to firmly confirm the existence of a dark halo. This may be attributed to M. Roberts[2] instead, who in 1972 and 1973, published rotation curves of three nearby galaxies [9, 10], with a clear conclusion in favor of a dark halo: *"The three galaxian rotation curves decline slowly, if at all, at large radii, implying a significant mass density at these large distances. [...] The present data also require that the mass to luminosity ratio vary with radius increasing in distance from the center."*

An often forgotten pioneer in the history of DM is the Swedish astronomer K. Lundmark.[3] In 1930, Lundmark used early spectrographic measurements of five nearby galaxies to estimate the mass-to-light ratios [11]. He found that the mass of the galaxies were dominated by DM—three years before Zwicky and 40 years before Rubin. Although the numbers understandably were inaccurate, this is—to the best of my knowledge—the first enduring evidence that there is much more DM than luminous matter in galaxies.

Even if the early pioneers, like Zwicky, Rubin, Ford and Lundmark, denoted the unknown and invisible matter as "dark matter", it was still believed to consist of cold and unobservable stellar objects, as becomes clear in, e.g., the original work by Zwicky [3]: *"We must know how much dark matter is incorporated in nebulae in the form of cool and cold stars, macroscopic and microscopic solid bodies, and gases."* In the modern cosmological paradigm, however, DM is synonymous with a cold, collisionless and non-baryonic relic abundance that makes up $\sim 85\,\%$ of the matter density of the Universe. The modern consensus—which slowly arose in the 1980s [6]—is that DM consists of a new particle[4] not explained by the SM. The introduction of DM in the modern cosmological paradigm should therefore be viewed as a community effort during the 19th century.

2.2 Why do we need dark matter?

The study of DM is the archetypical astroparticle physics topic: It is observed in *astrophysics*, has to be produced *cosmologically* and may be explained by *particle physics*.

[2] In fact, Rubin, Ford and Thonnard attribute the credit to Roberts in their seminal paper from 1978 [5].
[3] I would like to thank G. Raffelt for making me aware of the work by Lundmark, thereby motivating me to include this section in the thesis.
[4] Alternatively, it can be PBHs formed before Big Bang nucleosynthesis (BBN).

In this section, some motivations and evidences for the existence of DM will briefly be reviewed.

2.2.1 Motivations in particle physics

There are several shortcomings in the SM that indicate the presence of some yet unknown new physics. This includes phenomena such as the hierarchy problem, the strong CP problem, the $g-2$ anomaly and the neutrino mass problem. Since DM cannot be described by the SM, one may hope that it can be explained by a more fundamental theory that simultaneously addresses some deficiencies of the SM. Thus, the incompleteness of the SM can be used as a motivation for specific DM candidates. In the next two chapters, we will discuss how the hierarchy problem and the strong CP problem motivate the WIMP and the axion, respectively.

2.2.2 Motivations in astrophysics

The DM has been observed to be omnipresent in systems ranging from the faintest dwarf galaxies to clusters of galaxies. The amount of DM can be deduced by measuring the mass-to-light ratio in the system. This can be achieved by measuring the mass using galaxy rotation curves in axisymmetric systems (as done by V. Rubin), velocity dispersion (like by F. Zwicky) or gravitational lensing, and by estimating the baryonic mass by stellar count estimates or X-ray observations. Next, two concrete examples will be discussed: galaxy rotation curves and merging galaxy clusters.

Galaxy rotation curves

The most direct evidence for DM in the Milky Way and other spiral galaxies comes from measurements of their rotation curves, i.e. the orbital speed $v(r)$ as a function of the distance r from the galactic center. The rotation curve in the outer regions of a galaxy is expected to follow a Keplerian orbit. That is,

$$v(r) = \sqrt{\frac{GM(r)}{r}}, \tag{2.1}$$

where $M(r)$ is the mass within the radius r and G is the gravitational constant. The rotation curve can be calculated by measuring the Doppler shift of spectral lines from stars and gas [12]. In contradiction with the Keplerian expectation $v \sim 1/\sqrt{r}$, the result is that most rotation curves remain constant, or even increase, as far out as one is able to measure [12]. As an example, the rotation curve of the Milky Ways is plotted in Fig. 2.1. By using Eq. (2.1), one can see that a flat rotation curve can be explained by a spherical mass distribution with a density profile $\rho(r) = v^2/4\pi G r^2$. This decrease is much

slower than that of the visible matter, which is expected to roughly follow the exponential decrease in luminosity.

The most commonly used DM profile is the so-called Navarro-Frenk-White (NFW) profile [13, 14]

$$\rho(r) = \frac{\rho_0}{(r/a)(1 + r/a)^2}, \tag{2.2}$$

which has empirically been shown to describe the dark halos produced in N-body simulations.[5] Observations show, however, that rotation curves are less cuspy than those favored by simulations. This is known as the *core-cusp problem*, which is often used to motivate self-interacting, warm or fuzzy DM models. An alternative explanation is baryonic feedback.

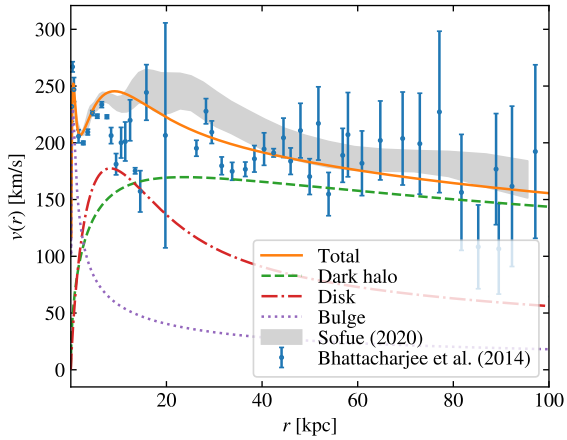

Figure 2.1: Measured Milky Way rotation curve including a fit for a simple model with a bulge (purple dotted line), an exponential disk (red dashed dotted line) and a dark halo with the NFW profile (green dashed line) (see Ref. [15] for details). The experimental data from Ref. [16] (blue error bars), as well as the averaged data from Ref. [15] (gray region) are shown.

The Bullet Cluster

The lensing maps of the galaxy clusters 1E0657-56 [17] (known as the "Bullet Cluster") and MACS J0025.4-1222 [18] give unique insights into the nature of DM. These galaxy clusters are examples of merging clusters, which consist of two clusters each that have

[5] Note that the NFW profile diverges for $r \to 0$ and falls off as r^{-3} at large distances.

Figure 2.2: Lensing (blue), X-ray (red) and optical maps of the Bullet Cluster (1E0657-56). The figure is taken from Ref. [20].

recently collided: Gravitational lensing studies reveal two substructures that are off-set compared to the baryonic distribution inferred by X-ray measurements, see Fig. 2.2. In other words, whereas the intercluster plasma was decelerated in the collision, the main mass component moved ballistically. Not only does the lensing reveal that most of the mass comes from DM, but is also a direct evidence that DM is collisionless.[6]

2.2.3 Motivations in cosmology

The fact that DM is an essential ingredient needed to explain structure formation is viewed by many as the most compelling evidence for DM . The density perturbation observed in the CMB is [1]

$$\frac{\delta\rho}{\rho} = 3\frac{\delta T}{T} \simeq 10^{-5}. \tag{2.3}$$

Since the density fluctuations grow linearly with the scale factor in the matter dominated era [21], the density perturbation today would be

$$\left.\frac{\delta\rho_b}{\delta_b}\right|_{\text{today}} \approx \frac{1}{a_{\text{rec}}} \left.\frac{\delta\rho_b}{\rho_b}\right|_{\text{rec}} \approx 10^{-2} \tag{2.4}$$

in the absence of DM.[7] This is in stark contrast to the observation $\delta\rho_b/\rho_b \gg 1$, which can be made with the naked eye. A solution to this clear discrepancy is the existence of a dominant cold (i.e. non-relativistic) matter component which decoupled well before recombination. In fact, the matter power spectrum and the CMB anisotropies predicted

[6] A direct limit on the DM self interaction cross section can be deduced from the colliding clusters [19].
[7] Recombination occurred at $T_{\text{rec}} \sim 3000\,\text{K}$. Thus, $a_{\text{rec}}^{-1} = T_{\text{rec}}/T_0 \approx 10^3$.

by ΛCDM are in remarkable agreement with the measurements of the CMB [1]. From this, one can deduce that the total matter content in the Universe is 84 % cold DM, or alternatively, a critical density $\Omega_\chi h^2 \simeq 0.12$ [1].

Note that the DM cannot be baryonic, which is perhaps simplest understood by BBN: The relative abundances of the light nuclei depend on the photon-to-baryon content, and thereby on the baryon density. Thus, from measurements of the abundances of light nuclei, one can fix the baryon content, $\Omega_b h^2 \simeq 0.022$ [1]. Since $\Omega_\chi \gg \Omega_b$, the DM cannot be baryonic.

2.3 Dark matter candidates

From the observations discussed in the previous section, one can conclude that the DM should be collisionless and non-baryonic. In addition, it has to be produced in the early Universe, and in order to explain structure formation, it must have been cold well before recombination. The only seemingly viable candidate from the SM are the neutrinos, but these would contribute only to a hot DM component due to their small mass. In this section, some possible DM candidates will be discussed.

2.3.1 Weakly interacting massive particles (WIMPs)

As the name suggests, WIMPs are a general class of particles beyond the SM, characterized by being weakly interacting and massive, with masses usually assumed to be in the range of 10–1000 GeV. These particles are particularly well motivated as they may solve the hierarchy problem and are naturally produced in the early Universe as a thermal relic. The fact that a thermally averaged annihilation cross section at the weak scale, $\langle \sigma_{\text{ann}} v \rangle \sim 10^{-26}\,\text{cm}^3/\text{s}$, reproduces the observed DM content has famously been dubbed *the WIMP miracle*. In Chapter 3, WIMPs will be discussed in more detail.

2.3.2 Axions

Axions were introduced by Peccei and Quinn in 1977 as a solution to the strong CP problem [22]. Despite their small mass, axions can be suitable DM candidates if they are produced via the so-called *misalignment mechanism*. We will discuss axions in more detail in Chapter 4.

2.3.3 Sterile neutrinos

The neutrino masses are zero in the SM, but the detection of neutrino oscillations has firmly established that the neutrinos indeed have small non-zero masses. However, it is still not clear whether neutrinos are Majorana (that is, their own antiparticle) or Dirac

fermions.[8] If the neutrinos are Majorana fermions, their mass can be described by including a Majorana mass terms like $-m\bar{\nu}_L\nu_L^c/2$ in the SM Lagrangian. To include such a term via the Higgs mechanism, one can extend the Higgs doublet to a Higgs triplet [23]. On the other hand, if they are Dirac fermions, a Dirac mass term can be created by extending the SM by additional singlet fermions, i.e. right-handed neutrinos. This would lead to mass terms like $-m\bar{\nu}_L\nu_R$.

The right-handed neutrinos are known as *sterile neutrinos* since they do not partake in the weak interactions (see e.g. Refs. [23] for a review). Their existence may solve some unsolved problems, such as explaining why the neutrinos are much lighter than the other fermions and induce the CP violation needed for baryogenesis [24]. In addition, their existence would equalize the apparent "mismatch" between the quark and lepton degrees of freedom. Sterile neutrinos can be produced as a thermal relic, and with masses $\mathcal{O}(10)\,\mathrm{keV}$, are suitable DM candidates. Small masses and small mixing are favored in order for the DM to be stable.

2.3.4 Hidden dark matter

Despite intensive searches, the DM candidate has yet to been found. This has lead to an increased interest in alternative models, such as hidden sectors, which only communicate with the SM via a new mediator. Hidden DM can be produced as a thermal relic in the early Universe: The relic abundance of a stable particle with mass m_χ interacting with the SM via a coupling g_χ is

$$\Omega_\chi \sim \langle\sigma_{\mathrm{ann}}v\rangle^{-1} \sim \frac{m_\chi^2}{g_\chi^4}. \tag{2.5}$$

The observation that the correct relic abundance, Ω_χ, is obtained for $m_\chi \sim m_{\mathrm{weak}}$ and $g_\chi \sim g_{\mathrm{weak}}$, is the well-known WIMP miracle. However, Eq. (2.5) indicates that the right relic abundance can be achieved for other values of m_χ and g_χ as well. This has amusingly been named the *WIMPless miracle* [25]. A hidden sector has its own matter content and couplings, and the lightest stable particle may be a suitable DM candidate.

One example of a simple hidden sector is the case of millicharged DM, where the DM particle has a small, but non-zero electric charge $qe \ll e$, thereby providing a coupling to the SM via the photon [26]. The small value of q could be explained, for example, by a kinetic mixing between the SM photon and a massive dark photon corresponding to a new U(1) symmetry.

[8] The measurement of, e.g., neutrino-less double beta decay would firmly conclude that neutrinos are Majorana particles.

2.3.5 Primordial black holes (PBHs)

Although it is usually assumed that the DM consists of a new particle, it is conceivable that it can be explained by a distribution of black holes, known as PBHs. The PBHs need to form well before recombination in order to contribute to the non-baryonic relic density, and has to be more massive than $\sim 10^{15}\,\mathrm{g}$ in order to not have been evaporated by now [27]. The PBHs are believed to be formed by the gravitational collapse of density fluctuations in the early Universe, induced by, e.g., primordial inhomogeneities, topological defects like cosmic strings or domain walls, an early phase of matter domination or a phase transition [27]. The idea of PBHs received a renewed interest after the detection of gravitational waves by LIGO in 2016 [28]. However, limits from, e.g., gravitational lensing, gravitational waves, CMB distortions, dynamical constraints and gamma-rays from Hawking radiation have constrained $\Omega_{\mathrm{PHB}} \sim 1$ to two narrow mass windows around $m \sim 10^{20}\,\mathrm{g}$ and $10^{50}\,\mathrm{g}$ at best [27].

2.3.6 Alternative models

Even if there is a strong consensus that DM exists, it is important to have an open mind and consider alternative models. Since all current evidence for the existence of DM rely on its gravitational effect, the obvious alternative is to modify the gravitational theory itself in the weak field limit. This is known as modified Newtonian dynamics (MOND), first proposed by M. Milgrom in 1983 [29] (see for example Refs. [14, 30] for reviews). The idea is to modify the Newtonian law of gravitation by introducing a phenomenological interpolation function $\mu(x)$:

$$\mu(a/a_0)\boldsymbol{a} = -\nabla\Phi_N, \tag{2.6}$$

where a_0 is the typical acceleration scale below which MOND becomes influential. One must require that $\mu(x \gg 1) = 1$ to recover the well-tested Newtonian dynamics in the strong field limit, and Milgrom postulated that $\mu(x \ll 1) = x$.

Consider now for demonstration a constant galaxy rotation curve. Using Eq. (2.1) with $a = v^2/r$ and $|\nabla\Phi_N| = GM/r^2$, one finds that the velocity at large r becomes

$$v = (GMa_0)^{1/4} \sim \text{const.} \tag{2.7}$$

From Fig. 2.1 one can deduce that $v(50\,\mathrm{kpc}) \sim 200\,\mathrm{km/s}$ and $M_{\mathrm{disc}}(50\,\mathrm{kpc}) \sim 10^{11} M_\odot$ for the Milky Way. Inserting this into Eq. (2.7) gives a characteristic acceleration scale $a_0 \sim 10^{-8}\,\mathrm{cm/s^2} \simeq 10c\,(\mathrm{km/s})/\mathrm{Mpc}$. The largest fine-tuning problem in modern physics is the small magnitude of the cosmological constant compared to the Planck scale: $\Lambda \sim 10^{-56}\,\mathrm{cm^{-2}} \simeq 10^{-122} l_p^2$. It is thus intriguing that the acceleration scale of MOND is on the same order of magnitude as the Hubble parameter, $a_0/c \sim H_0 = 100h\,(\mathrm{km/s})/\mathrm{Mpc}$, and only $\mathcal{O}(1\,\%)$ to the cosmological constant, $a_0^2/c^4 \sim 10^{-58}\,\mathrm{cm^{-2}} \sim 0.01\Lambda$.

There are, however, several issues with the MOND paradigm [1]. While MOND is able to explain certain effects usually attributed to DM, like the flatness of galaxy rotation

curves, it fails to do so globally and at cosmological scales. Perhaps most problematic, frameworks of modified gravity without DM have trouble predicting the observed density perturbations and anisotropies in the CMB, and explaining phenomena like the Bullet Cluster. In addition, any attempt to include MOND into a relativistic framework seems to require the introduction of additional degrees of freedom, and even then, has trouble describing cosmological observations without the presence of DM.

3 WIMPs and the detection of dark matter

The WIMP is the archetype DM candidate. It is naturally produced as a thermal relic in the early Universe with the correct DM abundance, and in specific models, may solve the hierarchy problem.

3.1 The hierarchy problem

After the discovery of the Higgs boson in 2012 and the measurement of its mass $m_h = (125.25 \pm 0.17)\,\text{GeV}$ [1], the SM appears to be complete at first sight. Now, the Higgs mechanism can provide the masses in the electroweak sector. However, in the SM, the Higgs mass is a free input parameter[1], and an important question therefore remains: "Why is the Higgs mass $\sim 125\,\text{GeV}$?"

The *natural* physical mass scale is the Planck mass, $M_{\text{pl}} \equiv \sqrt{\hbar c/G} \approx 1.22 \times 10^{-19}\,\text{GeV}$. It is thus natural to expect that dimensionful parameters in a Grand Unified Theory are either on the order of the Planck mass, or zero if enforced by a symmetry. This is much larger than the mass of the Higgs boson, the most massive particle in the SM. The *hierarchy problem* can in essence be rephrased as the question "why is the Higgs mass much smaller than the Planck mass?"

In order to fully appreciate the complexity of the problem, one must consider how quantum corrections impact the physical mass via renormalization. Consider the SM as an effective theory of a full theory that can be used to predict m_h. The effective theory will break down at some energy scale Λ. The physical Higgs mass in the SM is $\Delta m_h^2 = m_{h,0}^2 + \Delta m_h^2$, where $m_{h,0} \sim a\Lambda^2$ is the tree-level mass and

$$\Delta m_h^2 \sim \frac{\lambda^2}{16\pi^2} \int^{\Lambda} \frac{\mathrm{d}^4 p}{p^2} \sim \frac{\lambda^2}{16\pi^2} \Lambda^2 \tag{3.1}$$

(the integral being a generic integral over the momenta of the particles in the loop) is the quantum corrections from loop diagrams [25]. Here, a and λ are dimensionless coefficients,

[1] This is in contrast to the fermions: One cannot write down a mass term for the fermions in the Lagrangian for the electroweak theory due to the chiral structure. Therefore, the Higgs mechanism is an essential part of the SM that provides the masses to the fermions.

and the theory can be considered *natural* if $a, \lambda \sim \mathcal{O}(1)$. However, if the SM would be valid until the Planck scale, then $\Lambda \sim M_{\rm pl} \gg m_h$. Thus, in order to get the observed Higgs mass, $m_{h,0}^2$ and Δm_h^2 must cancel to 1 part in 10^{36}. This is an enormous *fine-tuning* problem. However, the issue is deeper than a mere accidental near cancellation between the bare mass and the quantum corrections: The fine-tuning implies that the correction somehow is suspiciously close to $-m_h^2/\Lambda^2$ despite being decoupled from the high-energy theory.

The simplest solution to the hierarchy problem is arguably that there exists new physics at the weak scale, $m_{\rm weak} \sim$ GeV–TeV. This is one of the leading motivations for WIMPs from particle physics.

3.2 The WIMP paradigm

The Big Bang model of cosmology has been immensely successful, leading to astoundingly accurate predictions for various observables in the early Universe, such as the abundance of light elements via BBN and predicting the existence of the CMB [31]. It is thus tempting to describe the production of DM as a thermal relic in the same framework, independent of the underlying particle physics model.

Motivated by e.g. the hierarchy problem, we assume that there exists a new particle—which we call χ—in the mass range GeV–TeV with a generic interaction with SM particles, $\chi+\chi \rightleftarrows$ SM. At sufficiently high temperatures ($T \gtrsim m_\chi$), χ will be in thermal equilibrium with the primordial thermal bath in the early Universe. As the Universe expands, however, the temperature decreases, and when $T \lesssim m_\chi$, χ is no longer in *chemical* equilibrium. The particles may still be in *kinetic* equilibrium with the thermal bath via elastic collisions. Thus, the distribution of χ can be approximated by the Maxwell-Boltzmann distribution[2], which, for a non-relativistic particle species, is

$$n = g\left(\frac{m_\chi T}{2\pi}\right)^{3/2} \mathrm{e}^{-m_\chi/T}. \tag{3.2}$$

Once the annihilation rate becomes smaller than the expansion rate—known as the *Gamov criterion*—the annihilation becomes inefficient and the number density freezes out. Quantitatively, the evolution of the number density, n_χ, can be described by the Boltzmann equation [24]

$$\frac{\mathrm{d}n_\chi}{\mathrm{d}t} = -3Hn_\chi - \langle\sigma_{\rm ann}v\rangle\left(n_\chi^2 - n_\chi^{\rm eq2}\right), \tag{3.3}$$

where H is the Hubble parameter, $\langle\sigma_{\rm ann}v\rangle$ is the thermally averaged annihilation cross section and $n_\chi^{\rm eq}$ is the equilibrium number density.

[2] Variations from the thermal distribution can in principle be parametrized as a time-dependent chemical potential, μ.

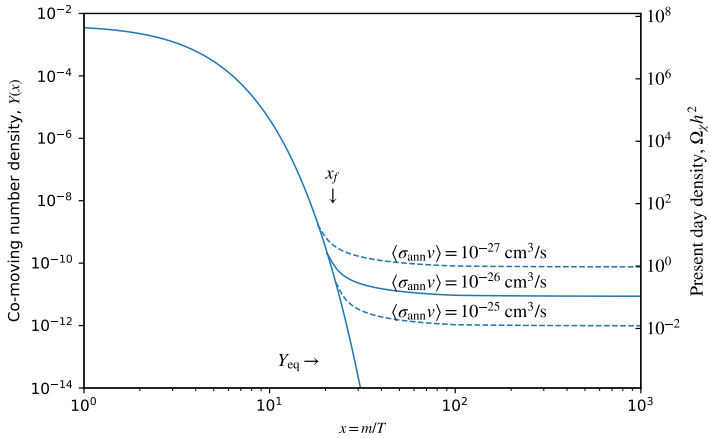

Figure 3.1: Example of evolution of the co-moving number density for a WIMP with mass $m \sim 100\,\text{GeV}$ for varying thermally averaged annihilation cross section (with the simplifying assumptions used in Ref. [24]). The right y-axis indicates the present day density expressed as $\Omega_\chi h^2$.

The exact relic abundance depends on the particle physics model contained in $\langle\sigma_{\rm ann} v\rangle$. Nevertheless, one can get an order of magnitude estimate by assuming that $\langle\sigma_{\rm ann} v\rangle = \sigma_0$ is constant during the freeze-out process, which corresponds to a pure s-wave annihilation. The solution[3] of Eq. (3.3) is shown in Fig. 3.1 for a Majorana fermion (i.e. two degrees of freedom $g = 2$) of mass $m_\chi = 100\,\text{GeV}$. A more complicated scenario (e.g. exact particle physics model and warm freeze-out) and more accurate calculation can be done using a numerical code, like DRAKE [32] or micrOMEGAs [33]. Nevertheless, from Fig. 3.1 it is evident that the relic abundance today can be estimated by a single physical quantity, namely the thermally averaged annihilation cross section at thermal decoupling. The observed value of the cold DM relic abundance today, $\Omega_\chi h^2 \simeq 0.12$, is obtained for $\sigma_0 \sim 10^{-26}\,\text{cm}^3/\text{s}$, which is a typical cross section for a weak interaction. Thus, these particles are famously known as Weakly Interacting Massive Particles, or WIMPs, and the production scenario is known as the *WIMP miracle*.

Lately, there has been an increased interest in alternative models with alternative thermal histories that may evade common constraints, since the standard WIMP has not yet been detected. A common alternative to the freeze-out process in the WIMP paradigm

[3] We consider for simplicity only the radiation dominated era and assume that kinetic freeze-out happens much later than thermal freeze-out. The Hubble parameter can then be represented as $H^2 = (8\pi/3)G\rho$, with $\rho = g_*\pi^2/30T^4$ where g_* is the number of relativistic degrees of freedom [24]. We use $g_* = 100$ for $T > 1\,\text{GeV}$, $g_* = 10\,\text{GeV}$ for $0.1 < T < 1$ and $g_* = 3.9$ for $T < 0.1\,\text{GeV}$.

is a so-called *freeze-in* process of, e.g., Feebly Interacting Massive Particles (FIMPs) [34]. In the case of FIMPs, the particle is so weakly interacting that it never attains thermal equilibrium, but is instead produced in collisional processes in the thermal bath. The produced particle may either be the observed DM itself, or decay into a lighter stable particle in a richer hidden sector. If the internal interactions within the hidden sector are sufficiently strong, the hidden sector may itself produce a thermal bath in the early Universe, and only communicate with the SM particles via a single mediator, see Ref. [35] for a review. In this case, the DM may be produced in a freeze-out process in the dark sector.

3.3 Candidates

There exists a plethora of possible WIMP (and similar) models that can explain the observed DM relic density, and new models are proposed regularly. To get a feeling for the possible extensions of the SM with a WIMP candidate, a few possible candidates will now be discussed briefly following Ref. [36].

The most popular WIMPs are those that arise in supersymmetry (SUSY) extensions of the SM. The Minimal Supersymmetric Standard Model (MSSM) is the most economical representation of SUSY, wherein each particle in the SM has a *super*partner that differs by spin 1/2, i.e. each fermion has a bosonic superpartner and each boson has a fermionic superpartner (see e.g. Ref. [37, 38] for reviews). The hierarchy problem can thereby be solved[4] since SUSY particles—known as "sparticles"—cancel all loop corrections in perturbation theory when SUSY is unbroken, thus leaving a finite correction $\Delta m_h^2 \sim \mathcal{O}(\alpha/\pi)(M_b^2 - M_f^2)$ [cf. Eq. (3.1)]. In MSSM, R-parity[5]—defined as $P_R = (-1)^{3(B-L)+2s}$ where B is the baryon number, L is the lepton number and s is the spin—is enforced as an exact symmetry. All particles have an R-parity of 1, while sparticles have -1. This has the fortunate consequence that it renders the lightest supersymmetric particle (LSP) completely stable. Thus, if the LSP is neutral, is can be a suitable DM candidate.

The lightest neutralino in the MSSM is perhaps the most popular WIMP candidate at present. It is the lightest of the four neutral composite states of the superpartners of the gauge bosons and Higgs boson. It has a mass in the range 2 GeV to 10 TeV with a large range of possible interaction cross sections. The lightest neutralino could be produced as a thermal relic via e.g. freeze-out, freeze-in or co-annihilation depending on the exact mass hierarchy and the interaction cross sections.

Another interesting LSP is the *gravitino*, the superpartner to the graviton [39]. The gravitino is massless in an unbroken SUSY, but can acquire a mass, ranging from eV to

[4] However, the much less serious *little hierarchy* problem arises since the superpartners have to be quite massive to evade current constraints.

[5] This was first introduced as a way to avoid interactions violating lepton or baryon number, such as proton decay.

TeV, in the *super*-Higgs mechanism. Gravitinos can be produced e.g. via the freeze-out mechanism or in the freeze-in mechanism as a decay product of the next lightest sparticle.

In the Two Higgs Doublet Model (2HDM), the Higgs sector is extended by an additional doublet giving rise to extra charged and neutral Higgs bosons. In the simplest extension (known as an inert doublet model), an additional Z_2 symmetry is imposed such that SM particles are even and the new Higgs bosons are odd. Then, one of the new additional neutral Higgs bosons may take the role of DM if it is the lightest odd particle.[6] In addition, the 2HDM can be used to induce an additional CP violation needed for baryogenesis.

In the *little Higgs* model, the SM Higgs boson is itself a pseudo-Goldstone boson of a new global SU(3) symmetry which is broken into the electroweak SU(2) symmetry, see Ref. [41] for a concise pedagogical introduction.[7] The Higgs mass is ensured by constructing the new Lagrangian as $\mathcal{L} = \mathcal{L}_0 + \lambda_1\mathcal{L}_1 + \lambda_2\mathcal{L}_2$, where $\mathcal{L}_0$ is the SU(3) conserving SM Lagrangian, while $\mathcal{L}_i$ $(i = 1, 2)$ are individually SU(3) conserving, but explicitly broken when combined. The little Higgs model is well motivated since it gives a natural solution to the hierarchy problem: New heavy states act as partners to the top quark and gauge boson in such a way that the divergences of the Higgs mass are cancelled at one-loop. Thus, the Higgs mass $m_h^2 \simeq (125\,\mathrm{GeV})^2 \sim \lambda_1^2/16\pi^2\ \lambda_2^2/16\pi^2\ \Lambda^2$ remains natural ($\lambda_i \sim 1$) even for cutoff scales as large as $\mathcal{O}(10)\,\mathrm{TeV}$. To have a suitable DM candidate, a Z_2 symmetry, often called a T-parity, has to be assumed. In this case, the lightest particle in the partner field is stable.

In the *twin Higgs model*, the hierarchy problem is solved by introducing a twin sector as a full or partial copy of the SM. The two sectors are connected via a Z_2 symmetry. Similar to the little Higgs model, the Higgs is a pseudo-Goldstone boson of a broken approximate symmetry, in this case a U(4) symmetry. The lightest particle in the twin sector may take the role as DM. Alternatively, DM can be explained by a scalar, similar to the 2HDM.

A vast number of other models exists in the literature, many of which lack a deeper theoretical framework. It is thus up to experiments to determine which of these is true. Nevertheless, most of these can be categorized by generic portals between the dark sector and the SM, thereby allowing for a model-independent study of the DM properties (see e.g. the excellent discussion is given in Ref. [42]).

[6] Note that this bares a resemblance to the lightest neutralino: In fact, the MSSM shares the same Higgs structure as the 2HDM model [40].

[7] The idea is similar to the pion masses: In the limit of equal and massless up and down quarks, quantum chromodynamics (QCD) can be regarded as an effective chiral SU(2) symmetry, which is spontaneously broken into $\mathrm{SU}(2) \times \mathrm{U}(1)_V$. The pions can be associated as the Goldstone bosons to this broken symmetry. However, since it is not an exact symmetry (the masses of the up and down quarks are non-zero), the pions have a small but non-zero mass.

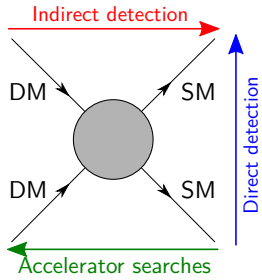

Figure 3.2: Graphical representation of the detection methods for WIMPs: Indirect detection makes searches for SM particles that are produced in DM annihilations, $\mathrm{DM} + \mathrm{DM} \rightarrow \mathrm{SM} + \mathrm{SM}$ (or decays). By crossing the Feynman diagram for the interaction, it is clear that also the interactions $\mathrm{DM} + \mathrm{SM} \rightarrow \mathrm{DM} + \mathrm{SM}$ (utilized in direct detection experiments) and $\mathrm{SM} + \mathrm{SM} \rightarrow \mathrm{DM} + \mathrm{DM}$ (utilized in accelerator searches) are allowed.

3.4 Detection

The detection methods of WIMPs are based on the generic observation that the WIMPs are produced in the early Universe via the interactions $\mathrm{SM} + \mathrm{SM} \leftrightarrow \mathrm{DM} + \mathrm{DM}$, and that by crossing the Feynman diagram as shown in Fig. 3.2, the interaction $\mathrm{SM} + \mathrm{DM} \rightarrow \mathrm{SM} + \mathrm{DM}$ may also occur. The detection schemes can as such be split into three categories: indirect, direct and accelerator searches. In *indirect detection* experiments, one tries to observe SM particles on Earth produced in the interaction $\mathrm{DM} + \mathrm{DM} \rightarrow \mathrm{SM} + \mathrm{SM}$. In *direct detection* experiments, the hope is that a DM particle will elastically scatter in the detector material, $\mathrm{DM} + \mathrm{SM} \rightarrow \mathrm{DM} + \mathrm{SM}$. Meanwhile, in *accelerator* searches, one tries to produce DM particles, $\mathrm{SM} + \mathrm{SM} \rightarrow \mathrm{DM} + \mathrm{DM}$, at a particle accelerator.

The three detection methods are highly complementary: Indirect detections are mostly dependent on the annihilation cross section or decay rate, direct detection on the DM-nucleon or DM-electron interaction cross section, and accelerator searches on the production cross section. Furthermore, the expected signals in direct and indirect searches depend strongly on the astrophysical assumptions made, such as the DM phase space distribution in the Milky Way. In all cases, the exact signal depends on the exact particle physics model of the DM. As a consequence, most searches are focused on being as model-independent as possible, and while the exact correlations between the different searches are highly model dependent, they can be achieved using, e.g., the global fitting package GAMBIT [43].

3.4.1 Direct detection

One may hope to detect DM by observing the scattering of nuclei or electrons in detectors on Earth. Due to the small interaction rate, large underground detectors are generally required to obtain a significant signal rate while evading noise from cosmic rays and neutrinos. The field of direct detection experiments is intensely active, and to do the experimental activity and the theory behind it justice with a short introduction is impossible. Therefore, we will refrain from discussing specific experiments, highlighting the physical motivation instead.

The existence of a dark halo in the Milky Way as inferred by rotation curve measurements imply that there will be a flux of DM,

$$\Phi_{\rm DM} \simeq 10^5\,{\rm cm}^{-2}{\rm s}^{-1}\left(\frac{m_{\rm DM}}{100\,{\rm GeV}}\right)^{-1}\left(\frac{v_\odot}{200\,{\rm km/s}}\right)\left(\frac{\rho_\odot}{0.3\,{\rm GeV/cm}^3}\right), \tag{3.4}$$

through the Earth. In addition, there is a seasonal variation from the motion of the Earth around the Sun as well as a daily perturbation, which can be used as a smoking gun signal. A direct detection experiment typically searches for elastic collisions between the DM and a nucleus in the detector. The differential recoil spectrum is [14]

$$\frac{{\rm d}R}{{\rm d}E_R} = \frac{\rho_\odot}{m_\chi m_N}\int_{v_{\rm min}}^{\infty} {\rm d}^3v\, v f(v)\frac{{\rm d}\sigma}{{\rm d}E_R}, \tag{3.5}$$

where m_N is the nucleon mass, $f(v)$ is the velocity distribution of the DM and ${\rm d}\sigma/{\rm d}E_R$ is the differential cross section for the elastic scattering with the nucleus. The upper integration is formally infinity, but one usually truncates the integration at the local Galaxy escape velocity, $v_{\rm esc} = \sqrt{2\Phi(r_\odot)} \sim 500\,{\rm km/s}$. Meanwhile, the minimum velocity that can lead to a signal event is $v_{\rm min} = (m_\chi + m_N)\sqrt{E_0/2m_N}/m_\chi$, where E_0 is the threshold energy of the detector. The signal rate becomes

$$R = \frac{\rho_\odot}{m_N m_\chi}\int_{E_0}^{\infty}{\rm d}E_R\int_{v_{\rm min}}^{v_{\rm esc}}{\rm d}^3v\, v f(v)\frac{{\rm d}\sigma}{{\rm d}E_R}. \tag{3.6}$$

For an isotropic, singular, isothermal DM distribution the velocity follows a simple Maxwellian[8],

$$f(v) = \frac{1}{\sqrt{2\pi\sigma^2}}{\rm e}^{-\frac{v^2}{2\sigma^2}}, \tag{3.7}$$

where $\sigma = \sqrt{3/2}v_c$ with $v_c = 220\,{\rm km/s}$ at the location of the Earth as inferred from rotation curves [14]. This is typically considered a valid approximation since DM is

[8] In addition, DM that can interact with the detector will generically be up-scattered by cosmic rays in the Milky Way [44]. This leads to a heavier tail than the standard Maxwellian velocity distribution assumed.

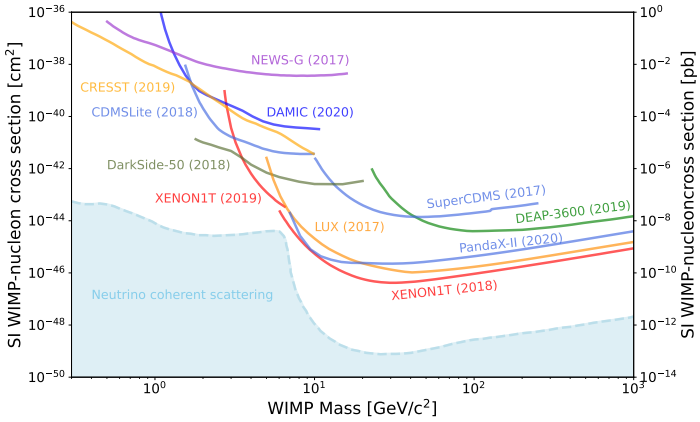

Figure 3.3: Current best limits on the SI DM-nucleon interaction cross section. The figure is taken from Ref. [1].

collisionless, but the uncertainties related to the velocity distribution can in any case be integrated out using the method described in Ref. [45].

The direct searches can qualitatively be characterized as either spin-dependent (SD) or spin-independent (SI). In the former case, one searches for the axial interaction ($\mathcal{L} \sim [\bar{\chi}\gamma^\mu\gamma_5\chi][\bar{q}\gamma_\mu\gamma_5 q]$), while the latter searches for a scalar ($\mathcal{L} \sim \bar{\chi}\chi\bar{q}q$) or vector ($\mathcal{L} \sim \bar{\chi}\gamma_\mu\chi\bar{q}\gamma^\mu q$) interaction instead [14]. For example, the neutralino interacts as a scalar in a SI interaction. In the non-relativistic limit, the elastic cross section can be written as [14]

$$\frac{\mathrm{d}\sigma(E_R, v)}{\mathrm{d}E_R} = \frac{m_N}{2v^2}\frac{(m_N + m_\chi)^2}{m_N^2 m_\chi^2}\left(\sigma_0^{\mathrm{SI}} F_{\mathrm{SI}}^2(E_R) + \sigma_0^{\mathrm{SD}} F_{\mathrm{SD}}^2(E_R)\right), \tag{3.8}$$

where σ_0^i is the elastic cross section at zero momentum transfer and $F(E_R)$ is the nucleon form factor.[9] In the SI interaction, the contribution from individual nucleons contribute coherently, implying that large nuclei are favored as detector material. In SD interactions, on the other hand, the interaction cross section will be determined to a large extent by the total spin of the nucleus.

In Fig. 3.3, the current upper limits on the SI DM-nucleon cross section is shown as a function of the DM mass. The experiments are most sensitive at WIMP masses in the range 10–100 GeV, since the experiment will be sensitive to most of the velocity distribution at these masses. At lower energies, the experiments loose sensitivity since the portion of the DM above the minimum energy v_{min} rapidly diminishes. At the same time, the sensitivity will fall off as $1/m_\chi$ at large masses, given that the DM number density is inversely proportional to the DM mass. As a consequence, to improve the

[9] The form factors must be included since the DM particle is sensitive to the entire nucleus.

sensitivity at higher masses, one must increase the statistics with more exposure time and by building larger detectors. At low masses, on the other hand, a reduced threshold is needed, since the average momentum transfer in an elastic nuclear recoil is $E = q^2/2m_N \simeq 1\,\text{eV}\ (m_\chi/100\,\text{MeV})^2(10\,\text{GeV}/m_N)$ (where m_N is the nucleus mass, $q \sim m_\chi v$ and $v \sim 10^{-3}$) [46]. It is thus apparent that an alternative process or observable is needed to detect sub-GeV DM directly, such as phonons excited from atomic de-excitation, or individual electrons and ions due to DM-electron interactions [46] (see Ref. [1] for a short overview). Furthermore, the blue region in Fig. 3.3, known as the *neutrino floor*, indicates the cross section at which the background noise from neutrino interactions becomes significant. In order to obtain sensitivities significantly below the neutrino floor, one either needs to have an accurate model for the background flux or to use directional information to disentangle the two signals.

Today, the best limits on DM-nucleus cross sections come from detectors using liquid Argon or Xenon as detector material. For example, the XENON1T experiment puts strong limits using the conventional nucleus recoil [47] and ionization signals [48]. The next generation liquid noble gas detectors, like Darkside-20, LZ, PandaX-4T and XENONnT, are expected to improve the sensitivities by 1–2 orders of magnitude, thus hitting the neutrino floor [1]. XENONnT is currently operational, and among the first science outcomes in 2022 [49] was the non-detection of the excess observed by XENON1T in electronic recoil events from 2020 [50]. In addition, there is much work done on alternative detector techniques for sub-GeV DM based on phonon excitation in solid state detectors.

3.4.2 Indirect detection

Indirect detection of WIMPs usually refers to the detection of SM particles produced in DM annihilations or decays in the Milky Way.[10] Upon annihilation, the particles may produce a number of SM particles depending on the exact particle physics model. Since DM cannot have a significant electromagnetic interaction, the particles can be produced as a continuum energy spectrum in a parton cascade initiated by a weak interaction, e.g., into two W bosons, $\chi\chi \to W^+W^-$, or two quarks, $\chi\chi \to q\bar{q}$. The source spectrum of a particle species i at a position $\boldsymbol{r}$ in the Milky Way can be written as[11]

$$Q^{(i)}(E, \boldsymbol{r}) = \frac{1}{2}\frac{\rho^2(\boldsymbol{r})}{m_\chi^2} \int \mathrm{d}^3r\, \mathrm{d}^3v_1\, \mathrm{d}^3v_2\, f(v_1) f(v_2) \sigma^{(i)}_{\text{ann}}(E)|v_1 - v_2|, \tag{3.9}$$

where $\sigma^{(i)}_{\text{ann}}$ is the annihilation cross section into the particle species i with energy E. For a standard WIMP, it is common to approximate the annihilation cross section by the

[10] For concreteness, we will only focus on annihilation processes, but the formulas can easily be modified to hold for decay processes.

[11] It is assumed that the DM particle is its own antiparticle. An additional factor 1/2 has to be included if this is not the case.

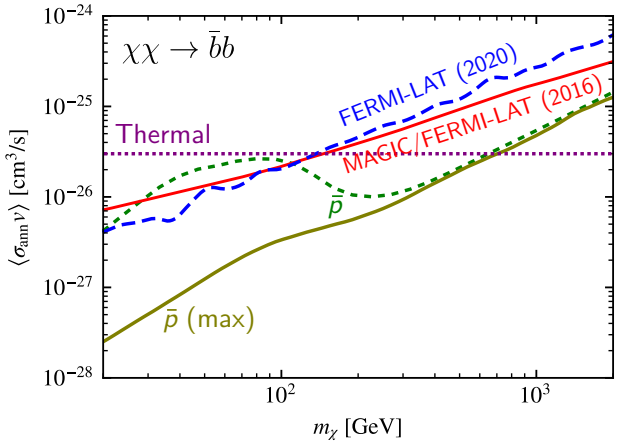

Figure 3.4: Upper limit (95 % CL) on the thermally averaged annihilation cross section from gamma-rays from dwarf satellite galaxies (blue dashed [55] and red solid [56] lines) and antiproton measured by AMS-02 (green dashed [57] and olive solid lines [58]) for the annihilation channel $\chi\chi \to \bar{b}b$. The olive line is obtained by pessimistically assuming that there is no excess in the AMS-02 antiproton data [58]. For comparison, the canonical thermal relic value $\langle\sigma_{\rm ann}v\rangle = 3 \cdot 10^{-26}\,\mathrm{cm}^3/\mathrm{s}$ is shown (purple dashed line).

partial wave expansion in $T/m_\chi \propto v^2$ as $\langle\sigma_{\rm ann}v\rangle = \sigma_0 + \sigma_2 v^2 + \cdots + \sigma_{2n}v^{2n}$ (see however Ref. [51] for some exceptions). Since the velocity today is smaller than the velocity at thermal freeze-out, the annihilation cross section will generally be dominated by the s-wave annihilation ($n = 0$).[12] In this case, the source spectrum takes the simplified form

$$Q^{(i)}(\boldsymbol{r}, E_\chi) = \frac{1}{2}\frac{\rho^2(\boldsymbol{r})}{m_\chi^2}\sum_j \langle\sigma_{\rm ann}v\rangle_j \frac{\mathrm{d}N^{(i)}}{\mathrm{d}E}, \tag{3.10}$$

where the sum goes over all possible branching ratios, $\chi\chi \to \{W^+W^-, \bar{b}b, \bar{c}c, \ldots\}$. Note that the particle physics model of the DM is encoded in the branching ratios and the annihilation cross section, $\langle\sigma_{\rm ann}v\rangle_j$, while the astrophysical modeling is contained in $\rho(\boldsymbol{r})$. The differential spectrum, $\mathrm{d}N^{(i)}/\mathrm{d}E_\chi$, should be computed using a Monte Carlo (MC) event generator, such as Pythia [53] or Herwig++ [54]. As an example, the upper limit on $\langle\sigma_{\rm ann}v\rangle$ is shown in Fig. 3.5 for a WIMP annihilating into $b\bar{b}$.

[12] On the other hand, Sommerfeld enhancement (effectively $n < 0$ in the partial wave expansion) may significantly enhance the annihilation rate (see e.g. Ref. [52] for a recent discussion on the subject).

In indirect detection searches, gamma-rays, neutrinos and antimatter are usually used as probes. *Gamma-rays* produced in DM annihilations or decays are created mainly by the decay of neutral pions produced in a hadronization process of a strongly interacting final state, as internal bremstrahlung photons, and as final state radiation. For decaying DM, the decay channel $\chi \to \gamma\gamma$ would be a smoking-gun signal; an emission line slightly broadened by the velocity distribution and possibly from $\chi \to \gamma Z$ if allowed kinematically. The main advantage of using gamma-rays as a probe for DM is that they propagate in a straight line and are easy to detect. One may thus hope to observe an excess of photons near gravitational wells, such as globular clusters, dwarf galaxies or the Galactic center, because over-densities of DM augment the annihilation rate. Gamma-ray detectors like Fermi-LAT, HESS, MAGIC and HAWC have provided an accurate measurement of the gamma-ray sky, ideal to search for such excesses. It is thus intriguing to note that an excess consistent with annihilating DM with $m_\chi \sim 50\,\text{GeV}$ and $\langle\sigma_{\text{ann}}v\rangle \sim 10^{-26}\,\text{cm}^3/\text{s}$ from the Galactic center was discovered in 2009 [59]. The excess still persists, but the interpretation is debated [60, 61], with the most favored alternative being an unknown population of millisecond pulsars [62, 63] (see Ref. [64] for a review).

The main disadvantage of using *neutrinos* is that they are notoriously difficult to detect. Nevertheless, this implies that neutrinos may be used as a probe for DM annihilations inside stellar object, such as the Sun or the Earth, as they would escape nearly freely.[13] The non-detection of high-energy neutrinos from e.g. the Sun can be reinterpreted as a limit on the DM-nucleon cross section, since a substantial elastic DM-nucleon cross section is needed to capture the DM [65]. This has been used to make competitive limits using IceCube [66] and ANTARES [67].

Both gamma-rays and neutrinos suffer from large background noise. *Cosmic ray antimatter*, on the other hand, has a reduced background due to the baryon asymmetry of the Universe, making positrons, antiproton and antinuclei promising detection channels. The main background for these particles is expected to originate in so-called secondary interactions, that is, in the collision between high-energy primary cosmic rays (mainly protons) and the interstellar matter (mainly hydrogen). However, the charged particles will diffuse in the Milky Way before reaching Earth, implying that any directional information is lost and that theoretical predictions suffer from large propagation uncertainties. Nevertheless, an excess of high-energy positrons at $E \sim 10$–$300\,\text{GeV}$ over the expected secondary production is firmly established [68]. This suggests the existence of a new primary source, such as pulsars or even DM annihilations. Unfortunately, the excess is not present in the antiproton data and the spectral shape is difficult to explain as a DM signal, putting strong constraints on the possible DM model [69–71]. Furthermore, a small excess in the antiproton data from AMS-02 around 10–20 GeV compatible with an $\sim 80\,\text{GeV}$ WIMP has been reported (e.g. Refs. [57, 72]). Unfortunately, the antiproton excess vanishes when

[13] Alternatively, the DM may annihilate into a semi-stable dark sector particle, which in turn decay into observable SM particles outside the stellar object.

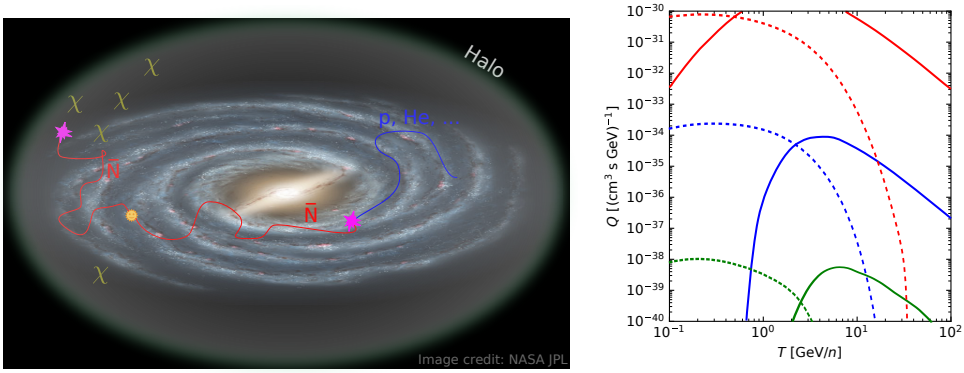

Figure 3.5: Left: The main background of cosmic antinuclei are expected to come from secondary production, where primary particles (p, He, ...) collide with the interstellar matter (mainly hydrogen and helium). In addition, a primary component may be produced in DM annihilations in the dark halo. The antinuclei will diffuse in the Milky Way before reaching Earth. Right: Example of the production spectrum of antiproton (red), antideuteron (blue) and antihelion (green) from secondary production (solid lines) and dark matter annihilations (dashed lines) [58, 75].

the correlations of the systematic uncertainties are taken into account [73].

Low energy antinuclei, such as antideuteron and antihelion, are often considered as the ideal probes for DM annihilations due to their extremely low background at low energies. The general idea is sketched in Fig. 3.5: Since the main background comes from high-energy particles impinging on the interstellar matter approximately at rest, the produced particles will in general have a large kinetic energy. The suppression of antideuterons will be larger than that of antiprotons, and antihelions larger than that of antideuterons, due to the increased threshold energies.[14] Meanwhile, the antinuclei produced by annihilating or decaying DM will in general have low energies. Thus, the detection of a low energetic antinucleus is a smoking-gun signal for new and exotic physics. The community was therefore intrigued when the AMS-02 collaboration reported the detection of a handful of antihelion candidates in 2018 [74]. Unfortunately, the results are not published yet, and the GAPS and AMS-02 experiments might not observe a signal due to the stringent limits from the antiproton data [58].

[14] e.g. $pp \to \bar{p}ppp$ for antiprotons compared to $pp \to ppp n \bar{p}\bar{n}$ for antideuterons.

3.4.3 Accelerator searches

The main advantage of accelerator searches is that they do not suffer from astrophysical uncertainties. In accelerator searches, one typically uses missing transverse momentum as a probe for a DM particle, since they will leave the detector without any interactions. Alternatively, one looks for decays of a DM mediator into a pair of quarks or leptons [76]. The experimental effort at CMS and ATLAS focus on the nature of the mediator (which could be a scalar, vector, pseudo-scalar or axial vector) and its coupling to quarks, leptons and the DM particle [76]. As such, scans over the DM and mediator masses are usually performed. The biggest disadvantage of accelerator searches is arguably that one searches for a generic (semi-)stable particle, and it is therefore not given that the new particle can indeed explain DM. Moreover, they can only probe new physics up to a threshold given by the collision energy.

4 Axions and axion-like particles

4.1 The strong CP problem

The strong CP problem is a *naturalness* problem in QCD related to the observation that the measured neutron dipole moment is miniscule, if not exactly zero, $|d_n| \lesssim 10^{-26} e\,\mathrm{cm}$ [1]. In order to get a more intuitive understanding of the problem, consider the simple "classical" quark model of the neutron consisting of two down-quarks at a distance r from one up-quark, as shown in Fig. 4.1. The electric dipole moment corresponding to this simple picture is $d_n^2 \sim 3\left\langle d_n^2 \right\rangle / 2 = e^2 \left\langle r^2 \right\rangle \left\langle \sin^2\theta \right\rangle$. With $\left\langle r^2 \right\rangle \sim 1/m_\pi^2 \approx 55\,\mathrm{GeV}^{-2}$ as a typical size of the distance between the quarks, the dipole moment becomes $d_n \approx 10^{-13} e\,\mathrm{cm} \langle \sin^2\theta \rangle^{1/2}$. This implies that $\theta \ll 1$, which contradicts the expectation $\theta \sim 1$ for a natural theory.[1]

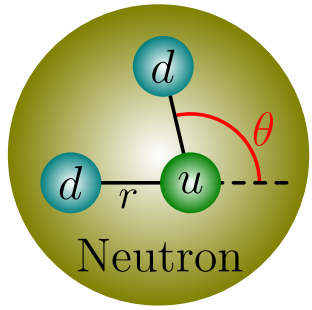

Figure 4.1: A "classical" quark model represent of the neutron consisting of two down-quarks and one up-quark. If $\theta \neq 0$, the neutron has an electric dipole moment.

The QCD Lagrangian should be constructed as the set of all mass dimension four operators. Thus, it will in general contain a term

$$\mathcal{L}_{\mathrm{QCD}} \supset \frac{g^2}{32\pi^2} \theta\, \mathrm{tr}\Big\{ G_{\mu\nu} \tilde{G}^{\mu\nu} \Big\}, \tag{4.1}$$

[1] It should be emphasized that this is a mere visualization of the strong CP problem intended to yield an intuitive understanding of the neutron electric dipole moment and the axion solution that will be discussed in Sec. 4.2. There is currently no simple relation between simple phenomenological models of the hadron structures and the CP violating term in the QCD Lagrangian in Eq. (4.1) [77].

where $G^a_{\mu\nu}$ is the gluon field strength tensor, $\tilde{G}^a_{\mu\nu}$ its dual, g is the coupling and θ is a dimensionless parameter. Nevertheless, the term $G_{\mu\nu}\tilde{G}^{\mu\nu}$ was neglected until the late 1970s—and is still neglected in introductory courses—since it is a four-divergence and therefore, does not contribute to the classical equation of motion. However, due to the non-trivial vacuum of QCD, the term can still give a contribution to the action and thus have physical consequences. The lowest energy associated with such a non-zero contribution happens for the *instanton* solutions to the Euclidean Yang-Mills theory, i.e. $\tilde{G}_{\mu\nu} = \pm G_{\mu\nu}$ [24]. If one considers the SU(2) subgroup[2] of QCD, the Euclidean action becomes [78]

$$S = \frac{1}{2}\int \mathrm{d}^4x\, \mathrm{tr}\{G_{\mu\nu}\tilde{G}_{\mu\nu}\} = \frac{16\pi^2}{g^2}. \tag{4.2}$$

Since SU(2) is isomorphic to the hypersurface $\mathcal{S}^3$, Eq. (4.2) corresponds to the simplest non-trivial mapping $\mathcal{S}^3 \to \mathcal{S}^3$. The mappings can in general characterized by an integer winding number ν, $S = 16\pi^2\nu/g^2$, which essentially describes[3] how many times $\mathcal{S}^3$ is covered under the mapping $\mathcal{S}^3 \to \mathcal{S}^3$. The angle θ in the Lagrangian (4.1) describes the true vacuum as a superposition of the vacua of fixed winding number [24]:

$$|\theta\rangle = \sum_\nu \mathrm{e}^{\mathrm{i}\theta\nu}\,|\nu\rangle\,, \tag{4.3}$$

where $\theta \in [0, 2\pi)$. Hence, the effect of the non-trivial vacuum is an effective symmetric potential[4], which as a first approximation, can be assumed to be

$$V_{\text{eff}} \sim \cos(\theta)\,. \tag{4.4}$$

One of the most substantial consequences of the CP violating term (4.1), is that it gives rise to an electric neutron dipole moment $d_n \sim 10^{-16}\theta e\,\mathrm{cm}$ [79]. Thus, from measurements of the neutron electric dipole moment, one finds $\theta \lesssim 10^{-10}$. This is a *true* naturalness problem, since θ will have an additional, unrelated contribution from the diagonalization of the quark mass matrix of the electroweak sector, $\bar{\theta} \equiv \theta - \arg\det M_q$, and there is no reason to a priori expect that $\bar{\theta} \simeq 0$. This naturalness problem is known as the *strong CP problem*.

4.2 The axion as a solution to the strong CP problem

As a solution to the strong CP problem, R. D. Peccei and H. Quinn postulated the existence of an additional U(1) symmetry—usually denoted as $\mathrm{U}(1)_{\mathrm{PQ}}$—that is spontaneously

[2] That is, the solution of $\tilde{G}_{\mu\nu} = G_{\mu\nu}$ which simultaneously is invariant under rotations and is isotropic.

[3] For a simple 1D correspondence, think about wrapping U(1) around a circle: The winding number then represents the number of times U(1) has gone around the circle as $\mathrm{e}^{\mathrm{i}\nu\theta}$ on $\mathcal{S}^1$.

[4] Since the action is $S \propto \nu$, the matrix element $\langle\nu'|\,H\,|\nu\rangle$ will only depend on $|\nu' - \nu|$. Thus, the instantons will lead to a symmetric and periodic effective potential V_{eff}, see e.g. [24] for the complete argument.

broken [22]. The Nambu-Goldstone boson associated with this broken symmetry is today known as the *axion*. Their idea is well visualized by the "strong CO_2 problem" in Fig. 4.2: The potential energy of the CO_2 molecule is minimum for $\theta = 0$, in which case the dipole moment vanishes. That is, Peccei and Quinn solved the strong CP problem by promoting the angle θ to a dynamical field, which relaxes to zero for an appropriate choice of potential. However, they did not take note of the physical consequences of their idea: Soon after the proposal by Peccei and Quinn, Weinberg and Wilczek independently noticed that the Nambu-Goldstone boson from the broken symmetry mixes with neutral pseudoscalar mesons[5] (π^0 and η), thus obtaining a small but non-zero mass [80, 81]. Hence, the particle becomes a pseudo-Goldstone boson with physical consequences. Wilczek could thus fulfill a dream of his adolescence, namely to name a particle [82]: *"A few years before, a supermarket display of brightly colored boxes of a laundry detergent named Axion had caught my eye. It occurred to me that 'axion' sounded like the name of a particle and really ought to be one. So when I noticed a new particle that 'cleaned up' a problem with an 'axial' current, I saw my chance."*

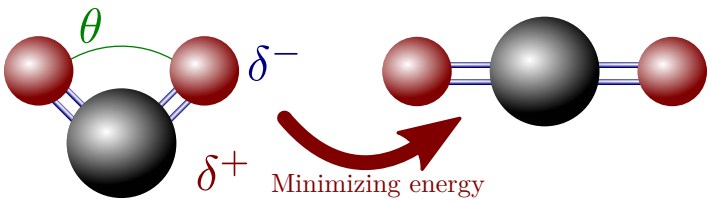

Figure 4.2: The CO_2 molecule consists of two oxygen and one carbon atoms. If the atoms are not on a single line, the molecule will have a small electric dipole moment, δ, since the shared electrons are closer to the oxygen atoms. However, the CO_2 molecule has a vanishing dipole moment experimentally. This can be explained by its double bindings, which makes sure that the atoms align at low temperatures.

Formally, the SM can be made $\mathrm{U}(1)_{\mathrm{PQ}}$ invariant by including the following terms in the SM Lagrangian [83]:

$$\mathcal{L} \supset \frac{1}{2}\left(\partial_\mu a\right)^2 - \left(\frac{a}{f_a} + \bar{\theta}\right)\frac{g^2}{32\pi^2} G\tilde{G} + \mathcal{L}_{\mathrm{int}}[\partial^\mu a/f_a, \Psi], \tag{4.5}$$

where a is the Nambu-Goldstone boson (i.e. the *axion*) associated with the broken $\mathrm{U}(1)_{\mathrm{PQ}}$ symmetry.[6] An $\mathrm{U}(1)_{\mathrm{PQ}}$ transformation leads to the shift $a \to a + \alpha f_a$ and the CP

[5] Note that the term $aG\tilde{G}$ in Eq. 4.1 resembles a two-gluon–axion vertex, which leads to mixing with the neutron pion via triangular Feynman diagrams.

[6] Note that $a\tilde{G}G$ is a dimension-5 operator and thus non-renormalizable. The axion therefore requires new physics at a scale of f_a, which is encoded in the interaction term $\mathcal{L}_{\mathrm{int}}$ in Eq. (4.5).

violating coefficient $\bar{\theta}$ can thereby be absorbed by an appropriate $\mathrm{U}(1)_{\mathrm{PQ}}$ transformation. The CP violating term $a/f_a + \bar{\theta}$ will be dynamically relaxed to zero in this way, since this minimized the effective potential provided by instanton effects [Eq. (4.4)]. At first glance, the problem is automatically solved without any side effect. However, as realized by Wilczek and Weinberg, a mass of the field a is generated as the second derivative of the potential, $m_a^2 = \langle \mathrm{d}^2 V_{\mathrm{eff}}/\mathrm{d}a^2 \rangle$, or alternatively, via the mixing with the pseudo-scalar mesons, $m_a f_a \approx m_{\pi^0} f_{\pi^0}$, with the current best calculation giving [1]

$$m_a = 5.691(51) \left(\frac{10^9\,\mathrm{GeV}}{f_a} \right) \mathrm{meV}. \tag{4.6}$$

4.3 Axion-like particles (ALPs)

Since the axion mixes with neutral pseudo-scalar mesons, it will inherit their two-photon coupling. Thus, the axion Lagrangian should effectively contain a term $\mathcal{L} \supset \frac{1}{4} g_{a\gamma} a F \tilde{F}$, where F is the electromagnetic field strength tensor and $\tilde{F}$ its dual. By an appropriate axial transformation of the quark mass matrix, one can show that [1, 84]

$$g_{a\gamma} \sim \frac{\alpha}{2\pi f_a} \sim 0.1 \frac{m_a}{\mathrm{GeV}^2}, \tag{4.7}$$

up do a factor $\mathcal{O}(1)$ depending on the exact implementation of the UV completion of the axion model.

A more general class of particles that shares the same two-photon coupling as the axion is known as *axion-like particles*, or ALPs. Although they do not solve the strong CP problem, they are nevertheless interesting since they arise naturally in string theories and other extensions of the SM [85, 86]. An ALP is a spin-less and neutral pseudo-scalar (or scalar) boson described by the Lagrangian

$$\mathcal{L}_{\mathrm{ALP}} = \frac{1}{2}(\partial_\mu a)(\partial^\mu a) - \frac{1}{2} m_a^2 a^2 - \frac{1}{4} g_{a\gamma} \tilde{F} F, \tag{4.8}$$

where m_a is its mass, $g_{a\gamma}$ is the two-photon coupling constant, and F is the electromagnetic field strength tensor and $\tilde{F}$ its dual. The two-photon coupling implies that an ALP can convert into a photon by interacting with a virtual photon from a transverse magnetic field, often known as the *Primakoff effect*.[7] This leads to a wide range of fascinating physical phenomena, such as photon-ALP oscillations in astrophysical magnetic fields and cooling of stellar objects. In Sec. 4.5, we will discuss how the Primakoff effect is used to search for axions and ALPs.

[7] The Primakoff effect first referred to the production of a pseudo-scalar meson from a photon interacting with a virtual photon from a magnetic field [87]. This is perhaps easiest realized experimentally in a resonant production of pseudo-scalar mesons for a photon interacting with a nucleus.

4.4 Axionic dark matter and the misalignment mechanism

Axions and ALPs will be produced as thermal relics in the early Universe, similar to the thermal production of WIMPs discussed in Sec. 3.2. They are in thermal equilibrium until the rate of the interaction $\pi\pi \to \pi a$ falls below the Hubble rate (see Refs. [88, 89] for additional contributing processes and complications), and may contribute significantly to the non-baryonic relic abundance if they are massive enough. However, the decay rate of ALPs into a pair of photons is [1]

$$\Gamma_{a\to\gamma\gamma} = \frac{g_{a\gamma\gamma}^2 m_a^3}{64\pi} \simeq 1.1 \cdot 10^{-24} \left(\frac{m_a}{\mathrm{eV}}\right)^5 \mathrm{s}^{-1}, \tag{4.9}$$

where the last equality holds for axions [from Eq. (4.7)]. Thus, in order to be stable on cosmological scales ($\Gamma \gtrsim t_{\mathrm{age}}^{-1} \simeq 2 \cdot 10^{-18}\,\mathrm{s}$), one must require that $m_a \lesssim 20\,\mathrm{eV}$. This becomes even more pronounced when considering stellar cooling limits (see Sec. 4.5). Thence, the population of thermal axions is negligible for a standard thermal history and will only contribute to the hot DM similar to the neutrinos. On the other hand, thermal ALPs with small coupling and large mass ($m_a \gtrsim 0.15\,\mathrm{eV}$ [89]) may contribute significantly to the non-baryonic relic density.

The axion (or ALP) can still be a suitable DM candidate despite its small mass if it is produced in the so-called *misalignment mechanism* [90–92]. The general idea visualized in Fig. 4.3 for a simple "Mexican hat" potential: In the early Universe, the $\mathrm{U}(1)_{\mathrm{PQ}}$ symmetry is unbroken, and the field can take any value between 0 and 2π. After the QCD phase transition, instanton effects generate the mass term, and the axion field starts oscillating around the new CP conserving minimum. The expansion of the Universe acts as friction, ensuring that the strong CP problem is solved in the present day, as visualized in Fig. 4.4. If the evolution is adiabatic, the energy density stored in the axion field will be converted into physical axions.

The misalignment mechanism can be described quantitatively by considering the evolution of the axion field in the Friedman-Robertson-Walker (FRW) metric [88],

$$\ddot{a}(t) + 3H\dot{a}(t) + m_a(t)^2 f_a \sin\left(\frac{a(t)}{f_a}\right) = 0 \tag{4.10}$$

for the axion potential

$$V_a = f_a^2 m_a^2(t)\left[1 - \cos(a/f_a)\right]. \tag{4.11}$$

Before the axion acquires a mass (around the QCD phase transition, $T_{\mathrm{QCD}} \sim$ GeV), the mass term can be neglected. Then, after remembering that $H = 1/2t$ in the radiation dominated era, the solution to Eq. (4.10) is $a(t) = A + Bt^{-1/2}$. As such, the expansion

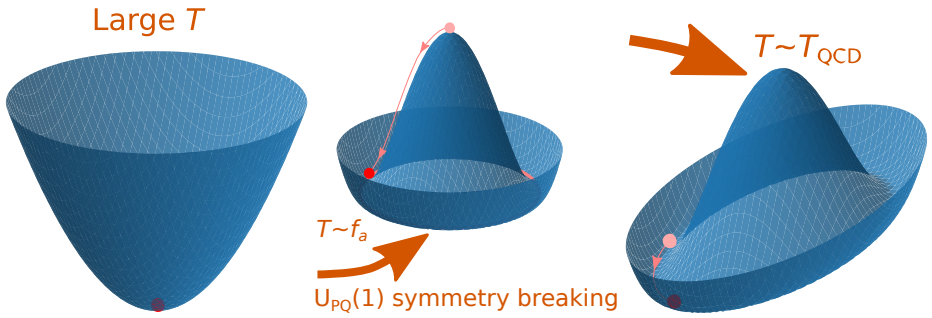

Figure 4.3: Visualization of the breaking of symmetries in the misalignment mechanism using a "Mexican-hat" potential. Left: Before the Peccei-Quinn symmetry breaking, the field is relaxed at the potential minimum. Middle: After the Peccei-Quinn symmetry breaking, the axion field will fall into the new potential minimum with some arbitrary misalignment angle. However, the angle is not physically relevant yet, since the axion has not acquired any mass. Right: After the axion starts mixing with the pseudo-scalar mesons around the QCD phase transition, the axion will obtain a mass and start oscillating around the new potential minimum.

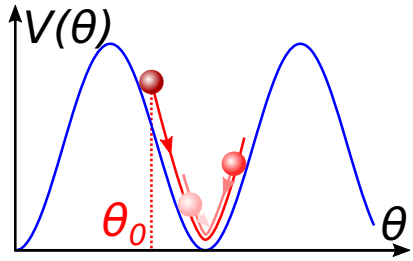

Figure 4.4: After the axion starts mixing with the pseudo-scalar mesons around the QCD phase transition, the axion will obtain a mass. Then, the axion will start to oscillate around the new potential minimum with an initial amplitude, or misalignment angle, θ_0. The expansion of the Universe will act as a friction, ensuring that the strong CP problem is solved today.

rate makes sure that the field settles quickly[8] at a constant misalignment angle, θ_1. After the QCD phase transition, the solution to Eq. (4.10) with a small initial misalignment angle can be written as

$$a(t) = A(t)\cos(m_a t), \tag{4.12}$$

assuming that $H \ll m_a$ and m_a changes slowly. Thus, the axion field has an energy density $\rho_a = m_a^2 A^2/2$, and can be regarded as a coherent state of $n_a = m_a A^2/2$ axions at rest. The amplitude satisfies $\mathrm{d}m_a A^2/\mathrm{d}t = -3H m_a A^2$. Solving for $m_a A^2$ gives $m_a A^2 \propto t^{-3/2} \propto R(t)^{-3}$, $R(t)$ being the scale factor. That is, the number of axions per co-moving volume is constant:

$$\rho_a \sim \frac{1}{2} m_a^2 f_a^2 \theta_1^2 \left(\frac{R_1}{R}\right)^3. \tag{4.13}$$

In other words, the coherently oscillating axion field will be converted into physical axions as the Universe expands. Since an approximately model-independent relation between m_a and f_a exists, the axionic DM abundance dependence only on f_a as [83][9]

$$\Omega_a h^2 \sim 0.1 \left(\frac{f_a}{10^{12}\,\mathrm{GeV}}\right)^{7/6} \theta_1^2. \tag{4.14}$$

Hence, axions with $f_a \sim 10^{12}\,\mathrm{GeV}$ can describe the present day DM abundance without any fine-tuning ($\theta \sim 1$), and is thus an excellent DM candidate.

Finally, a few complications are mentioned for completeness (see e.g. Ref. [88] for an overview). In the calculations and discussions above, it was assumed that the breaking of the $\mathrm{U}(1)_{\mathrm{PQ}}$ symmetry happens after inflation, $T_{\mathrm{PQ}} < T_{\text{re-heat}}$, implying that the axion fields are oscillating homogeneously and coherently such that classical field theory can be used. Furthermore, the discrete degeneracy from the periodicity of the axion potential implies the existence of topological defects, such as domain-walls and strings, if the $\mathrm{U}(1)_{\mathrm{PQ}}$ symmetry is broken after inflation. Axions can additionally be generated by the decay of such topological defects.

4.5 Detecting axions and ALPs

The majority of axion and ALP searches focuses on the two-photon coupling and its many physical implications (see Refs. [94, 95] for two recent reviews). The current excluded region in the $(g_{a\gamma}, m_a)$ parameter space is summarized in Fig. 4.5. The most solid limits at sub-eV masses, $g_{a\gamma} \lesssim 10^{-10}\,\mathrm{GeV}^{-1}$, are set by the CAST helioscope [96] by trying to convert solar ALPs into photons on Earth (aqua region in Fig. 4.5), and

[8] There has been an increasing interest for the so-called *kinetic misalignment mechanism* lately, wherein the initial kinetic energy $\dot{a}(0)$ is sufficiently large that the axion number density is determined by the initial velocity, rather than the initial misalignment angle [93].

[9] This calculation requires calculating $m_a(f_a, T)$ for QCD instantons at high energies.

by the lifetime of horizontal branch stars within globular clusters [97, 98] (olive region). The planned "shine light through a wall" experiment ALPS-II [99] and the solar helioscope IAXO [100] will improve these limits immensely. Meanwhile, the strongest limits at low masses ($m_a \lesssim 10^{-6}\,\mathrm{eV}$) are based on the non-detection of photon-ALP oscillations in astrophysical magnetic fields from photon sources. This includes X-ray observations by Chandra [101, 102] (red region) and gamma-ray observations by FERMI and HESS (maroon region) [103]. The Cherenkov Telescope Array (CTA) is expected to improve the limits from HESS and Fermi-LAT [104]. Furthermore, ALPs that are produced near or in the source can convert back into photons in e.g. the Galactic magnetic field, thus inducing an additional flux of photons. The non-detection of this re-conversion in X-ray observations of SN1987A [105], Betelgeuse [106], and super star clusters [107] has lead to strong limits (yellow region). In addition, linear polarization of magnetic white dwarfs [108] (lime region) and resonant conversion of ALPs sourced near the polar caps of neutron stars [109] (orange region) have recently been shown to yield leading limits.

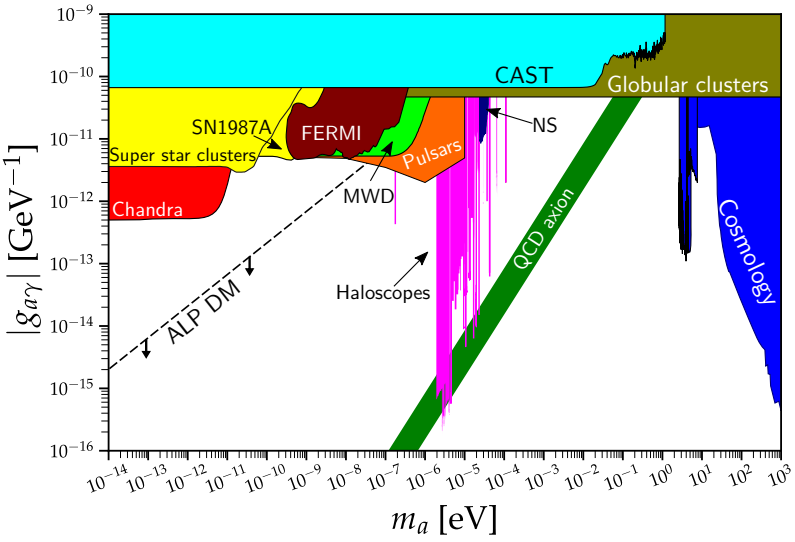

Figure 4.5: Exclusion plot for the ALP parameter space, $(g_{a\gamma}, m_a)$. The shaded regions correspond to the excluded parameters; their origins are explained in the main text. The black dashed line indicates the region where an ALP in principle can describe the DM [110], while the green band indicates the parameters for which the ALP can solve the strong CP problem. The plot is a simplified version of the exclusion plot from Ref. [111].

Note, however, that the aforementioned limits does not assume that the ALP makes up the DM. If this is the case, significantly stronger limits around $m_a \sim 10^{-6}\,\mathrm{eV}$ are

obtained for ALP dark matter in haloscope experiments (fuchsia region in Fig. 4.5.), such as ADMX [112] and the upcoming ABRACADABRA experiment [113], where the idea is to convert ALPs from the dark halo to photons. Another interesting idea that leads to strong limits is ALP DM resonantly converting into photons near neutron stars [114, 115] (navy region). Furthermore, at masses above $\sim 10\,\mathrm{eV}$ there are strong limits set by the cosmology of ALP DM (blue region), from, e.g., the non-observation of photons from ALP decays in the extragalactic background light (EBL) and in X-ray telescopes [95].

5 Summary

The existence of dark matter (DM) is needed to explain a wide range of astrophysical observations, from the faintest dwarf galaxies to the Universe as a whole: Galaxy rotation curves, gravitational lensing and velocity dispersion measurements indicate that galaxies and galaxy clusters contain much more mass than what can be inferred from X-ray observations and stellar count estimates. More importantly, however, DM is required to describe how large-scale structures in the Universe evolved from the tiny perturbations observed in the cosmic microwave background (CMB). Nonetheless, all current evidences for DM rely on the gravitational interaction to ordinary matter, and its nature is therefore yet to be uncovered.

The DM candidates that can solve one or more shortcomings of the Standard Model (SM) are usually considered as well-motivated. Two such candidates are axion-like particles (ALPs) and weakly interacting massive particles (WIMPs). The WIMP is the archetype DM candidate. It is motivated by the hierarchy problem, and can be produced naturally as a thermal relic in the early Universe. For a weak scale mass ($m_\chi \sim$ 10–1000 GeV) and interaction $\langle \sigma_{\text{ann}} v \rangle \sim 10^{-26}\,\text{cm}^3/\text{s}$, the correct DM density $\Omega_\chi h^2 \sim 0.12$ is obtained. This has famously been called the *WIMP miracle*. The most popular WIMP particle today is arguably the neutralino in supersymmetry (SUSY) extensions of the SM, like the Minimal Supersymmetric Standard Model (MSSM). The WIMPs may be detected *directly* in direct detection experiments on Earth, *indirectly* by SM particles—including gamma-rays, antiprotons, or even antinuclei—produced in DM annihilations or decays in the Milky Way, or be produced in particle *accelerators*.

Axions were first introduced as a solution to the strong CP problem. Despite its small mass, it is a suitable DM candidate if it is produced in e.g. the misalignment mechanism. The axion has a characteristic two-photon coupling inherited by its mixing with the neutral pion. A more general class of particles, known as ALPs, shares the two-photon coupling with the axion. Although they do not solve the strong CP problem, they are nevertheless interesting as they arise naturally in extensions of the SM, such as string theories. Most of the experimental effort focuses on the Primakoff effect: In the presence of a magnetic field, the ALP can convert into a detectable photon if it interacts with a virtual photon from a magnetic field. This process leads to a wide range of fascinating astrophysical phenomena, such as photon-ALP oscillations in astrophysical magnetic fields and cooling of main sequence stars.

Despite intensive searches, the nature of DM has yet to be revealed. The search for the elusive DM continues.

Bibliography

1. Workman, R. L. *et al.* "Review of Particle Physics". *PTEP* **2022,** 083C01 (2022).
2. Fan, X. *et al.* "Measurement of the Electron Magnetic Moment". *Phys. Rev. Lett.* **130,** 071801. arXiv: 2209.13084 [physics.atom-ph] (2023).
3. Zwicky, F. "Die Rotverschiebung von extragalaktischen Nebeln". *Helvetica Physica Acta* **6,** 110–127 (Jan. 1933).
4. Rubin, V. C. & Ford W. Kent, J. "Rotation of the Andromeda Nebula from a Spectroscopic Survey of Emission Regions". *Astrophys. J.* **159,** 379 (Feb. 1970).
5. Rubin, V. C., Ford W. K., J. & Thonnard, N. "Extended rotation curves of high-luminosity spiral galaxies. IV. Systematic dynamical properties, Sa → Sc." *Astrophys. J. Lett.* **225,** L107–L111 (Nov. 1978).
6. Bertone, G. & Hooper, D. "History of dark matter". *Rev. Mod. Phys.* **90,** 045002. arXiv: 1605.04909 [astro-ph.CO] (2018).
7. Lord Kelvin, W. T. *Molecular dynamics and the wave theory of light* (Cambridge University Press, 1906).
8. Poincare, H. "The Milky Way and the Theory of Gases". *Popular Astronomy* **14,** 475–488 (Oct. 1906).
9. Whitehurst, R. N. & Roberts, M. S. "High-Velocity Neutral Hydrogen in the Central Region of the Andromeda Galaxy". *Astrophys. J.* **175,** 347 (July 1972).
10. Roberts, M. S. & Rots, A. H. "Comparison of Rotation Curves of Different Galaxy Types". *Astron. Astrophys.* **26,** 483–485 (Aug. 1973).
11. Lundmark, K. "Über die Bestimmung der Entfernungen, Dimensionen, Massen und Dichtigkeit für die nächstgelegenen anagalaktischen Sternsysteme." *Meddelanden fran Lunds Astronomiska Observatorium Serie I* **125,** 1–13 (Jan. 1930).
12. Sofue, Y. & Rubin, V. "Rotation curves of spiral galaxies". *Ann. Rev. Astron. Astrophys.* **39,** 137–174. arXiv: astro-ph/0010594 (2001).
13. Navarro, J. F., Frenk, C. S. & White, S. D. M. "The Structure of cold dark matter halos". *Astrophys. J.* **462,** 563–575. arXiv: astro-ph/9508025 (1996).
14. Silk, J. *et al. Particle Dark Matter: Observations, Models and Searches* (ed Bertone, G.) (Cambridge Univ. Press, Cambridge, 2010).

15. Sofue, Y. "Rotation Curve of the Milky Way and the Dark Matter Density". *Galaxies* **8,** 37. arXiv: 2004.11688 [astro-ph.GA] (2020).

16. Bhattacharjee, P., Chaudhury, S. & Kundu, S. "Rotation Curve of the Milky Way out to $\sim$ 200 kpc". *Astrophys. J.* **785,** 63. arXiv: 1310.2659 [astro-ph.GA] (2014).

17. Clowe, D. *et al.* "A direct empirical proof of the existence of dark matter". *Astrophys. J. Lett.* **648,** L109–L113. arXiv: astro-ph/0608407 (2006).

18. Bradac, M. *et al.* "Revealing the properties of dark matter in the merging cluster MACSJ0025.4-1222". *Astrophys. J.* **687,** 959. arXiv: 0806.2320 [astro-ph] (2008).

19. Robertson, A., Massey, R. & Eke, V. "What does the Bullet Cluster tell us about self-interacting dark matter?" *Mon. Not. Roy. Astron. Soc.* **465,** 569–587. arXiv: 1605.04307 [astro-ph.CO] (2017).

20. Nemiroff, R. & Bonnell, J. *The Matter of the Bullet Cluster.* https://apod.nasa.gov/apod/ap170115.html (accessed Apr. 2023), 2017. [Image Credit: X-ray: NASA/CXC/CfA/ M. Markevitch et al.; Lensing Map: NASA/STScI; ESO WFI; Magellan/U.Arizona/ D.Clowe et al. Optical: NASA/STScI; Magellan/U.Arizona/D.Clowe et al.]

21. Bambi, C. & Dolgov, A. D. *Introduction to Particle Cosmology* (Springer, 2015).

22. Peccei, R. D. & Quinn, H. R. "CP Conservation in the Presence of Instantons". *Phys. Rev. Lett.* **38,** 1440–1443 (1977).

23. Drewes, M. "The Phenomenology of Right Handed Neutrinos". *Int. J. Mod. Phys. E* **22,** 1330019. arXiv: 1303.6912 [hep-ph] (2013).

24. Kachelrieß, M. *Quantum Fields: From the Hubble to the Planck Scale* (Oxford University Press, Oct. 2017).

25. Feng, J. L. "Dark Matter Candidates from Particle Physics and Methods of Detection". *Ann. Rev. Astron. Astrophys.* **48,** 495–545. arXiv: 1003.0904 [astro-ph.CO] (2010).

26. Ignatiev, A. Y., Kuzmin, V. A. & Shaposhnikov, M. E. "Is the Electric Charge Conserved?" *Phys. Lett. B* **84,** 315–318 (1979).

27. Carr, B. & Kuhnel, F. "Primordial Black Holes as Dark Matter: Recent Developments". *Ann. Rev. Nucl. Part. Sci.* **70,** 355–394. arXiv: 2006.02838 [astro-ph.CO] (2020).

28. Kashlinsky, A. "LIGO gravitational wave detection, primordial black holes and the near-IR cosmic infrared background anisotropies". *Astrophys. J. Lett.* **823,** L25. arXiv: 1605.04023 [astro-ph.CO] (2016).

29. Milgrom, M. "A Modification of the Newtonian dynamics as a possible alternative to the hidden mass hypothesis". *Astrophys. J.* **270,** 365–370 (1983).

30. Famaey, B. & McGaugh, S. "Modified Newtonian Dynamics (MOND): Observational Phenomenology and Relativistic Extensions". *Living Rev. Rel.* **15,** 10. arXiv: 1112.3960 [astro-ph.CO] (2012).

31. Peebles, P. J. E. *et al.* "The Case for the hot big bang cosmology". *Nature* **352,** 769–776 (1991).

32. Binder, T. *et al.* "Dark matter relic abundance beyond kinetic equilibrium". *Eur. Phys. J. C* **81,** 577. arXiv: 2103.01944 [hep-ph] (2021).

33. Belanger, G. *et al.* "MicrOMEGAs 2.0: A Program to calculate the relic density of dark matter in a generic model". *Comput. Phys. Commun.* **176,** 367–382. arXiv: hep-ph/0607059 (2007).

34. Hall, L. J. *et al.* "Freeze-In Production of FIMP Dark Matter". *JHEP* **03,** 080. arXiv: 0911.1120 [hep-ph] (2010).

35. Bernal, N. *et al.* "The Dawn of FIMP Dark Matter: A Review of Models and Constraints". *Int. J. Mod. Phys. A* **32,** 1730023. arXiv: 1706.07442 [hep-ph] (2017).

36. Roszkowski, L., Sessolo, E. M. & Trojanowski, S. "WIMP dark matter candidates and searches—current status and future prospects". *Rept. Prog. Phys.* **81,** 066201. arXiv: 1707.06277 [hep-ph] (2018).

37. Rodriguez, M. C. "The Minimal Supersymmetric Standard Model (MSSM) and General Singlet Extensions of the MSSM (GSEMSSM), a short review". arXiv: 1911.13043 [hep-ph] (Nov. 2019).

38. Martin, S. P. "A Supersymmetry primer". *Adv. Ser. Direct. High Energy Phys.* **18** (ed Kane, G. L.) 1–98. arXiv: hep-ph/9709356 (1998).

39. Steffen, F. D. "Gravitino dark matter and cosmological constraints". *JCAP* **09,** 001. arXiv: hep-ph/0605306 (2006).

40. Bhattacharyya, G. & Das, D. "Scalar sector of two-Higgs-doublet models: A minireview". *Pramana* **87,** 40. arXiv: 1507.06424 [hep-ph] (2016).

41. Schmaltz, M. "Physics beyond the standard model (theory): Introducing the little Higgs". *Nucl. Phys. B Proc. Suppl.* **117,** 40–49. arXiv: hep-ph/0210415 (2003).

42. Arcadi, G. *et al.* "The waning of the WIMP? A review of models, searches, and constraints". *Eur. Phys. J. C* **78,** 203. arXiv: 1703.07364 [hep-ph] (2018).

43. Athron, P. *et al.* "GAMBIT: The Global and Modular Beyond-the-Standard-Model Inference Tool". *Eur. Phys. J. C* **77.** [Addendum: Eur.Phys.J.C 78, 98 (2018)], 784. arXiv: 1705.07908 [hep-ph] (2017).

44. Bringmann, T. & Pospelov, M. "Novel direct detection constraints on light dark matter". *Phys. Rev. Lett.* **122,** 171801. arXiv: 1810.10543 [hep-ph] (2019).

45. Fox, P. J., Liu, J. & Weiner, N. "Integrating Out Astrophysical Uncertainties". *Phys. Rev. D* **83,** 103514. arXiv: 1011.1915 [hep-ph] (2011).

46. Essig, R., Mardon, J. & Volansky, T. "Direct Detection of Sub-GeV Dark Matter". *Phys. Rev. D* **85,** 076007. arXiv: 1108.5383 [hep-ph] (2012).

47. Aprile, E. *et al.* "Dark Matter Search Results from a One Ton-Year Exposure of XENON1T". *Phys. Rev. Lett.* **121,** 111302. arXiv: 1805.12562 [astro-ph.CO] (2018).

48. Aprile, E. *et al.* "Light Dark Matter Search with Ionization Signals in XENON1T". *Phys. Rev. Lett.* **123,** 251801. arXiv: 1907.11485 [hep-ex] (2019).

49. Aprile, E. *et al.* "Search for New Physics in Electronic Recoil Data from XENONnT". *Phys. Rev. Lett.* **129,** 161805. arXiv: 2207.11330 [hep-ex] (2022).

50. Aprile, E. *et al.* "Excess electronic recoil events in XENON1T". *Phys. Rev. D* **102,** 072004. arXiv: 2006.09721 [hep-ex] (2020).

51. Griest, K. & Seckel, D. "Three exceptions in the calculation of relic abundances". *Phys. Rev. D* **43,** 3191–3203 (1991).

52. Das, A. & Dasgupta, B. "Selection Rule for Enhanced Dark Matter Annihilation". *Phys. Rev. Lett.* **118,** 251101. arXiv: 1611.04606 [hep-ph] (2017).

53. Bierlich, C. *et al.* "A comprehensive guide to the physics and usage of PYTHIA 8.3". arXiv: 2203.11601 [hep-ph] (Mar. 2022).

54. Bahr, M. *et al.* "Herwig++ Physics and Manual". *Eur. Phys. J. C* **58,** 639–707. arXiv: 0803.0883 [hep-ph] (2008).

55. Hoof, S., Geringer-Sameth, A. & Trotta, R. "A Global Analysis of Dark Matter Signals from 27 Dwarf Spheroidal Galaxies using 11 Years of Fermi-LAT Observations". *JCAP* **02,** 012. arXiv: 1812.06986 [astro-ph.CO] (2020).

56. Ahnen, M. L. *et al.* "Limits to Dark Matter Annihilation Cross-Section from a Combined Analysis of MAGIC and Fermi-LAT Observations of Dwarf Satellite Galaxies". *JCAP* **02,** 039. arXiv: 1601.06590 [astro-ph.HE] (2016).

57. Cui, M.-Y. *et al.* "Possible dark matter annihilation signal in the AMS-02 antiproton data". *Phys. Rev. Lett.* **118,** 191101. arXiv: 1610.03840 [astro-ph.HE] (2017).

58. Kachelrieß, M., Ostapchenko, S. & Tjemsland, J. "Revisiting cosmic ray antinuclei fluxes with a new coalescence model". *JCAP* **08,** 048. arXiv: 2002.10481 [hep-ph] (2020).

59. Goodenough, L. & Hooper, D. "Possible Evidence For Dark Matter Annihilation In The Inner Milky Way From The Fermi Gamma Ray Space Telescope". arXiv: 0910.2998 [hep-ph] (Oct. 2009).
60. Abazajian, K. N. *et al.* "Strong constraints on thermal relic dark matter from Fermi-LAT observations of the Galactic Center". *Phys. Rev. D* **102,** 043012. arXiv: 2003.10416 [hep-ph] (2020).
61. Cholis, I. *et al.* "Return of the templates: Revisiting the Galactic Center excess with multimessenger observations". *Phys. Rev. D* **105,** 103023. arXiv: 2112.09706 [astro-ph.HE] (2022).
62. Gautam, A. *et al.* "Millisecond pulsars from accretion-induced collapse as the origin of the Galactic Centre gamma-ray excess signal". *Nature Astron.* **6,** 703–707. arXiv: 2106.00222 [astro-ph.HE] (2022).
63. Bartels, R., Krishnamurthy, S. & Weniger, C. "Strong support for the millisecond pulsar origin of the Galactic center GeV excess". *Phys. Rev. Lett.* **116,** 051102. arXiv: 1506.05104 [astro-ph.HE] (2016).
64. Murgia, S. "The Fermi–LAT Galactic Center Excess: Evidence of Annihilating Dark Matter?" *Ann. Rev. Nucl. Part. Sci.* **70,** 455–483 (2020).
65. De Dios Zornoza, J. "Review on Indirect Dark Matter Searches with Neutrino Telescopes". *Universe* **7,** 415 (2021).
66. Aartsen, M. G. *et al.* "Improved limits on dark matter annihilation in the Sun with the 79-string IceCube detector and implications for supersymmetry". *JCAP* **04,** 022. arXiv: 1601.00653 [hep-ph] (2016).
67. Adrian-Martinez, S. *et al.* "Limits on Dark Matter Annihilation in the Sun using the ANTARES Neutrino Telescope". *Phys. Lett. B* **759,** 69–74. arXiv: 1603.02228 [astro-ph.HE] (2016).
68. Cowsik, R., Burch, B. & Madziwa-Nussinov, T. "The origin of the spectral intensities of cosmic-ray positrons". *Astrophys. J.* **786,** 124. arXiv: 1305.1242 [astro-ph.HE] (2014).
69. Boezio, M. *et al.* "PAMELA and indirect dark matter searches". *New J. Phys.* **11,** 105023 (2009).
70. Feng, L. *et al.* "AMS-02 positron excess: new bounds on dark matter models and hint for primary electron spectrum hardening". *Phys. Lett. B* **728,** 250–255. arXiv: 1303.0530 [astro-ph.HE] (2014).
71. Profumo, S., Queiroz, F. & Siqueira, C. "Has AMS-02 Observed Two-Component Dark Matter?" *J. Phys. G* **48,** 015006. arXiv: 1903.07638 [hep-ph] (2020).

72. Cholis, I., Linden, T. & Hooper, D. "A Robust Excess in the Cosmic-Ray Antiproton Spectrum: Implications for Annihilating Dark Matter". *Phys. Rev. D* **99,** 103026. arXiv: 1903.02549 [astro-ph.HE] (2019).
73. Heisig, J., Korsmeier, M. & Winkler, M. W. "Dark matter or correlated errors: Systematics of the AMS-02 antiproton excess". *Phys. Rev. Res.* **2,** 043017. arXiv: 2005.04237 [astro-ph.HE] (2020).
74. Ting, S. *Latest Results from the AMS Experiment on the International Space Station*. Talk at CERN Colloquium. May 2018.
75. Kappl, R., Reinert, A. & Winkler, M. W. "AMS-02 Antiprotons Reloaded". *JCAP* **10,** 034. arXiv: 1506.04145 [astro-ph.HE] (2015).
76. Trevisani, N. "Collider Searches for Dark Matter (ATLAS + CMS)". *Universe* **4,** 131 (2018).
77. Baym, G. & Beck, D. H. "Elementary quantum mechanics of the neutron with an electric dipole moment". *Proc. Nat. Acad. Sci.* **113,** 7438–7442. arXiv: 1606.06774 [hep-ph] (2016).
78. Belavin, A. A. *et al.* "Pseudoparticle Solutions of the Yang-Mills Equations". *Phys. Lett. B* **59** (ed Taylor, J. C.) 85–87 (1975).
79. Crewther, R. J. *et al.* "Chiral Estimate of the Electric Dipole Moment of the Neutron in Quantum Chromodynamics". *Phys. Lett. B* **88.** [Erratum: Phys.Lett.B 91, 487 (1980)], 123 (1979).
80. Weinberg, S. "A New Light Boson?" *Phys. Rev. Lett.* **40,** 223–226 (1978).
81. Wilczek, F. "Problem of Strong P and T Invariance in the Presence of Instantons". *Phys. Rev. Lett.* **40,** 279–282 (1978).
82. Wilczek, F. "Time's (Almost) Reversible Arrow". *Quanta Magazine* (Jan. 2016).
83. Peccei, R. D. "The Strong CP problem and axions". *Lect. Notes Phys.* **741** (eds Kuster, M., Raffelt, G. & Beltran, B.) 3–17. arXiv: hep-ph/0607268 (2008).
84. Di Luzio, L. *et al.* "The landscape of QCD axion models". *Phys. Rept.* **870,** 1–117. arXiv: 2003.01100 [hep-ph] (2020).
85. Arvanitaki, A. *et al.* "String Axiverse". *Phys. Rev. D* **81,** 123530. arXiv: 0905.4720 [hep-th] (2010).
86. Cicoli, M., Goodsell, M. & Ringwald, A. "The type IIB string axiverse and its low-energy phenomenology". *JHEP* **10,** 146. arXiv: 1206.0819 [hep-th] (2012).
87. Primakoff, H. "Photoproduction of neutral mesons in nuclear electric fields and the mean life of the neutral meson". *Phys. Rev.* **81,** 899 (1951).
88. Sikivie, P. "Axion Cosmology". *Lect. Notes Phys.* **741** (eds Kuster, M., Raffelt, G. & Beltran, B.) 19–50. arXiv: astro-ph/0610440 (2008).

89. Marsh, D. J. E. "Axion Cosmology". *Phys. Rept.* **643,** 1–79. arXiv: 1510.07633 [astro-ph.CO] (2016).

90. Preskill, J., Wise, M. B. & Wilczek, F. "Cosmology of the Invisible Axion". *Phys. Lett. B* **120** (ed Srednicki, M. A.) 127–132 (1983).

91. Abbott, L. F. & Sikivie, P. "A Cosmological Bound on the Invisible Axion". *Phys. Lett. B* **120** (ed Srednicki, M. A.) 133–136 (1983).

92. Dine, M. & Fischler, W. "The Not So Harmless Axion". *Phys. Lett. B* **120** (ed Srednicki, M. A.) 137–141 (1983).

93. Co, R. T., Hall, L. J. & Harigaya, K. "Axion Kinetic Misalignment Mechanism". *Phys. Rev. Lett.* **124,** 251802. arXiv: 1910.14152 [hep-ph] (2020).

94. Graham, P. W. *et al.* "Experimental Searches for the Axion and Axion-Like Particles". *Ann. Rev. Nucl. Part. Sci.* **65,** 485–514. arXiv: 1602.00039 [hep-ex] (2015).

95. Irastorza, I. G. & Redondo, J. "New experimental approaches in the search for axion-like particles". *Prog. Part. Nucl. Phys.* **102,** 89–159. arXiv: 1801.08127 [hep-ph] (2018).

96. Anastassopoulos, V. *et al.* "New CAST Limit on the Axion-Photon Interaction". *Nature Phys.* **13,** 584–590. arXiv: 1705.02290 [hep-ex] (2017).

97. Ayala, A. *et al.* "Revisiting the bound on axion-photon coupling from Globular Clusters". *Phys. Rev. Lett.* **113,** 191302. arXiv: 1406.6053 [astro-ph.SR] (2014).

98. Dolan, M. J., Hiskens, F. J. & Volkas, R. R. "Advancing globular cluster constraints on the axion-photon coupling". *JCAP* **10,** 096. arXiv: 2207.03102 [hep-ph] (2022).

99. Bähre, R. *et al.* "Any light particle search II —Technical Design Report". *JINST* **8,** T09001. arXiv: 1302.5647 [physics.ins-det] (2013).

100. Armengaud, E. *et al.* "Physics potential of the International Axion Observatory (IAXO)". *JCAP* **06,** 047. arXiv: 1904.09155 [hep-ph] (2019).

101. Reynés, J. S. *et al.* "New constraints on light axion-like particles using Chandra transmission grating spectroscopy of the powerful cluster-hosted quasar H1821+643". *Mon. Not. Roy. Astron. Soc.* **510,** 1264–1277. arXiv: 2109.03261 [astro-ph.HE] (2021).

102. Matthews, J. H. *et al.* "How Do Magnetic Field Models Affect Astrophysical Limits on Light Axion-like Particles? An X-Ray Case Study with NGC 1275". *Astrophys. J.* **930,** 90. arXiv: 2202.08875 [astro-ph.HE] (2022).

103. Davies, J., Meyer, M. & Cotter, G. "Constraints on axionlike particles from a combined analysis of three flaring Fermi flat-spectrum radio quasars". *Phys. Rev. D* **107,** 083027. arXiv: 2211.03414 [astro-ph.HE] (2023).

104. Abdalla, H. *et al.* "Sensitivity of the Cherenkov Telescope Array for probing cosmology and fundamental physics with gamma-ray propagation". *JCAP* **02,** 048. arXiv: 2010.01349 [astro-ph.HE] (2021).

105. Payez, A. *et al.* "Revisiting the SN1987A gamma-ray limit on ultralight axion-like particles". *JCAP* **02,** 006. arXiv: 1410.3747 [astro-ph.HE] (2015).

106. Xiao, M. *et al.* "Constraints on Axionlike Particles from a Hard X-Ray Observation of Betelgeuse". *Phys. Rev. Lett.* **126,** 031101. arXiv: 2009.09059 [astro-ph.HE] (2021).

107. Dessert, C., Foster, J. W. & Safdi, B. R. "X-ray Searches for Axions from Super Star Clusters". *Phys. Rev. Lett.* **125,** 261102. arXiv: 2008.03305 [hep-ph] (2020).

108. Dessert, C., Dunsky, D. & Safdi, B. R. "Upper limit on the axion-photon coupling from magnetic white dwarf polarization". *Phys. Rev. D* **105,** 103034. arXiv: 2203.04319 [hep-ph] (2022).

109. Noordhuis, D. *et al.* "Novel Constraints on Axions Produced in Pulsar Polar Cap Cascades". arXiv: 2209.09917 [hep-ph] (Sept. 2022).

110. Arias, P. *et al.* "WISPy Cold Dark Matter". *JCAP* **06,** 013. arXiv: 1201.5902 [hep-ph] (2012).

111. O'Hare, C. *cajohare/AxionLimits: AxionLimits*. https://cajohare.github.io/AxionLimits/. Version v1.0. July 2020.

112. Braine, T. *et al.* "Extended Search for the Invisible Axion with the Axion Dark Matter Experiment". *Phys. Rev. Lett.* **124,** 101303. arXiv: 1910.08638 [hep-ex] (2020).

113. Ouellet, J. L. *et al.* "First Results from ABRACADABRA-10 cm: A Search for Sub-μeV Axion Dark Matter". *Phys. Rev. Lett.* **122,** 121802. arXiv: 1810.12257 [hep-ex] (2019).

114. Foster, J. W. *et al.* "Extraterrestrial Axion Search with the Breakthrough Listen Galactic Center Survey". *Phys. Rev. Lett.* **129,** 251102. arXiv: 2202.08274 [astro-ph.CO] (2022).

115. Battye, R. A. *et al.* "Searching for Time-Dependent Axion Dark Matter Signals in Pulsars". arXiv: 2303.11792 [astro-ph.CO] (Mar. 2023).

Papers

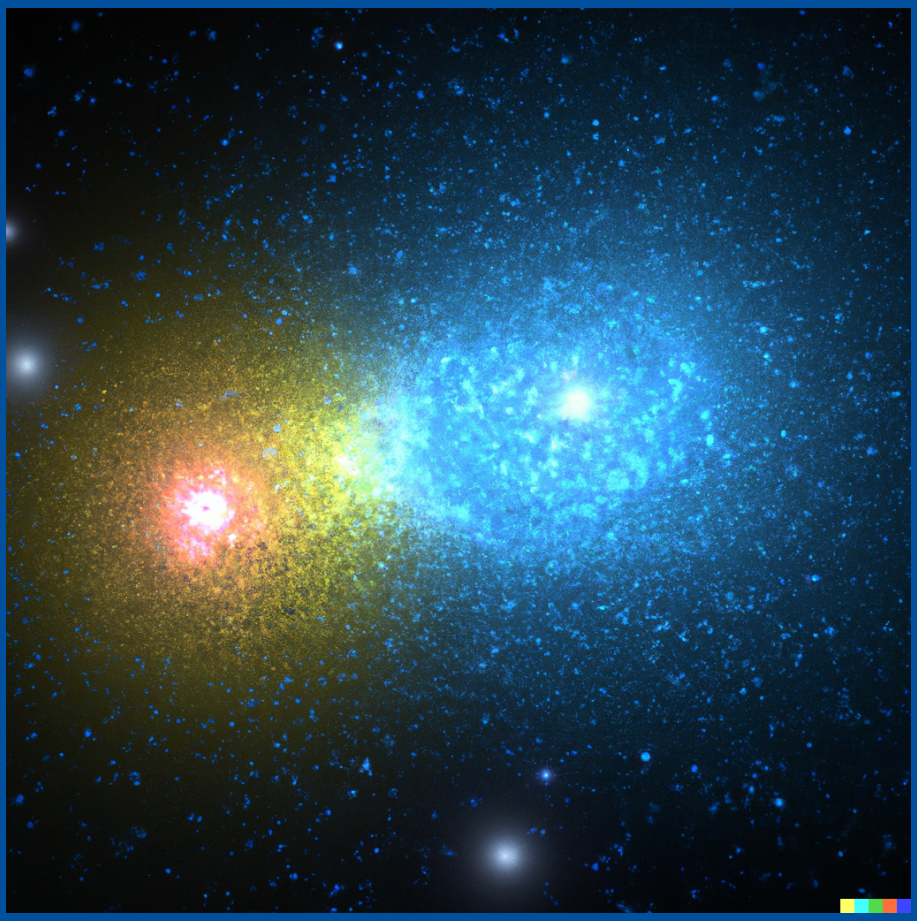

"Axion-like particles in the early Universe" by Dall·E (2023)

Aim and outcome of the papers

This PhD thesis has been motivated by dark matter (DM) and the indirect detection thereof, and is but a small part of the community effort to reveal the nature of DM. The work has resulted in 19 papers[1], of which 15 are either published or accepted for publication in scientific journals[2], two are submitted, one is an unpublished manuscript and one is a submitted conference proceeding without peer reviewing. Only the eleven (I–XI, ordered by time of submission) most imporant papers have been attached. The complete publication list can be found in the list of papers on page xi.

The papers can be split into three sub-categories: cosmic ray antinuclei, photon-ALP oscillations and millicharged particles. The overall aim has been to improve the theoretical description of DM signatures in cosmic ray and gamma-ray data.

Cosmic ray antinuclei

Papers I, II, IV, V, VII, IX, X, XII, XIII and XVII, are motivated by the search for antideuteron and antihelion in annihilations or decays of weakly interacting massive particles (WIMPs) in the Milky Way. There are two main sources of uncertainties in the theoretical estimation of cosmic ray antinuclei fluxes on Earth: production mechanism and propagation. In this PhD thesis, a major aim has been to improve the theoretical description of (anti)deuteron and (anti)helion production in small interacting systems relevant for astrophysical studies, such as e^+e^-, pp and pN collisions, and in particular, DM annihilations and decays. The main outcome has been a new coalescence model, which we named WiFunC (short for Wigner Function with Correlations). This work has been of particular importance for accelerator studies of (anti)nuclei production, which in turn may be used to improve theoretical predictions for the production in exotic processes.

Photon-ALP oscillations

Papers VIII, XI, XIV, XV and XVI are concerned with mixing between photons and axion-like particles (ALPs) in astrophysical magnetic fields. If ALPs exist, their two-photon coupling will lead to photon-ALP oscillation as photons propagate through a

[1] Two ongoing projects are planned to be finished during the last months of the PhD position: resonant conversion of axionic DM near neutron stars with J. McDonald and S. Witte, and electromagnetic cascades in realistic magnetic field models with M. Meyer and F. Vazza.

[2] as registered in the Norwegian Register for Scientific Journals

magnetic field. This will imprint important signatures on high-energy photon spectra regardless of whether they constitute the DM relic abundance or not. In this PhD thesis, the focus has been on the oscillatory features that photon-ALP oscillations induce on high-energy photon spectra, which we name "ALP wiggles". A major outcome of this work has been the implementation of photon-ALP oscillations into the photon propagation code `ELMAG`, which will be beneficial for future work on the topic. In addition, we proposed a statistical method for detecting ALP wiggles, which can be used to conduct searches for ALPs independent of the modelling of the magnetic field.

Millicharged dark matter

Papers III and VI consider the topic of millicharged particles. Despite intensive searches, none of the traditional DM particles, like WIMPs and ALPs, have been found. There has therefore been an increased interest in hidden DM, where the hidden sector is coupled to the Standard Model (SM) by a mediator. The small effective charge of a millicharged particle can be explained, e.g., if there is a kinetic mixing between the SM photon and a dark photon. In this PhD thesis, two topics related to millicharged DM have been studied: the effect of the presence of millicharged DM on the evolution of the turbulence in the Milky Way (Paper III), and the production of millicharged particles by neutral meson decays in air showers (Paper VI).

Paper I – Alternative coalescence model for deuteron, tritium, helium-3 and their antinuclei

Kachelrieß, M., Ostapchenko, S. & Tjemsland, J. "Alternative coalescence model for deuteron, tritium, helium-3 and their antinuclei". *Eur. Phys. J. A* **56,** 4. arXiv: 1905.01192 [hep-ph] (2020)

Abstract: Antideuteron and antihelium nuclei have been proposed as a detection channel for dark matter annihilations and decays in the Milky Way, due to the low astrophysical background expected. To estimate both the signal for various dark matter models and the astrophysical background, one usually employs the coalescence model in a Monte Carlo framework. This allows one to treat the production of antinuclei on an event-by-event basis, thereby taking into account momentum correlations between the antinucleons involved in the process. This approach lacks, however, an underlying microscopic picture, and the numerical value of the coalescence parameter obtained from fits to different reactions varies considerably. Here we propose instead to combine event-by-event Monte Carlo simulations with a microscopic coalescence picture based on the Wigner function representations of the produced antinuclei states. This approach allows us to include in a semi-classical picture both the size of the formation region, which is process dependent, and the momentum correlations. The model contains a single, universal parameter which is fixed by fitting the production spectra of antideuterons in proton–proton interactions, measured at the Large Hadron Collider. Using this value, the model describes well the production of various antinuclei both in electron–positron annihilation and in proton–proton collisions.

The common approach in the astroparticle community was to use a simple phenomenological coalescence model in momentum space, where an (anti)proton and (anti)neutron produce an (anti)deuteron if their relative momentum difference is smaller than the coalescence momentum, p_0. In this paper, a new coalescence model was developed for the production of light (anti)nuclei based on the Wigner function representation of the initial and final states. The new model takes into account both the size of the formation region and momentum correlations on an event-by-event basis. Although the emission length, σ, in principle was a free parameter of the model, it was expected to be close to 1 fm based on its physical interpretation. In Paper IV, it was indeed confirmed to be ~ 1 fm independent of the coalescence mechanism, implying that the model now is parameter free. The model was named WiFunC in Paper IV.

M. Kachelrieß, in collaboration with S. Ostapchenko, first proposed this project with the goal of creating a consistent coalescence model in *phase space*, including momentum correlations and the process dependent size of the emission volume. The topic was motivated by the paper by Blum et al. [*Phys.Rev.D* 96 (2017) 10, 103021], wherein results from the density matrix approach discussed by Scheibl & Heinz [*Phys.Rev.C* 59 (1999) 1585-1602] were applied to estimate the astrophysical flux of antideuteron and antihelion. In the approach by Scheibl & Heinz, the coalescence factor scales with the emission volume as $B_A \sim V^{A-1}$, but momentum correlations are neglected.

The preprint of this paper was made public three months before the official start of the PhD position, but it was revised and accepted during the PhD work. All the same, the theory presented in the paper is underlying the coming papers on the topic of antinuclei, and is included in its entirety to improve the consistency and coherency of the thesis.

Eur. Phys. J. A (2020) 56:4
https://doi.org/10.1140/epja/s10050-019-00007-9

THE EUROPEAN PHYSICAL JOURNAL A

Regular Article -Theoretical Physics

Alternative coalescence model for deuteron, tritium, helium-3 and their antinuclei

M. Kachelrieß[1,a], **S. Ostapchenko**[2,3], **J. Tjemsland**[1]

[1] Institutt for fysikk, NTNU, Trondheim, Norway
[2] Frankfurt Institute for Advanced Studies, Frankfurt, Germany
[3] D.V. Skobeltsyn Institute of Nuclear Physics, Moscow State University, Moscow, Russia

Received: 25 July 2019 / Accepted: 27 October 2019 / Published online: 9 January 2020

Communicated by R. Rapp

Abstract Antideuteron and antihelium nuclei have been proposed as a detection channel for dark matter annihilations and decays in the Milky Way, due to the low astrophysical background expected. To estimate both the signal for various dark matter models and the astrophysical background, one usually employs the coalescence model in a Monte Carlo framework. This allows one to treat the production of antinuclei on an event-by-event basis, thereby taking into account momentum correlations between the antinucleons involved in the process. This approach lacks, however, an underlying microscopic picture, and the numerical value of the coalescence parameter obtained from fits to different reactions varies considerably. Here we propose instead to combine event-by-event Monte Carlo simulations with a microscopic coalescence picture based on the Wigner function representations of the produced antinuclei states. This approach allows us to include in a semi-classical picture both the size of the formation region, which is process dependent, and the momentum correlations. The model contains a single, universal parameter which is fixed by fitting the production spectra of antideuterons in proton–proton interactions, measured at the Large Hadron Collider. Using this value, the model describes well the production of various antinuclei both in electron–positron annihilation and in proton–proton collisions.

1 Introduction

Antideuteron and antihelium nuclei have been suggested as promising detection channels for dark matter, because of the low astrophysical background expected for such signatures [1]: the dominant background source of antideuterons are cosmic ray protons interacting with the interstellar medium. The high threshold energy for this reaction channel implies that the antideuterons produced by cosmic rays have relatively large kinetic energies. Low-velocity antideuterons are therefore an ideal tool to search for exotic sources of antimatter. In the case of antihelium nuclei, the suppression of astrophysical backgrounds at low velocities is even stronger, but the maximal event rates expected in dark matter models are challenging for square-meter sized detectors. At present, the search for antinuclei is performed by the AMS-02 experiment on board of the International Space Station, while the GAPS balloon experiment is planned to fly in the next Solar minimum period around 2020 or 2021 [2,3].

The production of light clusters of antinuclei like antideuteron, antihelium or antitritium[1] is usually described in the context of coalescence [4–8] or of statistical–thermal models [9–15]. In coalescence models, cluster formation has been traditionally parametrized by an invariant coalescence factor B_A which relates the invariant yield $E_A\ \mathrm{d}^3N_A/\mathrm{d}P_A^3$ of nuclei with mass number A formed out of Z protons and N neutrons to the invariant yields $E_i\ \mathrm{d}^3N_i/\mathrm{d}P_i^3$ of protons ($i = p$) and neutrons ($i = n$) via

$$E_A\,\frac{\mathrm{d}^3N_A}{\mathrm{d}P_A^3} = B_A\left(E_p\,\frac{\mathrm{d}^3N_p}{\mathrm{d}P_p^3}\right)^Z\left(E_n\,\frac{\mathrm{d}^3N_n}{\mathrm{d}P_n^3}\right)^N\Bigg|_{P_p=P_n=P_A/A}. \tag{1}$$

In e^+e^- and pp collisions, one imposes typically the coalescence condition in momentum space, requiring that the momenta of merging nucleons in their two-body center-of-mass (CoM) system are smaller than some critical value

[1] Since our discussion applies equally well to the production of particles and of antiparticles in pp and e^+e^- collisions, the preposition 'anti' is dropped further on.

[a] e-mail: michael.kachelriess@ntnu.no

p_0. In the limit of isotropic and equal proton and neutron yields, the so-called coalescence momentum p_0 is related to B_A via

$$B_A = A \left(\frac{4\pi}{3} \frac{p_0^3}{m_\mathrm{N}} \right)^{A-1}, \tag{2}$$

where m_N denotes the nucleon mass. This scheme can be improved taking into account the momentum correlations between nucleons, which are provided by Monte Carlo (MC) simulations on an event-by-event basis. Such an approach, which was first suggested in Refs. [16,17], is commonly used for the prediction of the antideuteron yield both from dark matter annihilations or decays and from cosmic rays interactions [18–26], for a review see Ref. [27]. The only free parameter of this model is the coalescence momentum p_0, which should be independent of the reaction type and the center-of-mass energy $\sqrt{s}$ in order to be predictive. However, the numerical value of the coalescence parameter obtained from fits to different reactions varies considerably [19,27].

An alternative scheme was developed to describe the formation of light nuclear clusters in heavy-ion collisions. There, the coalescence condition was imposed in coordinate space, assuming that the coalescence factor B_A of a cluster with mass number A is proportional to V^{A-1}, where V denotes the volume of the emission region of hadrons from the expanding cloud of partons [28,29]. There have been made considerable efforts to combine these two approaches and to develop coalescence models which are based on a microscopical picture using, e.g., Wigner functions [30] or a diagrammatic approach [31]. Many of these attempts impose the coalescence condition in phase space, using either a classical or a quantum mechanical description as a starting point. Such models have been mainly applied to heavy-ion collisions and are reviewed, e.g., in Refs. [13,32,33]. An interesting application of this approach to the prediction of antideuteron and antihelium production by cosmic rays has been made recently in Ref. [34].

The coalescence process has also been modeled as a dynamical process where the formation probability of a deuteron is proportional to the scattering cross section of the reaction $\bar{N}_1 \bar{N}_2 \to \bar{d} X$. The amplitude for such processes has been derived, e.g., from models for the non-relativistic nucleon–nucleon potential. As an alternative, Ref. [35] used experimental data to determine the cross sections $\bar{p}\bar{n} \to \bar{d} X$ for $X = \{\gamma, \pi^0, \ldots\}$. The coalescence probability was then determined as $\sigma_\mathrm{tot}(\bar{N}_1 \bar{N}_2 \to \bar{d} X)/\sigma_0$ with σ_0 as a free parameter. As a result, antideuterons were mainly produced with momenta close to the delta resonance, ~ 1 GeV, and the fit to the antideuteron production data in pp collision data from the ALICE experiment improved significantly.

In this work, we develop a coalescence model for the formation of light nuclei in $\mathrm{e^+e^-}$ and pp collisions, which can be applied as well to dark matter annihilations and decays. Such a combined approach which describes successfully the production of light nuclei both in "point-like" reactions ($\mathrm{e^+e^-}$, dark matter) and in pp collisions is especially needed for indirect dark matter searches, where the consistent prediction of "signal" antinuclei produced by dark matter annihilations and of background antinuclei created in cosmic ray interactions is required. Our model is based on the Wigner function representations of the produced antinuclei states and allows us to include in a semi-classical picture both the size of the formation region, which is process dependent, and the momentum correlations. The model contains a single, universal parameter which is fixed by fitting the production spectra of antideuterons in pp collisions, measured by the ALICE experiment at the LHC [36]. The obtained value, $\sigma_{(\mathrm{e^+e^-})} = \sigma_{(pp)}/\sqrt{2} \simeq 5\,\mathrm{GeV}^{-1} \simeq 1$ fm, agrees with its physical interpretation as the size of the formation region of the light nuclei. Using this value, the model describes well the data on the production of antihelium in pp interactions and of antideuterons in $\mathrm{e^+e^-}$ annihilations at the Z-resonance [37,38].

2 Wigner function-based deuteron formation model

We develop our model first for the case of deuteron production. The generalization to helium-3 and tritium is straightforward and will be performed in the next section. In the following, we use the fact that the binding energy B of these nuclei is small, e.g. $B \simeq 2.2$ MeV for the deuteron. Therefore we can assume that a nucleus A is formed through the process $N_1 + \cdots + N_n \to A^*$, and that the excitation energy is later released by the emission of a photon.

2.1 Derivation

The starting point for the derivation of our new coalescence model is inspired by the approach using Wigner functions, presented in Ref. [33]. We consider a system consisting of a proton and a neutron in a frame where the motion of their CoM is nonrelativistic. The number of deuterons with a given momentum $\boldsymbol{P}_\mathrm{d}$ can be found by projecting the deuteron density matrix ρ_d onto the two-nucleon density matrix ρ_nucl,

$$\frac{\mathrm{d}^3 N_\mathrm{d}}{\mathrm{d} P_\mathrm{d}^3} = \mathrm{tr}\, \rho_\mathrm{d}\, \rho_\mathrm{nucl}. \tag{3}$$

The deuteron density matrix describes a pure state, $\rho_\mathrm{d} = |\phi_\mathrm{d}\rangle \langle \phi_\mathrm{d}|$. The spin and isospin values of the two-nucleon state can be taken care of by introducing a statistical factor $S = 3/8$ [39], so that the two-nucleon density matrix can be

written as $\rho_{\rm nucl} = |\psi_p\psi_n\rangle\langle\psi_n\psi_p|$ and is normalized as

$$\langle\psi_n\psi_p|\,|\psi_p\psi_n\rangle = N_p N_n. \tag{4}$$

Here, N_p and N_n are the average multiplicities of protons and neutrons per event, respectively.[2]

By evaluating the trace in the coordinate representation $|\boldsymbol{x}_1\boldsymbol{x}_2\rangle$, where the two indices refer to the positions of the two nucleons, one finds

$$\frac{\mathrm{d}^3N_{\rm d}}{\mathrm{d}P_{\rm d}^3} = S\int \mathrm{d}^3x_1\,\mathrm{d}^3x_2\,\mathrm{d}^3x_1'\,\mathrm{d}^3x_2'\phi_{\rm d}^*(\boldsymbol{x}_1,\boldsymbol{x}_2)\phi_{\rm d}(\boldsymbol{x}_1',\boldsymbol{x}_2') \times\left\langle\psi_n^\dagger(\boldsymbol{x}_2')\psi_p^\dagger(\boldsymbol{x}_1')\psi_p(\boldsymbol{x}_1)\psi_n(\boldsymbol{x}_2)\right\rangle, \tag{5}$$

where $\phi_{\rm d}(\boldsymbol{x}_1,\boldsymbol{x}_2)$ and $\psi_i(\boldsymbol{x})$ are the wave functions of the deuteron and nucleon i, respectively. Next we factorize the deuteron wave function into a plane wave describing the CoM motion with momentum $\boldsymbol{P}_{\rm d}$ and an internal wave function $\varphi_{\rm d}$,

$$\phi_{\rm d}(\boldsymbol{x}_1,\boldsymbol{x}_2) = (2\pi)^{-3/2}\exp\{\mathrm{i}\boldsymbol{P}_{\rm d}\cdot(\boldsymbol{x}_1+\boldsymbol{x}_2)/2\}\varphi_{\rm d}(\boldsymbol{x}_1-\boldsymbol{x}_2). \tag{6}$$

Then we replace the two-nucleon density matrix by its two-body Wigner function,

$$\begin{aligned}&\left\langle\psi_n(\boldsymbol{x}_2')^\dagger\psi_p(\boldsymbol{x}_1')^\dagger\psi_p(\boldsymbol{x}_1)\psi_n(\boldsymbol{x}_2)\right\rangle\\ &= \int\frac{\mathrm{d}^3p_n}{(2\pi)^3}\frac{\mathrm{d}^3p_p}{(2\pi)^3}W_{np}\left(\boldsymbol{p}_n,\boldsymbol{p}_p,\frac{\boldsymbol{x}_2+\boldsymbol{x}_2'}{2},\frac{\boldsymbol{x}_1+\boldsymbol{x}_1'}{2}\right)\\ &\quad\times\exp[\mathrm{i}\boldsymbol{p}_n\cdot(\boldsymbol{x}_2-\boldsymbol{x}_2')]\exp[\mathrm{i}\boldsymbol{p}_p\cdot(\boldsymbol{x}_1-\boldsymbol{x}_1')].\end{aligned} \tag{7}$$

Furthermore, we introduce as new coordinates the "average" positions of the proton and neutron, $\boldsymbol{r}_p = (\boldsymbol{x}_1+\boldsymbol{x}_1')/2$ and $\boldsymbol{r}_n = (\boldsymbol{x}_2+\boldsymbol{x}_2')/2$, as well as their separation $\boldsymbol{r} = \boldsymbol{r}_n - \boldsymbol{r}_p$, $\boldsymbol{\xi} = \boldsymbol{x}_1 - \boldsymbol{x}_1' - \boldsymbol{x}_2 + \boldsymbol{x}_2'$ and $\boldsymbol{\rho} = (\boldsymbol{x}_1 - \boldsymbol{x}_1' + \boldsymbol{x}_2 - \boldsymbol{x}_2')/2$. Changing also the momentum integration variables to $\boldsymbol{p} = \boldsymbol{p}_n + \boldsymbol{p}_p$ and $\boldsymbol{q} = (\boldsymbol{p}_n - \boldsymbol{p}_p)/2$, and performing then the $\boldsymbol{\rho}$ and $\boldsymbol{p}$ integrals, we arrive at

$$\frac{\mathrm{d}^3N_{\rm d}}{\mathrm{d}P_{\rm d}^3} = \frac{S}{(2\pi)^6}\int\mathrm{d}^3q\int\mathrm{d}^3r_p\,\mathrm{d}^3r_n\,\mathcal{D}(\boldsymbol{r},\boldsymbol{q}) \times W_{np}(\boldsymbol{P}_{\rm d}/2+\boldsymbol{q},\boldsymbol{P}_{\rm d}/2-\boldsymbol{q},\boldsymbol{r}_n,\boldsymbol{r}_p), \tag{8}$$

where

$$\mathcal{D}(\boldsymbol{r},\boldsymbol{q}) = \int\mathrm{d}^3\xi\exp\{-\mathrm{i}\boldsymbol{q}\cdot\boldsymbol{\xi}\}\varphi_{\rm d}(\boldsymbol{r}+\boldsymbol{\xi}/2)\varphi_{\rm d}^*(\boldsymbol{r}-\boldsymbol{\xi}/2) \tag{9}$$

is the Wigner function[3] of the internal deuteron wave function $\varphi_{\rm d}$.

Using a Gaussian as ansatz for the deuteron wave function,

$$\varphi_{\rm d}(\boldsymbol{r}) = \left(\pi d^2\right)^{-3/4}\exp\{-\frac{r^2}{2d^2}\}, \tag{10}$$

its Wigner function follows as

$$\mathcal{D}(\boldsymbol{r},\boldsymbol{q}) = 8\mathrm{e}^{-r^2/d^2}\mathrm{e}^{-q^2d^2}. \tag{11}$$

The measured deuteron rms charge radius $r_{\rm rms} = 1.96$ fm [40] is reproduced choosing[4] $d = 3.2$ fm. To proceed, we have to choose also an ansatz for the Wigner function of the two-nucleon state: while Ref. [33] choses a thermal equilibrium state, motivated by the picture of a "fireball" formed in heavy-ion collisions, in this work we are interested in the scattering of "small" systems as in $\mathrm{e}^+\mathrm{e}^-$, dark matter or pp collisions. Therefore we use the fact that Monte Carlo simulations of strong interactions provide the momentum distribution of the produced nucleons, $G_{np}(\boldsymbol{p}_n,\boldsymbol{p}_p)$, which includes also relevant momentum correlations. On the other hand, $G_{np}(\boldsymbol{p}_n,\boldsymbol{p}_p)$ can be obtained from the Wigner function:

$$\begin{aligned}&\int\mathrm{d}^3r_p\,\mathrm{d}^3r_n\,W_{np}(\boldsymbol{p}_n,\boldsymbol{p}_p,\boldsymbol{r}_n,\boldsymbol{r}_p)\\ &= N_pN_n\,|\psi_{np}(\boldsymbol{p}_n,\boldsymbol{p}_p)|^2 \equiv G_{np}(\boldsymbol{p}_n,\boldsymbol{p}_p),\end{aligned} \tag{12}$$

where $\psi_{np}(\boldsymbol{p}_n,\boldsymbol{p}_p)$ is the normalized two-nucleon wave function in momentum space. We assume therefore a factorization of the momentum and coordinate dependences,

$$\begin{aligned}&W_{np}(\boldsymbol{P}_{\rm d}/2+\boldsymbol{q},\boldsymbol{P}_{\rm d}/2-\boldsymbol{q},\boldsymbol{r}_n,\boldsymbol{r}_p)\\ &= H_{np}(\boldsymbol{r}_n,\boldsymbol{r}_p)\,G_{np}(\boldsymbol{P}_{\rm d}/2+\boldsymbol{q},\boldsymbol{P}_{\rm d}/2-\boldsymbol{q}).\end{aligned} \tag{13}$$

Note that this assumption implies a transition from a full quantum mechanical treatment to a semi-classical picture. Finally, we neglect spatial correlations between the proton and the neutron, $H_{np}(\boldsymbol{r}_n,\boldsymbol{r}_p) = h(\boldsymbol{r}_n)\,h(\boldsymbol{r}_p)$ and choose a Gaussian ansatz for $h(\boldsymbol{r})$,

$$h(\boldsymbol{r}) = \left(2\pi\sigma^2\right)^{-3/2}\exp\{-\frac{r^2}{2\sigma^2}\}. \tag{14}$$

Equation (8) then takes the form

$$\frac{\mathrm{d}^3N_{\rm d}}{\mathrm{d}P_{\rm d}^3} = \frac{3\zeta}{(2\pi)^6}\int\mathrm{d}^3q\,\mathrm{e}^{-q^2d^2}\,G_{np}(\boldsymbol{P}_{\rm d}/2+\boldsymbol{q},\boldsymbol{P}_{\rm d}/2-\boldsymbol{q}), \tag{15}$$

[2] We neglect for the moment the double counting of nucleons involved in different pairs.

[3] Our conventions for the normalization of the Wigner function are described in Appendix A.

[4] Note that the variable r in the deuteron wave function describes the diameter, so that $r_{\rm rms}^2 = \int\mathrm{d}^3r\,(r/2)^2|\varphi(r)|^2$.

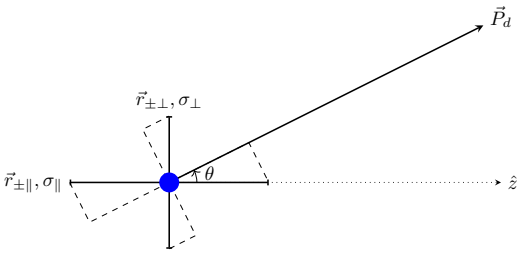

Fig. 1 Splitting of the width σ into a part parallel to the beam (z-axis), $\sigma_\parallel$, and a part perpendicular to the beam, $\sigma_\perp$. Only the components of $\boldsymbol{r}_\perp$ and $\boldsymbol{r}_\parallel$ parallel to the deuteron momentum $\boldsymbol{P}_\mathrm{d}$ are affected by the Lorentz transformation

where the factor

$$\zeta \equiv \left(\frac{d^2}{d^2+4\sigma^2}\right)^{3/2} \leq 1 \tag{16}$$

depends on the characteristic spatial spread of the nucleons and on the spatial extension of the deuteron wave function. The coalescence probability is also suppressed for large $q^2 d^2$ as a Gaussian in our model.

2.2 Parameter estimation

In order to estimate the characteristic values for the parameter σ in the spatial distribution $h(\boldsymbol{r})$ defined in Eq. (14), one generally has to consider separately the longitudinal and transverse directions,

$$h(\boldsymbol{r}) \propto \exp\left\{-\frac{\boldsymbol{r}_\parallel^2}{2\sigma_\parallel^2} - \frac{\boldsymbol{r}_\perp^2}{2\sigma_\perp^2}\right\}. \tag{17}$$

Let us discuss first the case of $\mathrm{e}^+\mathrm{e}^-$ annihilation into hadrons in the center-of-mass frame of the collision, choosing the z-axis along the direction of the outgoing quark and antiquark, as shown in Fig. 1. Before we proceed, it is worth remarking that this reaction involves three different time and distance scales [41]: the annihilation of the electron–positron pair into the quark and antiquark happens during the time $t_\mathrm{ann} \sim 1/\sqrt{s}$. For $s \gg \Lambda^2_\mathrm{QCD}$, the hard process is thus almost point-like in coordinate space. The perturbative cascading of the produced (anti-) quark proceeds via parton branchings with the characteristic momentum transfer squared $\Lambda^2_\mathrm{QCD} \ll |q^2| \ll s$. This implies that the corresponding longitudinal proper distance scales are smaller than $\Lambda^{-1}_\mathrm{QCD}$. Therefore, the third and last step, the nonperturbative conversion of the final partons into hadrons, corresponds to the longest time and distance scales: the so-called hadronization time or formation length L_had required for a hadron to build up its parton "coat" is

$$L_\mathrm{had} \sim \gamma L_0, \tag{18}$$

where γ is the gamma factor of the hadron in the considered frame and L_0 equals approximately the nucleon size, $L_0 \sim R_p \sim 1$ fm. The coalescence process involves nucleons which have (almost) completed their formation, and the process proceeds on distance scales which are comparable to L_had. Boosting to the rest frame of the produced deuteron compensates the gamma factor in Eq. (18); hence we expect $\sigma_\parallel \sim L_0 \sim 1$ fm in that frame.

The characteristic transverse spread of a produced hadron can be estimated using the uncertainty relation: the transverse displacement of the hadron is obtained summing over the perpendicular components of the random walk performed by the previous generations of partons during both the perturbative and the nonperturbative parton cascading. The contribution of a single branching is inversely proportional to the transverse momentum of the parton, $\Delta b_i \sim 1/p_{\perp,i}$. Also here, nonperturbative physics gives the dominating contribution with[5] $p_\perp \sim \Lambda_\mathrm{QCD}$. Since the bulk of deuterons is produced with relatively small transverse momenta, boosting to the rest frame has a small effect on $\sigma_\perp \sim \Lambda^{-1}_\mathrm{QCD}$. In the simplest option we consider, we neglect therefore this boost. Since $\Lambda^{-1}_\mathrm{QCD}$ is of the same order of magnitude as L_0, we set in the following $\sigma_\parallel = \sigma_\perp = \sigma$, to minimize the number of parameters. An alternative set-up which takes into account the effect of the transverse boost on $\sigma_\perp$, will be discussed at the end of this subsection.

Let us now move to proton–proton, proton–nucleus and nucleus–nucleus collisions. Here, the picture is modified by multiple scattering processes involving multiparton interactions: the proton and neutron taking part in the coalescence process can thus originate from different parton–parton interactions. Therefore it is necessary to take into account the longitudinal and transverse spread of the initial parton clouds of the projectile and the target. Starting with the former, it is important to keep in mind that the effect of the Lorentz contraction is different for fast and slow partons. At a given rapidity y in the laboratory system, partons from, say, the target proton cloud are distributed over the longitudinal distance $\sim R_p/\gamma = R_p\,\mathrm{e}^{-y}$. Boosting to the deuteron rest frame compensates again the gamma factor, so that the resulting "geometrical" contribution to $\sigma_\parallel$, due to the longitudinal extension of the parton cloud, equals $\sigma_{\parallel(\mathrm{geom})} \sim R_p \sim 1$ fm. Summing the two contributions in quadrature, we obtain

$$\sigma^2_{\parallel(pp)} = \sigma^2_{\parallel(\mathrm{e}^\pm)} + \sigma^2_{\parallel(\mathrm{geom})} \approx 2\sigma^2_{\parallel(\mathrm{e}^\pm)}. \tag{19}$$

[5] The numerical value of Λ_QCD depends on the renormalization scheme used and varies between 0.3 and 0.9 GeV for three flavors [42].

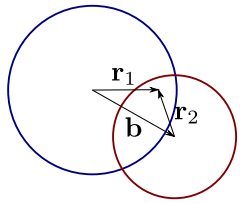

Fig. 2 Sketch of the parton clouds of two interacting hadrons

Finally, we have to consider the geometrical contribution to $\sigma_\perp$. One may naively expect it to depend on the impact parameter for a proton–proton (proton–nucleus) collision. Let us show that this is not the case in the simple geometrical picture of Fig. 2 and derive the geometrical contribution to $\sigma_\perp$. We define $\sigma_{\perp(\mathrm{geom})}$ as the transverse spread of the overlapping region (O) of the projectile and target parton clouds,

$$\sigma^2_{(\mathrm{geom})} = \langle r_1^2\rangle_O - \langle \boldsymbol{r}_1\rangle_O^2. \tag{20}$$

The expectation value $\langle A\rangle_O$ follows then as

$$\langle A\rangle = \frac{\int \mathrm{d}^2 r_1\, \mathrm{d}^2 r_2\, A\, \rho_1(r_1)\, \rho_2(r_2)\, w_{\mathrm{int}}(|\boldsymbol{b}-\boldsymbol{r}_1+\boldsymbol{r}_2|)}{\int \mathrm{d}^2 r_1\, \mathrm{d}^2 r_2\, \rho_1(r_1)\, \rho_2(r_2)\, w_{\mathrm{int}}(|\boldsymbol{b}-\boldsymbol{r}_1+\boldsymbol{r}_2|)}, \tag{21}$$

where $\boldsymbol{b}$ is the impact parameter for the collision, $\rho_i(r_i)$ are the transverse parton densities of the projectile ($i=1$) and the target ($i=2$), and w_{int} is the probability for a parton–parton interaction. Assuming for simplicity that the latter is point-like,

$$w_{\mathrm{int}}(|\boldsymbol{b}-\boldsymbol{r}_1+\boldsymbol{r}_2|) \propto \delta^{(2)}(\boldsymbol{b}-\boldsymbol{r}_1+\boldsymbol{r}_2), \tag{22}$$

and approximating the density distributions by Gaussians,

$$\rho_i = 1/(\pi\, R_i^2)\exp\left\{-r^2/R_i^2\right\}, \tag{23}$$

with R_i being the transverse radii of the projectile and the target, respectively, we obtain

$$\sigma^2_{\perp(\mathrm{geom})} = \frac{R_1^2 R_2^2}{R_1^2+R_2^2}. \tag{24}$$

For the particular case of pp collisions, we have $\sigma^2_{\perp(\mathrm{geom})} = R_p^2/2$. Since this is of the same order of magnitude as $\sigma^2_{\perp(\mathrm{e}^\pm)}$, we set

$$\sigma^2_{\perp(pp)} = \sigma^2_{\perp(\mathrm{e}^\pm)} + \sigma^2_{\perp(\mathrm{geom})} \approx 2\sigma^2_{\perp(\mathrm{e}^\pm)}, \tag{25}$$

so that we can also use for proton–proton collisions one universal parameter,

$$\sigma_{\parallel(pp)} = \sigma_{\perp(pp)} = \sigma_{(pp)} = \sqrt{2}\,\sigma_{(\mathrm{e}^\pm)}. \tag{26}$$

It is noteworthy that such an assumption would generally be unjustified in the case of proton–nucleus and nucleus–nucleus collisions since the corresponding geometrical contributions to $\sigma_\parallel$ and $\sigma_\perp$ may differ significantly. Considering, as an example, proton–lead collisions, we have[6] $\sigma_{\parallel(\mathrm{geom})} \sim R_{\mathrm{Pb}}$, while Eq. (24) yields for the transverse spread $\sigma_{\perp(\mathrm{geom})} \simeq R_p$.

Boosted $\boldsymbol{\sigma_\perp}$ In an alternative set-up, we take into account that $\sigma_\perp$ is defined in the collider frame, while in the derivation of Eq. (15), all quantities and wave functions were evaluated in the rest frame of the deuteron. This requires us to Lorentz transform $W(\boldsymbol{r},\boldsymbol{q}) \propto h(\boldsymbol{r})$ between the two frames. Such a transformation includes both a longitudinal boost, with a Lorentz factor $\gamma_\parallel \simeq \gamma\cos\theta \simeq \gamma$, and a transverse one. Here $\theta \simeq (p_{p\perp}+p_{n\perp})/(p_{p\parallel}+p_{n\parallel})$ is the small angle between the direction of motion of the nucleon pair in the CoM and the z-axis in the original frame, before the boost. While the former transformation has been accounted for in our definition for $\sigma_\parallel$, the effect of the latter is to replace $\sigma_\perp$ defined in the original frame by $\tilde{\sigma}_\perp$ in the CoM, with

$$\tilde{\sigma}_\perp = \frac{\sigma_\perp}{\sqrt{\cos^2\theta + \gamma^2\sin^2\theta}}. \tag{27}$$

Thus, the factor ζ in Eq. (16) changes to

$$\zeta = \frac{d^2}{d^2+4\tilde{\sigma}_\perp^2}\sqrt{\frac{d^2}{d^2+4\sigma_\parallel^2}}. \tag{28}$$

2.3 Numerical implementation

As one can see in Eq. (15), a given proton–neutron pair with momentum difference $2\boldsymbol{q}$ in its CoM has the probability

$$w = 3\zeta\,\mathrm{e}^{-q^2d^2} \tag{29}$$

to form a deuteron. Depending on whether we use the simplified approach or take into account the modification of $\sigma_\perp$

[6] Note that the geometrical contributions to $\sigma_\parallel$ and $\sigma_\perp$ should generally vary from event to event, depending on the corresponding rate of multiple scatterings. For proton–proton collisions, such a variation is expected to be relatively weak and, hence, may be neglected in a first approximation. This is, however, different for proton–nucleus and nucleus–nucleus interactions: our estimations are valid for relatively central collisions involving numerous pair-wise inelastic rescatterings between the projectile and target nucleons, which provide the bulk contribution to the formation of (anti-)nuclei. On the other hand, peripheral interactions at large impact parameters are dominated by a single binary collision between a pair of projectile and target nucleons, which gives rise to $\sigma_{\parallel(\mathrm{geom})} \sim R_p$, like in the proton–proton case. This leads to a pronounced correlation between the size of the source region and the multiplicity of secondary hadrons produced.

by the transverse boost, the factor ζ is defined by Eq. (16) or (28), respectively.

At this point, we have to take some care of potential double (triple, etc.) counting since a given proton may be paired with different neutrons and vice versa. Let us assume that, for a given event, the final state contains N_p protons and N_n neutrons. Denoting by w_{ij} the coalescence probability, Eq. (29), for a pair formed out of the ith proton and the jth neutron, we have the following expression for the average number of deuterons produced in such an event:

$$\begin{aligned} N_\mathrm{d} &= \sum_{i=1}^{N_p}\sum_{j=1}^{N_n} w_{ij} - \frac{1}{2}\sum_{i=1}^{N_p}\sum_{k\neq i}^{N_p}\sum_{j=1}^{N_n} w_{ij}\, w_{kj} \\ &\quad - \frac{1}{2}\sum_{i=1}^{N_p}\sum_{j=1}^{N_n}\sum_{l\neq j}^{N_n} w_{ij}\, w_{il} - \cdots \\ &\simeq \sum_{i=1}^{N_p}\sum_{j=1}^{N_n} w_{ij}\left[1 - \frac{1}{2}\sum_{k\neq i}^{N_p} w_{kj} - \frac{1}{2}\sum_{l\neq j}^{N_n} w_{il}\right], \end{aligned} \tag{30}$$

where in the last line we have taken into account the smallness of the coalescence probabilities and have neglected the contributions of triple and higher contributions.

As one can see from Eq. (30), the contribution of a given proton–neutron pair ij to the binning of the deuteron spectrum should be taken with the weight,

$$\Omega_{ij} = w_{ij}\left[1 - \frac{1}{2}\sum_{k\neq i}^{N_p} w_{kj} - \frac{1}{2}\sum_{l\neq j}^{N_n} w_{il}\right]. \tag{31}$$

Since we bin the deuteron distribution $\mathrm{d}^3N_\mathrm{d}/\mathrm{d}P_\mathrm{d}^3$ in the reference frame of the detector, no additional factor accounting for the Lorentz transformation of the yield is necessary.

2.4 Improving the deuteron wave function

In the treatment above, a Gaussian which reproduces the measured r_rms value of the deuteron charge distribution was used as wave function. However, it is well known that the deuteron wave function is more strongly peaked at $r = 0$ than a Gaussian. An alternative is the Hulthen wave function,

$$\phi_\mathrm{d}(\boldsymbol{r}) = \sqrt{\frac{ab(a+b)}{2\pi(a-b)^2}}\,\frac{\mathrm{e}^{-ar} - \mathrm{e}^{-br}}{r} \tag{32}$$

with $a = 0.23\,\mathrm{fm}^{-1}$ and $b = 1.61\,\mathrm{fm}^{-1}$, which gives a good description of the deuteron ground state [40]. Using this wave function, an analytical derivation of the weights would, however, not be possible. To obtain a better description of the deuteron, and at the same time to keep the problem analytical solvable, we use instead the sum of two Gaussians as an ansatz for the deuteron wave function,

$$\varphi_\mathrm{d}(\boldsymbol{r}) = \pi^{-3/4}\left[\frac{\Delta^{1/2}}{d_1^{3/2}}\mathrm{e}^{-r^2/(2d_1^2)} + \mathrm{e}^{\mathrm{i}\alpha}\frac{(1-\Delta)^{1/2}}{d_2^{3/2}}\mathrm{e}^{-r^2/(2d_2^2)}\right], \tag{33}$$

where we include a relative phase α between the two terms. Choosing $\mathrm{e}^{\mathrm{i}\alpha} = \mathrm{i}$ leads to some simplifications. First, the probability distribution

$$|\varphi_\mathrm{d}(\boldsymbol{r})|^2 = \pi^{-3/2}\left[\frac{\Delta}{d_1^3}\mathrm{e}^{-r^2/d_1^2} + \frac{1-\Delta}{d_2^3}\mathrm{e}^{-r^2/d_2^2}\right] \tag{34}$$

contains with this choice no mixed terms. Moreover, we will see below that this choice leads to the same weight function as in the one-Gaussian case.

Next we fit $|\varphi_\mathrm{d}(\boldsymbol{r})|^2$ to the Hulthen wave function (32) in order to fix Δ, d_1, and d_2. Two possible methods are to fit $|\varphi_\mathrm{d}(0)|^2$, $\langle r\rangle$, and $\langle r^2\rangle$, and to fit $\langle r\rangle$, $\langle r^2\rangle$, and $\langle r^3\rangle$. The first method will be called φ_0-fit and the second r^3-fit. The φ_0-fit yields $\Delta = 0.581$, $d_1 = 3.979\,\mathrm{fm}$, and $d_2 = 0.890\,\mathrm{fm}$, while the r^3-fit yields $\Delta = 0.247$, $d_1 = 5.343\,\mathrm{fm}$, and $d_2 = 1.810\,\mathrm{fm}$. The resulting probability distributions are plotted in Fig. 3 together with the one for the one-Gaussian (Eq. (10)) and the Hulthen (Eq. (32)) wave functions. One can see in the figure that the two-Gaussian ansatz resembles the Hulthen probability distribution more closely than the Gaussian wave function does, in particular, regarding the peak around $r = 0$. The φ_0-fit reproduces visually the behavior around $r = 0$ best and will therefore be used when comparing with experimental data later on.

The deuteron Wigner function follows then as

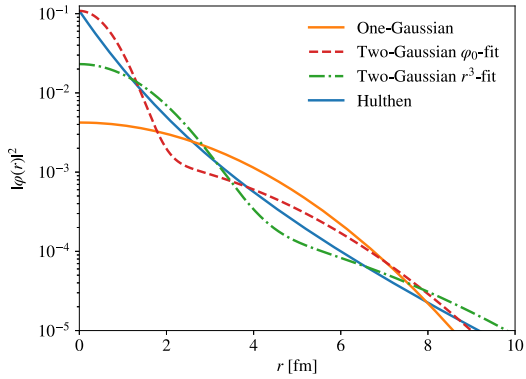

Fig. 3 Comparison between the different parametrizations for the deuteron wave function

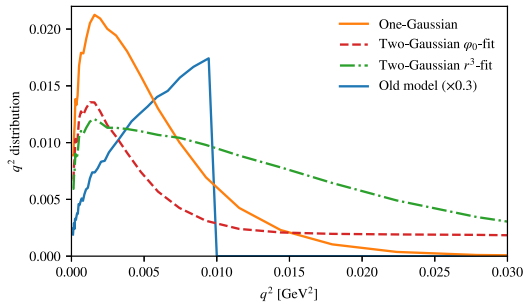

Fig. 4 Weighted q^2-distribution for the four considered cases

$$\mathcal{D}(\boldsymbol{r},\boldsymbol{q}) = 8\left[\Delta \mathrm{e}^{-r^2/d_1^2}\mathrm{e}^{-q^2 d_1^2} + (1-\Delta)\mathrm{e}^{-r^2/d_2^2}\mathrm{e}^{-q^2 d_2^2}\right] + A(\boldsymbol{r}\cdot\boldsymbol{q}), \tag{35}$$

where the function A is odd in $\boldsymbol{r}$, $A(-\boldsymbol{r}\cdot\boldsymbol{q}) = -A(\boldsymbol{r}\cdot\boldsymbol{q})$. Therefore the new term A drops out performing the spatial integrals over $\boldsymbol{r}_p$ and $\boldsymbol{r}_n$ in Eq. (8) and, thus, does not contribute to the weights in the binning procedure. The weights for the two-Gaussian case are thus

$$w = 3\left(\zeta_1 \Delta \mathrm{e}^{-q^2 d_1^2} + \zeta_2[1-\Delta]\mathrm{e}^{-q^2 d_2^2}\right), \tag{36}$$

where the ζ_i are given by Eq. (16).

The weighted q^2 distributions with the one-Gaussian weight and two-Gaussian weights for pp collisions at $\sqrt{s} = 7$ TeV are shown in Fig. 4 for the ALICE set-up discussed in Appendix B.1, using $\sigma = 7\,\mathrm{GeV}^{-1}$ and a constant ζ. For the old model, $p_0 = 0.2$ GeV is used and the resulting distribution is rescaled by a factor 0.3 to make the figure clearer. Double counting has in all cases only a minor effect on the resulting distributions. In the two-Gaussian case, the better description of the peak at $r = 0$ in the probability distribution significantly enhances the contribution from proton–neutron pairs with a relatively large momentum difference.

3 Formation of helium-3 and tritium

The cases of helium-3 and tritium nuclei are similar to the deuteron case, but the derivation of the weight is more cumbersome. We account for the Coulomb interaction between the two protons in the helium nucleus only insofar as we allow for a different rms radius of the two nuclei in the fitting procedure. In this approach, our model applies in the same way for helium-3 and tritium. Moreover, this assumption is supported by the data of the ALICE experiment which found a comparable yield of helium-3 and tritium nuclei. The binding energies of both nuclei are still low ($\simeq 8$ MeV), and the same approximations as in the deuteron case thus still apply.

The number of helium nuclei with momentum $\boldsymbol{P}_{\mathrm{He}}$ is found by projecting the helium density matrix onto the three-nucleon one, cf. with Eq. (3). As in the deuteron case, the nucleus wave function is factorized into a plane wave describing the CoM motion with momentum $\boldsymbol{P}_{\mathrm{He}}$ and an internal wave function which depends on the relative coordinates,

$$\phi_{\mathrm{He}}(\boldsymbol{x}_1,\boldsymbol{x}_2,\boldsymbol{x}_3) = (2\pi)^{-3/2}\exp\{\mathrm{i}\boldsymbol{P}_{\mathrm{He}}\cdot\boldsymbol{R}\}\;\varphi_{\mathrm{He}}(\boldsymbol{\rho},\boldsymbol{\lambda}). \tag{37}$$

Here, the Jacobi coordinates $\boldsymbol{R}$, $\boldsymbol{\rho}$, and $\boldsymbol{\lambda}$ are expressed via $\boldsymbol{x}_1, \boldsymbol{x}_2$ and $\boldsymbol{x}_3$ as

$$\boldsymbol{\lambda} = (\boldsymbol{x}_1 + \boldsymbol{x}_2 - 2\boldsymbol{x}_3)/\sqrt{6}, \tag{38a}$$

$$\boldsymbol{\rho} = (\boldsymbol{x}_1 - \boldsymbol{x}_2)/\sqrt{2}, \tag{38b}$$

$$\boldsymbol{R} = (\boldsymbol{x}_1 + \boldsymbol{x}_2 + \boldsymbol{x}_3)/3, \tag{38c}$$

with $\boldsymbol{x}_1^2 + \boldsymbol{x}_2^2 + \boldsymbol{x}_3^2 = 3\boldsymbol{R}^2 + \boldsymbol{\rho}^2 + \boldsymbol{\lambda}^2$, $\boldsymbol{\rho}^2 + \boldsymbol{\lambda}^2 = (\boldsymbol{x}_1 - \boldsymbol{x}_2)^2 + (\boldsymbol{x}_1 - \boldsymbol{x}_3)^2 + (\boldsymbol{x}_3 - \boldsymbol{x}_2)^2$, $\mathrm{d}^3 r_1\,\mathrm{d}^3 r_2\,\mathrm{d}^3 r_3 = 3^{3/2}\,\mathrm{d}^3 R\,\mathrm{d}^3\rho\,\mathrm{d}^3\lambda$. The internal wave function is again approximated by a Gaussian in the relative coordinates $\boldsymbol{\rho}$ and $\boldsymbol{\lambda}$,

$$\varphi_{\mathrm{He}}(\boldsymbol{\rho},\boldsymbol{\lambda}) = (3\pi^2 b^4)^{-3/4}\,\exp -\frac{\boldsymbol{\rho}^2+\boldsymbol{\lambda}^2}{2b^2}, \tag{39}$$

with b being the rms radius of the nucleus,

$$r_{\mathrm{rms}}^2 = 3^{3/2}\int \mathrm{d}^3\rho\,\mathrm{d}^3\lambda\,\frac{\rho^2+\lambda^2}{3}\,|\varphi_{\mathrm{He}}(\boldsymbol{\rho},\boldsymbol{\lambda})|^2 = b^2. \tag{40}$$

The ^{3}He and ^{3}H nuclei have rms radii equal to 1.96 fm and 1.76 fm, respectively [43].

Performing the same steps as in Eqs. (5) and (7) in the deuteron case, we obtain for the momentum spectrum of the produced nuclei

$$\begin{aligned}\frac{\mathrm{d}^3 N_{\mathrm{He}}}{\mathrm{d}P_{\mathrm{He}}^3} = {} & \frac{S}{(2\pi)^3}\int \mathrm{d}^3 r_1\,\mathrm{d}^3 r_2\,\mathrm{d}^3 r_3\,\mathrm{d}^3 r_1'\,\mathrm{d}^3 r_2'\,\mathrm{d}^3 r_3' \\ & \times \mathrm{e}^{-\mathrm{i}\boldsymbol{P}_{\mathrm{He}}\cdot(\boldsymbol{R}-\boldsymbol{R}')}\,\varphi_{\mathrm{He}}(\boldsymbol{\rho},\boldsymbol{\lambda})^*\,\varphi_{\mathrm{He}}(\boldsymbol{\rho}',\boldsymbol{\lambda}') \\ & \times \int \frac{\mathrm{d}^3 p_1}{(2\pi)^3}\frac{\mathrm{d}^3 p_2}{(2\pi)^3}\frac{\mathrm{d}^3 p_3}{(2\pi)^3}\,\mathrm{e}^{\mathrm{i}\boldsymbol{p}_1\cdot(\boldsymbol{x}_1-\boldsymbol{x}_1')+\mathrm{i}\boldsymbol{p}_2\cdot(\boldsymbol{x}_2-\boldsymbol{x}_2')+\mathrm{i}\boldsymbol{p}_3\cdot(\boldsymbol{x}_3-\boldsymbol{x}_3')} \\ & \times W_{N_1N_2N_3}\left(\boldsymbol{p}_1,\boldsymbol{p}_2,\boldsymbol{p}_3,\frac{\boldsymbol{x}_1+\boldsymbol{x}_1'}{2},\frac{\boldsymbol{x}_2+\boldsymbol{x}_2'}{2},\frac{\boldsymbol{x}_3+\boldsymbol{x}_3'}{2}\right),\end{aligned} \tag{41}$$

where $S = 1/12$ is the statistical factor accounting for the different isospin and spin states and $W_{N_1N_2N_3}$ is the Wigner function for the three-nucleon state. We approximate again $W_{N_1N_2N_3}$ by a product of momentum and coordinate distributions of the nucleons, neglecting spatial correlations between the latter,

Table 1 Fit results for the constant ζ factor, in comparison to the old model

Experiment	One-Gaussian		Two-Gaussian		Old model	
	σ [$\frac{1}{\text{GeV}}$]	$\frac{\chi^2}{N-1}$	σ [$\frac{1}{\text{GeV}}$]	$\frac{\chi^2}{N-1}$	p_0 [MeV]	$\frac{\chi^2}{N-1}$
ALICE 0.9 TeV	3.5 ± 0.7	7.5/2	6.2 ± 0.3	6.0/2	181	7.3/2
ALICE 2.76 TeV	4.3 ± 0.3	44/6	6.6 ± 0.1	32/6	174	45.6/6
ALICE 7 TeV	4.1 ± 0.2	182/19	6.6 ± 0.1	133/19	176	177/19
ALICE combined	4.1 ± 0.1	235/29	6.6 ± 0.1	172/29	176	229/19
ALICE helium-3	4.5 ± 0.9	1.7/2	–	–	179	1.2/2
ALEPH	$0^{+2.3}_{-0}$	–	$5.0^{+0.9}_{-0.6}$	–	214^{+21}_{-26}	–
ALEPH + OPAL	$0^{+4.4}_{-0}$	3.2/1	$5.5^{+1.3}_{-1.1}$	3.2/1	201	3.2/1

$$W_{N_1N_2N_3}(\boldsymbol{p}_1, \boldsymbol{p}_2, \boldsymbol{p}_3, \boldsymbol{r}_1, \boldsymbol{r}_2, \boldsymbol{r}_3) = G_{N_1N_2N_3}(\boldsymbol{p}_1, \boldsymbol{p}_2, \boldsymbol{p}_3) \prod_{i=1}^{3} h(\boldsymbol{r}_i), \tag{42}$$

where $h(\boldsymbol{r})$ is given by Eq. (14).

Expressing further the product $\varphi_{\text{He}}(\boldsymbol{\rho}, \boldsymbol{\lambda})^* \varphi_{\text{He}}(\boldsymbol{\rho}', \boldsymbol{\lambda}')$ via the Wigner function of the helium nucleus and doing the spatial integrals, changing to the coordinates (38), we finally obtain

$$\frac{\mathrm{d}^3 N_{\text{He}}}{\mathrm{d}P_{\text{He}}^3} = \frac{64 S \zeta}{(2\pi)^9} \int \mathrm{d}^3\, p_1\, \mathrm{d}^3\, p_2\, \mathrm{d}^3\, p_3 \times \delta^{(3)}(\boldsymbol{p}_1 + \boldsymbol{p}_2 + \boldsymbol{p}_3 - \boldsymbol{P}_{\text{He}})\, G_{N_1N_2N_3}(\boldsymbol{p}_1, \boldsymbol{p}_2, \boldsymbol{p}_3)\, \mathrm{e}^{-b^2 P^2}, \tag{43}$$

where

$$\zeta = \left(\frac{b^2}{b^2 + 2\sigma^2}\right)^3 \tag{44}$$

accounts for the overlap of the wave functions and

$$P^2 = \frac{1}{3}\left[(\boldsymbol{p}_1 - \boldsymbol{p}_2)^2 + (\boldsymbol{p}_1 - \boldsymbol{p}_3)^2 + (\boldsymbol{p}_2 - \boldsymbol{p}_3)^2\right] \tag{45}$$

is a measure of the relative momentum difference between the nucleons. The procedure for finding the correct Lorentz transformation is similar to the deuteron case. The result is

$$\zeta = \left(\frac{b^2}{b^2 + 2\tilde{\sigma}_\perp^2}\right)^2 \frac{b^2}{b^2 + 2\sigma_\parallel^2}, \tag{46}$$

where $\tilde{\sigma}_\perp$ is again given by (28).

The numerical procedure for treating the formation of tritium and helium-3 nuclei is identical to the one described in Sect. 2.3, apart from the different weight factor; P^2 is now defined in the CoM frame of the three-particle state. One may argue that it is sufficient to calculate the momentum differences between nucleons, entering Eq. (45), in the rest frames for the corresponding nucleon pairs since, because of the exponential factor in Eq. (43), those practically coincide with the ones defined in the rest frame of the nucleus. This approach was used throughout this work.

Table 2 Fit results obtained taking into account the modification of $\sigma_\perp$ by transverse boosts

Experiment	One-Gaussian		Two-Gaussian	
	σ [$\frac{1}{\text{GeV}}$]	$\frac{\chi^2}{N-1}$	σ [$\frac{1}{\text{GeV}}$]	$\frac{\chi^2}{N-1}$
ALICE 0.9 TeV	3.9 ± 0.8	6.7/2	6.9 ± 0.3	2.6/2
ALICE 2.76 TeV	4.9 ± 0.3	35/6	7.5 ± 0.1	8.6/6
ALICE 7 TeV	4.7 ± 0.2	143/19	7.6 ± 0.1	29/19
ALICE combined	4.7 ± 0.4	186/29	7.6 ± 0.1	45/29
ALICE helium-3	5.2 ± 1.0	1.1/2	–	–
ALEPH	$0^{+2.4}_{-0}$	–	$5.3^{+1.0}_{-0.6}$	–
ALEPH + OPAL	$0^{+4.6}_{-0}$	3.2/1	$5.8^{+1.4}_{-1.1}$	3.2/1

4 Comparison with experimental data

The predicted yield of antinuclei depends on the hadronization scheme [44], and a comparison to different experimental data sets should be therefore made using a single MC simulation. In this work, we choose to perform all our simulations of pp and $\mathrm{e}^+\mathrm{e}^-$ collisions with Pythia 8.230 [45,46], which describes the antiproton spectra at LHC energies within 20–30% [47]. We set $\Delta\tau = 0$, switching thereby decays of long-lived particles in Pythia off.[7] Thereby we exclude nucleons which are produced mostly outside the source region. In each run, we take into consideration all produced nucleon pairs with $q < 0.25$ GeV for the one-Gaussian case and with $q < 0.5$ GeV for the two-Gaussian ansatz for the deuteron wave function. There are two obvious methods to generalize the standard per-event coalescence model to helium-3 and tritium: One can require that each of the relative momenta lie within a sphere with radius p_0 in momentum space, or that the absolute momentum difference for each pair of particles is smaller than p_0 [48,49]. The latter approach was used here.

[7] This choice is similar to the approach of Ref. [19], as Pythia 8 only stores non-zero lifetimes in the event table that are relevant for displaced vertices in collider experiments.

Let us now test our model with available data on antideuteron production in e^+e^- annihilation at the Z resonance energy, from the ALEPH and OPAL experiments, and with ALICE data on antideuteron and antihelium production in pp collisions. Details of the experimental set-ups are described in Appendix B. Both for the parameter σ of the new model and for p_0 of the standard coalescence model, we perform χ^2 fits to these data sets. The best-fit values, their $1\,\sigma$ errors and the reduced χ^2 of the various fits are given in Table 1 for the case of constant $\sigma_\perp$. In turn, the fit results reported in Table 2 take into account the modification of $\sigma_\perp$ by transverse boosts, i.e., they have been obtained using ζ defined in Eq. (28), with $\tilde{\sigma}_\perp$ from Eq. (27). We first note that the two-Gaussian cases lead to significantly reduced χ^2 values, compared to the one-Gaussian ansatz or to the standard coalescence model. At the same time, they favor larger values for the parameter σ, which is related to an enhanced contribution from nucleon pairs with relatively large q^2. Taking into account the modification of $\sigma_\perp$ by transverse boosts improves significantly the quality of the fits, as one can see in Table 2. Moreover, in that case, the best-fit values of the parameter σ agree well with our estimates in Sect. 2.2: the ratio of the values of σ, determined from fits to the ALICE data for pp collisions and to the ALEPH data for e^+e^- annihilation, agrees well with the expected one, equal $\sqrt{2}$ (cf. Eq. 26), and the absolute value, $\sigma_{(e^+e^-)} \simeq 5\,\mathrm{GeV}^{-1} \simeq 1$ fm, is consistent with its interpretation as the characteristic hadronic length scale ($\sim R_p$).

In Fig. 5, we compare the ALICE antideuteron data with the best-fit spectra obtained for the various cases considered.

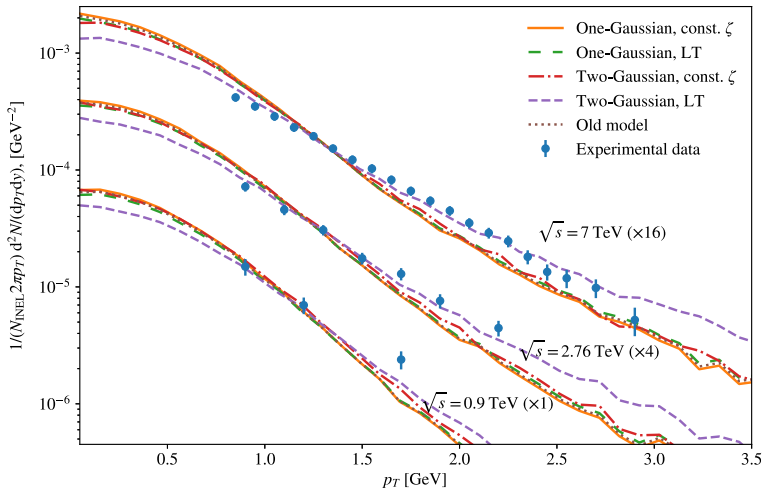

Fig. 5 Best combined fits to the ALICE antideuteron data for the considered models. The data and fits are multiplied by a constant factor to make the figure clearer. The curves labeled LT are obtained including the Lorentz boost of $\sigma_\perp$

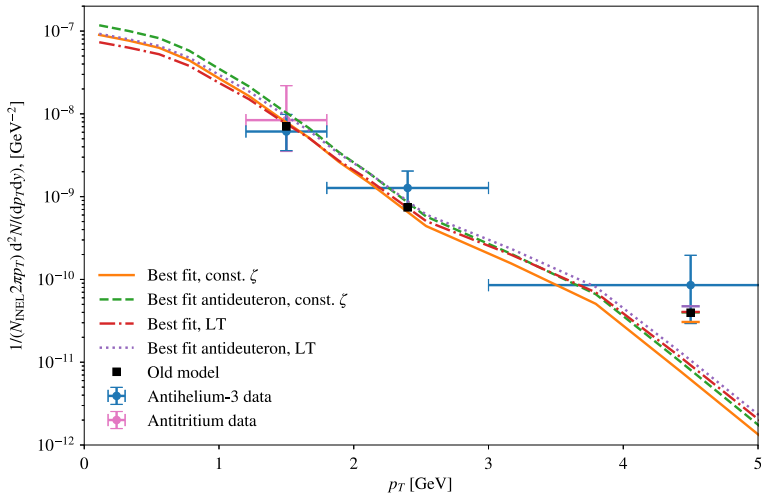

Fig. 6 Best fits to the ALICE antihelium data for the one-Gaussian models. The best fits using the parameters obtained from the best combined fit to the ALICE antideuteron data is also plotted

It becomes apparent that the slope of the $p_\perp$ distributions is best described using the two-Gaussian ansatz for the deuteron wave function, when the modification of $\sigma_\perp$ by transverse boosts is taken into account.

In Fig. 6, we compare the predictions of our model to the ALICE data for light antinuclei, antihelium and a single data point for tritium. Using the best-fit values for σ obtained from fitting the antideuteron data in the two-Gaussian case, the experimental data are satisfactorily reproduced. Additionally, we show the best-fit spectra obtained by fitting the antihelium data. Since the difference between the two fits compared to the error bars is small, we conclude that the two data sets can be consistently described using the same value of σ. The goodness-of-fit parameter is $\chi^2/(N-1) = 6.0/2$, when the σ determined in the combined antideuteron fit is used for the helium-3 and tritium data. Thus there is a slight tension, and it will be interesting to check it by future antihelium data with reduced errors.

5 Conclusion

We have developed a new coalescence model for the formation of antinuclei, which combines an event-by-event Monte Carlo description of the collision process with a microscopic coalescence treatment based on the Wigner function representations of the produced antinuclei states. This approach has allowed us to include in a semi-classical picture both the size σ of the formation region and the momentum correlations of the nucleons forming the nuclei. Since the size σ is process dependent, the difference in the observed antideuterons yields in e^+e^- and pp collisions can be naturally accounted for. Fitting the single, universal parameter contained in our model to the experimental data, we obtained a best-fit value, $\sigma \simeq 1$ fm, which corresponds well to its physical interpretation as the size of the formation region of the light nuclei. If, in the future, antideuteron and antihelium data sets with reduced errors and for a larger $p_\perp$ range will be available, an independent fit of the two parameters $\sigma_\perp$ and $\sigma_\parallel$ might be warranted.

We have examined different approximations for the deuteron wave functions as well as two different implementations of the transverse size $\sigma_\perp$ of the formation region. The fits to the ALICE antideuteron data prefer the two-Gaussian wave function and the approach where the effect on $\sigma_\perp$, due to a Lorentz boost to the deuteron frame, is taken into account. Both correspond to the physically expected choices: the two-Gaussian wave function takes into account that the deuteron wave function is rather peaked at $r = 0$, while $\sigma_\perp \simeq R_p$ is expected to hold in the CoM frame of the collider. Using the best-fit values for antideuteron, we could well describe the data for the production of antihelium in pp interactions and of antideuterons in e^+e^- annihilation at the Z-resonance energy.

Our model is therefore well suited to investigate in detail the antideuteron and antihelium fluxes predicted in models for dark matter annihilations and from cosmic ray interactions. In particular, it will be interesting to see whether and how the tentative antihelium events announced by the AMS-02 collaboration [50] can be explained within our model.

Acknowledgements M.K. and J.T. acknowledge partial support from the Research Council of Norway (NFR). S.O. acknowledges support from project OS 481/2-1 of the Deutsche Forschungsgemeinschaft.

Data Availability Statement This manuscript has no associated data or the data will not be deposited. [Authors' comment: The paper is of theoretical character and the data are contained in this article.]

Appendix A: Wigner function

Our definition (9) of the one-particle Wigner function implies in $d = 1$ as normalization (with $\hbar = 1 = h/(2\pi)$)

$$\int \frac{\mathrm{d}p}{2\pi} \mathrm{d}x \, W(x, p) = 1 \,. \tag{A.1}$$

The corresponding probability distributions for the space and momentum variables are obtained from

$$\int \mathrm{d}x \, W(x, p) = \psi^*(p) \, \psi(p), \tag{A.2}$$

$$\int \frac{\mathrm{d}p}{2\pi} \, W(x, p) = \phi^*(x) \, \phi(x). \tag{A.3}$$

For our ansatz $W(x, p) = h(x)g(p)$, it follows that $h(x)$ describes the probability distribution of the nucleon in coordinate space, while the probability distribution of the nucleon momenta $g(p)$ is normalized as

$$\int \frac{\mathrm{d}p}{2\pi} g(p) = 1 \,. \tag{A.4}$$

Appendix B: Experiments

Appendix B.1: ALICE

The ALICE collaboration measured the invariant differential yields of deuterons and antideuterons,

$$E \frac{\mathrm{d}^3 n}{\mathrm{d}p^3} = \frac{1}{N_{\mathrm{inel}}} \frac{1}{2\pi p_T} \frac{\mathrm{d}^2 N}{\mathrm{d}p_T \, \mathrm{d}y}, \tag{B.5}$$

in inelastic proton–proton collisions at center-of-mass energies $\sqrt{s} = 0.9, 2.76$ and 7 TeV, in the p_T range $0.8 <$

$p_T < 3$ GeV and for rapidity[8] $|y| < 0.5$ [36]. Here E and $\boldsymbol{p}$ are the deuteron energy and momentum, N_{inel} is the number of inelastic events, N is the total number of detected deuterons, and $n \equiv N/N_{\text{inel}}$. The experiment included a trigger (V0) consisting of two hodoscopes of 32 scintillators that covered the pseudo-rapidity ranges $2.8 < \eta < 5.1$ and $-3.7 < \eta < -1.7$, used to select non-diffractive (ND) inelastic events. An event was triggered by requiring a hit (charged particle) on either side (positive or negative η) of the V0 triggering set-up.

Pythia 8 generates general inelastic collisions, including single-diffractive (SD), double-diffractive (DD) and ND events. The minimum bias events selected by the V0 trigger generally include those that Pythia treats as SD and DD events. While we used Pythia 8 to generate general minimum bias pp collisions, only events satisfying the V0 trigger have been included in our analysis.

Appendix B.2: ALEPH and OPAL

The ALEPH collaboration at LEP studied the deuteron and antideuteron production in e^+e^- collisions at the Z resonance energy. The measured production rate of antideuterons was $(5.9 \pm 1.8 \pm 0.5) \times 10^{-6}$ per hadronic Z decay, for the antideuteron momentum range from 0.62 to 1.03 GeV and for the production angle θ satisfying $|\cos\theta| < 0.95$ [37].

In a similar experiment performed by the OPAL collaboration [38], no antideuteron events were detected. Reference [35] noted that the resulting upper limit on the antideuteron yield has previously been neglected, but should also be taken into account. The measurements were performed in the antideuteron momentum range $0.35 < p < 1.1$ GeV, with an estimated detection efficiency $\epsilon = 0.234$, which includes the angular acceptance. The expected total number of antideuterons was

$$N_{\bar{d}} = \epsilon N_{\text{ev}} n_{\bar{d},\text{MC}}, \tag{B.6}$$

where $N_{\text{ev}} = 1.64 \times 10^6$ is the number of events in the OPAL analysis and $n_{\bar{d},\text{MC}}$ is the MC prediction for the number of antideuterons per event. We follow Ref. [35] and assume a Poissonian uncertainty $\sigma_{\bar{d}} = \sqrt{N_{\bar{d}}}$ for the expected number of antideuterons. The χ^2 is in this case given by

$$\chi^2_{\text{OPAL}} = \frac{(N_{\text{obs}} - N_{\bar{d}})^2}{\sigma^2_{\bar{d}}} = N_{\bar{d}}. \tag{B.7}$$

[8] Note that, while an additional pseudo-rapidity cut $|\eta| < 0.8$ was required in the data selection, the measurements have been corrected to correspond to the $|y| < 0.5$ selection, including also the contribution of $|\eta| > 0.8$, using a MC simulation [36].

References

1. F. Donato, N. Fornengo, P. Salati, Phys. Rev. D **62**, 043003 (2000). https://doi.org/10.1103/PhysRevD.62.043003
2. R. Battiston, Nucl. Instrum. Methods **A588**, 227 (2008). https://doi.org/10.1016/j.nima.2008.01.044
3. T. Aramaki, C.J. Hailey, S.E. Boggs, P. von Doetinchem, H. Fuke, S.I. Mognet, R.A. Ong, K. Perez, J. Zweerink, Astropart. Phys. **74**, 6 (2016). https://doi.org/10.1016/j.astropartphys.2015.09.001
4. A. Schwarzschild, C. Zupancic, Phys. Rev. **129**, 854 (1963). https://doi.org/10.1103/PhysRev.129.854
5. S.T. Butler, C.A. Pearson, Phys. Rev. **129**, 836 (1963). https://doi.org/10.1103/PhysRev.129.836
6. K.J. Sun, L.W. Chen, Phys. Lett. B **751**, 272 (2015). https://doi.org/10.1016/j.physletb.2015.10.056
7. L. Zhu, C.M. Ko, X. Yin, Phys. Rev. C **92**(6), 064911 (2015). https://doi.org/10.1103/PhysRevC.92.064911
8. L. Zhu, H. Zheng, C. Ming Ko, Y. Sun, Eur. Phys. J. A **54**(10), 175 (2018). 10.1140/epja/i2018-12610-7
9. S. Acharya et al., Nucl. Phys. A **971**, 1 (2018). https://doi.org/10.1016/j.nuclphysa.2017.12.004
10. A. Andronic, P. Braun-Munzinger, K. Redlich, J. Stachel, Nature **561**(7723), 321 (2018). https://doi.org/10.1038/s41586-018-0491-6
11. V. Vovchenko, B. Dönigus, H. Stoecker, Phys. Lett. B **785**, 171 (2018). https://doi.org/10.1016/j.physletb.2018.08.041
12. F. Bellini, A.P. Kalweit, Phys. Rev. C **99**(5), 054905 (2019). https://doi.org/10.1103/PhysRevC.99.054905
13. J. Chen, D. Keane, Y.G. Ma, A. Tang, Z. Xu, Phys. Rep. **760**, 1 (2018). https://doi.org/10.1016/j.physrep.2018.07.002
14. X. Xu, R. Rapp, Eur. Phys. J. A **55**(5), 68 (2019). https://doi.org/10.1140/epja/i2019-12757-7
15. D. Oliinychenko, L.G. Pang, H. Elfner, V. Koch, Phys. Rev. C **99**(4), 044907 (2019). https://doi.org/10.1103/PhysRevC.99.044907
16. M. Kadastik, M. Raidal, A. Strumia, Phys. Lett. B **683**, 248 (2010). https://doi.org/10.1016/j.physletb.2009.12.005
17. L.A. Dal, Antideuterons as Signature for Dark Matter. Master's thesis, NTNU Trondheim. http://hdl.handle.net/11250/2456366 (2011)
18. Y. Cui, J.D. Mason, L. Randall, JHEP **11**, 017 (2010). https://doi.org/10.1007/JHEP11(2010)017
19. A. Ibarra, S. Wild, JCAP **1302**, 021 (2013). https://doi.org/10.1088/1475-7516/2013/02/021
20. N. Fornengo, L. Maccione, A. Vittino, JCAP **1309**, 031 (2013). https://doi.org/10.1088/1475-7516/2013/09/031
21. L.A. Dal, A.R. Raklev, Phys. Rev. D **89**(10), 103504 (2014). https://doi.org/10.1103/PhysRevD.89.103504
22. T. Delahaye, M. Grefe, JCAP **1507**, 012 (2015). https://doi.org/10.1088/1475-7516/2015/07/012
23. J. Herms, A. Ibarra, A. Vittino, S. Wild, JCAP **1702**(02), 018 (2017). https://doi.org/10.1088/1475-7516/2017/02/018
24. M. Korsmeier, F. Donato, N. Fornengo, Phys. Rev. D **97**(10), 103011 (2018). https://doi.org/10.1103/PhysRevD.97.103011
25. A. Coogan, S. Profumo, Phys. Rev. D **96**(8), 083020 (2017). https://doi.org/10.1103/PhysRevD.96.083020
26. V. Poulin, P. Salati, I. Cholis, M. Kamionkowski, J. Silk, Phys. Rev. D **99**(2), 023016 (2019). https://doi.org/10.1103/PhysRevD.99.023016
27. T. Aramaki et al., Phys. Rep. **618**, 1 (2016). https://doi.org/10.1016/j.physrep.2016.01.002
28. L.P. Csernai, J.I. Kapusta, Phys. Rep. **131**, 223 (1986). https://doi.org/10.1016/0370-1573(86)90031-1
29. J.L. Nagle, B.S. Kumar, D. Kusnezov, H. Sorge, R. Mattiello, Phys. Rev. C **53**, 367 (1996). https://doi.org/10.1103/PhysRevC.53.367

30. H. Sato, K. Yazaki, Phys. Lett. **98B**, 153 (1981). https://doi.org/10.1016/0370-2693(81)90976-X
31. R.P. Duperray, K.V. Protasov, A.Y. Voronin, Eur. Phys. J. A **16**, 27 (2003). https://doi.org/10.1140/epja/i2002-10074-0
32. P. Danielewicz, G.F. Bertsch, Nucl. Phys. A **533**, 712 (1991). https://doi.org/10.1016/0375-9474(91)90541-D
33. R. Scheibl, U.W. Heinz, Phys. Rev. C **59**, 1585 (1999). https://doi.org/10.1103/PhysRevC.59.1585
34. K. Blum, K.C.Y. Ng, R. Sato, M. Takimoto, Phys. Rev. D **96**(10), 103021 (2017). https://doi.org/10.1103/PhysRevD.96.103021
35. L.A. Dal, A.R. Raklev, Phys. Rev. D **91**(12), 123536 (2015). https://doi.org/10.1103/PhysRevD.91.123536, https://doi.org/10.1103/PhysRevD.92.089901, https://doi.org/10.1103/PhysRevD.92.069903. [Erratum: Phys. Rev. D92, no.8,089901(2015)]
36. S. Acharya et al., Phys. Rev. C **97**(2), 024615 (2018). https://doi.org/10.1103/PhysRevC.97.024615
37. S. Schael et al., Phys. Lett. B **639**, 192 (2006). https://doi.org/10.1016/j.physletb.2006.06.043
38. R. Akers et al., Z. Phys. C **67**, 203 (1995). https://doi.org/10.1007/BF01571281
39. R. Mattiello, H. Sorge, H. Stoecker, W. Greiner, Phys. Rev. C **55**, 1443 (1997). https://doi.org/10.1103/PhysRevC.55.1443
40. V.I. Zhaba (2017). arXiv:1706.08306
41. Y.L. Dokshitzer, V.A. Khoze, A.H. Mueller, S.I. Troian, *Basics of Perturbative QCD* (Edition Frontieres, Gif-sur-Yvette, 1991)
42. A. Deur, S.J. Brodsky, G.F. de Teramond, Prog. Part. Nucl. Phys. **90**, 1 (2016). https://doi.org/10.1016/j.ppnp.2016.04.003
43. S.G. Karshenboim, R. Beig, W. Beiglböck, W. Domcke, B.G. Englert, U. Frisch, P. Hänggi, G. Hasinger, K. Hepp, W. Hillebrandt, D. Imboden, R.L. Jaffe, R. Lipowsky, H.V. Löhneysen, I. Ojima, D. Sornette, S. Theisen, W. Weise, J. Wess, J. Zittartz, *Precision Physics of Simple Atoms and Molecules*, vol. 745, Lecture Notes in Physics (Springer, Berlin, 2008). https://doi.org/10.1007/978-3-540-75479-4
44. L.A. Dal, M. Kachelrieß, Phys. Rev. D **86**, 103536 (2012). https://doi.org/10.1103/PhysRevD.86.103536
45. T. Sjöstrand, S. Mrenna, P.Z. Skands, JHEP **05**, 026 (2006). https://doi.org/10.1088/1126-6708/2006/05/026
46. T. Sjöstrand, S. Ask, J.R. Christiansen, R. Corke, N. Desai, P. Ilten, S. Mrenna, S. Prestel, C.O. Rasmussen, P.Z. Skands, Comput. Phys. Commun. **191**, 159 (2015). https://doi.org/10.1016/j.cpc.2015.01.024
47. J. Adam et al., Eur. Phys. J. C **75**(5), 226 (2015). https://doi.org/10.1140/epjc/s10052-015-3422-9
48. E. Carlson, A. Coogan, T. Linden, S. Profumo, A. Ibarra, S. Wild, Phys. Rev. D **89**(7), 076005 (2014). https://doi.org/10.1103/PhysRevD.89.076005
49. M. Cirelli, N. Fornengo, M. Taoso, A. Vittino, JHEP **08**, 009 (2014). https://doi.org/10.1007/JHEP08(2014)009
50. S. Ting, The first five years of the alpha magnetic spectrometer on the international space station. CERN colloquium (2016). https://indico.cern.ch/event/592392/

Paper II – Revisiting cosmic ray antinuclei fluxes with a new coalescence model

Kachelrieß, M., Ostapchenko, S. & Tjemsland, J. "Revisiting cosmic ray antinuclei fluxes with a new coalescence model". *JCAP* **08,** 048. arXiv: 2002.10481 [hep-ph] (2020)

Abstract: Antideuteron and antihelium nuclei have been proposed as promising detection channels for dark matter because of the low astrophysical backgrounds expected. To estimate both potential exotic contributions and their backgrounds, one usually employs the coalescence model in momentum space. Here we use instead a newly developed coalescence model based on the Wigner function representations of the produced nuclei states. This approach includes both the process-dependent size of the formation region of antinuclei, and the momentum correlations of coalescing antinucleons in a semi-classical picture. The model contains a single universal parameter σ that we tune to experimental data on antideuteron production in electron-positron, proton-proton and proton-nucleus collisions. The obtained value $\sigma \simeq 1\,\mathrm{fm}$ agrees well with its physical interpretation as the size of the formation region of antinuclei in collisions of point-like particles. This model allows us therefore to calculate in a consistent frame-work the antideuteron and antihelium fluxes both from secondary production and from dark matter annihilations. We find that the antihelium-3 flux falls short by more than an order of magnitude of the detection sensitivity of the AMS-02 experiment, assuming standard cosmic ray propagation parameters, while the antideuteron flux can be comparable to the sensitivities of the AMS-02 and GAPS experiments.

In this paper, the WiFunC model was used to estimate the antideuteron and antihelion flux on Earth from secondary production and WIMP annihilations. This is the natural step after the new coalescence model was introduced in Paper I. Although our results are consistent with those from a simple coalescence model, the paper includes some important results and observations from a theoretical point of view. Firstly, the WiFunC model describes both antideuteron and antihelion with a single parameter σ (which is fixed in Paper IV). When the simple coalescence model is used, on the other hand, improvisational assumptions have to be used to relate the value of p_0 for antideuteron and antihelion. Secondly, the WiFunC model can describe all relevant processes (pp, pHe, Hep, HeHe, $\bar{p}p$ $\bar{p}$He and DM annihilation) since σ is interaction dependent. Thus, there is no need to use scaling relations, like the nuclear enhancement factor (see discussion in Paper IX). Finally, since pp, pHe, Hep, HeHe, $\bar{p}p$ $\bar{p}$He were simulated separately, we were able to observe the effect that pHe and HeHe collisions dominate the source spectrum at low energies due to the reduced threshold in these interactions.

Journal of Cosmology and Astroparticle Physics
An IOP and SISSA journal

Revisiting cosmic ray antinuclei fluxes with a new coalescence model

M. Kachelrieß,[a] **S. Ostapchenko**[b,c] **and J. Tjemsland**[a]

[a]Institutt for fysikk, NTNU,
7491 Trondheim, Norway
[b]Frankfurt Institute for Advanced Studies,
Ruth-Moufang-Straße 1, 60438 Frankfurt, Germany
[c]D.V. Skoveltsyn Institute of Nuclear Physics, Moscow State University,
1(2), Leninskie gory, GSP-1, 119991 Moscow, Russia

E-mail: Michael.Kachelriess@ntnu.no, Ostapchenko@fias.uni-frankfurt.de,
Jonas.Tjemsland@ntnu.no

Received March 2, 2020
Revised May 30, 2020
Accepted July 13, 2020
Published August 28, 2020

Abstract. Antideuteron and antihelium nuclei have been proposed as promising detection channels for dark matter because of the low astrophysical backgrounds expected. To estimate both potential exotic contributions and their backgrounds, one usually employs the coalescence model in momentum space. Here we use instead a newly developed coalescence model based on the Wigner function representations of the produced nuclei states. This approach includes both the process-dependent size of the formation region of antinuclei, and the momentum correlations of coalescing antinucleons in a semi-classical picture. The model contains a single universal parameter σ that we tune to experimental data on antideuteron production in electron-positron, proton-proton and proton-nucleus collisions. The obtained value $\sigma \simeq 1\,\mathrm{fm}$ agrees well with its physical interpretation as the size of the formation region of antinuclei in collisions of point-like particles. This model allows us therefore to calculate in a consistent frame-work the antideuteron and antihelium fluxes both from secondary production and from dark matter annihilations. We find that the antihelium-3 flux falls short by more than an order of magnitude of the detection sensitivity of the AMS-02 experiment, assuming standard cosmic ray propagation parameters, while the antideuteron flux can be comparable to the sensitivities of the AMS-02 and GAPS experiments.

Keywords: cosmic ray theory, dark matter theory

ArXiv ePrint: 2002.10481

 https://doi.org/10.1088/1475-7516/2020/08/048

JCAP08(2020)048

Contents

JCAP08(2020)048

1 Introduction

The low astrophysical backgrounds promote antideuteron [1] and antihelium-3 [2] nuclei to promising detection channels for dark matter (DM) annihilations and decays in the Galaxy, for a recent review see ref. [3]. The dominant background of light antinuclei is expected to originate from secondary production, that is, to be created in collisions of primary cosmic rays (CR) with the interstellar medium. The high threshold energy for the production of antideuterons ($\simeq 17 m_N$ in pp interactions, where m_N is the nucleon mass) and antihelium-3 ($\simeq 31 m_N$) implies that such secondary antinuclei have relatively high kinetic energies. This makes antideuterons and antihelium-3 with low kinetic energies an ideal dark matter probe. In contrast, the fluxes of heavier nuclei, as e.g. antihelium-4, are, both for the DM and secondary production channels, so strongly suppressed that they are undetectable by current experiments. Consequently, an identification of antihelium-4 nuclei in the Galactic CR flux would represent a true challenge to our current cosmological paradigm, requiring e.g. the presence of antimatter "islands" inside the Milky Way [4, 5].

The production of light antinuclei as CR secondaries and in DM annihilations is usually described by the coalescence model in momentum space [4, 6, 7]. It states that an antiproton-antineutron pair with an invariant momentum difference Δk less than the coalescence momentum p_0 merges and forms an antideuteron. Due to the lack of an underlying microphysical picture, p_0 must be determined by fits to experimental data. For the model to

be predictive, this parameter should be independent of both the reaction type and the center-of-mass (cm) energy $\sqrt{s}$. Traditionally, the cluster formation of nuclei has been parametrised by an invariant coalescence factor B_A as

$$E_A \frac{\mathrm{d}^3 N_A}{\mathrm{d}P_A^3} = B_A \left(E_p \frac{\mathrm{d}^3 N_p}{\mathrm{d}P_p^3} \right)^Z \left(E_n \frac{\mathrm{d}^3 N_n}{\mathrm{d}P_n^3} \right)^N \Bigg|_{P_p = P_n = P_A/A} , \tag{1.1}$$

which relates the invariant differential yield of a nucleus with mass number A, proton number Z and neutron number N to the invariant yields of protons and neutrons, $E_i \, \mathrm{d}^3 N_i / \mathrm{d}P_i^3$. In the limit of isotropic nucleon yields, the coalescence factor B_A is related to the coalescence momentum p_0 as

$$B_A = A \left(\frac{4\pi}{3} \frac{p_0^3}{m_N} \right)^{A-1} . \tag{1.2}$$

This "naive" coalescence model can be improved by taking into account two-particle momentum correlations provided by Monte Carlo event generators, if one imposes the coalescence condition on an event-by-event basis, as first proposed in refs. [8, 9]. The yield of antinuclei should, however, depend on the full *phase space density* of the coalescing antinucleons. Since both the "naive" and the "improved" coalescence models impose the coalescence condition only in momentum space, the reaction-dependent size of the formation region of antinuclei is neglected in these treatments. As a result, the coalescence parameter p_0 becomes process dependent applying such models also to hadronic reactions [10–12]. Using in such an approach the same p_0 for antinuclei formation in DM annihilations and in CR interactions will thus lead to incorrect results.

An alternative coalescence model was developed by us in ref. [13]. Starting from the Wigner function representation of the antinucleon and the antinuclei states, introduced in ref. [14], we employed a semi-classical treatment to include both the process-dependent size of the formation region and the momentum correlations of coalescing antinucleons. We showed that this new coalescence model successfully describes the data both from e^+e^- annihilations at the Z resonance [15, 16] and from pp collisions at $\sqrt{s} = 0.9, 2.7$ and 7 TeV, measured by the ALICE collaboration at the LHC [17]. As we aim in the present work to model the formation of light antinuclei as secondaries in CR interactions, it is, however, important to test the validity of our model also in hadron-nucleus and light nucleus-nucleus collisions. We consider therefore in addition experimental data on proton-beryllium and proton-aluminium collisions at 200 GeV/c [18, 19] as well as the spectra of antinuclei for pp collisions at $\sqrt{s} = 53$ GeV measured at the CERN ISR [20, 21]. The numerical values we derive for the single free parameter σ of our model are consistent between all the reactions considered and agree well with the physical interpretation of σ as the size of the formation region of light nuclei. This allows us to calculate in a self-consistent frame-work the expected fluxes of both antideuteron and antihelium-3 from secondary production as well as from DM annihilations. In the latter case, we estimate the antinuclei flux from DM particles with masses $m_\chi = \{20, 100, 1000\}$ GeV, annihilating into $b\bar{b}$ and W^+W^- pairs. We derive also the maximal annihilation cross sections compatible with the antiproton spectrum from AMS-02. We show that pHe and HeHe collisions dominate the secondary contribution to the antideuteron yield at low energies. The antihelium-3 flux we obtain falls short of the detection sensitivities of the AMS-02 experiment by more than an order of magnitude, assuming standard CR propagation parameters. In contrast, the antideuteron flux can be just below the sensitivities of the AMS-02 and GAPS

JCAP08(2020)048

experiments. Taking into account the large uncertainties, antideuterons remain therefore a promising target in searches for antimatter.

2 Antinuclei formation model

Our formalism for treating the production of (anti)nuclei[1] has been described in ref. [13]. We will follow the same approach here and refer the reader for details like cuts to exclude long-lived resonances to our previous work [13]. In this model, the probability that a nucleon pair with three-momentum $\boldsymbol{q}$ and $-\boldsymbol{q}$ in its cm frame coalesces is given by

$$w_{\text{Wigner}} = 3\left(\zeta_1 \Delta e^{-q^2 d_1^2} + \zeta_2 [1-\Delta] e^{-q^2 d_2^2}\right), \tag{2.1}$$

where

$$\zeta_i = \frac{d_i^2}{d_i^2 + 4\tilde{\sigma}_\perp^2} \sqrt{\frac{d_i^2}{d_i^2 + 4\sigma_\parallel^2}}. \tag{2.2}$$

The parameters $\Delta = 0.581$, $d_1 = 3.979\,\text{fm}$, and $d_2 = 0.890\,\text{fm}$ determine the internal wave-function of the deuteron, which was approximated in ref. [13] as a sum of two Gaussians.[2] Since the coalescence probability is very small, corrections to eq. (2.1), accounting for double counting of nucleons involved in different pairs, can in practice be neglected. An expression similar to eq. (2.1) has been obtained in ref. [13] for the probability of three nucleons to form a bound-state, like tritium or antihelium-3.

The parameters σ_i describe the spatial separation of the nucleons forming potentially a deuteron. For a "point-like" interaction, such as e^+e^- annihilations, the longitudinal spread $\sigma_\parallel$ is given in the deuteron frame by the formation length of nucleons, $\sigma_\parallel \simeq R_p \simeq 1\,\text{fm}$, with R_p as the proton size, while the perpendicular spread is of order $\sigma_\perp \simeq 1/\Lambda_{\text{QCD}}$ in the cm frame of the collision. Taking into account for the latter the boost into the deuteron frame gives

$$\tilde{\sigma}_\perp^2 = \frac{\sigma_\perp^2}{\cos^2\vartheta + \gamma^2 \sin^2\vartheta}, \tag{2.3}$$

where γ is the usual Lorentz factor, while ϑ denotes the angle between the antideuteron momentum and the momentum of the initially produced pair of particles in their cm frame. For instance, in the case of the annihilation of DM particles through the process $\chi\chi \to \bar{b}b$, the angle ϑ is defined with respect to the momentum of the produced b or $\bar{b}$. For hadronic events, ϑ is defined relative to the beam direction of the colliding hadrons in their cm system, as detailed in ref. [13].

In addition, the spreads σ_i obtain a geometrical contribution σ_{geom} in reactions involving hadrons or nuclei because of their finite extension. Adding these two contributions in quadrature yields

$$\sigma_\perp^2 = \sigma_{\perp(e^\pm)}^2 + \sigma_{\perp(\text{geom})}^2, \tag{2.4}$$

$$\sigma_\parallel^2 = \sigma_{\parallel(e^\pm)}^2 + \sigma_{\parallel(\text{geom})}^2. \tag{2.5}$$

Here, we have denoted with $\sigma_{(e^\pm)}$ the "point-like" contribution discussed above and set for simplicity $\sigma_{(e^\pm)} \simeq \sigma_{\perp(e^\pm)} \simeq \sigma_{\parallel(e^\pm)} \simeq 5\,\text{GeV}^{-1} \simeq 1\,\text{fm}$. The geometrical contributions in

[1] Since our discussion applies equally well to the formation of nuclei and of antinuclei, we will omit the preposition 'anti' further on in this section.

[2] The specified parameters correspond to the so-called φ_0-fit of the deuteron wave-function [13].

JCAP08(2020)048

hadron-hadron, hadron-nucleus, and nucleus-nucleus collisions can in turn be approximated by [13]

$$\sigma^2_{\perp(\mathrm{geom})} \simeq \frac{2R_1^2 R_2^2}{R_1^2 + R_2^2}, \tag{2.6}$$

$$\sigma^2_{\parallel(\mathrm{geom})} \simeq \max\{R_1^2, R_2^2\}, \tag{2.7}$$

where R_i are the radii of the two colliding particles. In the particular case of proton-proton collisions, $\sigma_\parallel \simeq \sigma_\perp$ so that $\sigma_{(pp)} \simeq \sqrt{2}\sigma_{(e^\pm)} \simeq 7\,\mathrm{GeV}^{-1}$. The radius R_A of a nucleus with mass number A scales approximately as

$$R_A = a_0 A^{1/3}, \tag{2.8}$$

where $a_0 \simeq 1.1\,\mathrm{fm}$, with an uncertainty of $\sim 20\%$ [22]. We will use this relation in eqs. (2.6) and (2.7) as an approximation for the size of the different nuclei considered. This allows us to use a single parameter, setting

$$\sigma \equiv \sigma_{(e^\pm)} = a_0 = \sigma_{(pp)}/\sqrt{2}. \tag{2.9}$$

If our model accounts correctly for the differences in the formation of light nuclei in different reaction types, the parameter σ obtained from fits of different reactions should be universal and close to 1 fm.

Finally, we want to comment briefly on the relation of our model to other approaches. The recent work [23] connects the production of light antinuclei to the two-proton correlation function measured in heavy-ion collisions. Its basic results can be recovered in our approach imposing two assumptions: first, the size of the production region has to be much larger than the deuteron size. Second, the proton-neutron density matrix has to factorise, i.e. their momentum correlations should be negligible. Neither of the two assumptions are justified for the small systems, as pp scattering and e^+e^- or DM annihilations, we consider here. Eventually, one may ask how the size σ of the production region is connected to the parameter p_0 used in the conventional coalescence picture. Formally, we note that σ is approximately related to p_0 as $p_0/0.2\,\mathrm{GeV} \sim 1\,\mathrm{fm}/\sigma$. Note, however, that important physical inputs like the shape of the momentum distributions of antinucleons or the wave-function of the antideuteron affect p_0 and σ differently. Therefore such a relation has to be interpreted with care.

3 Determination of the spread σ

In order to test the validity of our coalescence model, i.e., in particular the universality of its parameter σ, we compare our predictions to experimental data on antideuteron production in e^+e^-, pp and pA collisions. Differences between the results of the standard and the new coalescence models were already investigated in ref. [13], using as event generator PYTHIA. Here we focus instead on the new model, using the event generator QGSJET-II [24, 25], which reproduces experimental data over a wide energy range, for reactions involving nuclei as well as for pp collisions[3]. In addition, we employ PYTHIA 8.230 [28, 29] to simulate e^+e^- and DM annihilations as well as pp collisions. The considered experimental data sets are described in appendix A. In figure 1, we show the best fits to the data on antideuteron production in pAl

[3]We are using a new tune of QGSJET-II-04m [26] which slightly improves the fit to the ALICE data [27] on antiproton production in pp collisions at $\sqrt{s} = 7\,\mathrm{TeV}$.

JCAP08(2020)048

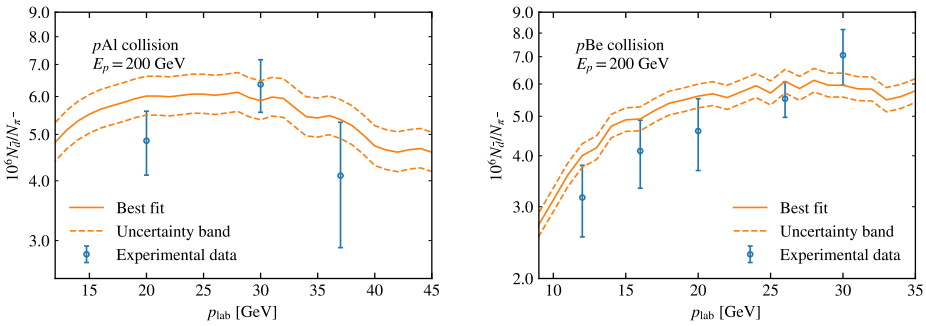

Figure 1. Best fit and 1σ uncertainty band for the antideuteron/pion ratio, obtained using QGSJET-IIm and the new coalescence model, for proton-aluminium (left) and proton-beryllium (right) collisions.

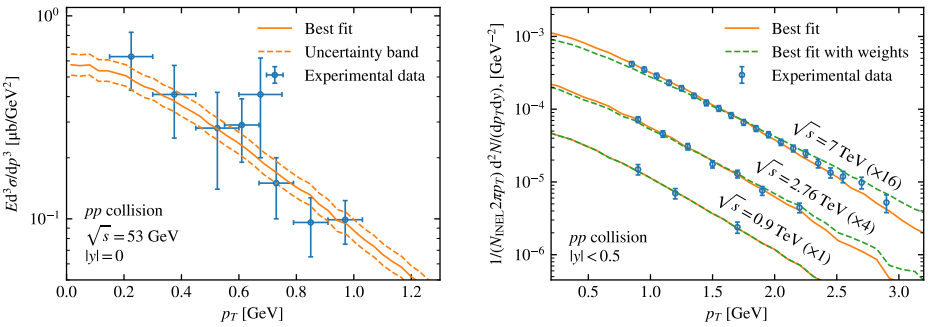

Figure 2. Best fit to antideuteron production data in pp collisions, using QGSJET-II and the new coalescence model. Left: results for $\sqrt{s} = 53$ GeV, including an uncertainty band, compared to CERN ISR data [20, 21]. Right: calculations for LHC energies, without and with the re-weighting to the pp data on antiproton production, as discussed in the text, compared to ALICE data [17].

and pBe collisions at 200 GeV/c, while the fits to the transverse momentum p_T spectra of antideuterons in pp interactions, measured at CERN ISR and LHC, are plotted in figure 2. Because of the relatively large experimental uncertainties, the fits are in all cases acceptable. The corresponding fit results for the parameter σ obtained using QGSJET-II are listed in table 1, while the results for PYTHIA are shown in table 2. The values obtained for σ using PYTHIA have a smaller variance and are closer to the expected value of $\sigma \simeq 1$ fm, compared to the results for QGSJET-II.

Taking these results at face-value, one might interpret, e.g., the change from $\sigma \simeq 0.5$ fm at 53 GeV to $\sigma \simeq 1.44$ fm at 7 TeV, using QGSJET-II, as an energy dependence of this parameter. However, such a change may also be caused by a systematic bias either in the experimental data and/or in the predictions of the used event generators. In order to clarify the reason for this change, we compare in figure 3 the invariant differential yield of protons and antiprotons, measured by the ALICE collaboration [27, 30, 31], to the values obtained using QGSJET-II at $\sqrt{s} = 900$, 2760 and 7000 GeV, and using PYTHIA at $\sqrt{s} = 7000$ GeV.

JCAP08(2020)048

	LT ζ		const. ζ		standard coal.	
Experiment	σ [fm]	$\chi^2/(N-1)$	σ [fm]	$\chi^2/(N-1)$	p_0 [MeV]	$\chi^2/(N-1)$
p-p 7 TeV	1.44 ± 0.01	10/19	1.23 ± 0.01	86/19	134	93/19
p-p 2.76 TeV	1.29 ± 0.03	2.1/6	1.11 ± 0.02	9.9/6	146	12/6
p-p 900 GeV	1.02 ± 0.05	0.30/2	0.90 ± 0.04	0.68/2	175	0.88/2
p-p 53 GeV	0.50 ± 0.03	3.2/7	0.47 ± 0.03	2.9/7	280	2.5/7
p-Be	1.00 ± 0.03	2.2/4	0.95 ± 0.03	2.4/4	126	3.0/4
p-Al	0.88 ± 0.04	1.4/2	0.84 ± 0.04	1.5/2	126	1.3/2

Table 1. Calibration results for antideuteron production, obtained using QGSJET-II: including the effect of the Lorentz transformation on $\sigma_\perp$ [eq. (2.3)], using constant $\sigma_\perp$, and employing the standard coalescence model.

	LT ζ		const. ζ		standard coal.	
Experiment	σ [fm]	$\chi^2/(N-1)$	σ [fm]	$\chi^2/(N-1)$	p_0 [MeV]	$\chi^2/(N-1)$
p-p 7 TeV	1.07 ± 0.01	29/19	0.92 ± 0.02	133/19	176	177/19
p-p 2.76 TeV	1.05 ± 0.02	8.7/6	0.93 ± 0.04	32/6	174	45.6/6
p-p 900 GeV	0.97 ± 0.05	2.6/2	0.87 ± 0.07	6.1/2	181	7.3/2
p-p 53 GeV	1.03 ± 0.06	3.3/7	0.96 ± 0.06	2.7/7	171	2.1/7
ALEPH	$1.04^{+0.20}_{-0.12}$	-	$0.99^{+0.18}_{-0.12}$	-	214^{+21}_{-26}	-
ALEPH+OPAL	$1.15^{+0.27}_{-0.22}$	3.2/1	$1.09^{+0.26}_{-0.22}$	3.2/1	201	3.2/1

Table 2. Calibration results for antideuteron production, obtained using PYTHIA 8.230.

As is easily seen in the figure, QGSJET-II fits the data at 900 GeV well, but overestimates the bulk of the produced antiprotons at 2760 and 7000 GeV. Therefore, the coalescence parameter σ must be artificially increased at these energies to compensate the overproduction of antinucleons. In the same manner, QGSJET-II underestimates the antiproton flux measured at the CERN ISR.[4] Thus, σ has to be decreased for QGSJET-II to compensate this deviation. In all the aforementioned cases, the deviations from the expected value $\sigma \simeq 1$ fm are caused by an imperfect description of antiproton production by the Monte Carlo event generators.

In order to quantify this effect, we tweak the antiproton spectra by adding a weight $w = ap_T^b + c$ and fix a, b and c by fits to the experimental data. This implies that the weight $w_{\bar{d}} = [a(p_T/2)^b + c]^2$ has to be included in the case of antideuteron production. We fit the weight w to the combined antiproton and proton data measured by ALICE [27, 30, 31], with the same experimental set-up as the antideuteron data, and to the antiproton data measured at the CERN ISR[5] [33]. The resulting best-fit yields shown in figure 3 reproduce nicely the experimental data. Then we repeat the analysis of the antideuteron data of ALICE and

[4] A short discussion of this effect on the standard coalescence model and CERN ISR data using PYTHIA and EPOS-LHC can be found in ref. [32].

[5] In the fit of the CERN ISR data, $b = 1$ was fixed and only the data points in the interval $0.2 \leq p_T \leq 1.3$ GeV were used.

JCAP08(2020)048

CERN ISR: the values of σ obtained using the re-weighted antinucleon spectra are listed in table 3 and the fits to the antideuteron data of ALICE are plotted in the right panel of figure 2. In all the cases, the results are significantly closer to the expected value $\sigma \simeq 1\,\mathrm{fm}$. Note that the weights are specific for each experimental set-up and kinematic range: they were chosen to affect mainly the shape of the antiproton spectra in the narrow kinematic range covered by experimental data. In contrast, the total yields important for astrophysical applications are less sensitive to the systematic uncertainties of the event generator at large p_T. For instance, the total antideuteron yield in pp collisions at 7 TeV, using $\sigma \simeq 1.1\,\mathrm{fm}$, would be decreased by $\simeq 40\%$, relative to the case of using no weights.

Finally, let us compare our results to those of ref. [34]. Imposing the coalescence condition in momentum space on an event-by-event basis, the authors of that work used EPOS-LHC to reproduce experimental data on the (anti)deuteron yield in pp and pA collisions. Based on these comparisons, they suggested that p_0 is strongly energy dependent at low energies.[6] Moreover, they proposed that the energy dependence differs for deuteron and antideuteron production: while p_0 increases for deuterons, it decreases for antideuterons as the kinetic energy of the projectile decreases. Such a behaviour is difficult to understand, if one accepts that the strong interaction does not distinguish between matter and antimatter. In contrast, a possible contamination by deuterons produced in the detector may easily explain the larger value of p_0 for deuterons than for antideuterons. From a theoretical point of view, we expect that the size of the formation region — and thus σ — is only logarithmically dependent on the cm energy. Furthermore, its size should be identical for deuteron and antideuteron production. However, we have seen that a relatively small bias in the production spectra of antinucleons or, alternatively, systematic errors in the experimental results may delude an energy dependence of σ. Correcting for such biases, we have verified that the present experimental data are consistent with the universal coalescence picture implemented in our model. However, we note that the old data at $p_{\mathrm{lab}} = 70\,\mathrm{GeV}$ from Serpukhov [35] are inconsistent with this picture. A confirmation of these data could falsify the assumption underlying our model.

Based on the best fit values after re-weighting, we fix for the following analyses $\sigma = (1.0 \pm 0.1)\,\mathrm{fm}$ for both PYTHIA and QGSJET II. This value describes in our model via eqs. (2.1)–(2.9) the formation of light antinuclei for all interaction types and energies. For comparisons, we set in the standard coalescence model $p_0 = 180\,\mathrm{MeV}$ for proton-proton, proton-nucleus and nucleus-nucleus collisions, while we use $p_0 = 210\,\mathrm{MeV}$ in DM annihilations.

4 Antinucleus source spectra

4.1 Secondary production

Light antinuclei are produced as secondaries in collisions of CRs with gas in the Galactic disc. We neglect elements heavier than helium but take into account the CR antiproton flux. The source term Q^{sec} of secondaries can then be written as

$$Q^{\mathrm{sec}}(T_{\bar{N}}, \boldsymbol{r}) = \sum_{i \in \{p,\mathrm{He},\bar{p}\}} \sum_{j \in \{p,\mathrm{He}\}} 4\pi n_j(\boldsymbol{r}) \int_{T_{\bar{N},\mathrm{min}}^{(i,j)}}^{\infty} \mathrm{d}T_i \, \frac{\mathrm{d}\sigma_{i,j}(T_i, T_{\bar{N}})}{\mathrm{d}T_{\bar{N}}} \Phi_i(T_i, \boldsymbol{r}), \tag{4.1}$$

[6] Note that their fit of p_0 as function of p_{lab} combines data from pp and pA collisions, which correspond to different cm energies. Moreover, the differences in the size of the formation region of deuterons as function of A are neglected in such an approach.

JCAP08(2020)048

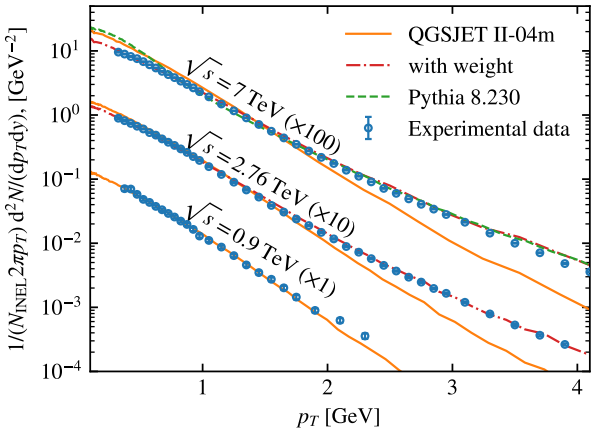

Figure 3. Combined invariant differential yield of protons and antiprotons in pp collisions, obtained using PYTHIA (green dashed line) and QGSJET-II (solid orange lines), compared to ALICE data [27, 30, 31]. The red dashed-dotted lines are obtained by adding a multiplicative weight $w = ap_T^b + c$ to the yield predicted by QGSJET-II.

	LT ζ		const. ζ		standard coal.	
Experiment	σ [fm]	$\chi^2/(N-1)$	σ [fm]	$\chi^2/(N-1)$	p_0 [MeV]	$\chi^2/(N-1)$
p-p 7 TeV	1.17 ± 0.01	19/19	0.97 ± 0.01	16.2/19	165	23/19
p-p 2.76 TeV	1.16 ± 0.02	3.6/6	0.99 ± 0.02	4.1/6	161	5.7/6
p-p 900 GeV	1.01 ± 0.05	0.30/2	0.89 ± 0.04	0.60/2	178	0.81/2
p-p 53 GeV	0.94 ± 0.06	2.7/7	0.89 ± 0.05	3.2/7	170	4.3/7

Table 3. Calibration results for antideuteron production in pp collisions, obtained by using QGSJET-II and applying an additional multiplicative weight $ap_T^b + c$ to the predicted antinucleon yield, as discussed in the text.

where $n_j(\boldsymbol{r})$ is the density of particle j in the Galactic disc, $T = (E - m)/n$ is the kinetic energy per nucleon of the particle i with mass $m = nm_{\rm N}$ and flux Φ_i, while $T_{\bar{N},\rm min}^{(i,j)}$ is the threshold for creating an antinucleus $\bar{N}$. We use as hydrogen density $n_{\rm H} = 1\,{\rm cm}^{-3}$, while the helium density is fixed to $n_{\rm He} = 0.07 n_{\rm H}$. The differential cross section for $ij \to \bar{N}X$ is calculated as

$$\frac{{\rm d}\sigma_{i,j}(T_i, T_{\bar{N}})}{{\rm d}T_{\bar{N}}} = \sigma_{ij,\rm inel} \frac{{\rm d}N_{\bar{N}}(T_i, T_{\bar{N}})}{{\rm d}T_{\bar{N}}}, \tag{4.2}$$

where $\sigma_{ij,\rm inel}$ is the total inelastic cross section, while ${\rm d}N_{\bar{N}}(T_i, T_{\bar{N}})/{\rm d}T_{\bar{N}}$ is computed using our coalescence model. The parametrisations for the primary fluxes $\Phi_i(T_i, \boldsymbol{r})$ used in this work are compared to experimental data in figure 4. We will employ two parametrisations, one with and one without spectral breaks; their details are discussed in appendix B.

We compute ${\rm d}\sigma_{ij}/{\rm d}T_{\bar{N}}$ for 100 logarithmically spaced energies E_i of the projectile up to 5×10^4 GeV for $i \in \{p, {\rm He}, \bar{p}\}$ and $j \in \{p, {\rm He}\}$. For each channel, we choose the lower end of the energy range for T_i such that all energies in which more than 10^{-9} antideuterons per event

JCAP08(2020)048

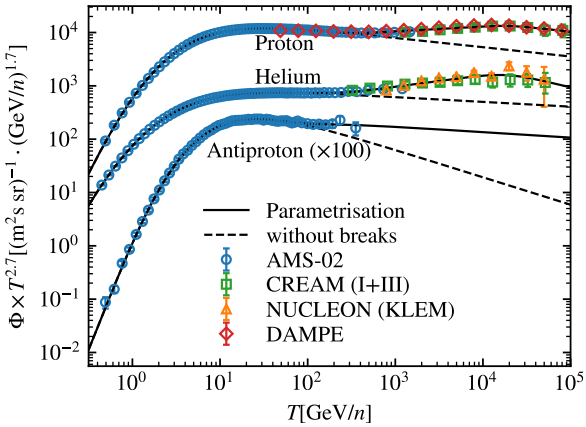

Figure 4. Parametrisations of the primary proton, helium and antiproton fluxes, compared to the data from AMS-02 [36–38], DAMPE [39], CREAM [40] and NUCLEON [41].

are produced are included. The contributions of all these processes, for different incoming energy ranges, are shown in figure 5. The differences caused by the breaks in the primary spectra are negligible below 10 GeV/n and small at higher energies; the largest difference appears for the contribution from primary helium. Furthermore, the difference between the new and standard coalescence models is small in pp and $\bar{p}p$ collisions, since the parameter p_0 is adjusted to reproduce the correct yield of antideuterons in pp collisions. However, the differences for the reactions involving helium are larger, up to a factor $\sim$ 2–3: while the new model takes into account the increase in the size of the formation region of antinucleons for helium, this effect is neglected in the case of the old coalescence model. Therefore the old treatment tends to over-predict the antideuteron yield in reactions involving helium.

The contributions of the different reactions to the total secondary source spectrum Q^{sec} of antideuterons are shown in figure 6. Our results can be compared to those of Lin et al. [42] and Ibarra and Wild [11]. Both groups used the standard coalescence model in a Monte Carlo approach: Lin *et al.* employed the event generators QGSJET-II-04m, EPOS-LHC and EPOS-1.99, while Ibarra and Wild used DPMJET-III and modified its results by adding a parametrised weight to the calculated antiproton spectra, in order to reproduce experimental data at low energies. We find that the main contribution to the secondary source term comes from pp collisions, as expected. However, the low energy part is dominated by pHe and HeHe interactions, which is a consequence of the kinematics of antideuteron production in these reactions, in particular, of their lower energy thresholds:[7] $T_{\bar{d},\mathrm{min}}^{(p,\mathrm{He})} = 10 m_N$ and $T_{\bar{d},\mathrm{min}}^{(\mathrm{He},\mathrm{He})} = 6 m_N$. These findings are in contrast to the results of both Lin *et al.* and Ibarra and Wild. Since both groups used the so-called nuclear enhancement factor ε, instead of performing a proper calculation of the antideuteron production in pHe, Hep and $\bar{p}$He collisions, they could not observe this low-energy behaviour. The limitations of the concept of a nuclear enhancement factor ε were studied in some detail in refs. [26, 43].

[7] In a proton-nucleus collision, $\bar{p}p$ and $\bar{n}n$ pairs may be produced by partial inelastic re-scatterings of the incident proton off two different target nucleons. In a nucleus-nucleus scattering, on the other hand, such pairs may be produced by partial inelastic interactions between two different pairs of the projectile and target nucleons.

JCAP08(2020)048

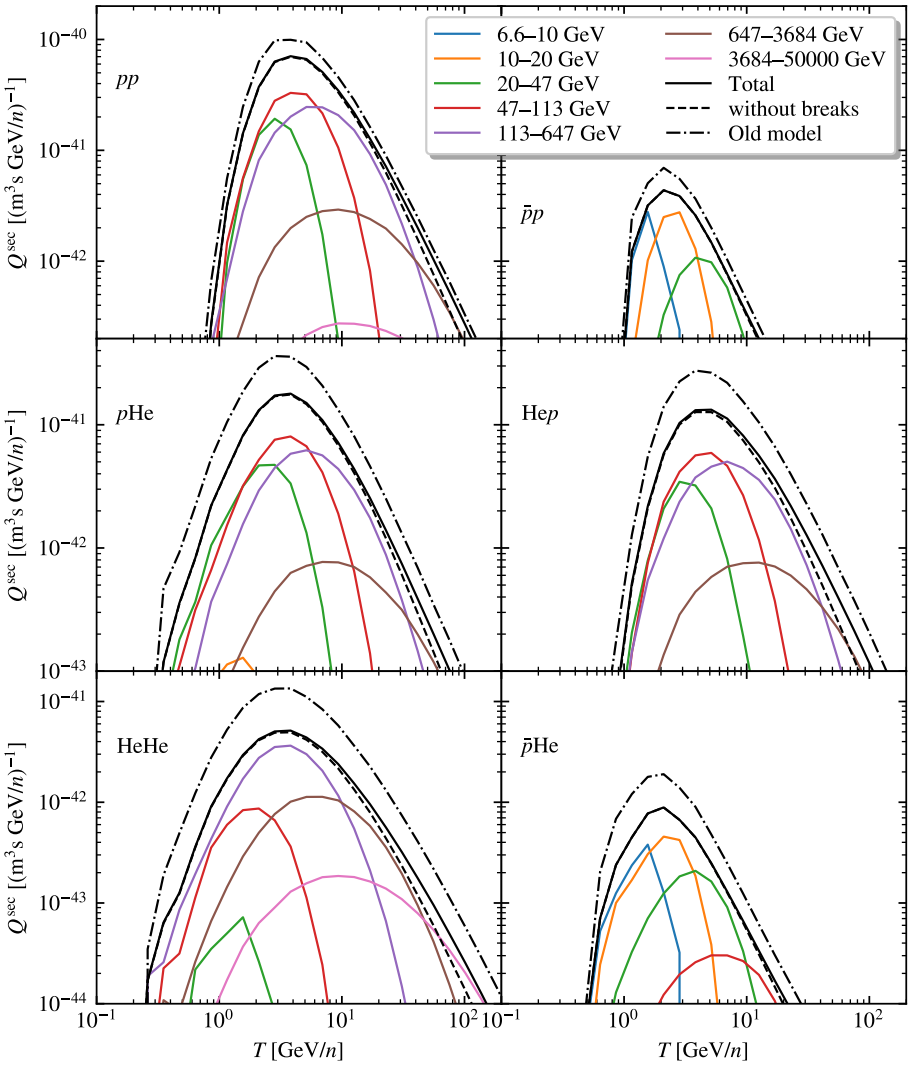

Figure 5. Partial contributions to the secondary source spectrum $Q^{\rm sec}$ of antideuterons for the six different reactions and from various energy ranges, for the new model and primary spectra with breaks. Additionally, the resulting total contributions (black solid lines) are compared to the ones obtained using the unbroken primary spectra (black dashed lines) and the old coalescence model (dashed-dotted black lines). The indicated energy ranges refer to the total energy per nucleon for the Hep contribution and to the total energy of the primary particle in all the other cases.

In particular, the definition of ε assumes that the primary CR fluxes are power laws without breaks. Moreover, the nuclear enhancement factors for the production of massive particles are modified by threshold effects and are thus strongly energy dependent in the energy range relevant for astrophysical applications [26].

JCAP08(2020)048

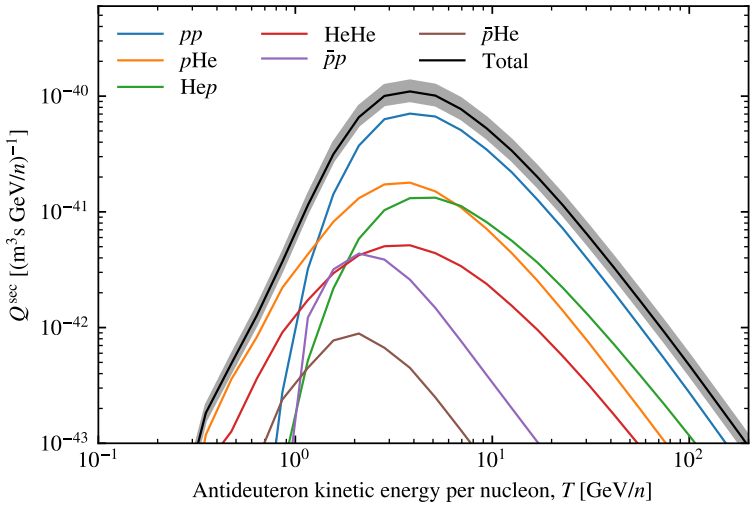

Figure 6. Contributions from different reaction types to the total secondary source term. The shaded area around the total corresponds to the estimated model uncertainty.

The contributions of different reaction types to the total secondary source term are shown in figure 6 for the new coalescence model and the broken primary spectra. The shaded area around the total contribution shown by the black solid line corresponds to the estimated model uncertainty obtained by varying σ in the range 0.9 to 1.1 fm. As one can see in figure 6, the "nuclear enhancement", i.e. the ratio of the values corresponding to the black[8] (total contribution) and blue (pp contribution) solid lines in the figure is indeed strongly energy-dependent. This applies, in particular, to the sub-GeV range where the partial contributions to the antideuteron source term from pHe and HeHe collisions exceed the one from proton-proton scattering by orders of magnitude. The strong energy-dependence of the relative importance of the partial contributions to $Q^{\rm sec}$ at energies $T/n \lesssim 10\,\mathrm{GeV}$ is shown also clearly in figure 7. We conclude from this figure that the use of a nuclear enhancement factor at low energies should be avoided.

Following the same procedure, we have calculated antihelium production in pp, pHe, Hep, HeHe, $\bar{p}p$ and $\bar{p}$He interactions, using 56 logarithmic bins from $E_p = 60$ to 5×10^3 GeV. The resulting contributions to the source spectrum are shown in figure 8 for different energy ranges of the primary particles. The relative contributions from the various interactions are compared in figure 9. Since tritium decays fast compared to the propagation time scale, the plotted antihelium source spectrum includes also the antitritium contribution.

Comparing the source term of antihelium to the one of antideuteron, we see that its maximum is reduced by a factor few $\times 10^4$ and shifted somewhat to larger T/n. Otherwise, the same qualitative features discussed above for the antideuteron source term are still present. In particular, because of the possibility to interact with multiple target nucleons simultaneously, the contribution to the source term from pHe and HeHe collisions dominates the one from pp interactions up to few GeV/nucleon. There is also a notable difference concerning the

[8]Modulo the small contributions from $\bar{p}p$ and $\bar{p}$He collisions.

JCAP08(2020)048

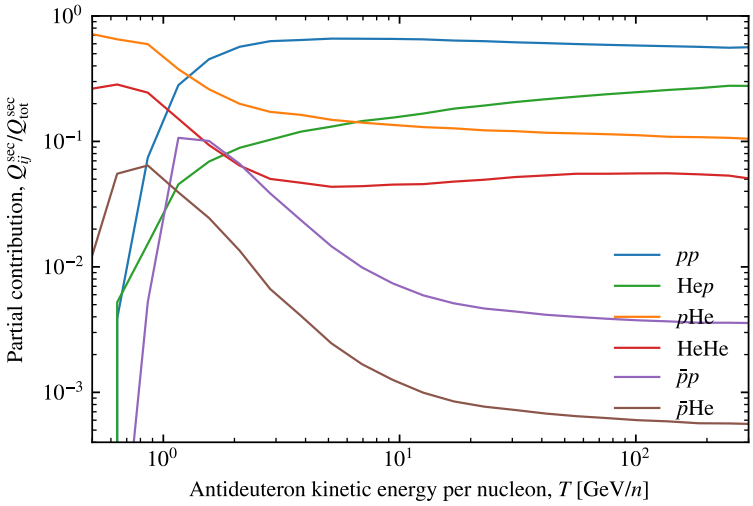

Figure 7. Relative contributions of the different reactions to the antideuteron source spectrum as function of kinetic energy per nucleon.

relative contributions of $\bar{p}p$ and $\bar{p}$He collisions: as expected from threshold effects,[9] those are up to a factor ~ 10 smaller, compared to the antideuteron case, at $T/n \lesssim 50\,\text{GeV}$. In any case, the contribution from $\bar{p}p$ interactions on the final antinuclei spectra is neglible.

4.2 Dark matter annihilations

In addition to the secondary production, we consider antinuclei originating from DM annihilations. We consider as DM particles Majorana fermions which annihilate purely into $\bar{b}b$ or W^+W^- pairs. These annihilations will be modelled in PYTHIA by generating a generic collision of a non-radiating e^+e^- pair with $\sqrt{s} = 2m_\chi$. The injection spectra $\mathrm{d}N/\mathrm{d}T$ are shown in figure 10 for antideuterons and in figure 11 for antihelium and antitritium. In both cases, we consider 100 and 1000 GeV as DM mass. Note that in the antideuteron injection spectra the differences between the standard and our new coalescence model can reach a factor of few, while they are much smaller in the spectra of antihelium-3. The reason for this mismatch are the wave-functions of the two nuclei: since the one of the antideuteron is stronger peaked at $r = 0$ than the one of antihelium, large values of q in eq. (2.1) are less suppressed for antideuterons, cf. with figure 4 of ref. [13]. As a result, the differences in the shape of the antideuteron energy spectrum are more pronounced compared to the case of antihelium.

The DM source spectrum can be written as [44]

$$Q(\boldsymbol{r}, T) = \frac{1}{2}\frac{\rho^2(\boldsymbol{r})}{m_\chi^2}\langle\sigma_{\rm ann}v\rangle\frac{\mathrm{d}N_{\bar{N}}^i}{\mathrm{d}T_{\bar{N}}}, \tag{4.3}$$

[9] Near threshold, an antideuteron is produced in the interactions $pp \to \bar{p}\bar{n}ppppn$ and $\bar{p}p \to \bar{p}\bar{n}pn$, while an antihelium is produced in $pp \to \bar{p}\bar{p}\bar{n}\bar{n}ppppn$ and $\bar{p}p \to \bar{p}\bar{p}\bar{n}\bar{n}ppppn$. Thus, there is a larger relative change in going from antideuteron to antihelium in $\bar{p}p$ interactions than in pp.

JCAP08(2020)048

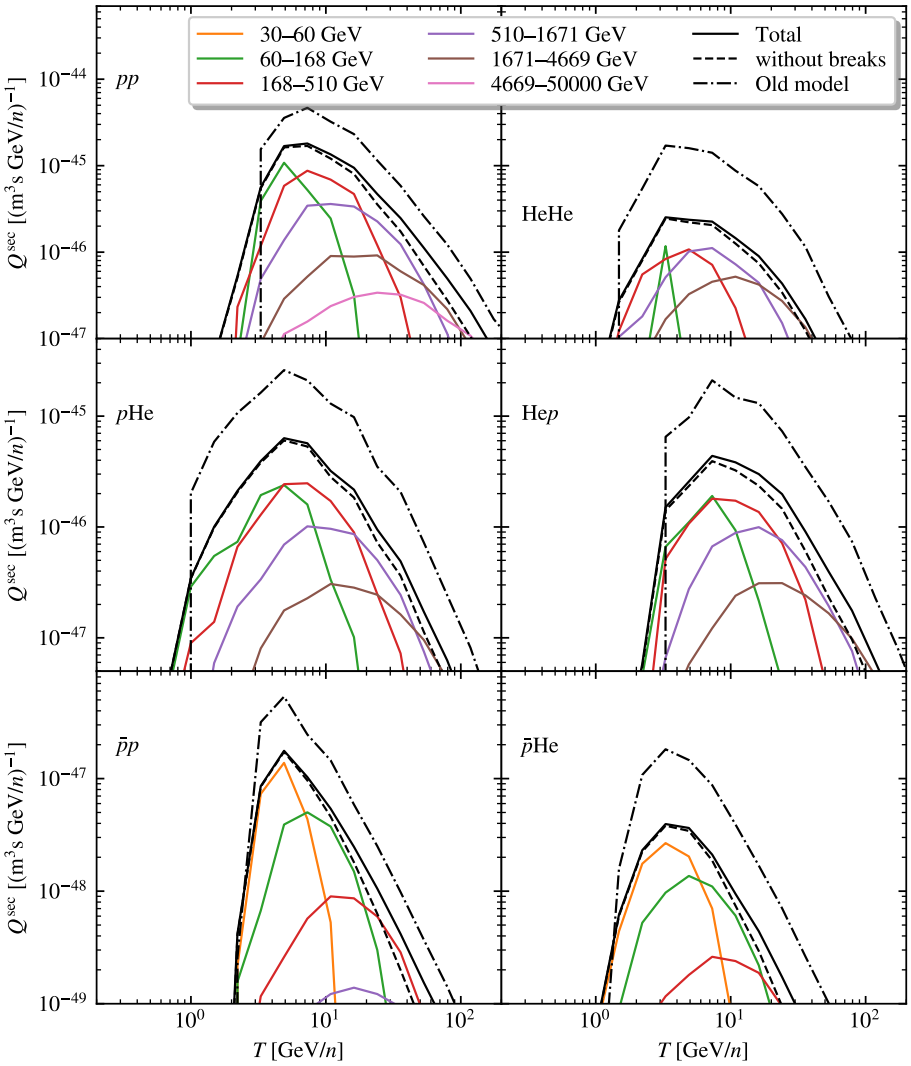

Figure 8. Partial contributions to the combined secondary source spectrum $Q^{\rm sec}$ of antihelium and antitritium, similar to figure 6.

where $\rho(\boldsymbol{r})$ is the DM mass density, m_χ its mass, $\langle\sigma_{\rm ann}v\rangle$ its thermally averaged annihilation cross section and $\mathrm{d}N_{\bar{N}}/\mathrm{d}T_{\bar{N}}$ is the differential number density of the antinuclei $\bar{N}$. An upper bound on $\langle\sigma_{\rm ann}v\rangle$ will be determined in section 5.2, requiring that the antiproton flux measured by AMS-02 is not exceeded. The effect of different DM density profiles $\rho(\boldsymbol{r})$ is small compared to the propagation uncertainty and has already been extensively discussed, see e.g. refs. [11, 45]. For simplicity, we will therefore only use an Einasto profile with $\alpha = 0.17$, $r_s = 28.4\,\mathrm{kpc}$ and $\rho_s = 0.033\,\mathrm{GeV/cm^3}$ [46].

JCAP08(2020)048

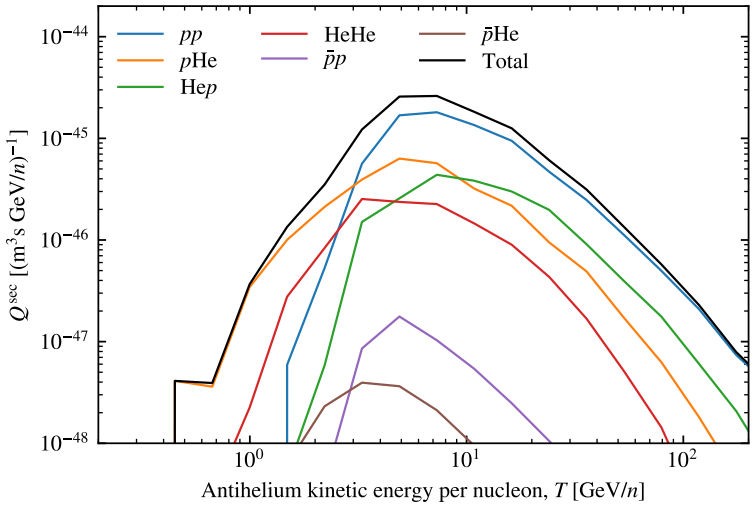

Figure 9. Contributions from different reaction types to the total secondary source term of antihelium.

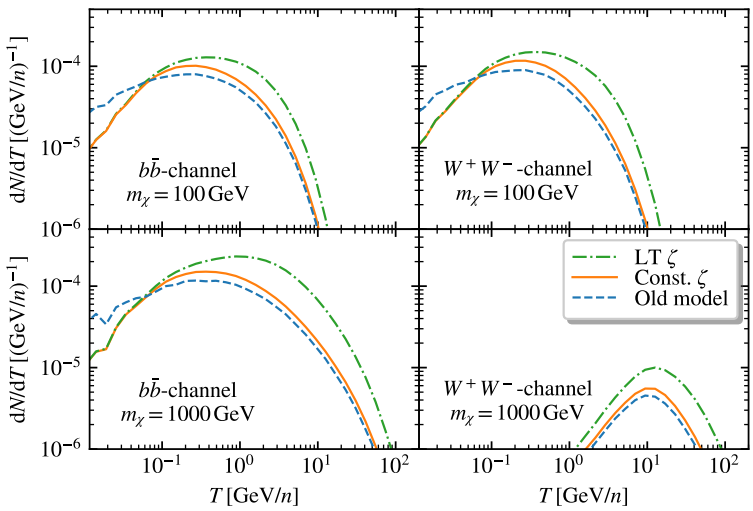

Figure 10. Antideuteron injection spectra from DM annihilations into $b\bar{b}$ (left) and W^+W^- (right), for $m_\chi = 100\,$GeV (top) and $m_\chi = 1000\,$GeV (bottom).

JCAP08(2020)048

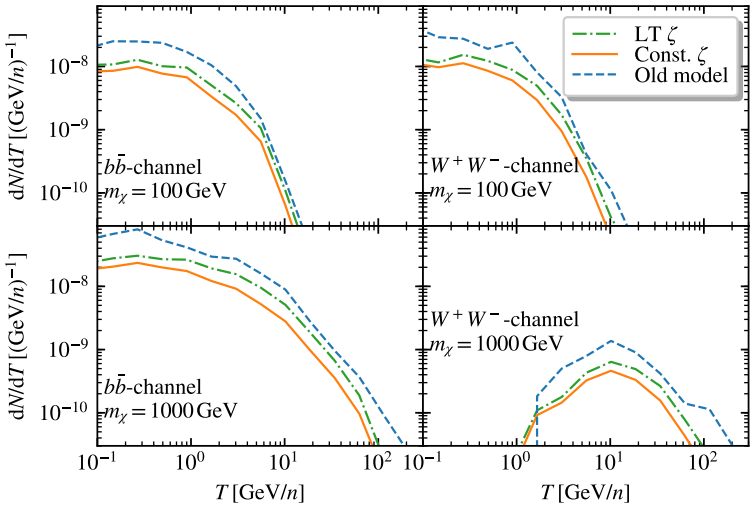

Figure 11. Antihelium (plus antitritium) injection spectra from DM annihilations into $b\bar{b}$ (left) and W^+W^- (right), for $m_\chi = 100\,\mathrm{GeV}$ (top) and $m_\chi = 1000\,\mathrm{GeV}$ (bottom).

5 Antinuclei fluxes

5.1 Propagation model

Charged particles diffuse in the turbulent Galactic magnetic field. We employ the two-zone diffusion model [47, 48] to describe the propagation of antinuclei through the Milky Way, which provides a simplistic but rather successful description of a variety of CR data. In this scheme, the Galaxy with radius $R = 20\,\mathrm{kpc}$ is modelled as a cylinder containing a large diffusive CR halo of half-height L and a thin disk of half-height $h \ll L$. The latter comprises the CR sources and the interstellar medium which serves as target for secondary production. In this model, the diffusion equation for the differential number density $n_{\bar{N}}$ of antinuclei can be written in cylindrical coordinates $\boldsymbol{r} = (r, z)$, where z is the height above the Galactic plane, as

$$\begin{aligned} -K\nabla^2 n_{\bar{N}} + \mathrm{sign}(z) V_c \partial_z n_{\bar{N}} + 2h\delta(z)\partial_E \left(b_{\mathrm{loss}} n_{\bar{N}} - D_{EE}\partial_E n_{\bar{N}}\right) \\ = Q^{\mathrm{prim}} + 2h\delta(z)\left[Q^{\mathrm{sec}} + Q^{\mathrm{ter}} - \Gamma_{\mathrm{ann}} n_{\bar{N}}\right], \end{aligned} \tag{5.1}$$

where we have taken the limit $h = 100\,\mathrm{pc} \ll L$. We parametrise the rigidity-dependent diffusion coefficient as a simple power law,

$$K(\mathcal{R}) = \beta K_0 (\mathcal{R}/\mathrm{GV})^\delta, \tag{5.2}$$

with $\mathcal{R} = E/(Ze)$, and K_0 and δ are free parameters. In turn, diffusion in momentum space, which is included as second-order re-acceleration in eq. (5.1), is related to $K(\mathcal{R})$ by

$$D_{EE}(\mathcal{R}) = \frac{4}{3\delta(4-\delta^2)(4-\delta)} V_{\mathrm{A}}^2 \frac{v_{\bar{N}}^2 p_{\bar{N}}^2}{K(\mathcal{R})}, \tag{5.3}$$

JCAP08(2020)048

where V_A is the Alfvén velocity, $v_{\bar{N}}$ is the velocity of the antinuclei and $p_{\bar{N}}$ their momentum. Moreover, V_c denotes the convection velocity which is assumed to be constant and directed away from the Galactic disc, while $\Gamma^{\bar{N}}_{\rm ann}$ is the annihilation rate of the antinuclei. The factor $b_{\rm loss}$ accounts for Coulomb, ionization and adiabatic energy losses. The primary proton, helium and antiproton fluxes are assumed to be the same in entire Galactic disc. The flux of antinuclei is related to the number density by $\Phi(E, \boldsymbol{r}) = v n_{\bar{N}}(E, \boldsymbol{r})/(4\pi)$.

The interaction rate of an antinucleus $\bar{N}$ will be approximated by $\Gamma_i^{\bar{N}p} = (n_{\rm H} + 4^{2/3} n_{\rm He}) v_{\bar{N}} \sigma^i_{\bar{N}p}$, where the factor $4^{2/3}$ accounts approximately for the cross section difference between helium and hydrogen, and $\sigma^{\rm ann}_{\bar{N}p}$ is the $\bar{N}p$ annihilation cross section. For antiprotons and antideuterons, we find the cross sections using the procedure discussed in ref. [49], while for antihelium-3 we follow ref. [50].

The tertiary term can be written as

$$Q^{\rm ter}(T_{\bar{N}}, \boldsymbol{r}) = 4\pi (n_{\rm H} + 4^{2/3} n_{\rm He}) \left[\int_{T_{\bar{N}}}^{\infty} {\rm d}T'_{\bar{N}} \, \frac{{\rm d}\sigma^{\rm non\text{-}ann}(\bar{N}(T'_{\bar{N}}) + p \to \bar{N}(T_{\bar{N}}) + X)}{{\rm d}T_{\bar{N}}} \Phi_{\bar{N}}(T'_{\bar{N}}, \boldsymbol{r}) \right.$$
$$\left. - \sigma^{\rm non\text{-}ann}(\bar{N}(T_{\bar{N}}) + p \to \bar{N}(T''_{\bar{N}}) + X) \Phi_{\bar{N}}(T_{\bar{N}}, \boldsymbol{r}) \right], \tag{5.4}$$

where $\Phi_{\bar{N}}(T_{\bar{N}}, \boldsymbol{r})$ is the antinucleus flux at energy $T_{\bar{N}}$. Thus, the tertiary terms are themselves dependent on the antinucleus flux and eq. (5.1) becomes an integro-differential equation that we solve using the method presented in ref. [51].

For antinuclei from WIMP annihilations, we neglect both re-acceleration and energy losses in eq. (5.1), as they have been shown to have little impact on the final primary spectrum for $T \gtrsim 1\,{\rm GeV}$ [52]. We also neglect the tertiary contribution to the primary flux, since it is small for antiprotons and antideuterons because of their small non-annihilating inelastic cross section. For comparison, neglecting the tertiary contribution in the case of helium-3 leads to a flux that is roughly 40% lower compared to the opposite limit of neglecting the non-annihilating interactions [50]. In this case, one can use the common semi-analytical solution detailed, e.g., in refs. [45, 46, 52]. Note, however, that parts of the estimated sensitivities of the upcoming GAPS and AMS-02 experiments fall within the region $T \lesssim 1\,{\rm GeV}$ [53], which means that one should include the losses in a complete analysis of the low-energy range.

The final propagation model depends on five parameters: L, K_0, δ, V_c and V_A. In order to ease the comparison to earlier works, we employ the two parameter sets dubbed 'med' and 'max' in ref. [54]. In addition, we use one parameter set inspired by a plain Kolmogorov diffusion model and the best-fit parameters from a recent B/C analysis [55] performed by Kappl[10] et al. For the former, we fix K_0 by requiring that the grammage $X = c\rho h L/(2K)$ crossed by CR protons with energy 10 GeV equals $10\,{\rm g/cm^2}$. The numerical values of the five parameters determining the propagation model are summarised in table 4. Finally, we account for Solar modulations using the force-field approximation [56, 57] with a Fisk potential $\phi = 0.6\,{\rm GV}$, as described in appendix B.

5.2 Upper bound on the annihilation cross section from AMS-02 antiproton data

The generic DM model used in this work has, apart from the branching ratios, two parameters: the DM mass m_χ and the thermally averaged annihilation cross section $\langle \sigma_{\rm ann} v \rangle$. We

[10] Note that Kappl et al. used $n_{\rm H} = 0.9\,{\rm cm^{-3}}$ and $N_{\rm He} = 0.1\,{\rm cm^{-3}}$, meaning that our results are 9% higher as if we would use their parameter set.

JCAP08(2020)048

Model	L [kpc]	δ	K_0 [kpc^2/Myr]	V_c [km/s]	V_A [km/s]
max	15	0.46	0.0765	5	117.6
med	4	0.7	0.0112	12	52.9
KRW	13.7	0.408	0.0967	0.2	31.9
Kolmogorov	5	1/3	0.018	0	0

Table 4. Parameters used for the two-zone propagation model.

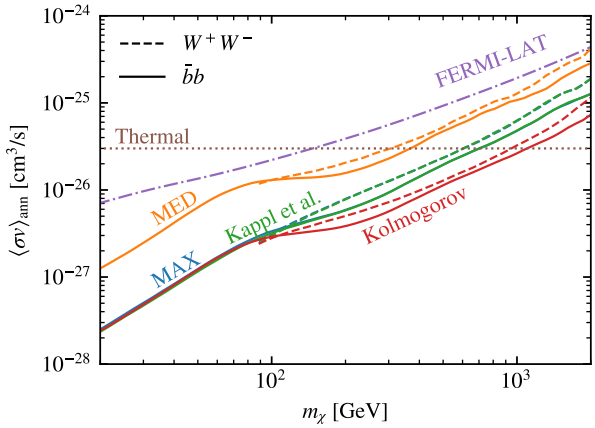

Figure 12. Upper limit compatible with the AMS-02 antiproton data for different propagation parameters. The upper limit from Fermi-LAT [59] (for $b\bar{b}$) and the value $\langle\sigma_{\rm ann}v\rangle$ favoured by cosmology are shown for comparison.

will here investigate the maximal flux of antinuclei consistent with the AMS-02 antiproton data [45]. There is currently no clear evidence for an exotic primary component in the antiproton spectrum and we use this absence to set an upper bound on the annihilation cross section for various DM masses. More precisely, we derive upper bounds on $\langle\sigma_{\rm ann}v\rangle$ by choosing as null-hypothesis the fit to the antiproton flux shown in figure 4. We then in turn vary the annihilation cross section until the χ^2 value differs by 3.84 from the null-hypothesis, corresponding to an 95% CL upper limit [58]. A stringent upper bound compatible with the antiproton flux is obtained when the same parameters are used in the antideuteron and antihelium cases. The results are shown in figure 12 for the considered parameter sets and the annihilation channels W^+W^- and $\bar{b}b$. The canonical value for a thermal relic, $\langle\sigma_{\rm ann}v\rangle = 3\times10^{-26}\,{\rm cm}^3/{\rm s}$, and the upper bound obtained by the Fermi-LAT collaboration using dwarf galaxies [59] are plotted for comparison too. Note that the antiproton limits are more stringent than the recent Fermi-LAT bound. However, we stress that these limits only hold for the specific propagation model and astrophysical parameters used.

5.3 Detection prospects

The expected flux of light antinuclei at Earth from DM annihilations and secondary production can now be estimated by employing the two-zone propagation model and the force-field

JCAP08(2020)048

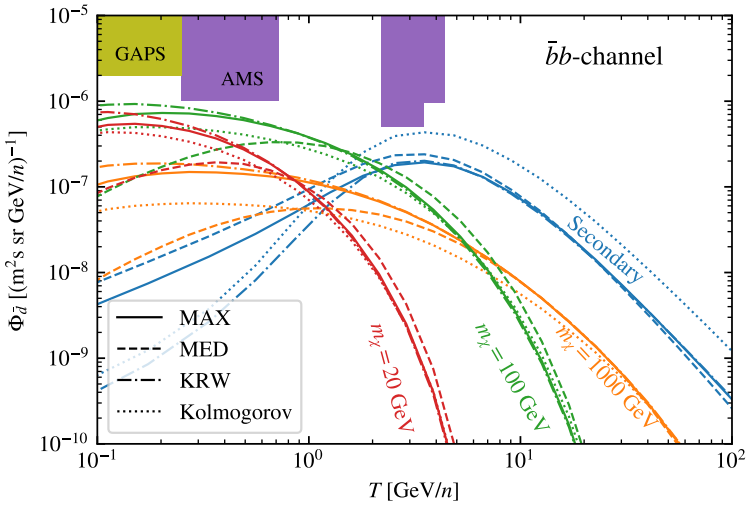

Figure 13. Estimated antideuteron flux on Earth from DM annihilations into $\bar{b}b$ pairs and from secondary production for the considered benchmark cases. The shaded areas on the top are the estimated AMS-02 and GAPS sensitivities.

approximation, using the source spectra computed previously as input. For concreteness, we consider only the Einasto DM density profile. The antideuteron flux obtained with the new coalescence model, using the four sets of parameters for the diffusion model, is shown in figures 13 and 14. Additionally, we use the upper limit on the annihilation cross section imposed by the AMS-02 antiproton data as constraint. The shaded areas correspond to the expected sensitivity for the GAPS long duration balloon flight (105 days) (yellow) and 10-year data-taking of AMS-02 (purple) [10, 60, 61]. We find that the predicted antideuteron flux can be, for optimistic parameters, close to the sensitivity of these two experiments.

The estimated antihelium-3 flux on Earth for the same benchmark cases as in the antideuteron case is shown in figure 15. The antihelium-3 sensitivity of AMS-02 is estimated by multiplying the 18-year $^3\bar{\mathrm{He}}$/He sensitivity from ref. [62] with the helium flux measured by AMS-02 [37], and is further rescaled to the 10-year sensitivity. The better sensitivity for antihelium-3 than for antideuteron may explain why AMS-02 has reported eight antihelium candidates, while the number of antideuteron candidate events is still unknown. From figure 15, one can see that antihelium nuclei from secondary production are more likely to be detected than from DM annihilations.

There have been various other recent works investigating the detection prospects of antihelium-3 [2, 5, 50, 63–66]. The range of p_0 values used in these works varies considerably, depending e.g. on the data sets used for the calibration [2, 50, 65], the hadronisation model and the event generator [67, 68]. Since the yield of antinuclei scales as p_0^{3A-3}, a relatively modest increase of p_0 can boost the predictions towards the experimental sensitivities. Alternatively, it may be a promising avenue to investigate, if modified propagation models allow higher antideuteron and antihelium-3 fluxes, without being in a conflict with other observations. For instance, ref. [66] proposed that strong re-acceleration can increase the number of expected antideuteron and antihelium-3 events considerably.

JCAP08(2020)048

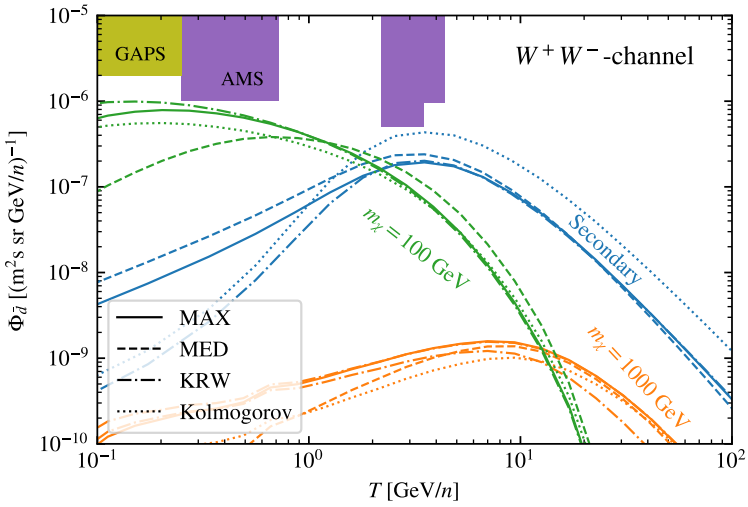

Figure 14. Estimated antideuteron flux on Earth from DM annihilations into W^+W^- pairs and from secondary production for the considered benchmark cases. The shaded areas on the top are the estimated AMS-02 and GAPS sensitivities.

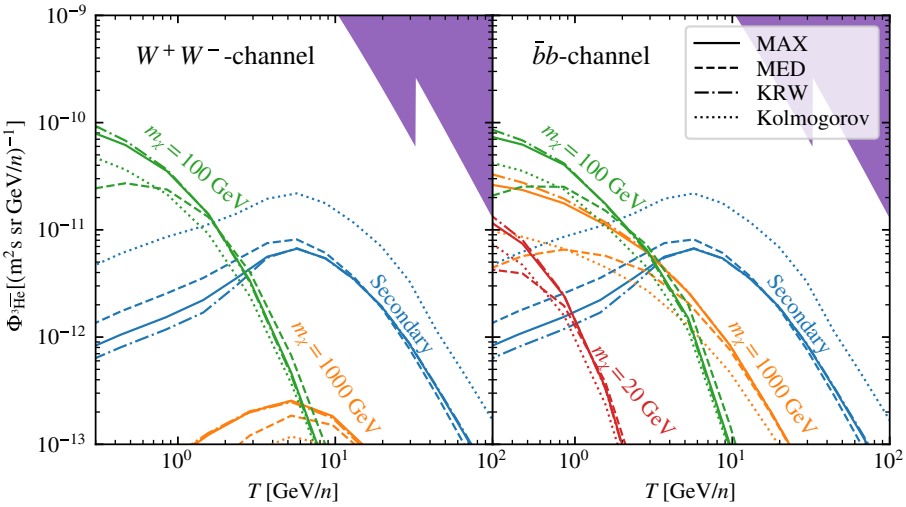

Figure 15. Estimated antihelium-3 flux on Earth from WIMP annihilations and secondary production for the considered benchmark cases and the considered propagation parameters. The shaded area on the top right is the estimated 10-year AMS-02 sensitivity.

JCAP08(2020)048

6 Summary and conclusions

The coalescence momentum p_0 of the usually employed coalescence models in momentum space is a free parameter that must be fitted to experimental data. Although p_0 should be independent on both the center-of-mass energy of the collision and the reaction type, the value obtained by fitting the model to data from different reactions varies considerably [10–12, 34]. In contrast, we have shown that the single parameter σ of our alternative coalescence model is universal, agreeing numerically well with its interpretation as the size of the formation region of antinuclei. Therefore, the production of antideuteron and antihelium-3 can be described successfully both for point-like interactions (e^+e^-, DM decays and annihilations) and for hadronic and nuclear interactions, using a single free parameter.

Combining our coalescence model with the event generator QGSJET-II-04m, we have calculated consistently the yield of antideuterons in proton-proton, proton-helium, helium-helium, antiproton-proton and antiproton-helium collisions. Thereby we avoided the use of a nuclear enhancement factor, which is generally ill-defined [26, 43]. In particular, we found that the low energy tail of the secondary source spectrum of antinuclei is strongly dominated by the contributions of proton-helium and helium-helium collisions. This is in contrast to previous works using a nuclear enhancement factor, which found that antiproton collisions should be dominant due to the low threshold energy. Moreover, our new coalescence model takes into account the increase of the size of the formation region of antinuclei in reactions involving helium, an effect which is neglected using the old coalescence model. Therefore the old treatment tends to over-predict the antideuteron yield in reactions involving helium.

Using a two-zone diffusion model, we derived the resulting fluxes of antideuterons and antihelium. Our results indicate that no antihelium nuclei from secondary production or from WIMP annihilations should be detected during 10-years of operation of AMS-02 and the long duration balloon flights of GAPS. In contrast, the antideuteron flux can be close to the sensitivities of the AMS-02 and GAPS experiments. Since our analysis contains several sources of uncertainties related to, e.g. the propagation model, nuclear cross sections, and the coalescence model, the true fluxes might be well higher and thus in reach of these experiments. We note also that updated sensitivity analyses for both antideuteron and antihelium are highly warranted. The GAPS experiment is most sensitive to low-energy antideuterons from light DM. In that energy range, a more complete numerical treatment of the CR propagation would be desirable. In the case of antihelium-3, the contribution from CR interaction on gas is closer to the expected sensitivity than from DM annihilations. An interesting avenue to investigate is whether modified propagation models allow higher antihelium-3 fluxes without being in a conflict with other observations.

Acknowledgments

S.O. acknowledges support from the project OS 481/2-1 of the Deutsche Forschungsgemeinschaft.

A Experimental data used

We only consider experiments on antideuteron production, i.e., we neglect the experimental data on deuteron production. In this way, we avoid possible contaminations from the production of deuterons in the detector material.

JCAP08(2020)048

A.1 e^+e^- annihilations

The ALEPH [15] and OPAL collaboration [16] at LEP measured the deuteron and the antideuteron fluxes in e^+e^- collisions at the Z resonance. The ALEPH collaboration measured a production of $(5.9 \pm 1.8 \pm 0.5) \times 10^{-6}$ antideuterons per hadronic Z decay in the antideuteron momentum range $0.62 < p < 1.03\,\mathrm{GeV}$ and a production angle $|\cos\vartheta| < 0.95$. Here, the first uncertainty is the statistical and the second one is the systematic error. In contrast, the OPAL collaboration did not detect any antideuterons in the momentum range $0.35 < p < 1.1\,\mathrm{GeV}$. We take the resulting upper limit into account by following the procedure discussed in ref. [12].

A.2 Proton-proton collisions

The ALICE collaboration measured the invariant differential yield $E\,\mathrm{d}^3n/\mathrm{d}p^3$ of antideuterons, antitritium and antihelium-3 in inelastic proton-proton collisions at centre of mass energies $\sqrt{s} = \{0.9, 2.76, 7\}\,\mathrm{TeV}$ in the p_T range $0.8\,\mathrm{GeV} < p_T < 3\,\mathrm{GeV}$ and rapidity range $|y| < 0.5$ [17]. The experiment included a trigger (V0) that required a hit (charged particle) in both of the two pseudo-rapidity ranges $2.8 < \eta < 5.1$ and $-3.7 < \eta < -1.7$, used to select non-diffractive inelastic events. We generate inelastic events and only include those which satisfy the V0 trigger.

The inclusive differential cross section of antideuterons at $\vartheta_{\mathrm{cm}} = 90°$ ($y = 0$) in $\sqrt{s} = 53\,\mathrm{GeV}$ pp collisions was measured at CERN ISR [20, 21]. We compute the differential cross section as $E\,\mathrm{d}^3\sigma/\mathrm{d}p^3 = \sigma_{\mathrm{inel}}/(2\pi p_T N_{\mathrm{inel}})(\mathrm{d}^2N/\mathrm{d}p_T\,\mathrm{d}y)$ and require that $|y| < 0.1$.

A.3 Proton-beryllium and proton-aluminium collisions

The production of d, t, ^{3}He, $\bar{d}$, $\bar{t}$ and $^3\bar{\mathrm{He}}$ at 0° with momenta between 12 and 37 GeV in the lab frame in p-beryllium and p-aluminium collisions at $200\,\mathrm{GeV}/c$ was reported in ref. [19]. The results are presented as ratios of antinuclei and π^- yields. The antideuteron results had been split into three and five bins between 20 and 37 GeV in p-aluminium and p-beryllium collisions, respectively. As the data are given for 0° in the lab frame, and we are only interested in the bulk of produced antinuclei, we include all produced π^- and antideuterons in the analysis.

B Parametrisation of the primary cosmic ray flux

In order to describe the secondary production of antinuclei, one needs the primary fluxes of protons, helium and antiprotons as input. The primary CR fluxes were traditionally parametrised by an unbroken power law up to the CR knee, as $\Phi(T) \propto T^{-\gamma}$, where T is the kinetic energy of the particle and $\gamma \sim 2.7$. However, recent experimental data, such as from the AMS-02 [36–38] and CREAM [40] experiments, clearly suggest that there is a hardening in the CR flux around the rigidity $\mathcal{R} \sim 400\,\mathrm{GeV}$. In addition, there are now several experiments, including CREAM and DAMPE [39], suggesting that there is an additional break around 10 TeV. For a spectrum with N statistical significant breaks, we fit the function

$$\Phi(T) = AT^{-\gamma}\left(\frac{T}{T+b}\right)^c \prod_{i=1}^{N} f(T_{\mathrm{b}i}, \Delta\gamma_i, s), \tag{B.1}$$

where

$$f(T_{\mathrm{b}}, \Delta\gamma, s) = \left[1 + \left(\frac{T}{T_{\mathrm{b}}}\right)^s\right]^{\Delta\gamma/s} \tag{B.2}$$

JCAP08(2020)048

	A	b	c	γ	$T_{\rm b1}$	$\Delta\gamma_1$	$T_{\rm b2}$	$\Delta\gamma_2$	χ^2/d.f.
	[m^{2}s sr /(GeV/n)][GeV/n]				[GeV/n]		[GeV/n]		
Proton	26714	0.49	6.81	2.88	343	0.265	19503	−0.264	0.39
Helium	1151	1.06	2.74	2.79	237	0.309	18849	−0.620	0.95
Antiproton	22.4	1.28	9.22	3.22	88.4	0.412			0.39

Table 5. Parameters for the fits of the primary proton, helium, and antiproton spectra at local interstellar space. The fitting procedure is discussed in the text.

accounts for the breaks, while the first parentheses is included to reproduce the low energy part of the spectra. We follow ref. [39] and fix the smoothness parameter $s = 5$ for proton and antiproton, while we find that $s = 3$ provides a good fit for helium. The parameters $\Delta\gamma_i$ describe the changes in the power-law index. Thus, for each additional break, we add two free parameters, while for the main spectrum, we have four free parameters. We fix the parameters by first fitting

$$\Phi_{\text{AMS-02}}(T) = AT^{-\gamma}\left(\frac{T}{T+b}\right)^{c}, \tag{B.3}$$

to the AMS-02 proton data up to the hardening at $T \sim 400\,\text{GeV}/n$ and in turn fix the remaining parameters by using eq. (B.1).

We take into account solar modulation by using the force field approximation [56]. Based on the Oulu NM database [69], we find the mean solar modulation force-field ϕ in the periods of data taking [70, 71]. Since solar modulation can be neglected at high energies, this is only relevant for the AMS-02 data. For the proton and helium fluxes, we obtained $\phi = 0.60\,\text{GV}$, while we found $\phi = 0.62\,\text{GV}$ for the antiproton flux. Our fit results are listed in table 5.

References

[1] F. Donato, N. Fornengo and P. Salati, *Anti-deuterons as a signature of supersymmetric dark matter*, *Phys. Rev. D* **62** (2000) 043003 [hep-ph/9904481] [INSPIRE].

[2] M. Cirelli, N. Fornengo, M. Taoso and A. Vittino, *Anti-helium from dark matter annihilations*, *JHEP* **08** (2014) 009 [arXiv:1401.4017] [INSPIRE].

[3] P. von Doetinchem et al., *Cosmic-ray antinuclei as messengers of new physics: status and outlook for the new decade*, arXiv:2002.04163 [INSPIRE].

[4] P. Chardonnet, J. Orloff and P. Salati, *The production of antimatter in our galaxy*, *Phys. Lett. B* **409** (1997) 313 [astro-ph/9705110] [INSPIRE].

[5] V. Poulin, P. Salati, I. Cholis, M. Kamionkowski and J. Silk, *Where do the AMS-02 antihelium events come from?*, *Phys. Rev. D* **99** (2019) 023016 [arXiv:1808.08961] [INSPIRE].

[6] A. Schwarzschild and C. Zupancic, *Production of tritons, deuterons, nucleons and mesons by 30-GeV protons on A-1, Be and Fe Targets*, *Phys. Rev.* **129** (1963) 854 [INSPIRE].

[7] S.T. Butler and C.A. Pearson, *Deuterons from high-energy proton bombardment of matter*, *Phys. Rev.* **129** (1963) 836 [INSPIRE].

[8] M. Kadastik, M. Raidal and A. Strumia, *Enhanced anti-deuteron dark matter signal and the implications of PAMELA*, *Phys. Lett. B* **683** (2010) 248 [arXiv:0908.1578] [INSPIRE].

[9] L.A. Dal, *Antideuterons as signature for dark matter*, MSc Thesis, NTNU Trondheim, available at http://hdl.handle.net/11250/246403 (2011).

JCAP08(2020)048

[10] T. Aramaki et al., *Review of the theoretical and experimental status of dark matter identification with cosmic-ray antideuterons*, *Phys. Rept.* **618** (2016) 1 [arXiv:1505.07785] [INSPIRE].

[11] A. Ibarra and S. Wild, *Prospects of antideuteron detection from dark matter annihilations or decays at AMS-02 and GAPS*, *JCAP* **02** (2013) 021 [arXiv:1209.5539] [INSPIRE].

[12] L.A. Dal and A.R. Raklev, *Alternative formation model for antideuterons from dark matter*, *Phys. Rev. D* **91** (2015) 123536 [*Erratum ibid.* **92** (2015) 069903] [*Erratum ibid.* **92** (2015) 089901] [arXiv:1504.07242] [INSPIRE].

[13] M. Kachelrieß, S. Ostapchenko and J. Tjemsland, *Alternative coalescence model for deuteron, tritium, helium-3 and their antinuclei*, *Eur. Phys. J. A* **56** (2020) 4 [arXiv:1905.01192] [INSPIRE].

[14] R. Scheibl and U.W. Heinz, *Coalescence and flow in ultrarelativistic heavy ion collisions*, *Phys. Rev. C* **59** (1999) 1585 [nucl-th/9809092] [INSPIRE].

[15] ALEPH collaboration, *Deuteron and anti-deuteron production in e^+e^- collisions at the Z resonance*, *Phys. Lett. B* **639** (2006) 192 [hep-ex/0604023] [INSPIRE].

[16] OPAL collaboration, *Search for heavy charged particles and for particles with anomalous charge in e^+e^- collisions at LEP*, *Z. Phys. C* **67** (1995) 203 [INSPIRE].

[17] ALICE collaboration, *Production of deuterons, tritons, ^{3}He nuclei and their antinuclei in pp collisions at $\sqrt{s}$ = 0.9, 2.76 and 7 TeV*, *Phys. Rev. C* **97** (2018) 024615 [arXiv:1709.08522] [INSPIRE].

[18] A. Bussière et al., *Particle production and search for longlived particles in 200-GeV/c to 240-GeV/c proton - nucleon collisions*, *Nucl. Phys. B* **174** (1980) 1 [INSPIRE].

[19] W. Bozzoli et al., *Search for longlived particles in 200-GeV/c proton - nucleon collisions*, *Nucl. Phys. B* **159** (1979) 363 [INSPIRE].

[20] B. Alper et al., *Large angle production of stable particles heavier than the proton and a search for quarks at the CERN intersecting storage rings*, *Phys. Lett. B* **46** (1973) 265 [INSPIRE].

[21] British-Scandinavian-MIT collaboration, *Production of deuterons and anti-deuterons in proton proton collisions at the CERN ISR*, *Lett. Nuovo Cim.* **21** (1978) 189 [INSPIRE].

[22] T.W. Donnelly, J.A. Formaggio, B.R. Holstein, R.G. Milner and B. Surrow, *Foundations of nuclear and particle physics*, Cambridge University Press (2017).

[23] K. Blum and M. Takimoto, *Nuclear coalescence from correlation functions*, *Phys. Rev. C* **99** (2019) 044913 [arXiv:1901.07088] [INSPIRE].

[24] S. Ostapchenko, *Monte Carlo treatment of hadronic interactions in enhanced Pomeron scheme: I. QGSJET-II model*, *Phys. Rev. D* **83** (2011) 014018 [arXiv:1010.1869] [INSPIRE].

[25] S. Ostapchenko, *QGSJET-II: physics, recent improvements and results for air showers*, *EPJ Web Conf.* **52** (2013) 02001 [INSPIRE].

[26] M. Kachelriess, I.V. Moskalenko and S.S. Ostapchenko, *New calculation of antiproton production by cosmic ray protons and nuclei*, *Astrophys. J.* **803** (2015) 54 [arXiv:1502.04158] [INSPIRE].

[27] ALICE collaboration, *Measurement of pion, kaon and proton production in proton–proton collisions at $\sqrt{s} = 7$ TeV*, *Eur. Phys. J. C* **75** (2015) 226 [arXiv:1504.00024] [INSPIRE].

[28] T. Sjöstrand, S. Mrenna and P.Z. Skands, *PYTHIA 6.4 physics and manual*, *JHEP* **05** (2006) 026 [hep-ph/0603175] [INSPIRE].

[29] T. Sjöstrand et al., *An introduction to PYTHIA 8.2*, *Comput. Phys. Commun.* **191** (2015) 159 [arXiv:1410.3012] [INSPIRE].

[30] ALICE collaboration, *Production of pions, kaons and protons in pp collisions at $\sqrt{s} = 900$ GeV with ALICE at the LHC*, *Eur. Phys. J. C* **71** (2011) 1655 [arXiv:1101.4110] [INSPIRE].

JCAP08(2020)048

[31] ALICE collaboration, *Production of charged pions, kaons and protons at large transverse momenta in pp and Pb-Pb collisions at $\sqrt{s_{\rm NN}}$ =2.76 TeV*, *Phys. Lett. B* **736** (2014) 196 [arXiv:1401.1250] [INSPIRE].

[32] ALICE collaboration, *Supplemental material: afterburner for generating light (anti-)nuclei with QCD-inspired event generators in pp collisions*, ALICE Public Note ALICE-PUBLIC-2017-010 (2017).

[33] BRITISH-SCANDINAVIAN collaboration, *Production spectra of pi+-, K+-, rho+- at large angles in proton proton collisions in the CERN intersecting storage rings*, *Nucl. Phys. B* **100** (1975) 237.

[34] D.-M. Gomez-Coral, A. Menchaca Rocha, V. Grabski, A. Datta, P. von Doetinchem and A. Shukla, *Deuteron and antideuteron production simulation in cosmic-ray interactions*, *Phys. Rev. D* **98** (2018) 023012 [arXiv:1806.09303] [INSPIRE].

[35] V.V. Abramov et al., *High p_T deuteron and anti-deuteron production in pp and p a Collisions at 70-GeV*, *Sov. J. Nucl. Phys.* **45** (1987) 845 [INSPIRE].

[36] AMS collaboration, *Precision measurement of the proton flux in primary cosmic rays from rigidity 1 GV to 1.8 TV with the alpha magnetic spectrometer on the international space station*, *Phys. Rev. Lett.* **114** (2015) 171103 [INSPIRE].

[37] AMS collaboration, *Precision measurement of the helium flux in primary cosmic rays of rigidities 1.9 GV to 3 TV with the alpha magnetic spectrometer on the international space station*, *Phys. Rev. Lett.* **115** (2015) 211101 [INSPIRE].

[38] AMS collaboration, *Antiproton flux, antiproton-to-proton flux ratio and properties of elementary particle fluxes in primary cosmic rays measured with the alpha magnetic spectrometer on the international space station*, *Phys. Rev. Lett.* **117** (2016) 091103 [INSPIRE].

[39] DAMPE collaboration, *Measurement of the cosmic-ray proton spectrum from 40 GeV to 100 TeV with the DAMPE satellite*, *Sci. Adv.* **5** (2019) eaax3793 [arXiv:1909.12860] [INSPIRE].

[40] Y.S. Yoon et al., *Proton and helium spectra from the CREAM-III Flight*, *Astrophys. J.* **839** (2017) 5 [arXiv:1704.02512] [INSPIRE].

[41] N. Gorbunov et al., *Energy spectra of abundant cosmic-ray nuclei in the NUCLEON experiment*, *Adv. Space Res.* **64** (2019) 2546 [arXiv:1809.05333] [INSPIRE].

[42] S.-J. Lin, X.-J. Bi and P.-F. Yin, *Expectations of the cosmic antideuteron flux*, arXiv:1801.00997 [INSPIRE].

[43] M. Kachelriess, I.V. Moskalenko and S.S. Ostapchenko, *Nuclear enhancement of the photon yield in cosmic ray interactions*, *Astrophys. J.* **789** (2014) 136 [arXiv:1406.0035] [INSPIRE].

[44] G. Jungman, M. Kamionkowski and K. Griest, *Supersymmetric dark matter*, *Phys. Rept.* **267** (1996) 195 [hep-ph/9506380] [INSPIRE].

[45] N. Fornengo, L. Maccione and A. Vittino, *Dark matter searches with cosmic antideuterons: status and perspectives*, *JCAP* **09** (2013) 031 [arXiv:1306.4171] [INSPIRE].

[46] M. Cirelli et al., *PPPC 4 DM ID: a poor particle physicist cookbook for dark matter indirect detection*, *JCAP* **03** (2011) 051 [*Erratum ibid.* **10** (2012) E01] [arXiv:1012.4515] [INSPIRE].

[47] V.L. Ginzburg and S.I. Syrovatskii, *The origin of cosmic rays*, New York: Gordon and Breach (1969).

[48] V.L. Ginzburg, I.M. Khazan and V.S. Ptuskin, *Origin of cosmic-rays: galactic models with halo. I. Proton nucleon component*, *Astrophys. Space Sci.* **68** (1980) 295.

[49] T. Delahaye and M. Grefe, *Antideuterons from decaying gravitino dark matter*, *JCAP* **07** (2015) 012 [arXiv:1503.01101] [INSPIRE].

[50] E. Carlson, A. Coogan, T. Linden, S. Profumo, A. Ibarra and S. Wild, *Antihelium from dark matter*, *Phys. Rev. D* **89** (2014) 076005 [arXiv:1401.2461] [INSPIRE].

[51] F. Donato, D. Maurin, P. Salati, A. Barrau, G. Boudoul and R. Taillet, *Anti-protons from spallations of cosmic rays on interstellar matter*, *Astrophys. J.* **563** (2001) 172 [astro-ph/0103150] [INSPIRE].

[52] D. Maurin, R. Taillet and C. Combet, *Approximate formulae for exotic GCR anti-protons and anti-deuterons: fluxes and astrophysical uncertainties*, astro-ph/0609522 [INSPIRE].

[53] GAPS collaboration, *Antideuteron sensitivity for the GAPS experiment*, *Astropart. Phys.* **74** (2016) 6 [arXiv:1506.02513] [INSPIRE].

[54] F. Donato, N. Fornengo and D. Maurin, *Antideuteron fluxes from dark matter annihilation in diffusion models*, *Phys. Rev. D* **78** (2008) 043506 [arXiv:0803.2640] [INSPIRE].

[55] R. Kappl, A. Reinert and M.W. Winkler, *AMS-02 antiprotons reloaded*, *JCAP* **10** (2015) 034 [arXiv:1506.04145] [INSPIRE].

[56] L.J. Gleeson and W.I. Axford, *Solar modulation of galactic cosmic rays*, *Astrophys. J.* **154** (1968) 1011 [INSPIRE].

[57] H. Moraal, *Cosmic-ray modulation equations*, *Space Sci. Rev.* **176** (2013) 299.

[58] Particle Data Group collaboration, *Review of particle physics*, *Chin. Phys. C* **40** (2016) 100001 [INSPIRE].

[59] Fermi-LAT collaboration, *Searching for dark matter annihilation from milky way dwarf spheroidal galaxies with six years of Fermi large area telescope data*, *Phys. Rev. Lett.* **115** (2015) 231301 [arXiv:1503.02641] [INSPIRE].

[60] AMS-02 collaboration, *Cosmic rays antideuteron sensitivity for AMS-02 experiment*, in *Proceedings, 30th International Cosmic Ray Conference (ICRC 2007): Merida, Yucatan, Mexico, 3–11 july 2007*, vol. 4, pp. 765–768 (2007).

[61] GAPS collaboration, *Antideuteron sensitivity for the GAPS experiment*, *Astropart. Phys.* **74** (2016) 6 [arXiv:1506.02513] [INSPIRE].

[62] A. Kounine, *Status of the AMS experiment*, arXiv:1009.5349 [INSPIRE].

[63] A. Coogan and S. Profumo, *Origin of the tentative AMS antihelium events*, *Phys. Rev. D* **96** (2017) 083020 [arXiv:1705.09664] [INSPIRE].

[64] K. Blum, K.C.Y. Ng, R. Sato and M. Takimoto, *Cosmic rays, antihelium and an old navy spotlight*, *Phys. Rev. D* **96** (2017) 103021 [arXiv:1704.05431] [INSPIRE].

[65] Y.-C. Ding, N. Li, C.-C. Wei, Y.-L. Wu and Y.-F. Zhou, *Prospects of detecting dark matter through cosmic-ray antihelium with the antiproton constraints*, *JCAP* **06** (2019) 004 [arXiv:1808.03612] [INSPIRE].

[66] I. Cholis, T. Linden and D. Hooper, *Anti-deuterons and anti-helium nuclei from annihilating dark matter*, arXiv:2001.08749 [INSPIRE].

[67] L.A. Dal and M. Kachelriess, *Antideuterons from dark matter annihilations and hadronization model dependence*, *Phys. Rev. D* **86** (2012) 103536 [arXiv:1207.4560] [INSPIRE].

[68] L.A. Dal and A.R. Raklev, *Antideuteron limits on decaying dark matter with a tuned formation model*, *Phys. Rev. D* **89** (2014) 103504 [arXiv:1402.6259] [INSPIRE].

[69] I. Usoskin, *Updated cosmic ray modulation strength (Phi) since 1951 for the LIS by Vos and Potgieter (2015)*, available at http://cosmicrays.oulu.fi/phi/phi.html, 2017.

[70] E.E. Vos and M.S. Potgieter, *New modeling of galactic proton modulation during the minimum of solar cycle 23/24*, *Astrophys. J.* **815** (2015) 119.

[71] I.G. Usoskin, A. Gil, G.A. Kovaltsov, A.L. Mishev and V.V. Mikhailov, *Heliospheric modulation of cosmic rays during the neutron monitor era: calibration using PAMELA data for 2006–2010*, *J. Geophys. Res. Space Phys.* **122** (2017) 3875 [arXiv:1705.07197] [INSPIRE].

Paper III – Reacceleration of charged dark matter

Kachelrieß, M. & Tjemsland, J. "Reacceleration of charged dark matter". *JCAP* **10,** 001. arXiv: 2006.10479 [astro-ph.HE] (2020)

Abstract: Charged particles scattering on moving inhomogenities of the magnetised interstellar medium can gain energy through the process of second-order Fermi acceleration. This energy gain depletes in turn the magnetic wave spectrum around the resonance wave-vector $k \sim 1/R_L$, where R_L is the Larmor radius of the charged particle. This energy transfer can prohibit the cascading of magnetic turbulence to smaller scales, leading to a drop in the diffusion coefficient and allowing the efficient exchange of charged dark matter particles in the disk and the halo. As a result, terrestial limits from direct detection experiments apply to charged dark matter. Together with the no-observation of a drop in the diffusion coefficient, this excludes charged dark matter for 10^3 GeV $\lesssim m/q \lesssim 10^{11}$ GeV, even if the charged dark matter abundance is only a small part of the total relic abundance.

M. Kachelrieß noticed that Chuzhoy & Kolb [*JCAP* 07 (2009)] claimed that the regular magnetic field in the Milky Way disc acts as a shield preventing millicharged DM reaching Earth, thus avoiding direct detection experiments. This seems to contradict Liouville's theorem, and therefore motivated us to study the propagation of charged DM. Unfortunately, we realized that much of what we wanted to do had already been discussed by Dunsky et al. [*JCAP* 07 (2019) 015]. But reacceleration of cosmic ray DM had not been discussed before. Given that ordinary cosmic rays may obtain as much as $\mathcal{O}(10)\,\%$ of their energy from reacceleration, we quickly realized that this may be an important effect for millicharged DM.

Journal of Cosmology and Astroparticle Physics
An IOP and SISSA journal

Reacceleration of charged dark matter

M. Kachelrieß and J. Tjemsland

Institutt for fysikk, NTNU, Trondheim, Norway

E-mail: Michael.Kachelriess@ntnu.no, Jonas.Tjemsland@ntnu.no

Received June 25, 2020
Accepted July 31, 2020
Published October 1, 2020

Abstract. Charged particles scattering on moving inhomogenities of the magnetised interstellar medium can gain energy through the process of second-order Fermi acceleration. This energy gain depletes in turn the magnetic wave spectrum around the resonance wave-vector $k \sim 1/R_L$, where R_L is the Larmor radius of the charged particle. This energy transfer can prohibit the cascading of magnetic turbulence to smaller scales, leading to a drop in the diffusion coefficient and allowing the efficient exchange of charged dark matter particles in the disk and the halo. As a result, terrestial limits from direct detection experiments apply to charged dark matter. Together with the no-observation of a drop in the diffusion coefficient, this excludes charged dark matter for $10^3\,\mathrm{GeV} \lesssim m/q \lesssim 10^{11}\,\mathrm{GeV}$, even if the charged dark matter abundance is only a small part of the total relic abundance.

Keywords: dark matter theory, Magnetohydrodynamics, cosmic ray theory

ArXiv ePrint: 2006.10479

https://doi.org/10.1088/1475-7516/2020/10/001

JCAP10(2020)001

Contents

JCAP10(2020)001

1 Introduction

There is overwhelming evidence for the presence of a non-baryonic component in the matter budget of the Universe through its gravitational effects. If this component consists of particles having only gravitational interactions, there would be little hope for their detection. Therefore it is commonly assumed that they participate in part of the gauge interactions of the standard model (SM). In order to keep the particles dark and collisionless, typically the weak interaction is chosen as coupling to the SM particles. However, no new weakly interacting particles have been detected yet, despite of intense searches. As a consequence, the interest in alternatives has been growing. One option is the case of millicharged dark matter (DM), where the DM particle has a small, but non-zero electric charge $qe \ll e$, thereby providing a coupling via the photon to the SM particles [1]. The smallness of q could be explained, e.g., by the kinetic mixing of the dark photon of an extra U(1) symmetry with the SM photon [2–6]. Alternatively, DM with charges of order one could form heavy bound states [7].

The case of millicharged DM has obtained increased attention lately following the reported discrepancy between predictions for the 21 cm absorption line induced by early stars and observations by the EDGES collaboration [8]. It has been suggested that this anomaly is caused by the cooling of baryons at redshift $z \simeq 17$ in baryon-dark matter interactions with a massless mediator [9]. Dark matter with a tiny electric charge q would be a natural candidate for such a new cooling agent. Unfortunately, a scenario where the EDGES observations are explained by millicharged DM that explains all the observed DM abundance is inconsistent

with bounds from the cosmic microwave background [10]. Therefore, DM theories in which there is a sub-dominant charged component, such as theories including a completely hidden sector have attracted attention, see e.g. refs. [11–14] for recent examples and refs. [15, 16] for reviews.

Cosmological observations and direct detection experiments put strong constraints on the possible mass-to-charge ratios of DM [17, 18]. However, Chuzhoy and Kolb [19] claimed in 2009 that the direct detection constraints on charged DM are invalid in a wide range of m/q values: they argued that the regular[1] Galactic magnetic field (GMF) in the disk prevents charged DM particles with $m/q \lesssim 10^{11}$ GeV from entering the plane from the halo. Taking in turn into account the acceleration of charged DM particles in the disk by shock fronts of supernova remnants and the subsequent loss of energetic DM particles into the halo, they argued that charged DM with $10^5 q^2 \lesssim m/\mathrm{GeV} \lesssim 10^{11} q$ is expelled from the disk and evades thereby the bounds from terrestrial direct DM searches. This range was later reduced to $m/q \lesssim 10^9$ GeV in ref. [20] by taking into account the effect of the turbulent magnetic field and the non-homogeneity of the background field. The authors of ref. [21] argued that the injection of charged DM into diffusive shock acceleration is suppressed, implying that these particles are not effectively accelerated in shock fronts of supernova remnants. The most recent and complete study treating charged DM as diffusive cosmic rays has been preformed in ref. [22]. In this analysis, it was found that there is a substantial amount of charged DM present in the Galactic disk today, some of which have recently been accelerated. This was used to set strong constraints on the possible (m, q) parameters.

In this work, we consider a generic DM particle with mass m and charge qe. As any electrically charged particle, charged DM will scatter on the inhomogeneities of the turbulent GMF. These inhomogeneities are moving with typical velocities of tens of km/s with respect to the Galaxy, either because static turbulence is advected alongside the plasma or because the turbulence consists of travelling Alfvén waves. Both cases lead to second-order Fermi acceleration of charged particles including charged DM. The energy gained by the charged DM depletes in turn the magnetic wave spectrum around the resonance wave-vector $k_{\mathrm{res}} \sim 1/R_L$, where R_L is the Larmor radius of the charged DM particle. If this energy drain is larger than the power injected into the turbulent GMF at the injection wave-number k_{min}, the cascading of magnetic turbulence from k_{min} to larger wave-numbers is stopped at k_{res}. In this case, all fluctuations in the inertial range above k_{res} are missing. As a result, charged DM from the halo can enter the disk and the limits from direct DM searches can be applied. Together with the no-observation of a drop in the diffusion coefficient, this excludes charged DM for a wide range of masses and charges.

2 Alfvén waves and diffusion

2.1 Diffusion equations

The propagation of charged particles through the magnetized interstellar medium (ISM) filling the Milky Way can be described phenomenologically as a combination of diffusion and advection using a Fokker-Planck equation [23, 24]: the scattering of charged particles on the inhomogeneities of the turbulent GMF leads to diffusion terms in the evolution equation for

[1]Note that Liouville's theorem implies that the intensity of charged DM is constant along a trajectory in the magnetic field. Thus a shielding effect analogue to the geomagnetic cutoff would require, e.g., a dipole component of the GMF.

JCAP10(2020)001

the phase space density $f(\boldsymbol{x}, \boldsymbol{p})$ of the charged DM particle,

$$\frac{\partial f}{\partial t} = Q + \boldsymbol{\nabla}(D(p)\boldsymbol{\nabla} f) + \frac{1}{4\pi p^2}\frac{\partial}{\partial p}\left(4\pi p^2 D_{pp}(p)\frac{\partial f}{\partial p}\right) + \dots . \tag{2.1}$$

Here, D and D_{pp} parametrise diffusion in position and momentum space, respectively, while Q is a source term and $p = |\boldsymbol{p}|$ the momentum of the charged DM particle. Moreover, we assumed for simplicity that the diffusion is isotropic, i.e. we replaced the diffusion tensor $D_{ij}(\boldsymbol{p})$ by the scalar diffusion coefficient $D(p)$. Additionally, charged particles are advected with the plasma.

Alfvén waves are solutions of the MHD equations which propagate approximately parallel to the magnetic field lines with the Alfvén velocity[2] $v_A = B_0/\sqrt{4\pi\rho} \simeq 30\,\mathrm{km/s}$, where ρ is the density of the plasma and B_0 the strength of the magnetic background field. Charged particles are dynamically coupled to the ISM via the self-generation of, and the scattering on, Alfvén waves. Thus, the usual "test-particle" approach, where charged particles propagate in a prescribed static background (or given diffusion coefficients D and D_{pp} in the diffusion picture) is in general not valid. Instead, one must check if their back-reaction on the turbulent magnetic field at scales comparable to their Larmor radius is negligible.

The rate at which energy is transferred between Alfvén waves and charged particles is given by[3]

$$\Gamma_{\mathrm{growth}} = \frac{16\pi^2}{3}\frac{p^4 v_A}{k W_k(t) B_0^2}\left(v\hat{\boldsymbol{n}}\cdot\boldsymbol{\nabla} f - \frac{\pi}{2} m\Omega_0 v_A k W_k(t)\frac{\partial f}{\partial p}\right), \tag{2.2}$$

where $\Omega = qeB_0/m$ is the cyclotron frequency of a particle with mass m and charge qe, v its velocity, and W_k denotes the spectral density of turbulent field modes with wave-vector $\boldsymbol{k}$ [25]. This interaction proceeds resonantly, such that k equals $k_{\mathrm{res}} \simeq \Omega/v\mu$ with $\mu = \cos\vartheta$ as the cosine of the pitch angle [26]. We normalise the spectral density of turbulent field modes W_k such that $\eta_B \equiv \delta B^2/B_0^2 = \int \mathrm{d}k\, W(k)$, where η_B denotes the ratio of the energy density in the turbulent and the regular magnetic field. Sources of this turbulence are the mechanical "stirring" of the plasma and the generation of Alfvén waves by charged particles. In the former case, stellar winds, supernova shocks and the differential rotation of the Milky Way inject energy into the ISM on scales of tens of parsecs, which then cascades down to smaller scales through the formation of smaller and smaller eddies. This energy cascade in the inertial range can be modelled as a diffusion process in k space [27],

$$\frac{\partial W_k(t)}{\partial t} = \frac{\partial}{\partial k}\left(D_{kk}\frac{\partial W_k(t)}{\partial k}\right) - \Gamma_{\mathrm{growth}}(k,t)W_k(t) + q_W, \tag{2.3}$$

with the diffusion coefficient [28]

$$D_{kk} = C_K v_A k^{\alpha_1} W_k(t)^{\alpha_2} \tag{2.4}$$

and $C_K \simeq 0.052$ [29]. The injection occurs via the source term $q_W \propto \delta(k - 2\pi/L_{\mathrm{max}})$ at the outer scale $L_{\mathrm{max}} \simeq 100\,\mathrm{pc}$. The parameters α_i are chosen as $\alpha_1 = 7/2$ and $\alpha_2 = 1/2$ such that the power-law spectrum

$$W(k) = W_0\left(\frac{k}{k_{\mathrm{min}}}\right)^{-s}, \qquad s = \frac{\alpha_1 - 1}{\alpha_2 + 1}, \qquad W_0 = (s-1)L_{\mathrm{max}}\eta_B, \tag{2.5}$$

[2] We use Gaussian units and set $c = 1$.

[3] We assume that the forward and backward scattering rates are the same.

JCAP10(2020)001

obtained as steady-state solution for $\Gamma_{\rm ex} = 0$ is a Kolmogorov spectrum. The wave-number $k_{\rm min} = 2\pi/L_{\rm max}$ is determined by the injection scale $L_{\rm max}$ of the turbulence.

Equations (2.1) and (2.3) form a set of coupled differential equations that must be solved iteratively in order to compute the time evolution of both the phase-space density f of charged DM and the spectrum W_k of magnetic field fluctuations.

2.2 Resonance condition

Since the interaction (2.2) between charged particles and Alfvén waves proceeds resonantly, we have to check that the resonant wave-vector $k_{\rm res}$ of the charged DM particle is contained in the inertial range $[k_{\rm min} : k_{\rm max}]$ of the turbulent cascade. Here, $k_{\rm max} = 2\pi/L_{\rm min}$ is given by the dissipation scale where the turbulent energy is converted into heat. While observations show that fluctuations extend down at least to $10^9\,{\rm cm}$ [30, 31], it is theoretically expected that the dissipation scale corresponds to the proton or even electron Larmor radius [32, 33]. For concreteness, we will use in the following the proton Larmor radius as the dissipation scale.

The resonant wave-number for the momentum $p = \gamma m v$ is [26]

$$k_{\rm res} = \frac{\Omega m}{p}\frac{1}{\mu \pm v_A/v} \geq \frac{\Omega m}{p}\frac{1}{1 \pm v_A/v}. \tag{2.6}$$

We first check that the condition $k_{\rm res} < k_{\rm max}$ is satisfied. Using that the maximum wave-number is limited by the proton cyclotron frequency, $k_{\rm max} \simeq \Omega_{\rm p}/v_A$, the momentum that can resonate with Alfvén waves must satisfy

$$p \gtrsim m v_A \left(\frac{q m_{\rm p}}{m} \mp 1\right) \tag{2.7}$$

in the non-relativistic case, $p = \gamma m v \approx m v$. In the for us interesting limit $m/q \gg m_{\rm p}$, this reduces[4] to $p \gtrsim m v_A$. Since the virial velocity of the DM, $v_{\rm vir} \sim 300\,{\rm km/s}$, is much larger than the Alfvén velocity, the majority of the charged DM particles fulfills this condition.

Next we examine when the condition $k_{\rm res} > k_{\rm min}$ is satisfied. Setting for simplicity $\mu = 1$, it is $k_{\rm res} = \Omega/v = 1/R_L$ with $R_L = \gamma m v/qeB_0$ as the Larmor radius. Thus, requiring

$$R_L \simeq 1.08 \times 10^{-3}\,{\rm pc}\left(\frac{v_{\rm vir}}{300\,{\rm km/s}}\right)\left(\frac{B_0}{1\,\mu{\rm G}}\right)^{-1}\left(\frac{m/q}{10^6\,{\rm GeV}}\right) \lesssim L_{\rm max} \tag{2.8}$$

with $L_{\rm max} = 100\,{\rm pc}$ gives the constraint

$$m/q \lesssim 10^{11}\,{\rm GeV}. \tag{2.9}$$

2.3 Diffusion coefficients

The diffusion coefficients can be written as

$$D = \frac{1}{3}\frac{v^2}{\nu_+ + \nu_-} \qquad \text{and} \qquad D_{pp} = \frac{4}{3}\gamma^2 m^2 v^2 v_A^2 \frac{\nu_+ \nu_-}{\nu_+ + \nu_-}, \tag{2.10}$$

where $\nu_\pm = \Omega k W(k)/\gamma$ are the collision frequencies of the forward and backward propagating Alfvén waves at the resonance $k_{\rm res}$, and γ is the Lorentz facor of the charged particle [25].

[4]The choice of sign means that the charged DM can resonate only with one of the two polarisation states of the Alfvén waves.

JCAP10(2020)001

Assuming again that the forward and backwards rates are equal and inserting the expression (2.5) for the wave spectrum, the diffusion coefficients can be rewritten as

$$D = \frac{vL_{\max}}{3}[\eta_B(s-1)]^{-1}\left(\frac{R_L}{L_{\max}}\right)^{2-s} \quad \text{and} \quad D_{pp} = \frac{1}{3}\gamma^2 m^2 v_A^2 L_{\max}\eta_B(s-1)\left(\frac{R_L}{L_{\max}}\right)^{s-2}, \tag{2.11}$$

where $s = (\alpha_1 - 1)/(\alpha_2 + 1) = 5/3$. Choosing then $\eta_B L_{\max} \simeq 1\,\mathrm{pc}$, this framework is consistent with the commonly used parametrisation $D = D_0 v (p/m)^\delta$ with $\delta = 2 - s$ and

$$D_0 = 3\times 10^{28}\,\frac{\mathrm{cm}^2}{\mathrm{s}}\left[\left(\frac{m/q}{10^6\,\mathrm{GeV}}\right)\left(\frac{B}{1\,\mu\mathrm{G}}\right)^{-1}\right]^{2-s}. \tag{2.12}$$

3 Power taken by millicharged dark matter

The power density required for the reacceleration of cosmic rays is discussed in ref. [34]. There, it is found that $\simeq 10\%$ of the power in the cosmic ray proton spectrum comes from reacceleration and affects mainly the non- and mildly relativistic part of the cosmic ray spectrum. The same process must occur for charged DM, which means that its effect is potentially important. Following the procedure in ref. [34] and using the diffusion coefficients given in section 2.3, we obtain as the reacceleration power density

$$P_R \approx \frac{1}{9}(4-\delta)\frac{v_A^2}{D_0} m \int_0^\infty \mathrm{d}p\, 4\pi p^2 \left(\frac{p}{m}\right)^{1-\delta} f(p), \tag{3.1}$$

where $f(p)$ is the momentum distribution of the particles. For comparison, we will consider protons with $f(p) \propto (p/m)^{-\gamma}$,

$$P_R^{\mathrm{protons}} \simeq 0.56\,\mathrm{eV/cm}^3\,\frac{v_A^2}{D_{0,\mathrm{proton}}}. \tag{3.2}$$

We consider a standard Maxwellian phase space density for the momentum distribution of the charged DM particles,

$$f(p,z) = (2\pi\varepsilon^2)^{-3/2}\exp\left\{-\frac{p^2}{2\varepsilon^2}\right\} n(z), \tag{3.3}$$

with $\varepsilon = \gamma m v_{\mathrm{vir}}/\sqrt{2}$ and $n(z) = n_0 \simeq 0.3\,(\mathrm{GeV}/m)/\mathrm{cm}^3$ as the local charged DM density. Thus, we obtain

$$\frac{P_R}{P_R^{\mathrm{protons}}} = 4\times 10^6 \left(\frac{m}{10^6\,\mathrm{GeV}}\right)^{2/3} q^{1/3} \left(\frac{v\gamma}{300\,\mathrm{km/s}}\right)^{1/2} \left(\frac{B}{1\,\mu\mathrm{G}}\right)^{1/3}. \tag{3.4}$$

This means that the power density going into the reacceleration of charged DM is potentially large, exceeding formally the available power density injected into the turbulent ISM.

4 Key rates

From the estimate in the previous subsection, it is clear that the reacceleration of charged DM has the potential of seriously disturbing the ISM. In order to understand the potential consequences, we have to estimate the relevant time-scales of the problem, which will be discussed in this section. We will focus on the case where the entire relic density consists of charged DM, but we will comment on the case of a subdominant component in the next section. A summary of the results is shown in figure 1.

JCAP10(2020)001

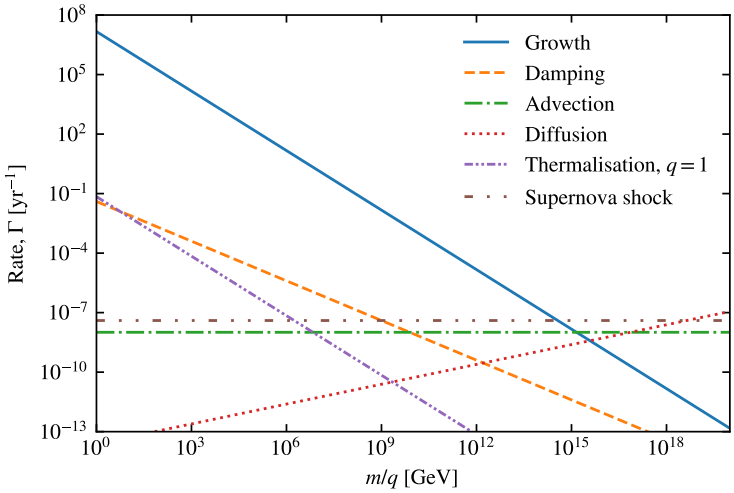

Figure 1. Various rates as a function of the charge-to-mass ratio of the charged DM.

4.1 Growth rate

In order to estimate the growth rate given in eq. (2.2), we consider a Maxwellian phase space distribution (3.3). That is, the momentum distribution becomes $4\pi p^2 f(p,z)$ so that the number of particles in the momentum range $(p, p+\mathrm{d}p)$ is $4\pi p^2 f(p,z)$.

With $\partial_z f \sim [n_0/H]\cdot[f/n(z)]$ and choosing $H \sim 3\,\mathrm{kpc}$ as the half-height of the confinement region, the growth rate induced by the spatial gradient is

$$\Gamma^{z}_{\mathrm{growth}} = \frac{2.4}{\mathrm{yr}}\left(\frac{m/q}{10^6\,\mathrm{GeV}}\right)^{-2/3}\left(\frac{v}{300\,\mathrm{km/s}}\right)^{4/3}\gamma^{1/3}\exp\left\{-\frac{p^2}{p_{\mathrm{vir}}^2}\right\} \left(\frac{B_0}{1\,\mu\mathrm{G}}\right)^{-4/3}\left(\frac{v_A}{30\,\mathrm{km/s}}\right)\left(\frac{\eta_B}{0.05}\right)^{-1}\left(\frac{L_{\mathrm{max}}}{50\,\mathrm{pc}}\right)^{2/3}\left(\frac{H}{3\,\mathrm{kpc}}\right)^{-1}. \tag{4.1}$$

Likewise, using $n(z)\sim n_0$, the momentum gradient leads to the growth rate

$$\Gamma^{p}_{\mathrm{growth}} = \frac{40}{\mathrm{yr}}\left(\frac{m/q}{10^6\,\mathrm{GeV}}\right)^{-1}\frac{p}{p_{\mathrm{vir}}}\exp\left\{-\frac{p^2}{p_{\mathrm{vir}}^2}\right\}\left(\frac{B_0}{1\,\mu\mathrm{G}}\right)^{-4/3}\left(\frac{v_A}{30\,\mathrm{km/s}}\right)^{2}. \tag{4.2}$$

Since we in our picture start without any spatial gradient and the corresponding growth rate $\Gamma^{z}_{\mathrm{growth}}$ is small even assuming a large gradient, it can be neglected relative to $\Gamma^{p}_{\mathrm{growth}}$. It is apparent from figure 1 that the growth rate is dominant for $m/q \lesssim 10^{15}\,\mathrm{GeV}$, where it has been evaluated using $p = p_{\mathrm{vir}}$ and the numerical values of the astrophysical parameters given in eqs. (4.1) and (4.2).

4.2 Damping, diffusion and advection rates

The relevant rates in the diffusion equations describing the propagation of charged DM particles and their interaction with the wave spectrum are the damping rate $\Gamma_{\mathrm{damp}} \sim D_{kk}/k^2$,

JCAP10(2020)001

the advection rate $\Gamma_{\rm adv} \sim v_{\rm adv}/H$ and the diffusion rate $\Gamma_{\rm diff} \sim 2D/H^2$. Numerically, we can estimate these rates as

$$\Gamma_{\rm damp} = \frac{4\times10^{-6}}{\rm yr}\left(\frac{m/q}{10^6\,{\rm GeV}}\right)^{-2/3}\left(\frac{v}{300\,{\rm km/s}}\right)^{-2/3}\gamma^{-2/3} \times\left(\frac{B_0}{1\,\mu{\rm G}}\right)^{2/3}\left(\frac{L_{\rm max}}{50\,{\rm pc}}\right)^{-1/3}\left(\frac{\eta_B}{0.05}\right)^{1/2}\left(\frac{v_A}{30\,{\rm km/s}}\right), \tag{4.3}$$

$$\Gamma_{\rm diff} = \frac{2\times10^{-12}}{\rm yr}\left(\frac{m/q}{10^6\,{\rm GeV}}\right)^{1/3}\left(\frac{v}{300\,{\rm km/s}}\right)^{4/3}\gamma^{-2/3}\left(\frac{B_0}{1\,\mu{\rm G}}\right)^{-1/3}\left(\frac{H}{3\,{\rm kpc}}\right)^{-2}, \tag{4.4}$$

$$\Gamma_{\rm adv} = \frac{1\times10^{-8}}{\rm yr}\left(\frac{v_{\rm adv}}{30\,{\rm km/s}}\right)\left(\frac{H}{3\,{\rm kpc}}\right)^{-2}. \tag{4.5}$$

Since charged DM is non-relativistic, advection dominates over diffusion except for the largest m/q values considered in figure 1. However, all three rates are well below the growth rate in the range where the resonance condition is satisfied.

4.3 Thermalisation rate

The thermalisation time scale for a particle with charge $q_1 e$, mass m_1 and velocity v passing through a medium consisting of particles with charge $q_2 e$, mass m_2 and density n is given by

$$t_c = \frac{m_1 m_2 v^3}{8\pi q_1^2 q_2^2 e^4 n_e \ln\Lambda}, \tag{4.6}$$

where we use $\ln\Lambda \sim 20$ as Gaunt factor [35]. The thermalisation is dominated by the warm ionized medium which has fractional volume $f_{\rm WIM} = 0.15$, electron density $n_e = 0.2\,{\rm cm}^{-3}$ and temperature $8\times10^3\,{\rm K}$ [36]. Since the velocity of the charged DM, $v_{\rm vir} \sim 300\,{\rm km/s}$, is smaller than the electron velocity in the warm ionized medium, $v_e \sim 600\,{\rm km/s}$, the charged DM will thermalise at a rate

$$\Gamma_{\rm therm} = \frac{1}{t_c} \sim \frac{7\times10^{-8}}{\rm yr}\left(\frac{m/q^2}{10^6\,{\rm GeV}}\right)^{-1}\left(\frac{v_e}{600\,{\rm km/s}}\right)^{-3}\left(\frac{n_e}{0.2\,{\rm cm}^3}\right)\left(\frac{f_{\rm WIM}}{0.15}\right) \tag{4.7}$$

in the thin disk. As visible from figure 1, this rate is much smaller than the other relevant rates. In addition, thermalisation only occurs in the thin Galactic disk, but the charged DM spend most of its time outside this region. Thus, thermalisation can be neglected in the present work.

4.4 Supernova shock encounter rate

The effect of supernova remnants on charged DM was studied in ref. [22]. The expected rate at which charged DM particles in the Galactic disc will encounter supernova shocks is [22]

$$\Gamma_{\rm SH} = \frac{4\times10^{-8}}{\rm yr}\left(\frac{R_{\rm max}}{40\,{\rm pc}}\right)^3\left(\frac{R_{\rm disc}}{15\,{\rm kpc}}\right)^{-2}\left(\frac{H_{\rm disc}}{300\,{\rm pc}}\right)^{-1}\left(\frac{\Gamma_{\rm SN}}{0.03\,{\rm yr}^{-1}}\right), \tag{4.8}$$

This rate is much smaller than the growth rate for $m/q \lesssim 10^{15}\,{\rm GeV}$. Thus, the acceleration of charged DM by supernova shocks can be neglected.

JCAP10(2020)001

4.5 Injection rate of turbulence

The turbulence is injected at scales $L_{\rm max} \sim 50$–$100\,{\rm pc}$ through the source term $q_W \propto \delta(k - 2\pi/L_{\rm max})$. Without the presence of charged DM, a Kolmogorov spectrum will develop. Thus, the source term can be found as

$$q_W(k) = \frac{5\times10^{-11}}{\rm yr}\left(\frac{\eta_B}{0.05}\right)^{3/2}\left(\frac{v_A}{30\,{\rm km/s}}\right)\left(\frac{L_{\rm max}}{50\,{\rm pc}}\right)^{-1}\delta(k-2\pi/L_{\rm max}). \tag{4.9}$$

Meanwhile, the rate for the absorption of wave power by charged DM can be estimated as

$$\begin{aligned}\int_{k_{\rm min}}^{k_{\rm max}} {\rm d}k\,\Gamma_{\rm growth}W &\simeq -\int_{\gamma m v_A}^{\infty}{\rm d}p\,\frac{qeB_0}{p^2c}\Gamma_{\rm growth}W \\ &= \frac{2\times10^{-4}}{\rm yr}\left(\frac{m/q}{10^6\,{\rm GeV}}\right)^{-1}\left(\frac{v_{\rm vir}}{300\,{\rm km/s}}\right)^{2/3}\gamma^{2/3}\left(\frac{\eta_B}{0.05}\right)\left(\frac{L_{\rm max}}{50\,{\rm pc}}\right)^{-2/3}\left(\frac{v_A}{30\,{\rm km/s}}\right)^2.\end{aligned} \tag{4.10}$$

In the second step, we extended the integration region from the resonance up to infinity, which is admissible since the gradients of f are strongly peaked. Moreover, we used $mv_A/p_{\rm vir} \sim 0.1$ to obtain a numerical value of the resulting Gamma function. According to this simple estimate, the absorption rate of turbulence is larger than the injection rate for $m/q \lesssim 10^{12}\,{\rm GeV}$, i.e. in all the range where the resonance condition is satisfied.

5 Time evolution and observable consequences

5.1 Time evolution

In order to better understand the process of cascading and absorption of wave power, we solve the time-dependent diffusion equations (2.1) and (2.3) using the Crank-Nicholson scheme. As initial condition, we use the Maxwellian phase space distribution (3.3) with $n(z) = n_0$. From the discussions in the previous section, we know that the reacceleration is dominant, and we therefore neglect convective and spatial diffusive terms[5] in the diffusion equation (2.1). Likewise, the growth due to the spatial gradient in eq. (2.2) is subdominant and can be neglected.

For concreteness, we consider $m = 10^6\,{\rm GeV}$ and $q = 10^{-3}$ as an example. Moreover, we assume first that the charged DM abundance $\Omega_{\rm cDM}$ equals the total DM abundance $\Omega_{\rm DM}$, i.e. $f_{\rm cDM} = \Omega_{\rm cDM}/\Omega_{\rm DM} = 1$. In the first row of figure 2, we show how the wave power cascades to larger wave-numbers and how this affects the phase space density of the charged DM setting by hand the growth term $\Gamma_{\rm growth}$ in eq. (2.2) to zero: as the time increases, the turbulence injected around the scale $k_{\rm min}$ cascades to larger and larger wave-numbers, forming a Kolmogorov power-law spectrum, while the phase-space density of charged DM develops an increasing high-energy tail. Switching on the growth term, however, the turbulent cascade stops at $k \sim qeB_0/(p_{\rm vir} \times {\rm few})$, as shown in the second row. Note that in this case the momentum distribution of charged DM does not change drastically.

For a fully developed Kolmogorov spectrum we know from eqs. (4.9) and (4.10) that all wave power is absorbed by the charged DM for $f_{\rm cDM}^{-1} m/q \lesssim 10^{12}\,{\rm GeV}$. For $m = 10^6\,{\rm GeV}$ and $q = 10^{-3}$ this transition occurs at $f_{\rm cDM} \sim 5\times10^{-4}$. To visualise the effect of partial absorption, we show in the third row of figure 2 the solution with $f_{\rm cDM} = 10^{-5}$. The wave-spectrum $W(k)$ has now a drop at the resonance momentum, but recovers at larger k. This drop leads via eq. (2.10) to a corresponding jump in the diffusion coefficient $D(p)$.

[5] These terms can in principle be taken into account by introducing a "leaky-box" loss term f/T and source term $f_{\rm vir}/T$.

JCAP10(2020)001

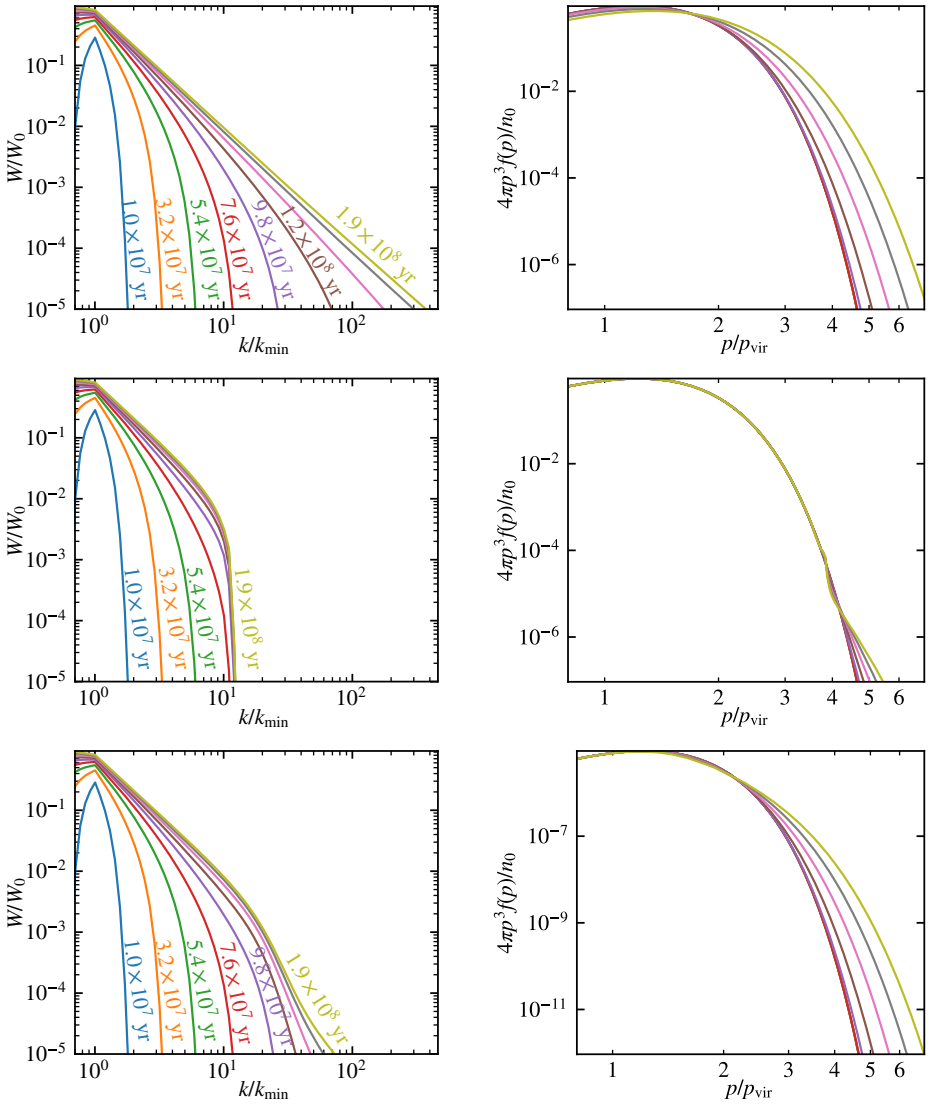

Figure 2. Time evolution of the wave power (left column) and the phase space density (right column). In the first row the growth rate is set to zero, while it is included in the second row. In the third row, the growth rate is included and $f_{\rm cDM} = 10^{-5}$.

5.2 Observable consequences

Turbulence injected at large scales $L_{\rm max} \sim 50$–$100\,{\rm pc}$ cascades to smaller wave lengths creating in the inertial range a power-law spectrum. In the presence of charged DM, however, the wave power will be absorbed when the cascade reaches $k_{\rm vir} \sim qeB_0/p_{\rm vir}$. Since the growth rate is for $f_{\rm cDM} = 1$ much larger than the damping rate, the entire wave energy will be absorbed

JCAP10(2020)001

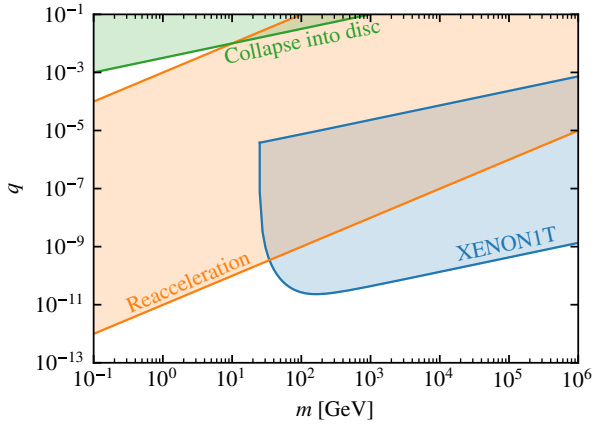

Figure 3. Exclusion plot of charged DM in the mass-charge plane for $f_{\rm cDM} = 1$. The orange area is excluded due to the unobserved drastic change in the diffusion coefficient expected due to reacceleration of charged DM. The Xenon 1T 90% exclusion (blue area) is obtained from ref. [38], and the exclusion due to possible collapse into the disc is obtained from ref. [22].

such that no waves can cascade above $\sim k_{\rm vir}$. Thus, for charged DM with $m/q \lesssim 10^{11}\,{\rm GeV}$ the cascading will stop at $k_{\rm vir}$. Thus no charged particles with momenta above $p_{\rm vir}$ be able to resonate with Alfvén waves. Effectively, this would lead to a sudden drop in the diffusion coefficient which is not observed in the cosmic ray spectra [37]. Similarly, cosmic rays with momenta above $p_{\rm vir}$ would not be isotropised by the GMF, in contradiction to the very low level of anisotropy observed [37]. Using the absence of anisotropies and a sudden drop in spectra observed above $\sim 0.1\,{\rm GeV}$, one can exclude $10^3\,{\rm GeV} \lesssim m/q \lesssim 10^{11}\,{\rm GeV}$. Additionally, charged DM is subject to upper limits set by terrestrial direct detection experiments, since in the absence of resonant Alfvén waves charged DM particles are exchanged freely between the Galactic disk and halo.

In figure 3, we show the upper limit in the (m,q) parameter space for $f_{\rm cDM} = 1$. The exclusion area for Xenon 1T is taken from ref. [38]. Furthermore, charged DM with $m/q^2 \lesssim 10^5\,{\rm GeV}$ would have collapsed into the disc and is thus excluded [22]. Additional constraints are discussed in, e.g., refs. [18, 22, 39].

Finally, we note that for $f_{\rm cDM} < 1$ most existing exclusion limits become weaker. In the case of reacceleration, however, we found that the exclusion is limited by the resonance condition and holds as long as $f_{\rm cDM}^{-1} m/q \lesssim 10^{12}\,{\rm GeV}$. Allowing for a partial transmission of wave-power to larger scales can further increase the excluded region in $f_{\rm cDM}$. For $f_{\rm cDM} \lesssim 10^{-6}$, the acceleration of charged DM will disturb its momentum distribution, and the methods to derive exclusion limits for charged cosmic rays worked out in ref. [22] might be applied.

6 Conclusions

In this work we have shown that the feedback due to second-order Fermi acceleration is an important effect that must be taken into account when analysing the propagation of charged dark matter. The growth rate turns out to be dominant at mass to charge ratios $m/q \lesssim 10^{15}\,{\rm GeV}$. As such, the absorption of Alfvén waves will stop the cascading of wave-power to smaller scales around the Larmor radius of the charged particles, $k_{\rm res} \sim 1/R_L$. This

JCAP10(2020)001

will in turn imply a significant and sudden change in the diffusion coefficient for ordinary cosmic rays at this scale. This unobserved consequence leads to the excluded region $10^3\,\mathrm{GeV} \lesssim m/q \lesssim 10^{11}\,\mathrm{GeV}$. Even more, this limit remains fixed as long as the charged dark matter abundance $f_X = \Omega_{\mathrm{cDM}}/\Omega_{\mathrm{DM}}$ satisfies $f_{\mathrm{cDM}}^{-1} m/q \lesssim 10^{12}\,\mathrm{GeV}$.

References

[1] A. Ignatiev, V.A. Kuzmin and M.E. Shaposhnikov, *Is the electric charge conserved?*, *Phys. Lett. B* **84** (1979) 315 [INSPIRE].

[2] L.B. Okun, M.B. Voloshin and V.I. Zakharov, *Electrical neutrality of atoms and grand unification models*, *Phys. Lett. B* **138** (1984) 115 [INSPIRE].

[3] H. Georgi, P.H. Ginsparg and S.L. Glashow, *Photon oscillations and the cosmic background radiation*, *Nature* **306** (1983) 765 [INSPIRE].

[4] B. Holdom, *Two U(1)'s and epsilon charge shifts*, *Phys. Lett. B* **166** (1986) 196 [INSPIRE].

[5] M.I. Dobroliubov and A. Ignatiev, *Millicharged particles*, *Phys. Rev. Lett.* **65** (1990) 679 [INSPIRE].

[6] P. Fayet, *Extra U(1)'s and new forces*, *Nucl. Phys. B* **347** (1990) 743 [INSPIRE].

[7] A. De Rujula, S.L. Glashow and U. Sarid, *Charged dark matter*, *Nucl. Phys. B* **333** (1990) 173 [INSPIRE].

[8] J.D. Bowman, A.E.E. Rogers, R.A. Monsalve, T.J. Mozdzen and N. Mahesh, *An absorption profile centred at 78 megahertz in the sky-averaged spectrum*, *Nature* **555** (2018) 67 [arXiv:1810.05912] [INSPIRE].

[9] R. Barkana, *Possible interaction between baryons and dark-matter particles revealed by the first stars*, *Nature* **555** (2018) 71 [arXiv:1803.06698] [INSPIRE].

[10] E.D. Kovetz, V. Poulin, V. Gluscevic, K.K. Boddy, R. Barkana and M. Kamionkowski, *Tighter limits on dark matter explanations of the anomalous EDGES 21 cm signal*, *Phys. Rev. D* **98** (2018) 103529 [arXiv:1807.11482] [INSPIRE].

[11] J.B. Muñoz and A. Loeb, *A small amount of mini-charged dark matter could cool the baryons in the early Universe*, *Nature* **557** (2018) 684 [arXiv:1802.10094] [INSPIRE].

[12] M.P. Hertzberg and M. Sandora, *Dark matter and naturalness*, *JHEP* **12** (2019) 037 [arXiv:1908.09841] [INSPIRE].

[13] H. Liu, N.J. Outmezguine, D. Redigolo and T. Volansky, *Reviving millicharged dark matter for 21-cm cosmology*, *Phys. Rev. D* **100** (2019) 123011 [arXiv:1908.06986] [INSPIRE].

[14] F. Kahlhoefer and E. Urdshals, *On dark atoms, massive dark photons and millicharged sub-components*, *Phys. Lett. B* **807** (2020) 135601 [arXiv:2001.04492] [INSPIRE].

[15] M. Fabbrichesi, E. Gabrielli and G. Lanfranchi, *The dark photon*, arXiv:2005.01515 [INSPIRE].

[16] A. Filippi and M. De Napoli, *Searching in the dark: the hunt for the dark photon*, *Rev. Phys.* **5** (2020) 100042 [arXiv:2006.04640] [INSPIRE].

[17] S. Davidson, B. Campbell and D.C. Bailey, *Limits on particles of small electric charge*, *Phys. Rev. D* **43** (1991) 2314 [INSPIRE].

[18] S.D. McDermott, H.-B. Yu and K.M. Zurek, *Turning off the lights: how dark is dark matter?*, *Phys. Rev. D* **83** (2011) 063509 [arXiv:1011.2907] [INSPIRE].

[19] L. Chuzhoy and E.W. Kolb, *Reopening the window on charged dark matter*, *JCAP* **07** (2009) 014 [arXiv:0809.0436] [INSPIRE].

JCAP10(2020)001

[20] F.J. Sanchez-Salcedo, E. Martinez-Gomez and J. Magana, *On the fraction of dark matter in charged massive particles (CHAMPs)*, *JCAP* **02** (2010) 031 [arXiv:1002.3145] [INSPIRE].

[21] J.-T. Li and T. Lin, *Dynamics of millicharged dark matter in supernova remnants*, *Phys. Rev. D* **101** (2020) 103034 [arXiv:2002.04625] [INSPIRE].

[22] D. Dunsky, L.J. Hall and K. Harigaya, *CHAMP cosmic rays*, *JCAP* **07** (2019) 015 [arXiv:1812.11116] [INSPIRE].

[23] V.L. Ginzburg and S.I. Syrovatskii, *The origin of cosmic rays*, New York, Gordon and Breach (1969).

[24] J. Skilling, *Cosmic ray streaming — I. Effect of Alfvén waves on particles.*, *Mon. Not. Roy. Astron. Soc.* **172** (1975) 557.

[25] J. Skilling, *Cosmic ray streaming — III. Self-consistent solutions.*, *Mon. Not. Roy. Astron. Soc.* **173** (1975) 255.

[26] D. Melrose, *The emission and absorption of waves by charged particles in magnetized plasmas*, *Astrophys. Space Sci.* **2** (1968) 171.

[27] J.A. Eilek, *Particle reacceleration in radio galaxies.*, *Astrophys. J.* **230** (1979) 373.

[28] Y. Zhou and W.H. Matthaeus, *Models of inertial range spectra of interplanetary magnetohydrodynamic turbulence*, *J. Geophys. Res.* **95** (1990) 14881.

[29] V.S. Ptuskin and V.N. Zirakashvili, *Limits on diffusive shock acceleration in supernova remnants in the presence of cosmic-ray streaming instability and wave dissipation*, *Astron. Astrophys.* **403** (2003) 1 [astro-ph/0302053] [INSPIRE].

[30] J.W. Armstrong, B.J. Rickett and S.R. Spangler, *Electron density power spectrum in the local interstellar medium*, *Astrophys. J.* **443** (1995) 209 [INSPIRE].

[31] A. Chepurnov and A. Lazarian, *Extending big power law in the sky with turbulence spectra from WHAM data*, *Astrophys. J.* **710** (2010) 853 [arXiv:0905.4413] [INSPIRE].

[32] F. Boulanger et al., *IMAGINE: a comprehensive view of the interstellar medium, Galactic magnetic fields and cosmic rays*, *JCAP* **08** (2018) 049 [arXiv:1805.02496] [INSPIRE].

[33] A.A. Schekochihin et al., *Kinetic and fluid turbulent cascades in magnetized weakly collisional astrophysical plasmas*, *Astrophys. J. Suppl.* **182** (2009) 310 [arXiv:0704.0044] [INSPIRE].

[34] A. Thornbury and L.O. Drury, *Power requirements for cosmic ray propagation models involving re-acceleration and a comment on second order Fermi acceleration theory*, *Mon. Not. Roy. Astron. Soc.* **442** (2014) 3010 [arXiv:1404.2104] [INSPIRE].

[35] M.S. Longair, *High energy astrophysics*, Cambridge University Press (2011).

[36] D.P. Cox, *The three-phase interstellar medium revisited*, *Ann. Rev. Astron. Astrophys.* **43** (2005) 337.

[37] M. Kachelriess and D.V. Semikoz, *Cosmic ray models*, *Prog. Part. Nucl. Phys.* **109** (2019) 103710 [arXiv:1904.08160] [INSPIRE].

[38] G. Bélanger, A. Mjallal and A. Pukhov, *Recasting direct detection limits within MicrOMEGAs and implication for non-standard Dark Matter scenarios*, arXiv:2003.08621 [INSPIRE].

[39] A. Caputo, L. Sberna, M. Frias, D. Blas, P. Pani, L. Shao et al., *Constraints on millicharged dark matter and axionlike particles from timing of radio waves*, *Phys. Rev. D* **100** (2019) 063515 [arXiv:1902.02695] [INSPIRE].

JCAP10(2020)001

Paper IV – On nuclear coalescence in small interacting systems

Kachelrieß, M., Ostapchenko, S. & Tjemsland, J. "On nuclear coalescence in small interacting systems". *Eur. Phys. J. A* **57,** 167. arXiv: 2012.04352 [hep-ph] (2021)

Abstract: The formation of light nuclei can be described as the coalescence of clusters of nucleons into nuclei. In the case of small interacting systems, such as dark matter and e^+e^- annihilations or pp collisions, the coalescence condition is often imposed only in momentum space and hence the size of the interaction region is neglected. On the other hand, in most coalescence models used for heavy ion collisions, the coalescence probability is controlled mainly by the size of the interaction region, while two-nucleon momentum correlations are either neglected or treated as collective flow. Recent experimental data from pp collisions at LHC have been interpreted as evidence for such collective behaviour, even in small interacting systems. We argue that these data are naturally explained in the framework of conventional QCD inspired event generators when both two-nucleon momentum correlations and the size of the hadronic emission volume are taken into account. To include both effects, we employ a per-event coalescence model based on the Wigner function representation of the produced nuclei states. This model reproduces well the source size for baryon emission and the coalescence factor B_2 measured recently by the ALICE collaboration in pp collisions.

After the introduction of the WiFunC model (Paper I), the ALICE collaboration published experimental results on the coalescence factor B_2 and its multiplicity dependence [*Eur.Phys.J.C* 80 (2020) 9, 889], as well as the transverse momentum dependence of the baryon emitting source [*Phys.Lett.B* 811 (2020) 135849], in pp collisions. We were therefore interested in comparing the predictions of the WiFunC model to the new experimental data. Importantly, we were able to show that the ansätze of the WiFunC model predict a similar size and m_T dependence of the baryon source as measured by ALICE. Since this prediction is independent of the coalescence mechanism and the event generator, it can be used to independently fix the parameter σ, so that the WiFunC model becomes parameter free.

Eur. Phys. J. A (2021) 57:167
https://doi.org/10.1140/epja/s10050-021-00469-w

THE EUROPEAN PHYSICAL JOURNAL A

Regular Article - Theoretical Physics

On nuclear coalescence in small interacting systems

M. Kachelrieß[1,a], **S. Ostapchenko**[2], **J. Tjemsland**[1]

[1] Institutt for fysikk, NTNU, Trondheim, Norway
[2] D.V. Skobeltsyn Institute of Nuclear Physics, Moscow State University, Moscow, Russia

Received: 15 December 2020 / Accepted: 17 April 2021 / Published online: 18 May 2021

Communicated by Che-Ming Ko

Abstract The formation of light nuclei can be described as the coalescence of clusters of nucleons into nuclei. In the case of small interacting systems, such as dark matter and e^+e^- annihilations or pp collisions, the coalescence condition is often imposed only in momentum space and hence the size of the interaction region is neglected. On the other hand, in most coalescence models used for heavy ion collisions, the coalescence probability is controlled mainly by the size of the interaction region, while two-nucleon momentum correlations are either neglected or treated as collective flow. Recent experimental data from pp collisions at LHC have been interpreted as evidence for such collective behaviour, even in small interacting systems. We argue that these data are naturally explained in the framework of conventional QCD inspired event generators when both two-nucleon momentum correlations and the size of the hadronic emission volume are taken into account. To include both effects, we employ a per-event coalescence model based on the Wigner function representation of the produced nuclei states. This model reproduces well the source size for baryon emission and the coalescence factor B_2 measured recently by the ALICE collaboration in pp collisions.

1 Introduction

The production mechanism for light clusters of nucleons, such as deuteron, helium-3, tritium and their antiparticles, in particle interactions has recently attracted increased attention from both the astroparticle and heavy ion communities. In heavy ion collisions, their small binding energies make these particles sensitive probes for two-nucleon correlations and density fluctuations, which may shed light on the QCD phase diagram [1]. These particles are also of particular interest in cosmic ray studies, because the expected low astrophysical backgrounds makes them ideal probes for exotic physics [2]. Furthermore, the sensitivities of the AMS-02 and GAPS experiments [3,4] are close to the expected fluxes of antideuterons from secondary production and, for optimistic parameters, from dark matter annihilations [5]. In order to correctly interpret the results of these experiments, a precise description of the production mechanism of light nuclei[1] is important.

In small interacting systems, such as dark matter and e^+e^- annihilations or pp collisions, the production of light nuclei is usually described by the coalescence model in momentum space [6–8], where nucleons originating from a particle collision merge to form a nucleus if their invariant momentum difference is smaller than the coalescence momentum p_0. Traditionally, the yield of a nucleus with mass number $A = Z + N$ and charge Z has been linked to the yields of protons p and neutrons n via the coalescence factor B_A as

$$E_A \frac{\mathrm{d}^3 N_A}{\mathrm{d}P_A^3} = B_A \left(E_p \frac{\mathrm{d}^3 N_p}{\mathrm{d}p_p^3} \right)^Z \left(E_n \frac{\mathrm{d}^3 N_n}{\mathrm{d}p_n^3} \right)^N . \tag{1}$$

Here, $P_A/A = p_n = p_p$ is the momentum of the nucleus and nucleons, respectively. In the limit of isotropic nucleon yields, the relation between B_A and p_0 is

$$B_A = A \left(\frac{4\pi}{3} \frac{p_0^3}{m_p} \right)^{A-1} . \tag{2}$$

This picture can be improved by taking into account two-particle correlations provided by Monte Carlo event generators for strong interactions, as proposed in Refs. [9,10]. Such two-particle correlations are especially important in small interacting systems, since there the nucleon yields deviate strongly from isotropy. This approach is commonly used to predict the antinucleus yield in cosmic ray interactions, as well as from dark matter decays or annihilations [11–22], for a recent review see Ref. [5]. In order to be predictive, B_A and

[a] e-mail: Michael.Kachelriess@ntnu.no (corresponding author)

[1] Most of the discussions in this work apply equally well to particles as to antiparticles, and the prefix "anti" will thus often be dropped.

p_0 must be independent of the centre-of-mass (c.m.) energy and the interaction process. However, the latter is not the case if the coalescence condition is only imposed in momentum space, since then the process dependent size of the formation region is neglected.

An alternative scheme where the coalescence condition is imposed in position space is often employed for heavy ion collisions [23,24]. Here, the coalescence factor scales with the volume of the emission region of hadrons as $B_A \propto V^{A-1}$. Much efforts have been spent on unifying these pictures using, e.g., Wigner functions [25] and imposing the coalescence condition in phase space, see Ref. [26] for a review of early works. Such models differ mainly in the way the Wigner function of the nucleons is determined: The phase-space distributions of nucleons used in the coalescence models may be obtained, e.g., from transport models like the AMPT scheme [27] or hybrid schemes combining a hydrodynamical with a microscopic hadron cascade model [28]. Alternatively, analytical coalescence formula like the COAL-SH scheme [29] or statistical models which relate the phase-space volume at kinetic freeze-out to the entropy per nucleon have been proposed [30]. Finally, Refs. [31,32] have studied the influence of preclustering of baryons due to nucleon interactions on the coalescence process.

A key observation in all approaches relying on the phase space picture is that the coalescence probability depends on the size of the hadronic emission region, which can be measured in femtoscopy (often also called Hanburry-Twiss-Brown) correlation experiments [25]. This connection has recently been applied to pp collisions, both in cosmic ray [33] and LHC studies [34,35]. In particular, it was argued in Ref. [35] that the success of the femtoscopy analysis is strong evidence that coalescence is the major production mechanism of light nuclei. Moreover, these authors suggested that the use of experimental data from femtoscopy correlation experiments allows one to reliably predict the yield of light antinuclei in cosmic ray interactions, thereby avoiding the need of additional theoretical inputs.

The approaches discussed above are all based on the coalescence picture, but differ on how the coalescence condition is implemented and how the two-nucleon states are determined. In a competing approach one employs statistical thermal models [36–42]. Here one assumes that both hadronisation and the formation of light nuclei occurs as a chemical freeze-out process in a radially expanding "fireball" of a Quark-Gluon Plasma (QGP). These models are motivated by the observation that the spectra of light nuclei are consistent with a thermal distribution, with the same freeze-out temperature as for mesons and nucleons [37]. Intriguingly, experimental data from collisions of small systems, such as pp and pPb, show features characteristic for collective flows, or even for the formation of a QGP, see Ref. [43] for a review. It has therefore been suggested that the thermal production of light nuclei can be applied even to small interacting systems [5,39,44,45]. However, it is difficult to reconcile how the nuclei with their small binding energies survive the chemical freeze-out. Even more, the energy spectrum of the nucleons is in the coalescence picture inherited by the nuclei (up to a quantum mechanical correction factor [23]), and the apparent quasi-thermal spectra of light nuclei can therefore be explained by coalescence as well.

In Refs. [46,47], we developed a coalescence model based on the Wigner function representation of the produced nuclei states, which includes two-nucleon momentum correlations obtained from QCD inspired event generators (we will use the abbreviation WiFunC, i.e. Wigner Functions with Correlations, for this model). In this work, we argue that neither two-particle correlations nor the source size can be neglected when describing the cluster formation in small interacting systems[2]. Furthermore, we will use this model to describe the production of hadrons and nuclei in high energy pp collisions and compare it to recent experimental data by the ALICE collaboration on the size of the baryon emitting source [48] and on the multiplicity and transverse momentum dependence of the coalescence factor B_2 [45,49,50]. Both data sets have been interpreted as evidence of collective flows, but we will show that the same characteristics are described using QCD inspired event generators, like QGSJET II [51,52] and Pythia 8.2 [53,54]. Finally, we comment on the suggestion that femtoscopy data alone are sufficient to predict the yield of light antinuclei for astrophysical applications.

This paper treats several different topics related to the formation of nuclei by the coalescence mechanism in small interacting systems, with a focus on recent experimental data, and is structured as follows. We review the WiFunC model in Sect. 2 and its relation to the femtoscopy framework in Sect. 3. In Sect. 4, we compare our predictions for the size of the baryon emitting source to recent measurements of the ALICE collaboration in a femtoscopy experiment. In Sect. 5, the multiplicity and transverse momentum dependencies of the coalescence factor B_2 in pp collisions at 13 TeV, measured by the ALICE collaboration, are compared to the WiFunC model. In Sect. 6 we make comments on the use of isotropic models in astrophysical applications.

2 The quantum mechanics of coalescence and the WiFunC model

The WiFunC model is based on the quantum mechanical description of the coalescence process reviewed in, e.g., Refs. [25,39]. Here we will highlight only the main steps.

[2] For concreteness, we will only discuss the production of deuterons, but the same considerations also hold for larger clusters of nucleons with small binding energies, such as helium-3 and tritium.

In this approach, the final state produced in a particle collision is described by a density matrix. Thus, one can find the deuteron spectrum in the sudden approximation by projecting the deuteron density matrix, $\rho_d = |\phi_d\rangle\langle\phi_d|$, onto the reduced density matrix $\rho_{\rm nucl} = |\psi_p\psi_n\rangle\langle\psi_p\psi_n|$ describing the coalescing nucleons,

$$\frac{\mathrm{d}^3N_d}{\mathrm{d}P_d^3} = \mathrm{tr}\{\rho_d\rho_{\rm nucl}\}. \tag{3}$$

By factoring out the c.m. motion of the deuteron, $\phi_d \propto \exp(i\boldsymbol{P}_d\cdot\boldsymbol{r}_d)\,\phi_d$, one can show that

$$\frac{\mathrm{d}^3N_d}{\mathrm{d}P_d^3} = \frac{3}{8}\int\frac{\mathrm{d}^3r_d\mathrm{d}^3r\mathrm{d}^3q}{(2\pi)^6}\mathcal{D}(\boldsymbol{r},\boldsymbol{q}) \times W_{np}(\boldsymbol{P}_d/2+\boldsymbol{q},\boldsymbol{P}_d/2-\boldsymbol{q},\boldsymbol{r}_n,\boldsymbol{r}_p), \tag{4}$$

where the statistical factor 3/8 arises from averaging over spin and isospin and $r \equiv r_n - r_p$. Here,

$$\mathcal{D}(\boldsymbol{r},\boldsymbol{q}) = \int \mathrm{d}^3\xi\,\mathrm{e}^{-i\boldsymbol{q}\cdot\boldsymbol{\xi}}\varphi_d(\boldsymbol{r}+\boldsymbol{\xi}/2)\varphi_d^*(\boldsymbol{r}-\boldsymbol{\xi}/2) \tag{5}$$

is the deuteron Wigner function, W_{np} is the Wigner function of the two-nucleon state, and φ_d is the internal deuteron wave function. If one approximates the deuteron wave function as a Gaussian, then $\mathcal{D}(r,q) = 8\exp\left(-r^2/d^2 - q^2d^2\right)$, with $d \simeq 3.2$ fm. However, apart from analytical estimates a more accurate wave function should be used, such as a two-Gaussian fit to the Hulthen wave function, chosen in Ref. [46].

To proceed, one has to specify the Wigner function W_{np} in Eq. (4). One possibility is to use simulations in order to determine the phase-space distribution of nucleons. Both the perturbative and non-perturbative evolution in Monte Carlo generators of strong interactions are based on momentum eigenstates and, hence, they provide only information on momentum correlations of nucleons. The addition of spatial information requires thus the transition to a semi-classical picture. Alternatively, one can neglect two-nucleon correlations and assume an isotropic source, as it is often done when describing heavy ion collisions. Finally, one can derive two-particle correlations from experimental data. This is the approach used in the femtoscopy framework that will be discussed in the next section.

The first case is used in the WiFunC model [46] which combines two-nucleon momentum correlations obtained from QCD inspired event generators, with a simple analytical model for the spatial distribution of nucleons. Assuming a factorisation of the momentum and position dependence in the Wigner function,

$$W_{np} = H_{np}(\boldsymbol{r}_n,\boldsymbol{r}_p)G_{np}(\boldsymbol{P}_d/2+\boldsymbol{q},\boldsymbol{P}_d/2-\boldsymbol{q}), \tag{6}$$

as well as neglecting spatial correlations, $H_{np}(\boldsymbol{r}_n,\boldsymbol{r}_p) = h(\boldsymbol{r}_n)h(\boldsymbol{r}_p)$, and choosing a Gaussian ansatz for the spatial distribution,

$$h(\boldsymbol{r}) = \left(2\pi\sigma^2\right)^{-3/2}\exp\left(-\frac{r^2}{2\sigma^2}\right), \tag{7}$$

Eq. (4) becomes

$$\frac{\mathrm{d}^3N_d}{\mathrm{d}P_d^3} = \frac{3\zeta}{(2\pi)^6}\int \mathrm{d}^3q\,\mathrm{e}^{-q^2d^2}G_{np}(\boldsymbol{P}_d/2+\boldsymbol{q},\boldsymbol{P}_d/2-\boldsymbol{q}). \tag{8}$$

The function ζ reflects the spatial distribution of the nucleons, and is thus clearly process dependent. It is in general given by

$$\zeta(\sigma_\parallel,\sigma_\perp,d) = \sqrt{\frac{d^2}{d^2+4\tilde{\sigma}_\perp^2}}\sqrt{\frac{d^2}{d^2+4\sigma_\perp^2}}\sqrt{\frac{d^2}{d^2+4\sigma_\parallel^2}}, \tag{9}$$

where $\tilde{\sigma}_\perp^2 = \sigma_\perp^2/(\cos^2\theta+\gamma^2\sin^2\theta)$. Here we distinguished between the longitudinal and transverse spreads $\sigma_{\parallel,\perp}$ of the emission volume. The transverse spread is modified when boosting from the c.m. frame of the original particle collision to the deuteron frame. Thus γ is the Lorentz factor of the produced deuteron in the collider frame, while θ is the angle between the deuteron momentum and the beam axis. Note that, in contrast to our earlier treatement in Refs. [46,47], we have included the Lorentz boost in only one of the two transverse components: If the xy cordinates are rotated such that $\boldsymbol{P}_d$ is contained in, e.g., the xz plane, then the σ_y component will not be affected by the Lorentz boost.

Nucleon momentum correlations are provided by the event generator, while the process dependence is incorporated in the spread σ. The spread will in general have a geometrical contribution due to a finite spatial extension of the colliding particles, and a contribution related to the perturbative cascade and hadronisation,

$$\sigma_{\parallel,\perp}^2 = \sigma_{\parallel,\perp(e^\pm)}^2 + \sigma_{\parallel,\perp(\rm geom)}^2. \tag{10}$$

The geometrical contributions can be approximated as

$$\sigma_{\perp(\rm geom)}^2 \simeq \frac{2R_1^2R_2^2}{R_1^2+R_2^2}, \qquad \sigma_{\parallel(geom)} \simeq \max\{R_1,R_2\}, \tag{11}$$

where R_1 and R_2 are the radii of the colliding particles, while the point-like contributions are given by $\sigma_{\parallel(e^\pm)} \simeq R_p \simeq 1$ fm and $\sigma_{\perp(e^\pm)} \simeq \Lambda_{\rm QCD}^{-1} \simeq 1$ fm. This simple picture is expected to give accurate results for pp interactions, while in the case of pA and AA collisions the geometrical contribution varies from event to event: While peripheral interactions which are dominated by binary collisions between a pair of projectile and target nucleons are characterised by $\sigma_{\parallel(\rm geom)} \simeq R_p$, the size may increase to $\sigma_{\parallel(\rm geom)} \simeq R_A$ for the most central

collisions. Consequently, the multiplicity of secondaries and the size of the source region are strongly correlated.

Neglecting for the moment this correlation, and approximating the radius of a nucleus by

$$R_A \simeq a_0 A^{1/3}, \tag{12}$$

with $a_0 \simeq 1.1$ fm, allows us to use only one free parameter,

$$\sigma \equiv \sigma_{(e^{\pm})} = a_0 = \sigma_{(pp)}/\sqrt{2} \simeq 1 \text{ fm}, \tag{13}$$

whose physical interpretation is the size of the emission region of nucleons.

Ideally, also the position integral in Eq. (4) should be evaluated event-by-event. It is therefore worth pointing out that some event generators like Pythia 8.2 have implemented semi-classical trajectories of the produced hadrons [55]. Thus, using Pythia one can instead directly evaluate

$$\frac{\mathrm{d}^3 N_d}{\mathrm{d}P_d^3} = 3 \int \frac{\mathrm{d}^3 r \mathrm{d}^3 q}{(2\pi)^6} \mathrm{e}^{-r^2/d^2 - q^2 d^2} W_{np}(\boldsymbol{p}_p, \boldsymbol{p}_n, \boldsymbol{r}_p, \boldsymbol{r}_n). \tag{14}$$

relying on the semi-classical description of the spatial correlations provided by the simulation. A simple model applying a hard cut-off in both momentum and position space has been considered using UrQMD in Ref. [56]. The approach of the WiFunC model could be carried over in straight-forward way to these models, replacing the hard cutoffs with Eq. (14).

Because of the generality of Eq. (8), the WiFunC model can in principle be used to describe the production of other nucleus-like systems with small binding energies if the approximate wave function of the produced system is known. One additional application of the WiFunC model could therefore be the production of exotic bound states such as the $X(3872)$ or the $Z_{cs}(3985)$, if they are deuteron-like bound states [57–62].

3 Relation to the femtoscopy framework

The emission volume probed in femtoscopy correlation experiments is directly linked to the distribution of nucleons, and can thus be used to check the validity of the WiFunC model. In a similar fashion, the emission volume can be related to the coalescence factor B_A, as was done in Refs. [25,34,35]. However, in order to derive their analytic relationship, the so-called smoothness approximation [63] was applied on top of the sudden approximation used in the previous section. In this approximation, the q dependence in the nucleon Wigner function is assumed to be negligible so that the q integral in Eq. (4) can be evaluated. As remarked in Ref. [35], this may be justified for heavy ion collisions where the size of the produced nuclear clusters can be neglected compared to the size of the emitting source. However, a more careful treatment is warranted for small interacting systems. To see this, we note that applying the sudden approximation to Eq. (8) implies that two-nucleon correlations are neglected, but these correlations should be kept for small interacting systems. The WiFunC model evades these problems because it evaluates the momentum integral using the momentum distributions supplied by an event generator.

Within the smoothness approximation, the deuteron spectrum (4) can be written as

$$\begin{aligned}\frac{\mathrm{d}^3 N_d}{\mathrm{d}P_d^3} =& \frac{3}{8} \int \frac{\mathrm{d}^3 r}{(2\pi)^3} |\varphi_d(\boldsymbol{r})|^2 \\ &\times \int \mathrm{d}^3 r_d W_{np}(\boldsymbol{P}_d/2, \boldsymbol{P}_d/2, \boldsymbol{r}_n, \boldsymbol{r}_p),\end{aligned} \tag{15}$$

while the nucleon spectra are given by[3]

$$\frac{\mathrm{d}^6 N}{\mathrm{d}p_p^3\, \mathrm{d}p_n^3} = \int \frac{\mathrm{d}^3 r}{(2\pi)^6} \int \mathrm{d}^3 r_d W_{np}(\boldsymbol{p}_p, \boldsymbol{p}_n, \boldsymbol{r}_p, \boldsymbol{r}_n). \tag{16}$$

Following the authors of Refs. [34,35], we assume for simplicity $E_d/(E_p E_n) = 2/m_N$ in the deutron rest frame. Then the coalescence factor (1) becomes

$$B_2(\boldsymbol{P}_d) \simeq \frac{3(2\pi)^3}{2m} \int \mathrm{d}^3 r |\varphi_d(\boldsymbol{r})|^2 \mathcal{S}_2(\boldsymbol{r}, \boldsymbol{P}_d), \tag{17}$$

with the source function defined as

$$\mathcal{S}_2(\boldsymbol{r}, \boldsymbol{P}_d) = \frac{\int \mathrm{d}^3 r_d W_{np}(\boldsymbol{P}_d/2, \boldsymbol{P}_d/2, \boldsymbol{r}_p, \boldsymbol{r}_n)}{\int \mathrm{d}^3 r_d \mathrm{d}^3 r W_{np}(\boldsymbol{P}_d/2, \boldsymbol{P}_d/2, \boldsymbol{r}_p, \boldsymbol{r}_n)}. \tag{18}$$

Measured particles will always be affected by final state interactions. This significantly affects two-particle correlation experiments: Even from initially uncorrelated particles one will measure a correlation

$$\mathcal{C}(\boldsymbol{q}) = \int \mathrm{d}^3 r S(\boldsymbol{r}) |\Psi(\boldsymbol{r}, \boldsymbol{q})|^2, \tag{19}$$

where $S(\boldsymbol{r})$ is the emission source function and the final state interactions are encoded in the wave function Ψ [63]. This is very similar to Eqs. (8) and (17): Coalescence is effectively a final state interaction that affects the two-nucleon correlations.

The authors of Refs. [34,35] used Eq. (17) to derive numerical estimates of the B_2 factor as a function of the source radius r measured in femtoscopy experiments. This approach looks very promising, since it allows one to express the coalescence factor only in terms of measurable quantities. Unfortunately, any numerical evaluation is additionally

[3] Notice that we have included here, in contrast to the coalescence factor (1), two-nucleon correlations. Since typically only the proton spectra will be available experimentally, it is common to assume factorised nucleon distributions. As the correlations are provided by Monte Carlo simulations and are included in the WiFunC model, we keep them in this expression.

based on three assumptions on the two-nucleon wave function: i) the spatial distribution has to be prescribed, ii) its characteristic size is assumed to be much larger than the one of the produced antinucleus states, such that the smoothness approximation can be used, iii) the two-nucleon momentum correlations are negligible. Yet, all these assumptions are generally not valid for collisions of small systems, as correctly noted already in Ref. [34]. Furthermore, the correlation function has to be inferred from experimental data, and is thus only available for the central rapidity region. The approximations required in the approach of Refs. [34,35] are avoided in the WiFunC model, since the used Monte Carlo generators provide two-nucleon momentum correlations which in turn leads to a non-trivial source function.

4 Size of baryon-emitting source

The source radius of the baryon emission in pp collisions at 13 TeV was recently measured by the ALICE collaboration, assuming a Gaussian source profile,

$$\mathcal{S}(|\boldsymbol{r}_p - \boldsymbol{r}_n|) \propto \exp - \left(\frac{(\boldsymbol{r}_p - \boldsymbol{r}_n)^2}{4r_0^2} \right), \tag{20}$$

using the femtoscopy framework, cf. with Eq. (19) of Ref. [48]. Here, the distance $\boldsymbol{r} = \boldsymbol{r}_p - \boldsymbol{r}_n$ between the two nucleons is defined in their pair rest frame. This study indicates that protons, antiprotons, Λ and $\bar{\Lambda}$ originate from the same source volume. Furthermore, a decrease in the source size with increasing transverse mass was observed. This decrease is often attributed to a collective flow, but is, as we will see next, also naturally described in the WiFunC model.

Inserting the Gaussian ansatz for the spatial distribution of nucleons (7) into the expression (18) for the source leads to

$$\mathcal{S}_2(r) \propto \int \mathrm{d}^2\Omega \exp - \left(\frac{r_z^2}{4\sigma_\parallel^2} - \frac{r_y^2}{4\sigma_\perp^2} - \frac{r_x^2}{4\sigma_\perp^2} \frac{m_T^2}{m^2} \right), \tag{21}$$

where we have taken into account that the Wigner functions and their spread, cf. with Eq. (9), are defined in the collider frame. Moreover, we chose the coordinate system such that $\hat{z}$ is directed along the initial beam direction and $\hat{y}$ is perpendicular to both $\hat{z}$ and P_d. Furthermore, we used the identity $m_T^2/m^2 = \gamma^2 \sin^2\theta + \cos^2\theta$, m_T being the transverse mass. Using the polar coordinates $r_x/r = \sin\varphi \sin\vartheta$ and $r_y/r = \cos\varphi \sin\vartheta$, we find

$$\mathcal{S}_2(r) \propto \mathrm{e}^{-r^2/4\sigma_\parallel^2} \times \mathcal{I}(r, m_T, \sigma_\parallel, \sigma_\perp), \tag{22}$$

with

$$\mathcal{I}(r, m_T, \sigma_\parallel, \sigma_\perp) = \int_0^{2\pi} \mathrm{d}\phi \int_0^{\pi} \mathrm{d}\vartheta \sin\vartheta \exp\left(-\frac{r^2 \sin^2\vartheta}{4\sigma_\parallel^2} \mathcal{F} \right) \tag{23}$$

and

$$\mathcal{F} = \cos^2\varphi \left(\frac{\sigma_\parallel^2}{\sigma_\perp^2} - 1 \right) + \sin^2\varphi \left(\frac{\sigma_\parallel^2}{\sigma_\perp^2} \frac{m_T^2}{m^2} - 1 \right). \tag{24}$$

Hence the WiFunC model predicts a non-trivial source function described by a Gaussian source modified by the function $\mathcal{I}(r, m_T, \sigma_\parallel, \sigma_\perp)$.

In order to compare the predicted source function to the measurement by the ALICE collaboration, Eq. (22) must be compared to the Gaussian source profile (20) to fix $r_0(m_T)$. In order to determine $r_0(m_T)$, we perform a least-squares fit using as uncertainty $\mu \propto 1/\sqrt{\mathcal{S}_2(r)}$ as the expected Gaussian error. Additionally, we consider also a simple analytical approximation: By comparing the Taylor expansion of Eqs. (20) and (22), one finds

$$r_0^2/\sigma_\parallel^2 = 3 \left[1 + \left(\frac{m_T^2}{m^2} + 1 \right) \frac{\sigma_\parallel^2}{\sigma_\perp^2} \right]^{-1} + \mathcal{O}(r^2/\sigma_\parallel^2). \tag{25}$$

In the analysis of the data on the source function in pp collisions at 13 TeV by ALICE only high multiplicity events (0–0.17% INEL $>$ 0) were included [48]. However, the WiFunC model says that there is no (or only a weak) multiplicity dependence of the emission volume in pp collisions. In Fig. 1, we compare the source size r_0 estimated for proton-proton pairs[4], using both the exact source function (22) (blue solid line) and the approximation (25) (orange dashed line). Additionally, we show the source size obtained in the limit $\sigma_\parallel \gg \sigma_\perp$ (green dashed-dotted line), which corresponds to the steepest slope $r_0(m_T)$ possible in our model. It is worth noticing that the data tend to give better fits for $\sigma_\parallel > \sigma_\perp$, as expected from their physical interpretations. Even so, we find not yet any need to fit them separately due to the relatively large experimental uncertainties.

From Fig. 1 one can infer $\sigma = (0.95 \pm 0.1)$ fm. Intriguingly, the WiFunC model thus describes the data well with values of σ similar to those obtained in Refs. [46,47] by a fit to antideuteron measurements. More importantly, we have shown that the decrease of the source size with increasing transverse momentum, which is often attributed to collective flows, is correctly described by the WiFunC model using QCD inspired MC generators.

[4] A similar analysis can be done for Λ by changing $m_p \to m_\Lambda$. In this case, a correspondingly larger σ is expected.

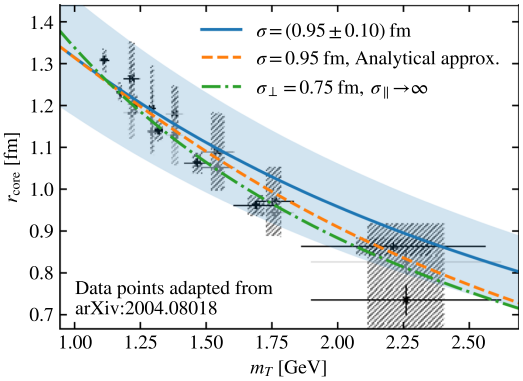

Fig. 1 The Gaussian emission size predicted by the WiFunC model is compared to experimental data. The blue solid line shows the prediction of the WiFunC model; the shaded area corresponds to the uncertainty $\Delta\sigma = 0.1$ fm. The simple analytical approximation in Eq. (25) is shown as a dashed orange line. Finally, the green dashed dotted line indicates the limit $\sigma_\parallel \gg \sigma_\perp$

5 Multiplicity dependence of coalescence in small interacting systems

In the previous section, we focused on how the emission region of nucleons is related to the source size measured in femtoscopy experiments. Now we consider the effect of two-particle correlations on the deuteron yield. To this end, we investigate how the coalescence factor B_2 of antideuterons measured at mid-rapidity ($|y| < 0.5$) in pp collisions at 13 TeV depends on multiplicity and transverse momentum[5].

The experimental results are reported for a specific event class (INEL > 0) and are divided into different multiplicity classes in terms of the percentage of the inclusive cross section, see Ref. [45] and references therein for their definition. We aim to reproduce the data, generating inelastic pp collisions at 13 TeV with QGSJET II and Pythia 8.2, while describing the coalescence by the WiFunC model with $\sigma = 0.9$ fm, using the two-Gaussian wave function for the deutron. We check the trigger condition and classify the multiplicity class on an event-by-event basis. For comparison, we consider the standard per-event coalescence model with a hard cutoff $p_0 \sim 0.2$ GeV. This serves as a benchmark on what effects are caused by particle correlations, and what by the source size in the WiFunC model.

The results are compared to the experimental data in Fig. 2. Both QGSJET II and Pythia 8 reproduce well the overall yield in the various multiplicity classes. Furthermore, the qualitative behaviour of an increasing transverse momentum

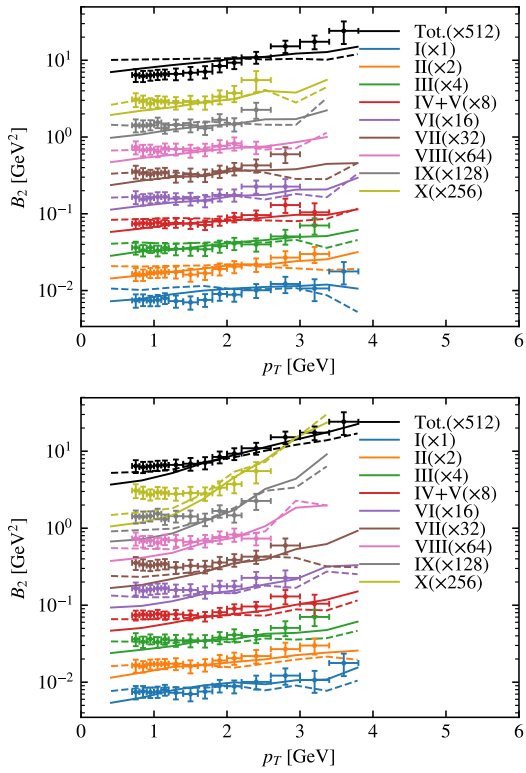

Fig. 2 The coalescence factor B_2 for different multiplicity classes, measured by the ALICE collaboration is compared to the predictions by QGSJET II (above) and Pythia 8.2 (below), using the WiFunC model (solid lines). The results for the standard coalescence model (dashed lines) are shown for comparison. Class I corresponds to largest multiplicities, while the multiplicity decreases with increasing class

p_T slope of B_2 with increasing multiplicity is also reproduced. This increase is often attributed to a collective flow, but our results indicate that it is also well described by the WiFunC model combined with QCD inspired event generators. While the overall behaviour and trends of the experimental data are reasonably well reproduced, deviations are expected as the event generators are not tuned to two-particle correlations. Comparing the results from the WiFunC model, shown as solid lines, to those of the standard coalescence model (dashed lines), one can notice that the multiplicity dependence of the slope of B_2 is stronger in the WiFunC model. Even so, there is also an increase in the slope of B_2 in the standard coalescence model, which is stronger in the case of Pythia. This indicates that two-particle correlations, although not the only effect responsible for the growing slope of B_2, are not negligible for pp collisions in the kinematical range considered.

[5] We constrain this discussion to the data obtained at 13 TeV because of their small experimental uncertainties, but the same qualitative features are seen also at 7 TeV [50].

In the WiFunC model, the multiplicity dependence emerges due to two-nucleon momentum correlations and the dependence of the emission region of nucleons on the event kinematics. In combination, these effects lead to the non-trivial multiplicity dependence visible in Fig. 2: For increasing multiplicity, the momentum phase space available for single nucleons will on average decrease, which implies an increased coalescence probability according to Eq. (8). The main multiplicity dependence of the emission region in pp collisions comes from the modification of the transverse spread by the Lorentz boost, as it can be seen from Eq. (9). In order to get a sense of this dependence, we plot in Fig. 3 the multiplicity dependence of the transverse spread using Pythia and QGSJET at 13 TeV. In both cases, $\sigma_\perp = 1$ fm is used. Both event generators lead qualitatively to the same multiplicity dependence: The average transverse momentum increases with increasing number of produced particles, leading to a decrease in the transverse spread. Such an increase of the average p_T with multiplicity has been observed by all experiments at LHC, being reasonably reproduced by Pythia (see, e.g., Ref. [64]) and leading to a gradual decrease of $\tilde{\sigma}_\perp$ up to the rather high values of $\mathrm{d}N_{\mathrm{ch}}/\mathrm{d}\eta$. On the other hand, this effect is not properly described by QGSJET-II, in which case the decrease of $\tilde{\sigma}_\perp$ is saturated already for relatively small values of $\mathrm{d}N_{\mathrm{ch}}/\mathrm{d}\eta$.

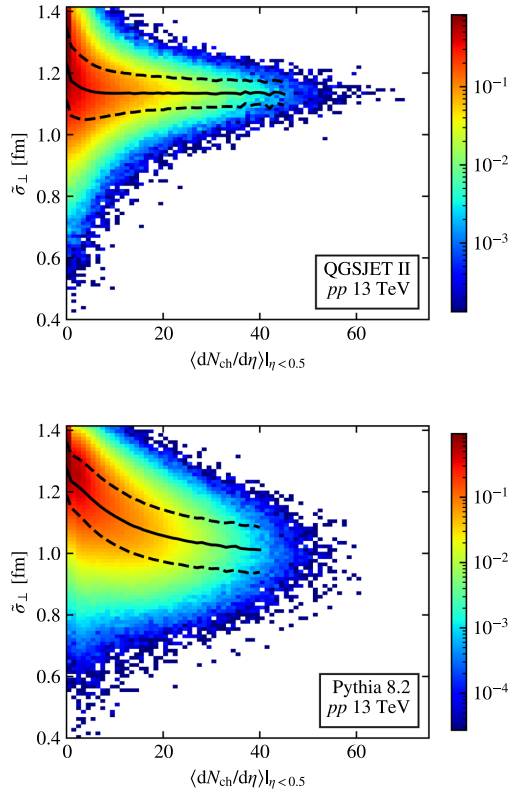

Fig. 3 Spread of $\tilde{\sigma}_\perp$ as a function of the number of charged particles in the central pseudo-rapidity region, for QGSJET II (above) and Pythia 8.2 (below). The mean value of $\tilde{\sigma}_\perp$ at each N_{ch} and its standard deviation are shown in solid and dashed lines, respectively; the colour code shows the probability density of events with a given $\tilde{\sigma}_\perp$ and $\mathrm{d}N_{\mathrm{ch}}/\mathrm{d}\eta$ ($\eta < 0.5$)

6 Astrophysical applications

Thus far, we have considered only particles at central (pseudo-) rapidity, which are accessible experimentally. The bulk of produced particles will, however, in general have large longitudinal momenta. In high energy collisions at the LHC, the use of a constant B_2 as function of p_z is a good approximation. Therefore, one may naively expect this assumption to be a good approximation for astrophysical processes as well. This is, as we will discuss in this section, however not the case. Even so, an isotropic model with constant $B_A(p_z)$ is still regularly applied in the literature to antinuclei production in proton-proton collisions [33,65,66].

Cosmic ray antideuterons are expected to originate in secondary production, i.e. in collisions between primary cosmic rays and the interstellar matter. The main contribution comes from protons with energies $E_{\mathrm{prim}} \sim 20$–$100$ GeV colliding with protons in the interstellar matter, while the bulk of the produced antideuterons has kinetic energies per nucleon in the range $T \sim 2$–20 GeV/n [47]. In order to check the validity of a constant $B_2(p_z)$ for astrophysical applications, we therefore plot the coalescence parameter $B_2(p_z)$ obtained using QGSJET II for primary energies[6] $E_{\mathrm{prim}} = 50$ and 100 GeV in Fig. 4 as function of the momentum p_z in the lab frame. The range of B_2 determined using the femtoscopy framework in Ref. [33] is shown as a violet band. For comparison, we also show the coalescence factors B_2 obtained for $\sqrt{s} = 50$ GeV and 13 TeV. In the case of collider energies, the values obtained agree well with the value inferred by femtoscopy experiments in Ref. [33]. At energies most relevant for astrophysical processes, however, the femtoscopy data at the LHC overestimate the coalescence parameter. More importantly, the coalescence parameter depends strongly on the longitudinal momentum at these energies[7]. In order to obtain the correct energy spectra of the produced antinuclei in astrophysical processes, a careful treatment taking into account two-particle correlations is therefore required.

[6] Notice that we consider p_z, E_{prim} and T in the rest frame of the target.

[7] The decrease of B_2 with p_z arises mostly from a reduction of the kinematic space available for a production of an antinucleon pair. In particular, $B_2 \to 0$ when p_z approaches $E_{\mathrm{prim}}/2$.

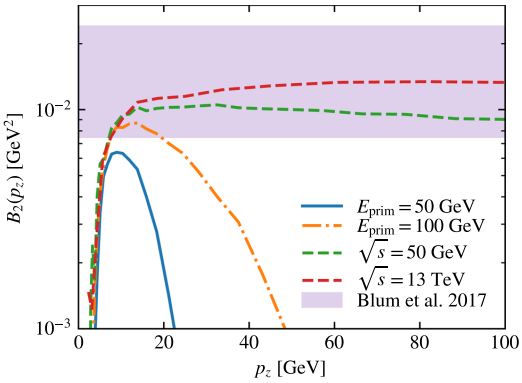

Fig. 4 The coalescence factor for $\bar{d}$ production, as a function of longitudinal momentum in the lab frame in pp collisions for various energies relevant for astrophysical processes and collider energies

7 Conclusions

The WiFunC model is a per-event coalescence model based on the Wigner function representation of the produced nuclei states, which allows one to account for both two-nucleon momentum correlations and the size of the hadronic emission volume. We have shown that this model reproduces well the source size for baryon emission and the coalescence factor B_2 measured recently by the ALICE collaboration in pp collisions. While these measurements have characteristics that are often attributed to the collective flow of the Quark-Gluon Plasma, our results show that the same properties are well reproduced describing the underlying physical processes by conventional QCD inspired event generators as QGSJET or Pythia. Finally, we have demonstrated that the coalescence parameter depends strongly on the longitudinal momentum for the energy range most relevant for astrophysical processes. Therefore, the use of a constant B_A value in astrophysical applications should be abandoned.

Acknowledgements We are grateful to David Dobrigkeit Chinellato for supplying us with the data from Ref. [45] before its official publication. We thank Bruce Yabsley for pointing out the possible application of the WiFunC model to exotic bound-states like the $X(3872)$.

Funding Open access funding provided by NTNU Norwegian University of Science and Technology (incl St. Olavs Hospital - Trondheim University Hospital).

Data Availability Statement This manuscript has no associated data or the data will not be deposited. [Authors' comment: This paper is of theoretical character and the data are contained in this article.]

References

1. H. Caines, Nucl. Phys. A **967**, 121 (2017). https://doi.org/10.1016/j.nuclphysa.2017.05.116
2. F. Donato, N. Fornengo, P. Salati, Phys. Rev. D **62**, 043003 (2000). https://doi.org/10.1103/PhysRevD.62.043003
3. R. Battiston, Nucl. Instrum. Meth. **588**(1), 227 (2008). https://doi.org/10.1016/j.nima.2008.01.044 **(Proceedings of the First International Conference on Astroparticle Physics)**
4. T. Aramaki, C.J. Hailey, S.E. Boggs, P. von Doetinchem, H. Fuke, S.I. Mognet, R.A. Ong, K. Perez, J. Zweerink, Astropart. Phys. **74**, 6 (2016). https://doi.org/10.1016/j.astropartphys.2015.09.001
5. P. von Doetinchem et al., JCAP **08**, 035 (2020). https://doi.org/10.1088/1475-7516/2020/08/035
6. A. Schwarzschild, C. Zupancic, Phys. Rev. **129**, 854 (1963). https://doi.org/10.1103/PhysRev.129.854
7. S.T. Butler, C.A. Pearson, Phys. Rev. **129**(2), 836 (1963). https://doi.org/10.1103/PhysRev.129.836
8. P. Chardonnet, J. Orloff, P. Salati, Phys. Lett. B **409**, 313 (1997). https://doi.org/10.1016/S0370-2693(97)00870-8
9. L.A. Dal, Antideuterons as signature for dark matter. Master's thesis, NTNU Trondheim, http://hdl.handle.net/11250/246403 (2011)
10. M. Kadastik, M. Raidal, A. Strumia, Phys. Lett. B **683**, 248 (2010). https://doi.org/10.1016/j.physletb.2009.12.005
11. Y. Cui, J.D. Mason, L. Randall, JHEP **11**, 017 (2010). https://doi.org/10.1007/JHEP11(2010)017
12. A. Ibarra, S. Wild, JCAP **1302**, 021 (2013). https://doi.org/10.1088/1475-7516/2013/02/021
13. N. Fornengo, L. Maccione, A. Vittino, JCAP **1309**, 031 (2013). https://doi.org/10.1088/1475-7516/2013/09/031
14. L.A. Dal, A.R. Raklev, Phys. Rev. D **89**(10), 103504 (2014). https://doi.org/10.1103/PhysRevD.89.103504
15. T. Delahaye, M. Grefe, JCAP **1507**, 012 (2015). https://doi.org/10.1088/1475-7516/2015/07/012
16. J. Herms, A. Ibarra, A. Vittino, S. Wild, JCAP **02**, 018 (2017). https://doi.org/10.1088/1475-7516/2017/02/018
17. A. Coogan, S. Profumo, Phys. Rev. D **96**(8), 083020 (2017). https://doi.org/10.1103/PhysRevD.96.083020
18. S.J. Lin, X.J. Bi, P.F. Yin, (2018). arXiv:1801.00997 [astro-ph.HE]
19. E. Carlson, A. Coogan, T. Linden, S. Profumo, A. Ibarra, S. Wild, Phys. Rev. D **89**(7), 076005 (2014). https://doi.org/10.1103/PhysRevD.89.076005
20. M. Cirelli, N. Fornengo, M. Taoso, A. Vittino, JHEP **08**, 009 (2014). https://doi.org/10.1007/JHEP08(2014)009
21. A. Shukla, A. Datta, P. von Doetinchem, D.M. Gomez-Coral, C. Kanitz, Phys. Rev. D **102**(6), 063004 (2020). https://doi.org/10.1103/PhysRevD.102.063004
22. Y.C. Ding, N. Li, C.C. Wei, Y.L. Wu, Y.F. Zhou, JCAP **1906**(06), 004 (2019). https://doi.org/10.1088/1475-7516/2019/06/004
23. L. Csernai, J.I. Kapusta, Phys. Rep. **131**, 223 (1986). https://doi.org/10.1016/0370-1573(86)90031-1
24. J. Nagle, B. Kumar, D. Kusnezov, H. Sorge, R. Mattiello, Phys. Rev. C **53**, 367 (1996). https://doi.org/10.1103/PhysRevC.53.367
25. R. Scheibl, U.W. Heinz, Phys. Rev. C **59**, 1585 (1999). https://doi.org/10.1103/PhysRevC.59.1585

26. P. Danielewicz, G. Bertsch, Nucl. Phys. A **533**, 712 (1991). https://doi.org/10.1016/0375-9474(91)90541-D
27. K.J. Sun, C.M. Ko, (2020). arXiv:2005.00182 [nucl-th]
28. W. Zhao, C. Shen, C.M. Ko, Q. Liu, H. Song, Phys. Rev. C **102**(4), 044912 (2020). https://doi.org/10.1103/PhysRevC.102.044912
29. K.J. Sun, L.W. Chen, C.M. Ko, Z. Xu, Phys. Lett. B **774**, 103 (2017). https://doi.org/10.1016/j.physletb.2017.09.056
30. K.J. Sun, L.W. Chen, C.M. Ko, J. Pu, Z. Xu, Phys. Lett. B **781**, 499 (2018). https://doi.org/10.1016/j.physletb.2018.04.035
31. E. Shuryak, J.M. Torres-Rincon, Phys. Rev. C **100**(2), 024903 (2019). https://doi.org/10.1103/PhysRevC.100.024903
32. E. Shuryak, J.M. Torres-Rincon, Phys. Rev. C **101**(3), 034914 (2020). https://doi.org/10.1103/PhysRevC.101.034914
33. K. Blum, K.C.Y. Ng, R. Sato, M. Takimoto, Phys. Rev. D **96**(10), 103021 (2017). https://doi.org/10.1103/PhysRevD.96.103021
34. K. Blum, M. Takimoto, Phys. Rev. C **99**(4), 044913 (2019). https://doi.org/10.1103/PhysRevC.99.044913
35. F. Bellini, K. Blum, A.P. Kalweit, M. Puccio, Phys. Rev. C **103**(1), 014907 (2021). https://doi.org/10.1103/PhysRevC.103.014907
36. S. Acharya et al., Nucl. Phys. A **971**, 1 (2018). https://doi.org/10.1016/j.nuclphysa.2017.12.004
37. A. Andronic, P. Braun-Munzinger, K. Redlich, J. Stachel, Nature **561**(7723), 321 (2018). https://doi.org/10.1038/s41586-018-0491-6
38. V. Vovchenko, B. Dönigus, H. Stoecker, Phys. Lett. B **785**, 171 (2018). https://doi.org/10.1016/j.physletb.2018.08.041
39. F. Bellini, A.P. Kalweit, Phys. Rev. C **99**(5), 054905 (2019). https://doi.org/10.1103/PhysRevC.99.054905
40. J. Chen, D. Keane, Y.G. Ma, A. Tang, Z. Xu, Phys. Rep. **760**, 1 (2018). https://doi.org/10.1016/j.physrep.2018.07.002
41. X. Xu, R. Rapp, Eur. Phys. J. A **55**(5), 68 (2019). https://doi.org/10.1140/epja/i2019-12757-7
42. D. Oliinychenko, L.G. Pang, H. Elfner, V. Koch, Phys. Rev. C **99**(4), 044907 (2019). https://doi.org/10.1103/PhysRevC.99.044907
43. J.L. Nagle, W.A. Zajc, Ann. Rev. Nucl. Part. Sci. **68**, 211 (2018). https://doi.org/10.1146/annurev-nucl-101916-123209
44. J. Cleymans, S. Kabana, I. Kraus, H. Oeschler, K. Redlich, N. Sharma, Phys. Rev. C **84**, 054916 (2011). https://doi.org/10.1103/PhysRevC.84.054916
45. S. Acharya et al., Eur. Phys. J. C **80**(9), 889 (2020). https://doi.org/10.1140/epjc/s10052-020-8256-4
46. M. Kachelrieß, S. Ostapchenko, J. Tjemsland, Eur. Phys. J. A **56**(1), 4 (2020). https://doi.org/10.1140/epja/s10050-019-00007-9
47. M. Kachelrieß, S. Ostapchenko, J. Tjemsland, JCAP **08**, 048 (2020). https://doi.org/10.1088/1475-7516/2020/08/048
48. S. Acharya et al., Phys. Lett. B **811**, 135849 (2020). https://doi.org/10.1016/j.physletb.2020.135849
49. S. Acharya et al., Phys. Rev. C **97**(2), 024615 (2018). https://doi.org/10.1103/PhysRevC.97.024615
50. S. Acharya et al., Phys. Lett. B **794**, 50 (2019). https://doi.org/10.1016/j.physletb.2019.05.028
51. S. Ostapchenko, Phys. Rev. D **83**, 014018 (2011). https://doi.org/10.1103/PhysRevD.83.014018
52. S. Ostapchenko, EPJ Web Conf. **52**, 02001 (2013). https://doi.org/10.1051/epjconf/20125202001
53. T. Sjöstrand, S. Mrenna, P.Z. Skands, JHEP **05**, 026 (2006). https://doi.org/10.1088/1126-6708/2006/05/026
54. T. Sjöstrand, S. Ask, J.R. Christiansen, R. Corke, N. Desai, P. Ilten, S. Mrenna, S. Prestel, C.O. Rasmussen, P.Z. Skands, Comput. Phys. Commun. **191**, 159 (2015). https://doi.org/10.1016/j.cpc.2015.01.024
55. S. Ferreres-Solé, T. Sjöstrand, Eur. Phys. J. C **78**(11), 983 (2018). https://doi.org/10.1140/epjc/s10052-018-6459-8
56. S. Sombun, K. Tomuang, A. Limphirat, P. Hillmann, C. Herold, J. Steinheimer, Y. Yan, M. Bleicher, Phys. Rev. C **99**(1), 014901 (2019). https://doi.org/10.1103/PhysRevC.99.014901
57. A. Esposito, A.L. Guerrieri, F. Piccinini, A. Pilloni, A.D. Polosa, Int. J. Mod. Phys. A **30**, 1530002 (2015). https://doi.org/10.1142/S0217751X15300021
58. F.K. Guo, C. Hanhart, U.G. Meißner, Q. Wang, Q. Zhao, B.S. Zou, Rev. Mod. Phys. **90**(1), 015004 (2018). https://doi.org/10.1103/RevModPhys.90.015004
59. Y.S. Kalashnikova, A. Nefediev, Phys. Usp. **62**(6), 568 (2019). https://doi.org/10.3367/UFNe.2018.08.038411
60. Y. Yamaguchi, A. Hosaka, S. Takeuchi, M. Takizawa, J. Phys. G **47**(5), 053001 (2020). https://doi.org/10.1088/1361-6471/ab72b0
61. Z.F. Sun, C.W. Xiao, (2020). arXiv:2011.09404 [hep-ph]
62. M.Z. Liu, J.X. Lu, T.W. Wu, J.J. Xie, L.S. Geng, (2020). arXiv:2011.08720 [hep-ph]
63. M.A. Lisa, S. Pratt, R. Soltz, U. Wiedemann, Ann. Rev. Nucl. Part. Sci. **55**, 357 (2005). https://doi.org/10.1146/annurev.nucl.55.090704.151533
64. T. Sjöstrand, M. Utheim, Eur. Phys. J. C **80**(10), 907 (2020). https://doi.org/10.1140/epjc/s10052-020-8399-3
65. M. Korsmeier, F. Donato, N. Fornengo, Phys. Rev. D **97**(10), 103011 (2018). https://doi.org/10.1103/PhysRevD.97.103011
66. V. Poulin, P. Salati, I. Cholis, M. Kamionkowski, J. Silk, Phys. Rev. D **99**(2), 023016 (2019). https://doi.org/10.1103/PhysRevD.99.023016

Paper V – Formation of light (anti)nuclei

Tjemsland, J. "Formation of light (anti)nuclei". *PoS* **TOOLS2020,** 006. arXiv: 2012.12252 [hep-ph] (2021)

Abstract: The production mechanism of light nuclei, such as deuteron, helium-3, tritium and their antiparticles, has recently attracted an increased attention from the astroparticle and heavy ion communities. The expected low astrophysical background of light antinulei makes them ideal probes for exotic astrophysical processes, such as dark matter annihilations. At the same time, they can be used to measure two-nucleon correlations and density fluctuations in heavy ion collisions, which may shed light on the QCD phase diagram. Motivated by the importance of light antinuclei in cosmic ray studies, we developed a new coalescence model for light (anti)nuclei that includes both the size of the formation region, which is process dependent, and momentum correlations in a semi-classical picture. We have employed the model as an afterburner to the event generators Pythia 8 and QGSJET II, and find that the model agrees well with experimental data on antideuteron and antihelium-3 production in e^+e^-, pp, ppBe and pAl collisions at various energies. In this paper, we review this model and update existing fits to experimental data based on new insights.

In Papers I, II and IV, the WiFunC model was fitted and compared to various experimental data on e^+e^-, pp and pN collisions, using both QGSJET-II and Pythia 8 as event generators. Therefore, this proceeding was used to summarize the WiFunC model and its fits to experimental data. In particular, it highlights visually that the observed energy dependence of the coalescence momentum, p_0—which was frequently accepted in the literature—is an artifact of the process dependent size of the interaction region.

It is important to emphasize that we remarked in Paper IV that we had wrongly included the Lorentz boost of the interaction region in two directions, and not one, in Papers I and II. The fits and plots in this proceeding use the correct boost.

PROCEEDINGS OF SCIENCE

Formation of light (anti)nuclei

J. Tjemsland[a,*]

[a] *Institutt for fysikk, NTNU, Trondheim, Norway*

E-mail: jonas.tjemsland@ntnu.no

The production mechanism of light nuclei, such as deuteron, helium-3, tritium and their antiparticles, has recently attracted an increased attention from the astroparticle and heavy ion communities. The expected low astrophysical background of light antinulei makes them ideal probes for exotic astrophysical processes, such as dark matter annihilations. At the same time, they can be used to measure two-nucleon correlations and density fluctuations in heavy ion collisions, which may shed light on the QCD phase diagram. Motivated by the importance of light antinuclei in cosmic ray studies, we developed a new coalescence model for light (anti)nuclei that includes both the size of the formation region, which is process dependent, and momentum correlations in a semi-classical picture. We have employed the model as an afterburner to the event generators Pythia 8 and QGSJET II, and find that the model agrees well with experimental data on antideuteron and antihelium-3 production in e^+e^-, pp, pBe and pAl collisions at various energies. In this paper, we review this model and update existing fits to experimental data based on new insights.

Tools for High Energy Physics and Cosmology - TOOLS2020
2-6 November, 2020
Institut de Physique des 2 Infinis (IP2I), Lyon, France

*Speaker

PoS(TOOLS2020)006

1. Introduction

The production mechanism of light nuclei, such as deuteron, helium-3, tritium and their antiparticles, has attracted attention from both the astroparticle and heavy ion communities. These particles are of particular importance in cosmic ray studies due to their low expected background at small kinetic energies, for a recent review see Ref. [1]. This makes them a promising detection channel for exotic physics, such as dark matter annihilations and decays. Currently, the measurement of astrophysical antinuclei is performed by the AMS-02 experiment on-board the International Space Station, while the balloon-borne GAPS experiment is expected to be launched in December 2022 [2, 3]. Unfortunately, the AMS-02 collaboration has not yet published any results regarding antinuclei measurements, even though the expected antideuteron flux from secondary production and optimistic dark matter models is close to its estimated sensitivity [1]. In heavy ion collisions, (anti)nuclei measurements are of particular interest due to their small binding energies. This make them sensitive probes for two-nucleon correlations and density fluctuations that may shed light on the QCD phase diagram [4]. In order to correctly interpret the results of both collider and cosmic ray experiments, a precise description of the production mechanism is important. The focus in this work is on small interacting systems.

In Ref. [5], we developed a new coalescence model for deuteron, tritium and helium-3 based on the Wigner function representation of the produced nuclei states (the abbreviation WiFunC, short for Wigner Function with Correlations, will be used for this model). The model was later refined and applied in Ref. [6] for astrophysical processes, and in Ref. [7] for recent collider data. In contrast to existing production models, the WiFunC model includes both the size of the nucleon formation region and two-particle correlations in a semi-classical picture. In this work, the WiFunC model is reviewed.

This paper is structured as follows. In section 2 the standard coalescence model in momentum space commonly used for small interacting systems is discussed. This serves as a motivation for the WiFunC model, which is discussed in section 3. In subsection 3.4 we update and extend the fits to experimental data from Refs. [5, 6] based on new insights. The numerical implementation of the WiFunC model is outlined in section 4. Finally, we summarise in section 5.

2. The coalescence model in momentum space

The production of light nuclei is often described using coalescence models. In this type of models, a nucleus is produced from nucleons that have (nearly) completed their formation. Traditionally, the yield of a nucleus consisting of Z protons and N neutrons is parametrised as

$$E_A \frac{\mathrm{d}^3 N_A}{\mathrm{d}P_A^3} = B_A \left(E_p \frac{\mathrm{d}^3 N_p}{\mathrm{d}p_p^3} \right)^Z \left(E_n \frac{\mathrm{d}^3 N_n}{\mathrm{d}p_n^3} \right)^N \Bigg|_{P_A/A = p_n = p_p}, \tag{1}$$

where B_A is the so-called coalescence factor and $A = Z + N$ is the nucleon number. Motivated by the small binding energies of light nuclei, the coalescence condition is often applied in momentum

Most of the discussions related to coalescence apply equally well to particles as to antiparticles, and the prescription "anti" will thus often be neglected.

space for small interacting systems. In this case, two nucleons coalesce if their invariant momentum difference is less than the phenomenological coalescence momentum p_0 [8–10]. In the limit of isotropic nucleon yields, one can show that $B_A \propto p_0^{3(A-1)}$. This can in turn be improved by considering the coalescence condition per-event using momentum correlations provided by a Monte Carlo generator, as first proposed in Refs. [11, 12]. Furthermore, it was later noted in Ref. [13] that particles have to be close to the primary interaction to be able to coalesce, which essentially mean that weak decays should be considered as a separate cluster [14]. For heavy ion-collisions, an alternative scheme was developed where the coalescence factor instead scales with the nucleon emission volume as $B_A \propto V^{A-1}$ [15, 16].

Clearly, the coalescence model in momentum space is purely phenomenological and classical. Furthermore, the coalescence momentum p_0 should be independent of both the process type and the center of mass (c.m.) energy to be predictive, which is not the case. In Fig. 1 we plot the coalescence momentum p_0 obtained by a fit to various experimental data in Refs. [6, 17]. As noted in Ref. [17], the result in Fig. 1 may suggest that the coalescence momentum p_0 exhibits an energy dependence: p_0 rapidly decreases to zero for small $\sqrt{s}$. There are, however, two problems with this conclusion: the process dependence has not been accounted for and the energy dependence has not been explained. These are two motivations for the WiFunC model, in which the apparent energy dependence is removed by taking into account the process dependence. More importantly, the WiFunC model is semi-classical and has a clear microphysical interpretation that can be used to predict its free parameter.

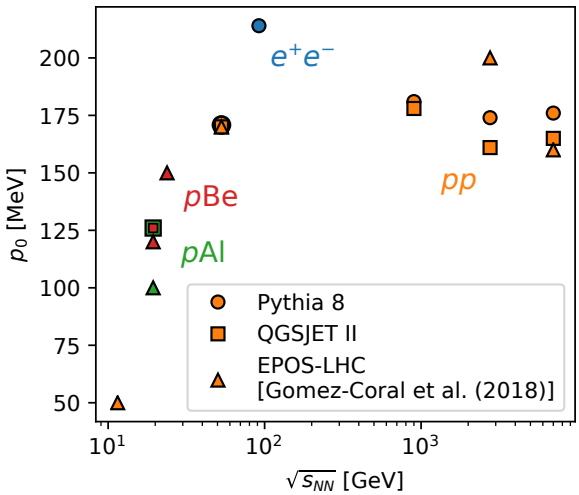

Figure 1: Best fit value of p_0 for experiments on pp (orange), e^+e^- (blue), pN (red and green) interactions using QGSJET II (squares), Pythia 8.2 (circles) and EPOS LHC (triangles) from Refs. [6, 17].

Note that we have not considered the data point at $\sim$ 12 GeV from Ref. [18]. An independent confirmation of this data point will thus falsify our model.

3. The WiFunC model

3.1 Motivation

One of the main goals of the WiFunC model is to take into account both two-particle correlations and the size of the nucleon formation region when describing the production of light nuclei. Two-particle correlations are naturally important for small interacting systems as the production is highly non-isotropic. Meanwhile, the importance of the formation region becomes apparent when inspecting the relevant timescales of the problem [19]: the initial hard scattering occurs on timescales $t_{\text{ann}} \sim 1/\sqrt{s}$, and is succeeded by a perturbative cascade with a characteristic momentum transfer $\Lambda^2_{\text{QCD}} \ll |q^2| \ll s$. This means that the largest time and distance scales in the problem is related to the hadronisation length, $L_{\text{had}} \sim \gamma L_0$ with $L_0 \sim 1$ fm. The light nuclei is in turn in the coalescence picture formed by nucleons that have (nearly) completed their formation. Since the nucleus wave functions have a size $r^N_{\text{rms}} \sim$ few fm comparable to the hadronisation length, the emission volume should not be neglected even in point-like processes.

3.2 The underlying physics and theory

The WiFunC model is based on the quantum mechanical description of coalescence, as reviewed in e.g. Ref. [20]. The deuteron spectrum can in this picture be found by projecting the reduced density matrix describing the nucleons onto the nucleus density matrix: $\mathrm{d}^3N_d/\mathrm{d}{P_d}^3 = \mathrm{tr}(\rho_d \rho_{nucl})$. Rewriting this in terms of the two-nucleon Wigner function, W_{np}, and the deuteron Wigner function, $\mathcal{D}$, leads to

$$\frac{\mathrm{d}^3N_d}{\mathrm{d}P_d^3} = \frac{3}{8}\int \mathrm{d}^3r_d \int \frac{\mathrm{d}^3q\mathrm{d}^3r}{(2\pi)^6}\mathcal{D}(\mathbf{r},\ \mathbf{q})W_{np}(\mathbf{P}_d/2+q,\ \mathbf{P}_d/2-\mathbf{q},\ \mathbf{r}_n,\ \mathbf{r}_p), \tag{2}$$

where the factor $3/8$ is obtained by averaging over spin and isospin. It is convenient to approximate the deuteron wave function as a Gaussian, in which case $\mathcal{D}(\mathbf{r},\ \mathbf{q}) = 8\exp\{-r^2/d^2 - q^2d^2\}$ with $d \simeq 3.2$ fm. The effect of two-particle correlations on the coalescence probability is, however, sensitive to the shape of the deuteron wave function. Thus, a more accurate wave function should be used when momentum correlations are taken into account, using e.g. the sum of two Gaussians as introduced in Ref. [5].

In order to proceed, one has to provide a prescription for the nucleon Wigner function. In the WiFunC model, a factorisation of the momentum and position dependence in the Wigner function is assumed,

$$W_{np} = H_{np}(\mathbf{r}_n,\ \mathbf{r}_p)G_{np}(\mathbf{P}_d/2+\ \mathbf{q},\ \mathbf{P}_d/2-\ \mathbf{q}), \tag{3}$$

and the spatial nucleon distributions are assumed to be uncorrelated, $H_{np}(\mathbf{r}_n,\ \mathbf{r}_p) = h(\mathbf{r}_n)h(\mathbf{r}_p)$. In turn, the spatial distributions are taken to be Gaussians,

$$h(\mathbf{r}) = (2\pi\sigma^2)^{-3/2}\exp\left\{-\frac{r^2}{2\sigma^2}\right\}. \tag{4}$$

For concreteness, only the production of deuteron is discussed in this subsection. The model for helium-3 and tritium is derived using the same procedure.

The numerical implementation discussed in section 4 includes such an improved wave function.

Note that this implies a transition to a semi-classical treatment.

Inserting the ansätze (3) and (4) into Eq. (2) leads to the WiFunC model,

$$\frac{\mathrm{d}^3 N_d}{\mathrm{d}P_d^3} = \frac{3\zeta}{(2\pi)^6} \int \mathrm{d}^3 q \, e^{-q^2 d^2} G_{np}(\, \mathbf{P}_d/2 + \, \mathbf{q}, \, \mathbf{P}_d/2 - \, \mathbf{q}). \tag{5}$$

The function ζ describes the distribution of the nucleons, and it is in general given by

$$\zeta(\sigma_\parallel, \sigma_\perp, d) = \sqrt{\frac{d^2}{d^2 + 4\sigma_\perp^2/(\cos^2\theta + \gamma^2 \sin^2\theta)}} \sqrt{\frac{d^2}{d^2 + 4\sigma_\perp^2}} \sqrt{\frac{d^2}{d^2 + 4\sigma_\parallel^2}}, \tag{6}$$

where θ is the angle between the deuteron momentum and the z-axis of the c.m. frame of the particle collision, while $\sigma_{\perp/\parallel}$ describes the characteristic spatial spread of nucleons in the perpendicular/parallel direction in the lab frame. The effective Lorentz boost of the transverse spread is included to account for the boost between the lab frame and the deuteron rest frame [5].

In Eq. (5) one particular choice for the semi-classical emission volume was used. Some event generators like Pythia 8 [21, 22] and UrQMD [23] have implemented a semi-classical treatment of the particle trajectories in the event. In this case, one can instead evaluate directly

$$\frac{\mathrm{d}^3 N_d}{\mathrm{d}P_d^3} = 3 \int \frac{\mathrm{d}^3 q \mathrm{d}^3 r}{(2\pi)^6} \, \mathrm{e}^{-r^2/d^2 - q^2 d^2} W_{np}(\, \mathbf{P}_d/2 + q, \, \mathbf{P}_d/2 - \, \mathbf{q}, \, \mathbf{r}_n, \, \mathbf{r}_p), \tag{7}$$

thereby relying on the spatial correlations provided by the event generator instead of Eqs. (3) and (4).

3.3 Process dependence

The free parameters in the WiFunC model, $\sigma_\perp$ and $\sigma_\parallel$, have the physical interpretation as the size of the formation region of nucleons. They will, in general, have a contribution from the perturbative cascade and hadronisation, and a contribution related to the finite size of the colliding particles:

$$\sigma_{\parallel,\perp}^2 = \sigma_{\parallel,\perp(e^+e^-)}^2 + \sigma_{\parallel,\perp(\mathrm{geom})}^2. \tag{8}$$

Here, the subscripts (e^+e^-) and (geom) denote respectively the point-like contribution from the cascade and the geometrical contribution from the finite size of the particles.

For point-like processes the spatial spread in the longitudinal direction is given by $\sigma_\parallel \simeq R_p \simeq 1$ fm. Meanwhile, the spread in the transverse direction comes from the random walk behaviour of the perturbative cascade. This means that $\sigma_\perp \simeq \Lambda_{\mathrm{QCD}}^{-1} \simeq 1$ fm.

The geometrical contributions can be approximated by [5, 6]

$$\sigma_{\perp(\mathrm{geom})}^2 \simeq \frac{2R_1^2 R_2^2}{R_1^2 + R_2^2}, \tag{9}$$

$$\sigma_{\parallel(\mathrm{geom})}^2 \simeq \max\{R_1, R_2\}, \tag{10}$$

where R_1 and R_2 are the Gaussian radii of the parton clouds in the colliding particles. For nuclei, these can be well approximated as

$$R_A \simeq a_0 A^{1/3}, \tag{11}$$

For annihilation processes, θ, $\sigma_\perp$ and $\sigma_\parallel$ is defined relative to the initial quark pair in the hard process.

with $a_0 \simeq 1$ fm, where A is the number of nucleons in the nucleus that take part in the interaction [24]. Thus, we can describe the coalescence of light nuclei using a single universal parameter by setting

$$\sigma \equiv \sigma_{(e^+e^-)} = a_0 = \sigma_{(pp)}/\sqrt{2}. \tag{12}$$

3.4 Comparison with experimental data

In Fig. 2 we plot the best fit of σ to the experimental data considered in Refs. [5–7] as a function of the c.m. energy of the collision using Pythia 8 [21, 25] and QGSJET II [26, 27]. The data points are well described by a constant spread $\sigma = (1.0 \pm 0.1)$ fm, as expected by the WiFunC model. Thus, the apparent energy dependence seen in Fig. 1 is alleviated by taking into account the nucleon emission volume.

The WiFunC model improves significantly the fit to experimental data at large transverse momenta compared to the standard coalescence model. This is readily seen in Fig. 3, where the best fit to the invariant differential yield of antideuterons measured by the ALICE collaboration [28] is plotted using Pythia 8 and QGSJET II. Furthermore, it describes the behaviour of the non-trivial baryon emission volume as measured by the ALICE collaboration [7, 29]. This is particularly important as it provides a method of determining the parameter σ independent of an event generator (orange triangle in Fig. 2).

3.5 Comment on helium-3 and tritium production

In contrast to the deuteron wave function, the helium-3 and tritium wave functions are not well known. Therefore, the rms charge radii $r^{^3\mathrm{He}}_{\mathrm{rms}} = 1.96$ fm and $r^{t}_{\mathrm{rms}} = 1.76$ fm were used in Refs. [5, 6] to describe the wave functions as a Gaussian. This will lead to an artificially small spread σ if in reality either the matter radius is smaller than the charge radius or the wave function is more peaked than a Gaussian.

In the coalescence picture, deuteron, helium-3 and tritium are expected to be created by nucleons with the same spread, and the parameter σ should thus be the same for all three particles. In the previous subsection, we saw that the spread is already well determined by antideuteron experiments, which has been confirmed independently by the measurements on the baryon emission volume by the ALICE collaboration [7, 29]. Thus, we can allow ourselves to degrade $r^{^3\mathrm{He}}_{\mathrm{rms}}$ to a free parameter to better describe the effective ground state of the nucleus. In the spirit of simplicity and for consistency with Eq. (11), we set $r^{^3\mathrm{He}}_{\mathrm{rms}} = b = 3^{1/3}\sigma$. Remarkably, this choice leads to $\sigma = (0.93 \pm 0.04)$ fm for Pythia 8 and $\sigma = (1.07 \pm 0.03)$ fm for QGSJET II when fitted to the antihelium-3 spectrum at 7 TeV measured by the ALICE collaboration [28], consistent with the antideuteron fits in Fig. 2. These

Notice the ambiguity of this choice: we expect in general $\sigma_\parallel \gtrsim \sigma_\perp$ and we could therefore have chosen a different scaling between the parameters. Nevertheless, we find that this choice well describes the physics and experimental data. If more accurate data and event generators become available in the future, a separate fit of $\sigma_\perp$ and $\sigma_\parallel$, or even the geometrical and point-like spread, may be needed.

In addition to including also the data on helium production for QGSJET, we have made the following changes compared to Refs. [5, 6]. First, we now vary the spread σ in pN collisions on an event by event basis depending on the number of nucleons that participate in the interaction using Eq. (11). Second, we now use the distribution factor ζ with boost in only one transverse component [Eq. (6)]. Finally, the size of the helium wave function is treated as discussed in section 3.5.

Since the spectra of tritium and helium-3 are expected to be similar, it is convenient to assume $r^{t}_{\mathrm{rms}} = r^{^3\mathrm{He}}_{\mathrm{rms}}$ [5].

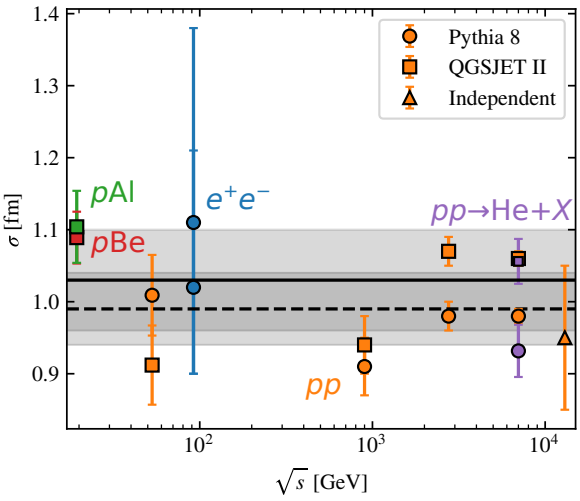

Figure 2: The best fit of σ to experimental data on antinuclei production in e^+e^- (blue), pp (orange), pBe (red) and pAl (green) collisions using Pythia 8 (circles) and QGSJET II (squares). The result obtained in Ref. [7] from comparison with the measured baryon emission volume is also shown (triangle). The mean of the data points for Pythia (dashed line) and QGSJET (solid line) and their standard deviations (transparent gray regions) are plotted without regards to the uncertainties in order to visualise the variation.

values corresponds to a rms radius 1.3–1.6 fm, which is by no means far-fetched. Nevertheless, it should be emphasised that theoretical uncertainties related to the wave function has not been properly accounted for.

3.6 Comment on thermal models

The production of light nuclei in heavy ion collisions is often described using thermal statistical models, where it is assumed that the nuclei are produced around chemical freeze-out in an expanding "fireball" consisting of a quark gluon plasma. Such models are motivated by the observation that the nucleus spectra are near thermal with a similar freeze-out temperature as for nucleons and mesons [30]. It is, however, hard to resolve the issue on how particles with small binding energies can survive the freeze-out process. Furthermore, since the hadron spectra already are thermal-like, coalescence models also predicts thermal-like nucleus spectra up to a quantum mechanical correction factor [15].

Intriguingly, recent observations show characteristic signs for the production of a quark gluon plasma in small interacting systems, such as pp and pPb collisions [31]. Such hints have been used as a motivation for using thermal models to describe the nucleus production even in small interacting systems [1, 32–34]. However, many of these, e.g. the behaviour of the B_2 factor as a function of multiplicity and transverse momentum in pp collisions [34] and the decrease in the

This change may lead to an increase in the cosmic ray antihelium spectra in Ref. [6] by a factor of a few.

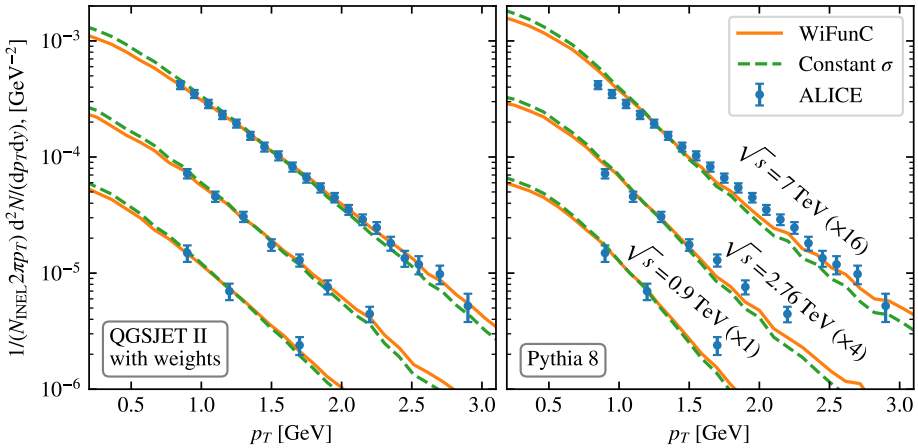

Figure 3: The best fit of the WiFunC model using QGSJET II (left) and Pythia 8.2 (right) to the invariant differential yield of antideuterons as a function of the transverse momentum measured by the ALICE collaboration [28] at 0.9, 2.76 and 7 TeV (blue points). The data are multiplied by a constant factor to make the figure clearer. In the fit using QGSJET, a weight is included in order to better reproduce corresponding nucleon measurements [6]. The WiFunC model (orange line) reproduce well the data points. The WiFunC model without any Lorentz boost gives a similar fit as the standard coalescence model and is shown for comparison (green dashed line).

baryon emission volume with increasing transverse momentum [29], is also naturally described by the WiFunC model [7]. Moreover, the hints are irrelevant for astrophysical processes since they are at present only observed at high energies and multiplicities.

Regardless of the underlying hadron production, the WiFunC model is applicable as long as the nuclei are produced in a coalescence process. It is thus worth pointing out that it is argued in Ref. [35] that two-particle correlation experiments can be used to validate the coalescence hypothesis, and that the success of the femtoscopy analysis is strong evidence that coalescence is a major production mechanism for nuclei.

4. Numerical implementation of the WiFunC model

In this section, we briefly summarise how the WiFunC model can be evaluated for deuteron, helium-3 and tritium. The momentum of the nucleons produced in a particle collision is to be computed on an event-by-event basis using an event generator. Double counting can in all relevant applications be neglected [5].

In the WiFunC model, the probability that a given proton-neutron pair coalesce is

$$w = 3\Delta\zeta_1\, \mathrm{e}^{-d_1^2 q^2} + 3(1-\Delta)\zeta_2\, \mathrm{e}^{-d_2^2 q^2}, \tag{13}$$

where

$$\zeta_i = \sqrt{\frac{d_i^2}{d_i^2 + 4\tilde{\sigma}_\perp^2}}\sqrt{\frac{d_i^2}{d_i^2 + 4\sigma_\perp^2}}\sqrt{\frac{d_i^2}{d_i^2 + 4\sigma_\parallel^2}}, \tag{14}$$

and $\tilde{\sigma}_\perp^2 = \sigma_\perp^2/(\cos^2\theta + \gamma^2 \sin^2\theta)$. The quantities that vary event-by-event are indicated in Fig. 4: $|\mathbf{q}|$ is the momentum of the nucleons in the deuteron rest frame, θ is the angle between the deuteron momentum and the z-axis of the particle collision in the c.m. frame of the collision and γ is the deuteron Lorentz factor in the c.m. frame of the collision. The parameters $\Delta = 0.581$, $d_1 = 3.979$ fm, $d_2 = 0.890$ fm are fixed by fitting a two-Gaussian wave function to the Hulthen wave function that well describes the ground state of the deuteron [5]. The process dependence of the nucleon spread can be taken into account using Eqs. (8)–(12). In particular, the longitudinal and transverse spreads in e^+e^- and pp collisions can be set equal and is given by $\sigma \equiv \sigma_{(e^+e^-)} = \sigma_{(pp)}/\sqrt{2} \simeq (1.0 \pm 0.1)$ fm.

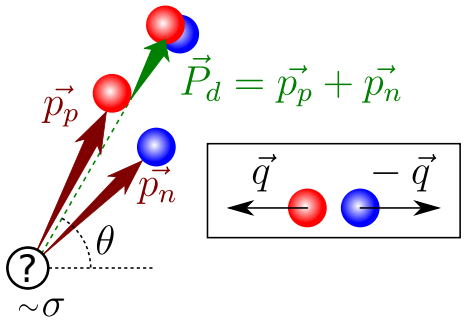

Figure 4: Sketch of the coalescence process in the c.m. frame of the particle collision. A proton with momentum $\mathbf{p}_p$ and neutron with momentum $\mathbf{p}_n$ may coalesce into a deuteron with momentum $\mathbf{P}_d = \mathbf{p}_p + \mathbf{p}_n$ if their momentum difference in the deuteron rest frame, $2|\mathbf{q}|$, is small. The exact probability is determined by Eq. (13).

The model for helium-3 and tritium production is similar to that for deuteron. In this case, the probability that a proton-proton-neutron or proton-neutron-neutron triplet coalesce is

$$w = \frac{64}{12}\zeta^{\mathrm{He}}\, \mathrm{e}^{-b^2P^2}, \tag{15}$$

with

$$P^2 = \frac{1}{3}\left[(\mathbf{p}_1 - \mathbf{p}_2)^2 + (\mathbf{p}_1 - \mathbf{p}_3)^2 + (\mathbf{p}_2 - \mathbf{p}_3)^2\right] \tag{16}$$

and

$$\zeta^{\mathrm{He}} = \frac{b^2}{b^2 + 2\tilde{\sigma}_\perp^2}\frac{b^2}{b^2 + 2\sigma_\perp^2}\frac{b^2}{b^2 + 2\sigma_\parallel^2}. \tag{17}$$

Here, $\mathbf{p}_i$ $(i = 1,2,3)$ is the momentum of the nucleons in the rest frame of the three-particle state. Due to the Gaussian suppression in Eq. (15), one can to a good approximation evaluate the momentum difference of the nucleons entering Eq. (16) in the corresponding two-particle rest frames.

In Eq. (15) the nucleus wave function is approximated by a Gaussian with a rms radius b. In Refs. [5, 6] it was set equal to the measured helium-3 rms charge radius $b = 1.96$ fm. However, this choice may lead to an artificially low nucleus yield. Since σ is already well constrained by antideuteron measurements, b can be degraded to a free parameter e.g. by setting $b = 3^{1/3}\sigma_{(e^+e^-)}$.

5. Summary and Outlook

The WiFunC model is a per-event coalescence model based on the Wigner function representation of the nucleon and nucleus states. This model includes in a semi-classical picture both two-nucleon momentum correlations provided by a Monte Carlo event generator and the size of the nucleon emission volume. Since the emission volume is process dependent, it explains naturally the differences in (anti)nucleus yields observed in e^+e^-, pp and pN collisions. The value obtained by fits to experimental data, $\sigma = (1.0 \pm 0.1)$ fm, agrees well with its physical interpretation.

The spread σ is currently well constrained by antideuteron data in pp collisions at large energies and large p_T. Thus, experimental studies on antinuclei production in small interacting systems at low energies in the forward direction is highly warranted. This will reduce uncertainties related to antinuclei production in astrophysical processes, as well as test the WiFunC model. Furthermore, two-particle correlation experiments can be used to directly measure σ [7] and test the coalescence hypothesis [35, 36].

The WiFunC model can, in principle, describe the coalescence of nucleons in any particle collision as long as the event generator is able to describe the underlying physics. Currently, the prescription of σ is expected to describe well coalescence is small interacting systems, such as e^+e^-, pp and pN collisions. However, the uncertainties in σ will in general increase with increasing system size. Therefore, it would be interesting to instead use the space-time descriptions implemented in event generators like Pythia [21, 22, 25] or UrQMD [23, 37] by evaluating Eq. (7) directly.

Acknowledgments

I would like to thank S. Ostapchenko and M. Kachelrieß for fruitful collaborations on which this review is based and M. Kachelrieß for comments on this text.

References

[1] P. von Doetinchem et al., *Cosmic-ray Antinuclei as Messengers of New Physics: Status and Outlook for the New Decade*, *JCAP* **08** (2020) 035 [2002.04163].

[2] N. Saffold et al., *Cosmic Antihelium Nuclei Sensitivity of the GAPS Experiment*, 2012.05834.

[3] AMS 02 collaboration, *The antimatter spectrometer (ams-02): A particle physics detector in space*, *Nucl. Instrum. Meth.* **588** (2008) 227.

[4] H. Caines, *The Search for Critical Behavior and Other Features of the QCD Phase Diagram – Current Status and Future Prospects*, *Nucl. Phys.* **A967** (2017) 121.

[5] M. Kachelrieß, S. Ostapchenko and J. Tjemsland, *Alternative coalescence model for deuteron, tritium, helium-3 and their antinuclei*, *Eur. Phys. J.* **A56** (2020) 4 [1905.01192].

[6] M. Kachelrieß, S. Ostapchenko and J. Tjemsland, *Revisiting cosmic ray antinuclei fluxes with a new coalescence model*, *JCAP* **08** (2020) 048 [2002.10481].

[7] M. Kachelriess, S. Ostapchenko and J. Tjemsland, *On nuclear coalescence in small interacting systems*, 2012.04352.

[8] A. Schwarzschild and C. Zupancic, *Production of Tritons, Deuterons, Nucleons, and Mesons by 30-GeV Protons on A-1, Be, and Fe Targets*, *Phys. Rev.* **129** (1963) 854.

[9] S. T. Butler and C. A. Pearson, *Deuterons from high-energy proton bombardment of matter*, *Phys. Rev.* **129** (1963) 836.

[10] P. Chardonnet, J. Orloff and P. Salati, *The production of antimatter in our galaxy*, *Phys. Lett.* **B409** (1997) 313 [astro-ph/9705110].

[11] M. Kadastik, M. Raidal and A. Strumia, *Enhanced anti-deuteron dark matter signal and the implications of PAMELA*, *Phys. Lett.* **B683** (2010) 248 [0908.1578].

[12] L. A. Dal, *Antideuterons as signature for dark matter*, master's thesis, NTNU Trondheim, available at http://hdl.handle.net/11250/246403, 2011.

[13] A. Ibarra and S. Wild, *Prospects of antideuteron detection from dark matter annihilations or decays at AMS-02 and GAPS*, *JCAP* **1302** (2013) 021 [1209.5539].

[14] M. W. Winkler and T. Linden, *Dark Matter Annihilation Can Produce a Detectable Antihelium Flux through $\bar{\Lambda}_b$ Decays*, 2006.16251.

[15] L. Csernai and J. I. Kapusta, *Entropy and Cluster Production in Nuclear Collisions*, *Phys. Rept.* **131** (1986) 223.

[16] J. Nagle, B. Kumar, D. Kusnezov, H. Sorge and R. Mattiello, *Coalescence of deuterons in relativistic heavy ion collisions*, *Phys. Rev. C* **53** (1996) 367.

[17] D.-M. Gomez-Coral, A. Menchaca Rocha, V. Grabski, A. Datta, P. von Doetinchem and A. Shukla, *Deuteron and Antideuteron Production Simulation in Cosmic-Ray Interactions*, *Phys. Rev.* **D98** (2018) 023012 [1806.09303].

[18] V. Abramov et al., *High p_T Deuteron and Anti-deuteron Production in pp and p a Collisions at 70-{GeV}*, *Sov. J. Nucl. Phys.* **45** (1987) 845.

[19] Y. L. Dokshitzer, V. A. Khoze, A. H. Mueller and S. Troian, *Basics of perturbative QCD*. 1991.

[20] R. Scheibl and U. W. Heinz, *Coalescence and flow in ultrarelativistic heavy ion collisions*, *Phys. Rev.* **C59** (1999) 1585 [nucl-th/9809092].

[21] T. Sjöstrand, S. Ask, J. R. Christiansen, R. Corke, N. Desai, P. Ilten et al., *An Introduction to PYTHIA 8.2*, *Comput. Phys. Commun.* **191** (2015) 159 [1410.3012].

[22] S. Ferreres-Solé and T. Sjöstrand, *The space–time structure of hadronization in the Lund model*, *Eur. Phys. J. C* **78** (2018) 983 [1808.04619].

[23] M. Bleicher et al., *Relativistic hadron hadron collisions in the ultrarelativistic quantum molecular dynamics model*, *J. Phys. G* **25** (1999) 1859 [hep-ph/9909407].

[24] T. W. Donnelly, J. A. Formaggio, B. R. Holstein, R. G. Milner and B. Surrow, *Foundations of Nuclear and Particle Physics*. Cambridge University Press, 2017.

[25] T. Sjöstrand, S. Mrenna and P. Z. Skands, *PYTHIA 6.4 Physics and Manual*, *JHEP* **05** (2006) 026 [hep-ph/0603175].

[26] S. Ostapchenko, *Monte Carlo treatment of hadronic interactions in enhanced Pomeron scheme: I. QGSJET-II model*, *Phys. Rev.* **D83** (2011) 014018 [1010.1869].

[27] S. Ostapchenko, *QGSJET-II: physics, recent improvements, and results for air showers*, *EPJ Web Conf.* **52** (2013) 02001.

[28] ALICE collaboration, *Production of deuterons, tritons, ^{3}He nuclei and their antinuclei in pp collisions at $\sqrt{s} = 0.9$, 2.76 and 7 TeV*, *Phys. Rev.* **C97** (2018) 024615 [1709.08522].

[29] ALICE collaboration, *Search for a common baryon source in high-multiplicity pp collisions at the LHC*, *Phys. Lett. B* **811** (2020) 135849 [2004.08018].

[30] A. Andronic, P. Braun-Munzinger, K. Redlich and J. Stachel, *Decoding the phase structure of QCD via particle production at high energy*, *Nature* **561** (2018) 321 [1710.09425].

[31] J. L. Nagle and W. A. Zajc, *Small System Collectivity in Relativistic Hadronic and Nuclear Collisions*, *Ann. Rev. Nucl. Part. Sci.* **68** (2018) 211 [1801.03477].

[32] F. Bellini and A. P. Kalweit, *Testing production scenarios for (anti-)(hyper-)nuclei and exotica at energies available at the CERN Large Hadron Collider*, *Phys. Rev. C* **99** (2019) 054905 [1807.05894].

[33] J. Cleymans, S. Kabana, I. Kraus, H. Oeschler, K. Redlich and N. Sharma, *Antimatter production in proton-proton and heavy-ion collisions at ultrarelativistic energies*, *Phys. Rev. C* **84** (2011) 054916 [1105.3719].

[34] ALICE collaboration, *(Anti-)deuteron production in pp collisions at $\sqrt{s} = 13$ TeV*, *Eur. Phys. J. C* **80** (2020) 889 [2003.03184].

[35] F. Bellini, K. Blum, A. P. Kalweit and M. Puccio, *On coalescence as the origin of nuclei in hadronic collisions*, 2007.01750.

[36] K. Blum and M. Takimoto, *Nuclear coalescence from correlation functions*, *Phys. Rev. C* **99** (2019) 044913 [1901.07088].

[37] S. Sombun, K. Tomuang, A. Limphirat, P. Hillmann, C. Herold, J. Steinheimer et al., *Deuteron production from phase-space coalescence in the UrQMD approach*, *Phys. Rev. C* **99** (2019) 014901 [1805.11509].

Paper VI – Meson production in air showers and the search for light exotic particles

Kachelrieß, M. & Tjemsland, J. "Meson production in air showers and the search for light exotic particles". *Astropart. Phys.* **132,** 102622. arXiv: 2104.06811 [hep-ph] (2021)

Abstract: Decays of mesons produced in cosmic ray induced air showers in Earth's atmosphere can lead to a flux of light exotic particles which can be detected in underground experiments. We evaluate the energy spectra of the light neutral mesons π^0, η, ρ^0, ω, ϕ and J/ψ produced in interactions of cosmic ray protons and helium nuclei with air using QCD inspired event generators. Summing up the mesons produced in the individual hadronic interactions of air showers, we obtain the resulting fluxes of undecayed mesons. As an application, we re-consider the case of millicharged particles created in the electromagnetic decay channels of neutral mesons.

In the novel work by Plestid et al. [*Phys.Rev.D* 102 (2020) 115032], the production of millicharged particles in meson decays in air showers was discussed. They noted that their estimations were conservative, given that they only included the initial interaction at the top of the atmosphere. We therefore decided to re-evaluate their fluxes, taking the entire air shower into account. The effect was, however, smaller than we expected. Nevertheless, the work resulted in tables for intermediate meson production in the atmosphere and an estimation of the theoretical uncertainties involved.

Astroparticle Physics 132 (2021) 102622

Contents lists available at ScienceDirect

Astroparticle Physics

journal homepage: www.elsevier.com/locate/astropartphys

Meson production in air showers and the search for light exotic particles

M. Kachelrieß *, J. Tjemsland

Institutt for fysikk, NTNU, Trondheim, Norway

ARTICLE INFO

Keywords:
Cosmic ray interactions
Dark matter
Search for exotic particles

ABSTRACT

Decays of mesons produced in cosmic ray induced air showers in Earth's atmosphere can lead to a flux of light exotic particles which can be detected in underground experiments. We evaluate the energy spectra of the light neutral mesons π^0, η, ρ^0, ω, ϕ and J/ψ produced in interactions of cosmic ray protons and helium nuclei with air using QCD inspired event generators. Summing up the mesons produced in the individual hadronic interactions of air showers, we obtain the resulting fluxes of undecayed mesons. As an application, we re-consider the case of millicharged particles created in the electromagnetic decay channels of neutral mesons.

1. Introduction

While overwhelming evidence has been accumulated for the existence of dark matter (DM) from astrophysical and cosmological observations, the experimental searches for such particles in direct detection experiments have not been successful yet. Combined with the null results in searches for new physics at the LHC, this indicates that new particles with masses below the TeV scale are only weakly coupled to the standard model. The prime candidate for such a DM particle, a thermal relic with mass around the weak scale, has been constrained severely and is on the eve of being excluded: For instance, the upper limit on the annihilation cross section obtained by the Fermi-LAT collaboration using dwarf galaxies excludes thermal relics with masses below $\sim 100\,\mathrm{GeV}$ [1], while model dependent limits from antiproton data are typically even more stringent [2,3]. Therefore, both model building and experimental searches have expanded their phenomenological scope considerably the last decade, investigating e.g. light DM particles with masses in the sub-GeV range.

Traditionally, this mass range has been considered to be inaccessible to direct detection experiments, since the recoil energy of a DM particle with typical Galactic velocities, $v \sim 10^{-3}c$, is below the threshold energy of such experiments. However, Refs. [4,5] recently pointed out that cosmic rays (CRs) colliding with DM can up-scatter them, leading to a significantly increased DM flux above the threshold energy of direct detection experiments. Another generic source of light DM particles are CR interactions in the atmosphere of the Earth [6–11]. If mesons produced in these interactions decay partially into DM, an energetic DM flux that can be detected in underground experiments results. While the up-scattering mechanism relies on a sufficiently large abundance of the DM particle considered, CR interactions in the atmosphere depend only on the well-known flux of incident cosmic rays. This mechanism can moreover produce other long-lived exotic particles, thereby extending the reach of searches for new physics.

In this work, we re-evaluate the atmospheric fluxes of undecayed π^0, η, ρ, ω, ϕ and J/ψ mesons, which we denote collectively by m. In a previous study by Plestid et al. [12], these fluxes were computed using parametrizations for the relevant production cross sections in pp collisions. Here, we improve upon this in several aspects: First, we use QCD inspired event generators to model the particle production in single hadronic interactions. This allows us to account for the contribution of helium in the CR primary flux as well as for the effect of air as target nuclei. Comparing the results of different event generators we obtain an estimate for the uncertainties of their predictions. Moreover, we model the complete hadronic air shower by considering interactions of secondaries such as $\pi^\pm p \to mX$ and $K^\pm p \to mX$. Our main result is thus an improved description of the atmospheric flux of undecayed mesons produced in air showers. Our tabulated results can be used to evaluate the flux of exotic particles produced by atmospheric meson decays within generic extensions of the standard model.[1] Possible applications include, for instance, the decay of π^0 and η mesons into a pair of DM particles through a bosonic mediator [11], and the case of millicharged DM that couples to the Standard Model (SM) via a photon [13]. As an illustration for the application of our atmospheric flux of undecayed mesons, we consider the production of a generic millicharged particle (mCP) and compare our results with those of Ref. [12]. Such particles arise naturally through, e.g., the kinetic mixing between the SM photon and a dark photon [14–18]. The possible mass-to-charge ratio $m/\epsilon e$ of

* Corresponding author.
E-mail address: michael.kachelriess@ntnu.no (M. Kachelrieß).

[1] Tables for the integrated meson fluxes are attached to the arxiv submission.

https://doi.org/10.1016/j.astropartphys.2021.102622
Received 22 April 2021; Received in revised form 18 June 2021; Accepted 21 June 2021
Available online 24 June 2021

models in which the DM is charged are already strongly constrained by astrophysical processes as well as ground based experiments, see e.g. Refs. [19–21]. However, these limits can be avoided, if the charged component is unstable on cosmological time scales or constitutes only a small part of the total DM abundance. Therefore, DM theories with a sub-dominant charged component in a hidden sector have attracted attention, for recent reviews see Refs. [22,23]. An additional motivation for such models is the EDGES anomaly which can be explained in a small window in parameter space close to the limits from direct detection experiments [24,25].

This paper is structured as follows. In Section 2, we first compare the meson production cross sections calculated using various QCD inspired event generators to experimental data, and compute next the atmospheric flux of undecayed neutral mesons. As an example for the applicability of the tabulated fluxes, we re-evaluate the flux of mCPs from atmospheric meson decays in Section 3. Finally, a summary is given in Section 4.

2. Meson production in air showers

High energy cosmic rays entering the atmosphere interact with air nuclei. The produced long-lived hadrons will in turn interact with other air nuclei, thus creating a so-called hadronic air shower. The short-lived particles, on the other hand, may decay. About 1/3 of the energy is transferred in each generation of the air shower into the electromagnetic component, mainly via the decay of short-lived mesons. Thus, the decay of mesons in a hadronic air shower may be a promising detection channel for exotic particles that interact with the SM via a photon, such as mCPs. To describe the hadronic interactions, we utilize the QCD inspired event generators DMPJET III 19.1 [26–28], Pythia 8.303 [29], QGSJET II-04 [30,31], Sibyll 2.3d [32], and UrQMD 3.4 [33]. The focus will be on DPMJET and Sibyll which are event generators widely used in the field of CR physics. An exception is the production of J/ψ mesons, where we rely on the event generator Pythia which is focused on accelerator physics.

2.1. Production cross sections

Parametrizations of hadronic interactions relying on empirical scaling laws are often used as an efficient tool to reproduce inclusive quantities like total cross sections. The use of such parametrizations becomes, however, dangerous when they are extrapolated outside the kinematical range of the data they are based on. Moreover, such parametrizations are generally not available for the cases where nuclei are employed as CR primaries or targets. In this work, we use therefore Monte Carlo event generators in the description of hadronic interactions to compute the atmospheric meson fluxes. While this approach avoids the disadvantages of parametrizations, it has also its own drawbacks: In particular, QCD inspired event generators cannot be used below a minimal energy, which is typically in the range of 5–10 GeV/n of the projectile in the lab frame. While this implies that most of the CR interactions in the atmosphere cannot be simulated using these event generators, we will see that the bulk of the produced mesons is still well described due to the strong suppression of particle production near threshold.

To test the event generators, we compare in Fig. 1 the production cross sections of η, ρ, ω and ϕ mesons computed using DPMJET, Sibyll and UrQMD to the experimental data on the inclusive meson production cross section $\sigma_{pp\to mX}$ in pp collisions from Refs. [34–36]. Additionally, we show the parametrizations used in Ref. [12]. There is overall a good agreement between the experimental data and the predictions of the event generators. We do, however, note a few deficiencies: First, we see that UrQMD overproduces ϕ mesons by an energy-dependent factor. Next, we note that DPMJET overproduces ρ and ω mesons. In this case, we obtain a good description of the

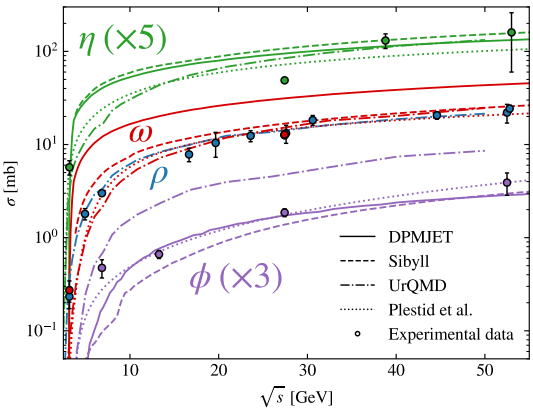

Fig. 1. The total production cross section of η (green), ρ (blue), ω (red) and ϕ (purple) mesons computed using DPMJET (solid), Sibyll (dashed) and UrQMD (dashed dotted) is compared to experimental data on the total inclusive cross sections from Refs. [34–36]. The parametrizations used in Ref. [12] are shown for comparison (dotted). The η and ϕ cross sections are multiplied by a constant factor to make the figure clearer. In the case of Sibyll and DPMJET, the ρ and ω cross sections are close to overlapping, thus only the ω flux is shown.

data by rescaling[2] the production cross sections of ρ and ω mesons by a factor 0.5. Finally, we comment on the case of J/ψ mesons: DPMJET predicts a J/ψ production cross section that is 3–4 orders of magnitude below those of Sibyll and Pythia, indicating that the most important production channels of this meson are not included in this event generator. We have therefore decided to focus in the following mainly on DPMJET and Sibyll computing the production of η, ρ, ω and ϕ mesons, as they describe well the experimental data (after the rescaling) and are reasonably fast. The other aforementioned event generators will be used as basis for comparison. In addition, Pythia will be used to describe the production of J/ψ mesons.

2.2. Flux of undecayed mesons

Next we compute the flux of undecayed mesons of the types π^0, η, ρ^0, ω, ϕ and J/ψ in hadronic air showers induced by cosmic ray proton and helium nuclei using a self-written Monte Carlo code in which the interactions of hadrons are handled using QCD inspired event generators. We consider He, p, $\pi^\pm$ and $K^\pm$ as stable[3] projectiles and nitrogen as target.[4] All short-lived particles that are not treated as a projectile are set to decay using the decay subroutines in Pythia. Since we are mainly interested in the integrated meson fluxes as a function of energy, we neglect the direction of the produced particles, keeping all down-going particles. Moreover, practically all primaries above the production threshold will interact, and we can therefore ignore the

[2] A proper solution which would require to increase appropriately the production cross sections of other particles as, e.g., a_0 and f_0 mesons is planned for a future version of DPMJET [37].

[3] At low energies, charged mesons will decay, implying that this treatment will lead to an overestimation of the meson yields. Considering for concreteness $E_c = 30$ GeV [38] as a hard cut-off and $\pi^\pm$ as primaries, we can estimate that there will only be an effect at meson energies $E < (m_N^2 + m_{\pi^\pm}^2 + 2m_N E_c)^{1/2} - m_N - m_{\pi^\pm} \simeq 6.5$ GeV. The effect will be small as there will be a large contribution from charged pions at higher energies. In particular, the effect on interesting observables in the production of exotic particles above detector thresholds will be negligible.

[4] With Pythia, we consider only pp interactions and take into account the helium flux by rescaling the proton flux appropriately.

finite extension of the atmosphere. Finally, we can neglect the tertiary contribution to meson production due to the electromagnetic shower component, because the average energy per produced secondary is for photons/electrons smaller than for mesons and the cross sections for, e.g., photo-pion production are suppressed relative to electromagnetic ones. For the primary CR fluxes, we use the parametrizations fitted to proton and helium data from AMS-02, DAMPE and CREAM given in Ref. [3].

Before proceeding, the chosen energy cutoffs should be discussed. We use 2 GeV/n as a low-energy threshold for DPMJET, QGSJET and UrQMD, while we set 8 GeV/n and 60 GeV/n for Sibyll[5] and Pythia, respectively. These energy cutoffs should be compared to the threshold energy in the interaction $pp \to ppm$ which are 1.2, 2.2, 2.8, 3.5 and 12 GeV for π^0, η, ρ^0, ω, ϕ and J/ψ mesons, respectively. Thus the chosen cut-off in DPMJET, QGSJET and UrQMD is sufficiently small for all considered mesons except for the π^0; the results for this meson must therefore be considered with care.[6] Even more, the threshold suppression in the production cross section will at some point be stronger than the power law increase in the primary CR flux. This means that even if Sibyll cannot describe most particle interactions, it will still describe the bulk of produced mesons more massive than π^0. Likewise, Pythia will describe well the atmospheric J/ψ flux, as is readily seen by Fig. 2 in Ref. [12].

The main contribution to the meson production comes from the first interaction at the top of the atmosphere, because the cosmic ray flux is a steeply falling function of energy, $\Phi^{\rm CR}(E) \propto E^{-2.7}$. Moreover, the cosmic ray flux is at low energies dominated by protons. Therefore, we start by plotting in Fig. 2 the integrated meson fluxes from pp interactions weighted by the cosmic ray flux $\Phi^{\rm CR}(E) \simeq \Phi_p(E) + 4\Phi_{\rm He}(E/4)$ as a simple benchmark case. Note that the production yields of ρ and ω mesons are divided by a factor 2 in the case of DPMJET, as described in the previous subsection. As a basis for comparison, we plot also the result obtained using QGSJET (only for π^0), Pythia (only ϕ and J/ψ) and UrQMD (only π^0, η, ρ and ω). The effect of the chosen cutoffs are clearly visible: Lowering the energy threshold extends the power law to lower energies and increases the flux of produced mesons at low energies. For instance, the maximum of the π^0 flux computed with Sibyll is suppressed by a factor $\simeq 10$ compared to DPMJET. This effect is smaller for heavier mesons, because of their increased production threshold. The remaining overall differences for heavier mesons can be explained by the differences in the computed production cross sections (see Section 2.1). The differences between DPMJET and Sibyll (for mesons heavier than π^0) capture well the uncertainties in the different event generators, which are below a factor 2–3.

In Fig. 3, the computed undecayed meson fluxes from hadronic air showers are shown. The effect of including the cascade leads to a noticeable increase in the flux at low meson energies, and shifts its maximum slightly to smaller energies. However, the difference in the fluxes for Sibyll and DPMJET are larger than the gain in including the complete cascade, even at low energies. These effects are more visible in Fig. 4. Here, the ratios of the meson fluxes of π^0, η, ρ and ω from pN initiated air showers, $\Phi_{pN}^{\rm cascade}$, and from a single pp interaction at the top of the atmosphere, Φ_{pp}, are shown. For comparison, the ratio $\Phi_{pp}^{\rm cascade}/\Phi_{pp}$ of the fluxes from a pp air shower and a single pp interaction is shown for Pythia. Interestingly, the effect of including target nuclei lowers the flux at large energies, because the kinetic energy in the center of mass frame of the interaction is effectively reduced. This effect is larger for DPMJET than for Sibyll.

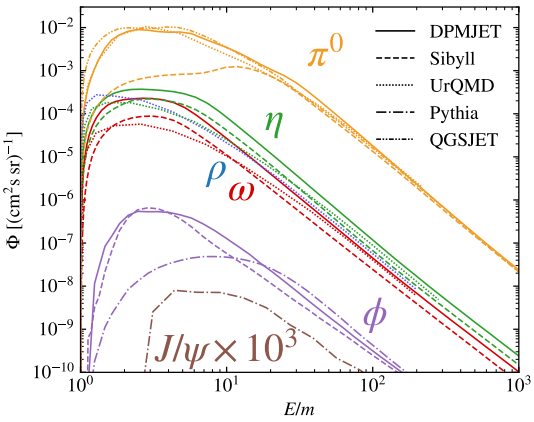

Fig. 2. The flux of produced π^0 (orange), η (green), ρ (blue), ω (red), ϕ (purple) and J/ψ (brown) mesons in pp and Hep collisions at the top of the atmosphere are computed using DPMJET (solid lines), Sibyll (dashed), QGSJET (dashed–dotted–dotted), Pythia (dashed–dotted) and UrQMD (dotted). Only a selection of meson species are shown for different event generators to make the figure clearer. In the case of Sibyll and DPMJET, the ρ and ω fluxes are close to overlapping, thus only the ω flux is shown.

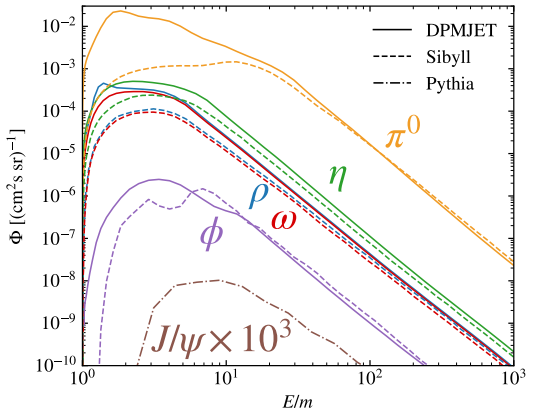

Fig. 3. Meson flux produced in air showers using DPMJET, Sibyll and Pythia (only J/ψ). The line-styles are the same as in Fig. 2.

The meson fluxes in Fig. 3 differ significantly[7] from those computed in Ref. [12]: For small meson energies, our fluxes are suppressed more strongly, leading to a difference of about one order of magnitude around the maximum. Meanwhile, for large meson energies the differences are small and consistent with the differences in the production cross sections discusses in Section 2.1.

3. Application: Atmospheric production of millicharged particles

In this section we analyze the production of mCP from the intermediate meson decays in the atmosphere. This serves as a (conservative) benchmark model for mCP, with the advantage of having only two free

[5] The chosen threshold for Sibyll is lower that the intended validity range, but as seen in Section 2.1 Sibyll describes well the production cross sections down to $E_{\rm lab} \simeq 6.4$ GeV.

[6] Note that we consider π^0 mesons only for completeness. As we will see in the next section, exotic particle production from π^0 decays is already strongly constrained by collider experiments. It is therefore doubtful that the decay of π^0 in atmospheric cascade can give leading constraints.

[7] One should note that the meson fluxes found in Ref. [12] were considered as *a useful byproduct*, while their main result—the integrated flux of mCPs above detector thresholds—are mostly sensitive to the total production cross sections.

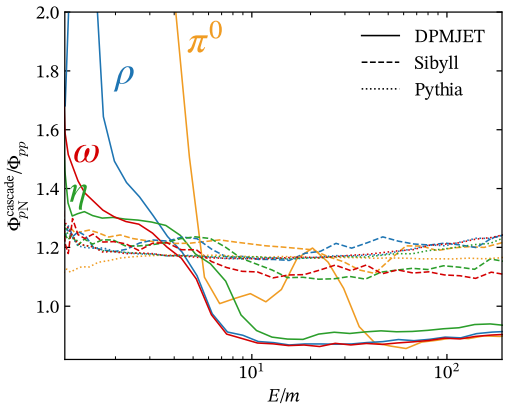

Fig. 4. Ratio $\Phi_{pN}^{\rm cascade}/\Phi_{pp}$ of the meson fluxes in pN air showers and a single pp collision computed using DPMJET (solid lines) and Sibyll (dashed lines). For comparison, $\Phi_{pp}^{\rm cascade}/\Phi_{pp}$ of the fluxes from a pp air shower and a single pp interaction is shown in the case of Pythia. The color-scheme indicating the various mesons are the same as in the previous figures.

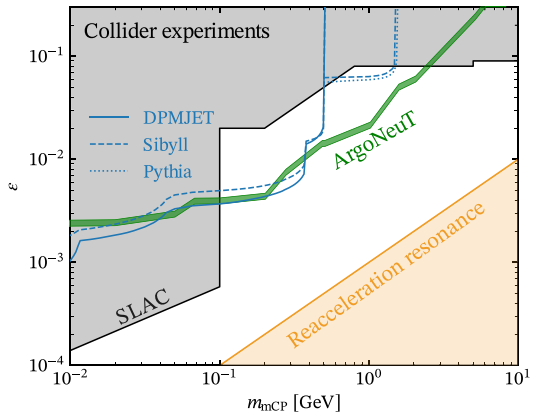

Fig. 6. The upper limit in (m, q)-parameter space of mCPs set by the non-detection supernova neutrino events in Super-Kamiokande [39]. The result is similar to that of Ref. [12]. To put it in perspective, the upper limit set by various collider experiments [43–47] and the ArgoNeuT experiment [41] are shown. The strong limit below the π^0 threshold comes from the search for millicharged particles at SLAC [43]. The lower limit set by the reacceleration condition [21] is only valid if the mCPs make up more that $\sim 10^{-6}$ of the relic abundance.

parameters: its mass m and charge $e\epsilon$. We take into account the decays $\pi^0 \to \{\bar\chi\chi, \bar\chi\chi\gamma\}$, $\eta \to \{\bar\chi\chi, \bar\chi\chi\gamma\}$, $\rho \to \bar\chi\chi$, $\omega \to \{\bar\chi\chi, \bar\chi\chi\pi^0\}$, $\phi \to \bar\chi\chi$ and $J/\psi \to \bar\chi\chi$. The corresponding branching ratios are estimated by rescaling the dilepton and diphoton branching ratios, as explained in Appendix A. We handle the $1 \to 3$ decays using the decay subroutines in Pythia 8, whereas the momentum distribution in the $1 \to 2$ decays is taken to be monoenergetic and isotropic in the rest frame of the mother particle.

The integrated mCP fluxes computed using DPMJET and Sibyll are shown in Fig. 5 as a function of the mCP mass. The result obtained for J/ψ using Pythia is also shown. The step-like behavior arises from the various thresholds at $m_m/2$, as indicated in the figure. In addition, we show the integrated mCP flux with a cutoff at the Lorentz factor $\gamma_{\rm mCP} = E/m_{\rm mCP} = 6$, which corresponds approximately to the cut-off of the Super-Kamiokande experiment used in their search for relic supernova neutrinos [39] (see Appendix B): The upper line of the shaded gray region corresponds to the mCP flux for $\gamma_{\rm mCP} > 6$ calculated with DPMJET, while the lower line uses Sibyll.

For completeness, we also show an exclusion plot using data from Super-Kamiokande [39] employing the procedure introduced in Ref. [12]. A brief description of the procedure is given in Appendix B. The result is shown in Fig. 6 where it is compared to a minor subset of existing limits (see e.g. Ref. [40] for additional bounds). Intriguingly, the limit set by atmospheric mesons is comparable to the existing strong limit set by the ArgoNeuT experiment [41]. Note also that neutrino detectors may have a significantly lower threshold energy than used here for Super-Kamiokande. For example, the Borexino detector has in principle a threshold of ~ 200 keV only limited by the natural presence of ^{14}C [42]. Thus, the limit set by atmospheric mesons could in principle be significantly improved. This strengthens the importance of an accurate description of atmospheric mesons, and motivates future work on using neutrino detectors to search for exotic physics as introduced in Ref. [12].

4. Summary

In this work we have computed the flux of atmospheric mesons by simulating hadronic air showers using the event generators DPMJET III 19.1, Pythia 8.303, QGSJET II-04, Sibyll 2.3d and UrQMD 3.4. The emphasis was put on Sibyll and DPMJET, as they describe well the

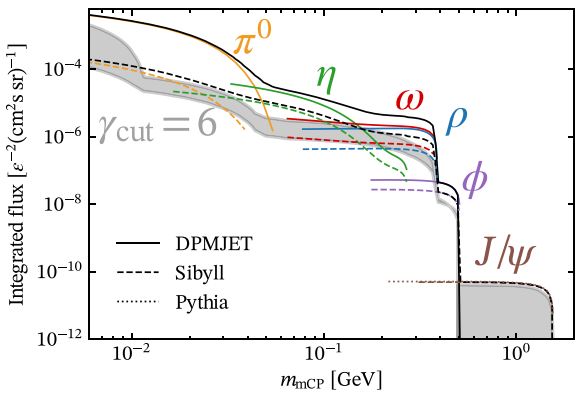

Fig. 5. The integrated flux of mCPs from meson decays in the atmosphere for varying mCP mass using DPMJET (solid), Sibyll (dashed) and Pythia (dotted; only J/ψ) are shown in black. The contributions from the different meson species are indicated using the same colors as in Fig. 2. The shaded gray region indicates the integrated flux above $\gamma_{\rm cut} = 6$.

total production cross sections and are fast. Moreover, the difference between these two event generators may serve as an estimate for the theoretical uncertainties of our flux predictions. We have focused on the production of mesons with large electromagnetic decay channels, π^0, η, ρ, ω, ϕ and J/ψ.

This work was motivated by Ref. [12], where the meson fluxes produced in pp collisions at the top of the atmosphere were computed by fitting various parametrizations to measurements of meson production cross sections. The obtained fluxes were in turn used to set constraints on generic BSM models with a (meta-)stable millicharged component. Our results are in good agreement with those of Ref. [12]. The largest differences (up to orders of magnitude at low meson energies) arise due to the different treatment of the cross sections. The Monte Carlo approach has several advantages compared to using parametrizations: secondary interactions as well as the effect of interacting nuclei can be taken into account. Moreover, no assumption has to be made on the momentum dependence of the differential cross section. By comparing the results obtained using DPMJET and Sibyll for mesons more massive than π^0 we found an estimated uncertainty of the theoretical predictions of a factor 2–3. This uncertainty is larger than the changes resulting from adding secondary interactions and simulating helium as projectile and nitrogen as target. The effect of the larger interaction threshold in Sibyll compared to DPMJET is small for all considered mesons, except for π^0 at low meson energies.

Our tabulated results can be used to evaluate the flux of exotic particles produced by atmospheric meson decays within generic extensions of the standard model. As an example, we re-considered the production of millicharged particles, and found that their production in atmospheric meson decays can set leading constraints in the possible charge-to-mass ratio. The in principle lower thresholds for neutrino experiments is a strong motivation for continuing the study of exotic particles produced in meson decay in the atmosphere.

Declaration of competing interest

The authors declare that they have no known competing financial interests or personal relationships that could have appeared to influence the work reported in this paper.

Acknowledgment

We would like to thank Anatoli Fedynitch for helpful comments on DPMJET III.

Appendix A. Meson branching ratios into millicharged particles

The branching ratios of mesons m into mCPs χ can be found by rescaling the branching ratios of their electromagnetic decay channels into charged leptons $l^{\pm}$. The direct decay of mesons into mCPs, $m \to \bar{\chi}\chi$, the Dalitz decays of pseudoscalar mesons, $P \to \bar{\chi}\chi\gamma$, and the three-particle decay of vector mesons, $V \to \bar{\chi}\chi P$ will give the dominant contributions to the mCP production in hadronic interactions. We use for evaluation[8] of the relevant branching ratios the experimental values given by the particle data group [48].

The branching ratio of a direct meson decay into two mCPs, $m \to \bar{\chi}\chi$, can be found by rescaling the dilepton branching ratio [49] as

$$\frac{\mathrm{BR}(m \to \bar{\chi}\chi)}{\mathrm{BR}(m \to l^+l^-)} = \varepsilon^2 \sqrt{\frac{1-4m_\chi^2/m_m^2}{1-4m_l^2/m_m^2}} \frac{1+2m_\chi^2/m_m^2}{1+2m_l^2/m_m^2}. \tag{A.1}$$

In this work, we consider the direct decays of π^0, η, ρ, ω, ϕ and J/ψ.

[8] We use, except for π^0 decays, muons for comparisons, $l^{\pm} = \mu^{\pm}$.

The branching ratio of a pseudoscalar mesons into a photon and a mCP pair, $P \to \gamma\bar{\chi}\chi$, can be computed by rescaling the diphoton branching ratio [49] as

$$\frac{\mathrm{BR}(P \to \gamma\bar{\chi}\chi)}{\mathrm{BR}(m \to \gamma\gamma)} = \frac{2\alpha\varepsilon^2}{3\pi} \int_{4m_\chi^2}^{m_m^2} \mathrm{d}q^2 \sqrt{1-\frac{4m_\chi^2}{q^2}} \left(1+2\frac{m_\chi^2}{q^2}\right) \times \frac{1}{q^2}\left(1-\frac{q^2}{m_m^2}\right)^3 |F_m(q^2)|^2, \tag{A.2}$$

with $F_m(q^2)$ being the meson form factor and q^2 the invariant mass of the virtual photon. Likewise, the branching ratio for a vector (pseudoscalar) meson into two mCPs and a pseudoscalar (vector) meson is given by

$$\frac{\mathrm{BR}(m \to A\bar{\chi}\chi)}{\mathrm{BR}(m \to \gamma\gamma)} = \frac{\alpha\varepsilon^2}{3\pi} \int_{4m_\chi^2}^{(m_m-m_\chi)^2} \mathrm{d}q^2 \sqrt{1-\frac{4m_\chi^2}{q^2}} \left(1+2\frac{m_\chi^2}{q^2}\right) \frac{1}{q^2} \times \left[\left(1+\frac{q^2}{m_m^2-m_A^2}\right)^2 - \frac{4m_m^2q^2}{(m_m^2-m_A^2)^2}\right]^{3/2} |F_m(q^2)|^2. \tag{A.3}$$

In this work, we consider the three-body decays $\pi^0 \to \gamma\bar{\chi}\chi$, $\eta \to \gamma\bar{\chi}\chi$ and $\omega \to \pi^0\bar{\chi}\chi$. We take into account the meson form factors using the parametrizations from Refs. [48,49]:

$$F_{\pi^0}(q^2) \approx 1 + q^2 b_{\pi^0}, \quad b_{\pi^0} = (5.5 \pm 1.6)\ \mathrm{GeV}^{-2}, \tag{A.4}$$

and

$$F_i(q^2) = \left(1-\frac{q^2}{\Lambda_i^2}\right)^{-1}, \quad \Lambda_\eta = (0.716 \pm 0.011)\ \mathrm{GeV}, \quad \Lambda_\omega = 0.65\ \mathrm{GeV}. \tag{A.5}$$

Appendix B. Upper limit from neutrino experiments

Water Cherenkov detectors like Super-Kamiokande [39] search for the light signal emitted by the relativistic charged particles. Therefore the light signal emitted by the scattered electrons in the elastic interactions $\chi e^- \to \chi e^-$ can be used to constrain the flux of mCP with scatterings within a kinetic energy range $T_{\min} < T < T_{\max}$. This leads to a "windowed cross section" for mCP-electron interactions that can approximated as

$$\tilde{\sigma}_{e\chi}(\gamma_\chi) = \int_{q^2_{\min}}^{q^2_{\max}} \frac{\mathrm{d}\sigma_{e\chi}}{\mathrm{d}q^2}\mathrm{d}q^2 \approx \frac{2\pi\alpha^2\varepsilon^2}{2T_{\min}m_e}\left(1-\frac{T_{\min}}{T_{\max}}\right)\Theta(\gamma_\chi - \gamma_{\mathrm{cut}}) \tag{B.1}$$

with $\gamma_{\mathrm{cut}} \approx 0.6\sqrt{2T_{\min}/m_e} + 0.4\sqrt{2T_{\max}/m_e}$ [12]. The expected number of events is then

$$N_{e\chi} \approx N_e t \int_{\gamma_{\mathrm{cut}}}^{\infty} \tilde{\sigma}_{e\chi}(\gamma_\chi)\frac{\mathrm{d}\Phi_\chi}{\mathrm{d}\gamma_\chi}(\gamma_\chi)\mathrm{d}\gamma_\chi \tag{B.2}$$

with N_e as the number of electrons in the detector and t as the sampling period. For Super-Kamiokande, $T_{\min} = 16$ MeV and $T_{\max} = 88$ MeV [39], corresponding to $\gamma_{\mathrm{cut}} \approx 6$ [12]. Since the event shape of mCPs is similar to that of the supernova background (see Fig. 10 in Ref. [12]), one can make use of the analysis performed in Ref. [39] for Super-Kamiokande, which essentially leads to an exclusion of ~ 4 events are excluded with 90 % CL.

References

[1] M. Ackermann, et al., Searching for dark matter Annihilation from Milky way Dwarf Spheroidal galaxies with six years of Fermi large area telescope data, Phys. Rev. Lett. 115 (23) (2015) 231301, http://dx.doi.org/10.1103/PhysRevLett.115.231301, arXiv:1503.02641.

[2] N. Fornengo, L. Maccione, A. Vittino, Dark matter searches with cosmic antideuterons: status and perspectives, J. Cosmol. Astropart. Phys. 1309 (2013) 031, http://dx.doi.org/10.1088/1475-7516/2013/09/031, arXiv:1306.4171.

[3] M. Kachelrieß, S. Ostapchenko, J. Tjemsland, Revisiting cosmic ray antinuclei fluxes with a new coalescence model, J. Cosmol. Astropart. Phys. 08 (2020) 048, http://dx.doi.org/10.1088/1475-7516/2020/08/048, arXiv:2002.10481.

[4] T. Bringmann, M. Pospelov, Novel direct detection constraints on light dark matter, Phys. Rev. Lett. 122 (17) (2019) 171801, http://dx.doi.org/10.1103/PhysRevLett.122.171801, arXiv:1810.10543.

[5] Y. Ema, F. Sala, R. Sato, Light dark matter at neutrino experiments, Phys. Rev. Lett. 122 (18) (2019) 181802, http://dx.doi.org/10.1103/PhysRevLett.122.181802, arXiv:1811.00520.

[6] A. Kusenko, S. Pascoli, D. Semikoz, New bounds on MeV sterile neutrinos based on the accelerator and Super-Kamiokande results, J. High Energy Phys. 11 (2005) 028, http://dx.doi.org/10.1088/1126-6708/2005/11/028, arXiv:hep-ph/0405198.

[7] P.-f. Yin, S.-h. Zhu, Detecting light long-lived particle produced by cosmic ray, Phys. Lett. B 685 (2010) 128–133, http://dx.doi.org/10.1016/j.physletb.2010.01.067, arXiv:0911.3338.

[8] P.-K. Hu, A. Kusenko, V. Takhistov, Dark Cosmic Rays, Phys. Lett. B 768 (2017) 18–22, http://dx.doi.org/10.1016/j.physletb.2017.02.035, arXiv:1611.04599.

[9] C. Argüelles, P. Coloma, P. Hernández, V. Muñoz, Searches for Atmospheric long-Lived Particles, 2019, arXiv:1910.12839.

[10] P. Coloma, P. Herández, V. Muñoz, I.M. Shoemaker, New constraints on heavy neutral leptons from Super-Kamiokande data, 2019, arXiv:1911.09129.

[11] J. Alvey, M. Campos, M. Fairbairn, T. You, Light dark matter from inelastic Cosmic Ray collisions, Phys. Rev. Lett. 123 (26) (2020) 261802, http://dx.doi.org/10.1103/PhysRevLett.123.261802, arXiv:1905.05776; Phys. Rev. Lett. 123 (2019) 261802.

[12] R. Plestid, V. Takhistov, Y.-D. Tsai, T. Bringmann, A. Kusenko, M. Pospelov, New constraints on Millicharged Particles from Cosmic-ray Production, 2020, arXiv:2002.11732.

[13] A.Y. Ignatiev, V.A. Kuzmin, M.E. Shaposhnikov, Is the electric charge conserved?, Phys. Lett. B 84 (1979) 315–318, http://dx.doi.org/10.1016/0370-2693(79)90048-0.

[14] L.B. Okun, M.B. Voloshin, V.I. Zakharov, Electrical neutrality of atoms and Grand Unification models, Phys. Lett. 138B (1984) 115–120, http://dx.doi.org/10.1016/0370-2693(84)91884-7.

[15] H. Georgi, P.H. Ginsparg, S. Glashow, Photon Oscillations and the Cosmic background radiation, Nature 306 (1983) 765–766, http://dx.doi.org/10.1038/306765a0.

[16] B. Holdom, Two U(1)'s and Epsilon charge shifts, Phys. Lett. 166B (1986) 196–198, http://dx.doi.org/10.1016/0370-2693(86)91377-8.

[17] M.I. Dobroliubov, A.Yu. Ignatiev, Millicharged particles, Phys. Rev. Lett. 65 (1990) 679–682, http://dx.doi.org/10.1103/PhysRevLett.65.679.

[18] P. Fayet, Extra U(1)'s and New Forces, Nuclear Phys. B 347 (1990) 743–768, http://dx.doi.org/10.1016/0550-3213(90)90381-M.

[19] D. Dunsky, L.J. Hall, K. Harigaya, CHAMP cosmic rays, J. Cosmol. Astropart. Phys. 1907 (07) (2019) 015, http://dx.doi.org/10.1088/1475-7516/2019/07/015, arXiv:1812.11116.

[20] S.D. McDermott, H.-B. Yu, K.M. Zurek, Turning off the Lights: How dark is dark matter?, Phys. Rev. D 83 (2011) 063509, http://dx.doi.org/10.1103/PhysRevD.83.063509, arXiv:1011.2907.

[21] M. Kachelrieß, J. Tjemsland, Reacceleration of charged dark matter, J. Cosmol. Astropart. Phys. 10 (2020) 001, http://dx.doi.org/10.1088/1475-7516/2020/10/001, arXiv:2006.10479.

[22] M. Fabbrichesi, E. Gabrielli, G. Lanfranchi, The dark photon, 2020, arXiv:2005.01515.

[23] A. Filippi, M. De Napoli, Searching in the dark: the hunt for the dark photon, Rev. Phys. 5 (2020) 100042, http://dx.doi.org/10.1016/j.revip.2020.100042, arXiv:2006.04640.

[24] J.D. Bowman, A.E.E. Rogers, R.A. Monsalve, T.J. Mozdzen, N. Mahesh, An absorption profile centred at 78 megahertz in the sky-averaged spectrum, Nature 555 (7694) (2018) 67–70, http://dx.doi.org/10.1038/nature25792, arXiv:1810.05912.

[25] E.D. Kovetz, V. Poulin, V. Gluscevic, K.K. Boddy, R. Barkana, M. Kamionkowski, Tighter limits on dark matter explanations of the anomalous EDGES 21 cm signal, Phys. Rev. D 98 (10) (2018) 103529, http://dx.doi.org/10.1103/PhysRevD.98.103529, arXiv:1807.11482.

[26] R. Engel, Photoproduction within the two component dual parton model. 1. Amplitudes and cross-sections, Z. Phys. C 66 (1995) 203–214, http://dx.doi.org/10.1007/BF01496594.

[27] S. Roesler, R. Engel, J. Ranft, The Monte Carlo event generator DPMJET-III, in: International Conference on Advanced Monte Carlo for Radiation Physics, Particle Transport Simulation and Applications (MC 2000), 2000, pp. 1033–1038, http://dx.doi.org/10.1007/978-3-642-18211-2_166, arXiv:hep-ph/0012252.

[28] A. Fedynitch, Cascade Equations and Hadronic Interactions at Very High Energies (Ph.D. thesis), KIT, Karlsruhe, Dept. Phys., 2015, http://dx.doi.org/10.5445/IR/1000055433.

[29] T. Sjöstrand, S. Ask, J.R. Christiansen, R. Corke, N. Desai, P. Ilten, S. Mrenna, S. Prestel, C.O. Rasmussen, P.Z. Skands, An introduction to PYTHIA 8.2, Comput. Phys. Comm. 191 (2015) 159–177, http://dx.doi.org/10.1016/j.cpc.2015.01.024, arXiv:1410.3012.

[30] S. Ostapchenko, Monte Carlo treatment of hadronic interactions in enhanced Pomeron scheme: I. QGSJET-II model, Phys. Rev. D 83 (2011) 014018, http://dx.doi.org/10.1103/PhysRevD.83.014018, arXiv:1010.1869.

[31] S. Ostapchenko, QGSJET-II: physics, recent improvements, and results for air showers, EPJ Web Conf. 52 (2013) 02001, http://dx.doi.org/10.1051/epjconf/20125202001.

[32] F. Riehn, H.P. Dembinski, R. Engel, A. Fedynitch, T.K. Gaisser, T. Stanev, The hadronic interaction model SIBYLL 2.3c and Feynman scaling, PoS ICRC 2017 (2018) 301, http://dx.doi.org/10.22323/1.301.0301, arXiv:1709.07227.

[33] S.A. Bass, et al., Microscopic models for ultrarelativistic heavy ion collisions, Prog. Part. Nucl. Phys. 41 (1998) 255–369, http://dx.doi.org/10.1016/S0146-6410(98)00058-1, arXiv:nucl-th/9803035; Prog. Part. Nucl. Phys. 41 (1998) 225.

[34] G. Agakishiev, et al., Inclusive dielectron spectra in p+p collisions at 3.5 GeV, Eur. Phys. J. A 48 (2012) 64, http://dx.doi.org/10.1140/epja/i2012-12064-y, arXiv:1112.3607.

[35] M. Aguilar-Benitez, et al., Inclusive particle production in 400-GeV/c p p interactions, Z. Phys. C 50 (1991) 405–426, http://dx.doi.org/10.1007/BF01551452.

[36] A. Baldini, V. Flaminio, W.G. Moorhead, D.R.O. Morrison, Total Cross-Sections for Reactions of High Energy Particles (Including Elastic, Topological, Inclusive and Exclusive Reactions) / Totale Wirkungsquerschnitte Für Reaktionen Hochenergetischer Teilchen (Einschließlich Elastischer, Topologischer, Inklusive), in: Landolt-Boernstein - Group I Elementary Particles, Nuclei and Atoms, vol. 12b, Springer, 1988, http://dx.doi.org/10.1007/b35211.

[37] A. Fedynitch, private communication.

[38] R. Engel, D. Heck, T. Pierog, Extensive air showers and hadronic interactions at high energy, Ann. Rev. Nucl. Part. Sci. 61 (2011) 467–489, http://dx.doi.org/10.1146/annurev.nucl.012809.104544.

[39] K. Bays, et al., Supernova relic neutrino search at Super-Kamiokande, Phys. Rev. D 85 (2012) 052007, http://dx.doi.org/10.1103/PhysRevD.85.052007, arXiv:1111.5031.

[40] G. Magill, R. Plestid, M. Pospelov, Y.-D. Tsai, Millicharged particles in neutrino experiments, Phys. Rev. Lett. 122 (7) (2019) 071801, http://dx.doi.org/10.1103/PhysRevLett.122.071801, arXiv:1806.03310.

[41] R. Acciarri, et al., Improved limits on millicharged particles using the ArgoNeuT experiment at Fermilab, Phys. Rev. Lett. 124 (13) (2020) 131801, http://dx.doi.org/10.1103/PhysRevLett.124.131801, arXiv:1911.07996.

[42] G. Alimonti, et al., The Borexino detector at the Laboratori Nazionali del Gran Sasso, Nucl. Instrum. Methods A 600 (2009) 568–593, http://dx.doi.org/10.1016/j.nima.2008.11.076, arXiv:0806.2400.

[43] A.A. Prinz, et al., Search for millicharged particles at SLAC, Phys. Rev. Lett. 81 (1998) 1175–1178, http://dx.doi.org/10.1103/PhysRevLett.81.1175, arXiv:hep-ex/9804008.

[44] S. Chatrchyan, et al., Search for fractionally charged particles in pp collisions at $\sqrt{s} = 7$ TeV, Phys. Rev. D 87 (9) (2013) 092008, http://dx.doi.org/10.1103/PhysRevD.87.092008, arXiv:1210.2311.

[45] S. Davidson, S. Hannestad, G. Raffelt, Updated bounds on millicharged particles, J. High Energy Phys. 05 (2000) 003, http://dx.doi.org/10.1088/1126-6708/2000/05/003, arXiv:hep-ph/0001179.

[46] E. Golowich, R.W. Robinett, Limits on millicharged matter from beam dump experiments, Phys. Rev. D 35 (1987) 391, http://dx.doi.org/10.1103/PhysRevD.35.391.

[47] S. Davidson, B. Campbell, D.C. Bailey, Limits on particles of small electric charge, Phys. Rev. D 43 (1991) 2314–2321, http://dx.doi.org/10.1103/PhysRevD.43.2314.

[48] P. Zyla, et al., Review of particle physics, PTEP 2020 (8) (2020) 083C01, http://dx.doi.org/10.1093/ptep/ptaa104.

[49] L.G. Landsberg, Electromagnetic decays of light mesons, Phys. Rep. 128 (1985) 301–376, http://dx.doi.org/10.1016/0370-1573(85)90129-2.

Paper VII – Comment on "Dark Matter Annihilation Can Produce a Detectable Antihelium Flux through $\bar{\Lambda}_b$ decays"

Kachelrieß, M., Ostapchenko, S. & Tjemsland, J. "Comment on "Dark Matter Annihilation Can Produce a Detectable Antihelium Flux through $\bar{\Lambda}_b$ Decays"". arXiv: 2105.00799 [hep-ph] (May 2021)

Abstract: In a recent Letter, it was suggested that a previously neglected Standard Model process, namely, the production of antihelium-3 nuclei through decays of "$\bar{\Lambda}_b$" baryons can lead to a flux of antihelium-3 from dark matter annihilations detectable by AMS-02. We show that an essential condition for its detectability – the introduction of the "$\bar{\Lambda}_b$" of Pythia – is excluded by a wealth of measurements of (anti-) baryon and (anti-) meson production at accelerators. Moreover, we argue that Monte Carlo generators like Pythia should not be used to predict branching ratios like $\mathrm{BR}(\bar{\Lambda}_b \to \bar{u}\bar{d}u(ud)_0)$, which control the formation rate of antihelium-3. In particular, we show that $\bar{\Lambda}_b$ decays which proceed via diquark formation are overestimated by Pythia using its standard settings, which are further enhanced in the "$\bar{\Lambda}_b$ tune".

After the Letter by Winkler & Linden [Phys.Rev.Lett. 126 (2021) 10, 101101] was accepted for publication, we noticed some secluded, optimistic assumptions that were made in the Letter. In our opinion, this made the idea in the Letter uninteresting for DM searches, and we decided that a Comment was the correct venue to publicly state our disagreement and start a discussion. The comment was submitted to Physical Review Letters, but was not accepted for publication: *"My recommendation is that the Comment submitted by KOT should not be published. I strongly urge the authors to modify their Comment into a regular Letter or Article which would be the proper venue for presenting and detailing their criticisms."* Therefore, for the benefit of the community working on the production of (anti)nuclei, the revised version of the comment is made public by including it in this thesis.

Comment on "Dark Matter Annihilation Can Produce a Detectable Antihelium Flux through $\bar{\Lambda}_b$ Decays"

M. Kachelrieß[1], S. Ostapchenko[2], and J. Tjemsland[1]
[1] *Institutt for fysikk, NTNU, Trondheim, Norway and*
[2] *D.V. Skobeltsyn Institute of Nuclear Physics, Moscow State University, Moscow, Russia*

In a recent Letter, Winkler and Linden [1] (hereafter WL21) suggested that a previously neglected standard model process, namely the production of antihelium-3 nuclei through decays of $\bar{\Lambda}_b$ baryons, can significantly boost the flux of antihelium-3, induced by annihilations or decays of dark matter. This suggestion uses the fact that dark matter particles will annihilate typically into the heaviest quark–anti-quark pair, i.e. $\bar{b}b$ pairs, if the particle is a Majorana fermion and its mass is below the mass of the standard model gauge bosons [2]. These (anti-) b quarks will in turn hadronise and form (anti-) b-mesons and (anti-) b-baryons which then decay weakly. As pointed out by WL21, the $\bar{\Lambda}_b$ baryon is especially suited for the production of antihelium-3 through a coalescence process, because its rest mass of 5.6 GeV is not much above the rest mass of 5 (anti)-nucleons. As a result of the small relative momenta of these nucleons, the production of antihelium-3 via coalescence is enhanced in $\bar{\Lambda}_b$ decays.

A condition that the scenario of WL21 leads to a detectable antihelium flux is that the branching ratio $\mathrm{BR}(b \to \Lambda_b)$ is sufficiently large. In order to achieve such a large branching ratio, WL21 increased the diquark formation parameter `probQQtoQ` of Pythia in their so-called "$\bar{\Lambda}_b$ tune". WL21 noted that this change also significantly boosts prompt antinucleon production. They compensated the resulting over-production of antideuterons by reducing at the same time the coalescence momentum, which is a free parameter in their approach, by a factor 0.6.

The conceptual error of WL21 is that the change of `probQQtoQ` cannot simply be compensated by a reduction of the coalescence momentum, since this change affects all types of processes involving baryon and meson production. As an example, one can consider (anti-) proton production in electron-positron annihilations, $e^+e^- \to \bar{p}pX$. For a change of `probQQtoQ` from the default value 0.09 to 0.24—which is the value reproducing the value of the branching ratio $b \to \Lambda_b = 0.1$ chosen in WL21—the resulting proton multiplicity is compared in Table 1 to measurements. For instance at $\sqrt{s} = 91\,\mathrm{GeV}$, the predicted proton multiplicity in the "$\bar{\Lambda}_b$ tune" is 33σ away from the one measured [3]. For comparison, the standard settings in Pythia predict a Λ_b multiplicity in electron-positron annihilations at the Z-resonance of 0.016, which is less than $1\,\sigma$ away from the value 0.031 ± 0.016 given in Ref. [3].[1] As an example for the effects of a changed diquark formation parameter on pp collisions, we show in Table 2 the integrated yield at mid-rapidity, $\mathrm{d}N/\mathrm{d}y\,|_{|y|<0.5}$, of protons, kaons and pions measured by ALICE at LHC at $\sqrt{s} = 7\,\mathrm{TeV}$ [4]. Note also that the increased diquark formation reduces the production rate of all mesons, aggravating the variance of the "$\bar{\Lambda}_b$ tune" with observations. The offset in the production of light baryons do translate into a significant increase in the antihelium-3 yield (cf. Fig. 2). In fact, even if Pythia is only off recent averages of f_{baryon} by a factor ~ 2, the fix by WL21 increases the antihelium-3 flux by an order of magnitude. Finally, the condition not to overproduce the antiproton flux measurements [5] from AMS-02 requires to reduce the annihilation rate of dark matter in the "$\bar{\Lambda}_b$ tune" relative to the value allowed using the default version of Pythia.

$\sqrt{s}$	$\approx 10\,\mathrm{GeV}$	29–35 GeV	91 GeV	130–200 GeV
Obs.	0.266 ± 0.008	0.640 ± 0.050	1.050 ± 0.032	1.41 ± 0.18
WL21	0.640	1.161	2.102	2.33

TABLE I: Multiplicity of (anti-) protons in electron-positron annihilations

Particle	proton	kaon	pion
$\mathrm{d}N/\mathrm{d}y$, LHC	0.124 ± 0.009	0.286 ± 0.016	2.26 ± 0.10
$\mathrm{d}N/\mathrm{d}y$, Λ_b tune	0.328	0.231	1.90

TABLE II: Measurements of $\mathrm{d}N/\mathrm{d}y$ at mid-rapidity ($|y| < 0.5$) in proton-proton collisions at $\sqrt{s} = 7\,\mathrm{TeV}$ for p, K^+ and π^+

Another caveat in the approach of WL21 is the use of Pythia to "predict" the branching ratio $\mathrm{BR}(\bar{\Lambda}_\mathrm{b} \to \bar{\mathrm{u}}\mathrm{du}(\mathrm{ud})_0) = 0.012$ which controls the formation rate of antihelium-3. Such ratios are external input parameters into Pythia, which represent in the case of yet unobserved decays simply educated guesses. In this specific case, the ratio is $\simeq |V_{ub}|^2/|V_{cb}|^2$, while one expects an additional suppression due to the diquark present in the decay channel. Comparing branching ratios of such

[1] Note that WL21 use an old average of f_{baryon} in their tuning. In fact, according to the recent world average 0.088 ± 0.012 given in [6], both standard Pythia and the Λ_b tune are off by just over 3σ. The standard settings of Pythia underpredicts this number by less than a factor 2.

$\bar{\Lambda}_b$, B_0 or $\bar{\Lambda}_c^+$ decays to observations, we find indeed that Pythia overestimates their rate by a factor 4–5, which is further enhanced in the Λ_b tune. In particular, Pythia using the standard settings overestimates the measured branching ratio $\mathrm{BR}(\bar{\Lambda}_\mathrm{b} \to \Lambda_\mathrm{c}^- \bar{\mathrm{p}}\mathrm{p}\pi^+) = (2.65 \pm 0.29) \times 10^{-4}$ [3] by a factor 5.6 and in the Λ_b-tune by a factor 17. This corresponds to a 42σ and 144σ deviation from measurements, respectively. Reducing $\mathrm{BR}(\bar{\Lambda}_\mathrm{b} \to \bar{\mathrm{u}}\mathrm{du}(\mathrm{ud}_0))$ correspondingly would make the antihelium-3 flux undetectable for AMS-02 even if the "$\bar{\Lambda}_b$ tune" would be viable.

In conclusion, the "$\bar{\Lambda}_b$ tune" of Pythia which WL21 argue to lead to an antihelium-3 flux detectable by AMS-02 is excluded by a wealth of measurements of (anti-) baryon and (anti-) meson production at accelerators. Even so, the future observation of (anti-) helium-3 production in baryon decays can potentially have a profound impact on the study of hadronisation, as noted already by WL21. This rate varies by orders of magnitude between event generators based on different hadronisation models and may thus be used to discriminate these models. Even though we have only discussed Pythia in this comment, the same considerations also apply to the other MC configurations examine by WL21. The three MCs that yielded a significant increase in the antihelium production (Pythia, Λ_b tune and Herwig+EvtGen) all rely on the same hadronisation procedure and similar decay tables to describe the decay of Λ_b. The only independent MC, Herwig, yielded no significant increase.

We would like to thank Philip Ilten, Uli Nierste and Torbjörn Sjöstrand for helpful comments.

[1] M. W. Winkler and T. Linden, Phys. Rev. Lett. **126**, no.10, 101101 (2021) doi:10.1103/PhysRevLett.126.101101 [arXiv:2006.16251 [hep-ph]].

[2] H. Goldberg, Phys. Rev. Lett. **50**, 1419 (1983) Erratum: [Phys. Rev. Lett. **103**, 099905 (2009)]. doi:10.1103/PhysRevLett.103.099905, 10.1103/PhysRevLett.50.1419

[3] P. A. Zyla *et al.* [Particle Data Group], PTEP **2020**, no.8, 083C01 (2020) doi:10.1093/ptep/ptaa104

[4] J. Adam *et al.* [ALICE], Eur. Phys. J. C **75** (2015) no.5, 226 doi:10.1140/epjc/s10052-015-3422-9 [arXiv:1504.00024 [nucl-ex]].

[5] M. Aguilar *et al.* [AMS], Phys. Rev. Lett. **117**, no.9, 091103 (2016) doi:10.1103/PhysRevLett.117.091103

[6] Y. Amhis *et al.* [HFLAV Collaboration], Eur. Phys. J. C **77** (2017) no.12, 895 doi:10.1140/epjc/s10052-017-5058-4 [arXiv:1612.07233 [hep-ex]].

Paper VIII – On the origin and the detection of characteristic axion wiggles in photon spectra

Kachelrieß, M. & Tjemsland, J. "On the origin and the detection of characteristic axion wiggles in photon spectra". *JCAP* **01,** 025. arXiv: 2111.08303 [astro-ph.HE] (2022)

Abstract: Photons propagating in an external magnetic field may oscillate into axions or axion-like particles (ALPs). Such oscillations will lead to characteristic features in the energy spectrum of high-energy photons from astrophysical sources that can be used to probe the existence of ALPs. In this work, we revisit the signatures of these oscillations and stress the importance of a proper treatment of turbulent magnetic fields. We implement axions into ELMAG, a standard tool for modelling in a Monte Carlo framework the propagation of gamma-rays in the Universe, complementing thereby the usual description of photon-axion oscillations with a Monte Carlo treatment of high-energy photon propagation and interactions. We also propose an alternative method of detecting axions through the discrete power spectrum using as observable the energy dependence of wiggles in the photon spectra.

We started this work by implementing photon-ALP oscillations into the photon propagation program `ELMAG`, allowing for a wide range of possible applications. When we noticed the effect that the modeling of the magnetic field had on the ALP signals in photon spectra, we decided to write a paper with a focus on the importance of a proper treatment of the magnetic field. In addition, we included a part about detection of ALP wiggles using the discrete power spectrum, an idea motivated by work on the Earth matter effects on neutrino oscillations [*JCAP* 06 (2003) 006, *JCAP* 01 (2004) 004].

Journal of Cosmology and Astroparticle Physics
An IOP and SISSA journal

On the origin and the detection of characteristic axion wiggles in photon spectra

M. Kachelrieß and J. Tjemsland

Institutt for fysikk, NTNU,
Trondheim, Norway

E-mail: Michael.Kachelriess@ntnu.no, Jonas.Tjemsland@ntnu.no

Received November 23, 2021
Accepted December 27, 2021
Published January 17, 2022

Abstract. Photons propagating in an external magnetic field may oscillate into axions or axion-like particles (ALPs). Such oscillations will lead to characteristic features in the energy spectrum of high-energy photons from astrophysical sources that can be used to probe the existence of ALPs. In this work, we revisit the signatures of these oscillations and stress the importance of a proper treatment of turbulent magnetic fields. We implement axions into `ELMAG`, a standard tool for modelling in a Monte Carlo framework the propagation of gamma-rays in the Universe, complementing thereby the usual description of photon-axion oscillations with a Monte Carlo treatment of high-energy photon propagation and interactions. We also propose an alternative method of detecting axions through the discrete power spectrum using as observable the energy dependence of wiggles in the photon spectra.

Keywords: dark matter theory, extragalactic magnetic fields, gamma ray theory

ArXiv ePrint: 2111.08303

JCAP01(2022)025

 https://doi.org/10.1088/1475-7516/2022/01/025

Contents

1 Introduction

The Standard Model of particle physics has attained immense success over the years. Yet, it has several theoretical shortcomings such as the strong CP problem. Moreover, there are some experimental indications for its incompleteness, with the absence of a suitable dark matter candidate as the most striking one. As a solution to the strong CP problem, Peccei and Quinn [1, 2] postulated in 1977 the existence of an additional U(1) symmetry that is spontaneously broken, thereby giving rise to a Nambu-Goldstone boson — the axion a. The two-gluon-axion vertex introduced to solve the strong CP problem induces a small axion mass through pion mixing, $m_a f_a \approx m_\pi f_\pi$, degrading the axion to a pseudo-Goldstone boson [3, 4]. Intriguingly, this promotes the axion into a suitable cold dark matter candidate despite its small mass if it is produced through, e.g., the so-called misalignment mechanism [5–8]. Other light pseudo-scalars bosons which have the same characteristic two-photon coupling as the axion, $\mathcal{L} = -\frac{1}{4} g_{a\gamma} F_{\mu\nu} \tilde{F}^{\mu\nu} = g_{a\gamma} \boldsymbol{E} \cdot \boldsymbol{B}$, are collectively known as axion-like particles (ALPs). In the case of the QCD axion, the two-photon vertex is inherited from the two-gluon vertex, thus fixing the relation of the mass and decay constant as $|g_{a\gamma}|\text{GeV} \approx 10^{-16} m_a/\mu\text{eV}$ up to a $\mathcal{O}(1)$ constant [9] (see ref. [10] for a recent review on axion models). While ALPs do not solve the strong CP problem, they are theoretically well motivated as they arise naturally in string theories and other extensions of the Standard Model [11, 12].

Most axion and ALP searches are based on their two-photon coupling, see e.g. refs. [13, 14] for recent reviews. Such a coupling leads to a conversion between photons and axions in the presence of an external magnetic field. This phenomenon has been utilised in, e.g., the ADMX haloscope [15] and the CAST helioscope [16] experiments which aim to reconvert respectively DM and solar axions in the fields of strong magnets. The most extensive limits on the coupling at sub-eV masses, $g_{a\gamma} < 6.6 \times 10^{-11}$, are currently set by CAST ($m_a \lesssim$ eV) [16] and by studying the lifetime of stars in the horisontal branch ($m_a \lesssim$ keV) [17]. The planned "shine light through a wall" experiment ALPS-II [18] and solar axion experiment

JCAP01(2022)025

IAXO [19] are expected to improve these limits significantly. At present, however, the possible mass of the QCD axion is practically unconstrained at sub-eV masses. An exception is the ADMX haloscope which excludes some parts of the QCD axion parameter space around few μeV under the condition that axions account for the observed dark matter. The planned ABRACADABRA [20] experiment is expected to improve limits on axionic dark matter immensely, while the IAXO experiments will probe QCD axions in the 1 meV$\sim$1 eV mass range [19].

The leading limits on $g_{a\gamma}$ for ALPs with $m_a \lesssim 10^{-6}\,\mathrm{eV}$, $g_{a\gamma} \lesssim (10^{-13}\text{–}10^{-11})\,\mathrm{GeV}^{-1}$, are currently set by astrophysical observations which utilise that the two-photon coupling leads to a number of interesting changes in gamma-ray spectra. Most notably, photon-ALP oscillations may effectively increase the mean-free path of photons in the extragalactic background light (EBL), since ALPs travel practically without any interactions [21]. Additionally, photon-axion oscillations may lead to characteristic features in the spectra of astrophysical sources of high-energy photons. The most stringent limits on $g_{a\gamma}$ for sub-μeV masses rely on the non-observation of such spectral signatures and are derived from, e.g., gamma-ray observations by HESS [22], Fermi-LAT [23], of SN1987A [24], and X-ray observations of Betelgeuse [25], the active galactive nuclei NGC1275 [26], the cluster-hosted quasar H1821+643 [27] and super star clusters [28]. The former two focus on "irregularities" induced by photon-axion oscillations, while the latter three focus on the production of axions through the Primakoff effect. A significant improvement is expected from the upcoming Cherenkov Telescope Array (CTA) [29]. The interpretation of such results depend, however, significantly on the treatment of the magnetic fields in and around the source as well as in the extragalactic space [30–33]. This applies in particular for the turbulent component of the magnetic field, for which often only oversimplified models are used. Moreover, one should note that large scale spectral features can also be produced by a number of astrophysical effects, including e.g. an electron-beam driven pair cascade [34] or even cascades from primary gamma-rays or nuclei [35]. It is therefore important to identify the features characteristic for axion-photon[1] oscillations.

In this work, we study the effect of photon-axion oscillations in a Monte-Carlo framework based on the `ELMAG`[2] code [36, 37], which is a Monte Carlo program made to simulate electromagnetic cascades initiated by high-energy photons interacting with the extragalactic background light. The use of `ELMAG` allows us to include properly the interplay of cascading and oscillations, and in addition `ELMAG` provides tools to generate turbulent magnetic fields. We consider for concreteness only a turbulent extragalactic magnetic field, but `ELMAG` can use any magnetic field as input. We discuss the characteristic signatures expected in the photon spectra from distant gamma-ray sources, and using domain-like and Gaussian turbulent fields as examples, show that the predicted signatures depend rather strongly on the chosen magnetic field model. As a result, we argue that while the application of domain-like magnetic fields may be tenable for some quantitative discussions, it should be abandoned in qualitative studies. Finally, we propose the use of the discrete power spectrum to detect photon-axion oscillations in upcoming gamma-ray experiments such as CTA. This method directly uses the expected characteristic signatures as observable, namely the energy-dependent wiggles in the photon spectra induced by photon-axion oscillations. We show that these signatures can in principle be used to infer information about the magnetic field environment. While we focus oscillatory features in photon spectra, which we call axion wiggles, we comment also

[1] We will from now on refer to both axions and ALPs simply as 'axions'.

[2] The code used in this work will be made publicly available in a future release of `ELMAG`.

JCAP01(2022)025

on the effect of photon-axion oscillations on the opacity of the Universe. In particular, we show that the apparent size of this effect depends strongly on the approximation used for the turbulent magnetic field.

This paper is structured as follows: in section 2, we present the numerical treatment of photon-axion oscillations and our Monte Carlo implementation. Next, we discuss in section 3 the treatment of turbulent magnetic fields. Thereafter, in section 4, we discuss the characteristic oscillatory features produced by photon-axion oscillations in the photon spectra and their dependence on the modelling of the magnetic field, followed by examples in section 5. In section 6, we present the suggestion to use the energy dependence of the oscillatory features as observable in the detection of axions. Finally, we comment on the importance of a proper treatment of the magnetic fields when considering the opacity of the Universe, before we conclude in section 8.

2 Numerical implementation of photon-axion oscillations

The physics underlying photon-axion oscillations is discussed clearly in the classic paper by Raffelt and Stodolsky [38]. Here, we only highlight the main features of the Lagrangian[3] describing the low-energy interactions between axions, photons and vacuum fluctuations of electrons,

$$\begin{aligned}\mathcal{L} = \mathcal{L}_{aa} + \mathcal{L}_{a\gamma} + \mathcal{L}_{\gamma\gamma} = \frac{1}{2}\partial^\mu a \partial_\mu a - \frac{1}{2}{m_a}^2 a^2 - \frac{1}{4} g_{a\gamma} F_{\mu\nu}\tilde{F}^{\mu\nu} a \\ - \frac{1}{4}F_{\mu\nu}F^{\mu\nu} + \frac{\alpha^2}{90{m_e}^4}\left[(F_{\mu\nu}F^{\mu\nu})^2 + \frac{7}{4}(F_{\mu\nu}\tilde{F}^{\mu\nu})^2\right].\end{aligned} \tag{2.1}$$

The first two terms describe the axion a as a free scalar field with mass m_a, while the third term includes the interaction of axions with photons, which in the presence of an external magnetic field will result in axion-photon oscillations. The last term is the Euler-Heisenberg effective Lagrangian that takes into account vacuum polarisation effects below the creation threshold of electron-positron pairs. In particular, this term leads to a refractive index for photons in an external electromagnetic field which influences the propagation and oscillation of axions and photons. Following the usual convention of the wave vector $\boldsymbol{k}$ pointing in the direction of the photon electric field, the refractive indices of the photon in the longitudinal ($\parallel$) and transverse ($\perp$) directions are given by

$$n_\perp = 1 + \frac{4}{2}\xi \qquad \text{and} \qquad n_\parallel = 1 + \frac{7}{2}\xi \tag{2.2}$$

with $\xi \equiv (\alpha/45\pi)(B_\perp/B_{\rm cr})^2$.

The Lagrangian (2.1) leads after linearisation to the equation of motion

$$(E + \mathcal{M} - \mathrm{i}\partial_z)\,\phi(z) = 0, \tag{2.3}$$

where we denote the energy of photons and axions by E, have chosen the z-axis as propagation direction and have introduced the wave function

$$\phi(z) = \begin{pmatrix} A_\perp \\ A_\parallel \\ a \end{pmatrix}. \tag{2.4}$$

[3]We use rationalised natural units with $\hbar = c = 1$ and $\alpha = e^2/4\pi \simeq 1/137$. Then the critical magnetic field is given by $B_{\rm cr} = m_e^2/e \simeq 4.414 \times 10^{13}\,\mathrm{G}$.

JCAP01(2022)025

The mixing matrix is given by

$$\mathcal{M} = \begin{pmatrix} \Delta_\perp & 0 & 0 \\ 0 & \Delta_\parallel & \Delta_{a\parallel} \\ 0 & \Delta_{a\parallel} & \Delta_a \end{pmatrix}, \tag{2.5}$$

where $\Delta_{\parallel,\perp} = (n_{\parallel,\perp} - 1)E$ and $\Delta_a = -{m_a}^2/(2E)$. The two polarisation states of the photon are given as linear polarisation states perpendicular and parallel to the transverse magnetic field at a given position. The off-diagonal terms lead to photon-axion mixing in the presence of an external magnetic field,

$$\Delta_{a\parallel} = \frac{g_{a\gamma}}{2} B_\perp. \tag{2.6}$$

In general, the diagonal terms $\Delta_{\parallel,\perp}$ in eq. (2.3) should include the total refractive index of the photon. Other contributions describing the photon dispersive effects of the medium and the EBL, as well as the chosen numerical values, will be discussed in section 4.

It is useful to consider the propagation through a homogeneous magnetic field to obtain an understanding of the problem. In this case, eq. (2.3) simplifies to

$$\left[E - \mathrm{i}\partial_z + \begin{pmatrix} \Delta_\parallel & \Delta_{a\parallel} \\ \Delta_{a\parallel} & \Delta_a \end{pmatrix}\right] \begin{pmatrix} A_\parallel \\ a \end{pmatrix} = 0. \tag{2.7}$$

The photon conversion probability then becomes

$$P_s(\gamma \to a) = \left|\left\langle A_\parallel(0) \middle| a(s) \right\rangle\right|^2 = \left(\Delta_{a\parallel} s\right)^2 \frac{\sin^2(\Delta_{\mathrm{osc}} s/2)}{(\Delta_{\mathrm{osc}} s/2)^2} \tag{2.8}$$

with

$$\Delta_{\mathrm{osc}}^2 = (\Delta_\parallel - \Delta_a)^2 + 4\Delta_{a\parallel}^2. \tag{2.9}$$

Similarly, the oscillation length in any sufficiently smooth environment is given by $L_{\mathrm{osc}} \simeq 2\pi/\Delta_{\mathrm{osc}}$. Thus, one can see that the oscillation length, the correlation length L_{c} of the magnetic field and the mixing strength $2\pi/\Delta_{a\parallel}$ are the main parameters determining the effects of photon-axion oscillations. For example, when $\Delta_{\mathrm{osc}} \sim 2\Delta_{a\parallel}$, we enter the strong mixing regime where eq. (2.8) gives $P_s(\gamma \to a) = \sin^2(\Delta_{a\parallel} s)$.

We describe now how the photon-axion equation of motion (2.3) is implemented into `ELMAG` [36, 37]. For convenience, we will refer to the superposition of a photon and an axion as a 'phaxion'. The probability that the phaxion interacts with the EBL at position s is $\mathrm{d}P = P_s(\gamma \to \gamma)\sigma_{\mathrm{pair}}(s)\,\mathrm{d}s$ with $P_s(\gamma \to \gamma) = 1 - P_s(\gamma \to a)$. This is equivalent to checking first whether a photon would interact at that position and next to account for the probability that a phaxion would be measured as a photon. This motivates the following numerical scheme which takes into account the absorption of photons:

1. start with a pure photon with an energy drawn from the distribution for the injection energy. For an unpolarised gamma-ray source, choose randomly a linear polarisation state.

2. Draw the interaction length of a phaxion, λ, at the current position in accordance to the mean free path length a photon.

3. Propagate the phaxion from s to $s + \lambda$ according to the phaxion equation of motion.

JCAP01(2022)025

4. If $P_{\gamma\gamma} > r$ for a random number r chosen from a uniform distribution $r \in [0, 1]$, the phaxion wave function collapses into a photon and the photon undergoes pair production in interaction with the EBL. If not, go to point 2.

5. Treat the electromagnetic cascade that arises, and for each photon go to point 2.

The Monte Carlo treatment of the photon-axion oscillations implemented in this work has several advantages compared to conventional (semi-)analytical approaches (see e.g. ref. [39] and references therein) and the procedure in ref. [40], at the cost of being computationally more demanding. First, the implementation of realistic magnetic fields and additional effects like an inhomogeneous electron density is trivial. Second, photon absorption can be considered on an event-by-event basis and the resulting electromagnetic cascade can be accounted for. Third, polarisation effects are by default included. Finally, this method allows to include the effect of photon-axion oscillations into other studies of electromagnetic cascades. For example, a potential increase in the size of gamma-ray halos around astrophysical sources because of the increased mean-free path of photon could be studied using `ELMAG` in a straight-forward way, see e.g. ref. [41] for a recent review on the subject.

3 Turbulent magnetic fields

We describe in this work turbulent magnetic fields as isotropic, divergence-free Gaussian random fields with zero mean, r.m.s. value $B_{\rm rms}$ and zero helicity. The algorithm implemented in `ELMAG` for the generation of such fields is based on the method suggested in refs. [42, 43] and described in ref. [37]. In this approach, the turbulent magnetic field is modelled as a superposition of n left- and right-circular polarised Fourier modes. The spectrum of the modes is chosen as a power-law

$$B_j = B_{\rm min}(k_j/k_{\rm min})^{-\gamma/2} \tag{3.1}$$

between $k_{\rm min}$ and $k_{\rm max}$, corresponding to the largest $L_{\rm max} = 2\pi/k_{\rm min}$ and smallest scales $L_{\rm min} = 2\pi/k_{\rm max}$, respectively. The quantity $B_{\rm min}$ is fixed by normalising the total field strength to $B_{\rm rms}$. The coherence length is in turn connected to $L_{\rm max}$ and $L_{\rm min}$ as

$$L_{\rm c} = \frac{L_{\rm max}}{2}\frac{\gamma-1}{\gamma}\frac{1-(L_{\rm min}/L_{\rm max})^{\gamma}}{1-(L_{\rm min}/L_{\rm max})^{\gamma-1}} \simeq \frac{L_{\rm max}}{2}\frac{\gamma-1}{\gamma}, \tag{3.2}$$

the last equality being valid for $L_{\rm min} \ll L_{\rm max}$. For definiteness, we will consider a time-independent $B_{\rm rms}$ and a Kolmogorov spectrum with $\gamma = 5/3$ for which $L_{\rm c} \simeq L_{\rm max}/5$.

In the literature, a so-called domain-like magnetic field has often been used to describe photon-axion oscillations in turbulent astrophysical magnetic fields, see e.g. [26, 27, 39, 40, 44–50]. In this approach, the magnetic field along the line of sight is divided into patches with size equal to the coherence length $L_{\rm c}$ of the field. The field in each patch is assumed to be homogeneous, while its direction is chosen randomly. Such an approximation certainly breaks down when the oscillation length becomes smaller than the coherence length, $L_{\rm osc} \lesssim L_{\rm c}$: in this case, oscillations probe the magnetic field structure on scales smaller than the domain size, which are neglected in this simple model. Thus, a more realistic description of the turbulent magnetic field, including fluctuations on various scales, should be used.

In the case of a large oscillation length, $L_{\rm osc} \gtrsim L_{\rm c}$, on the other hand, one may expect the approximation of domains to be valid since the power of the turbulent magnetic field is

JCAP01(2022)025

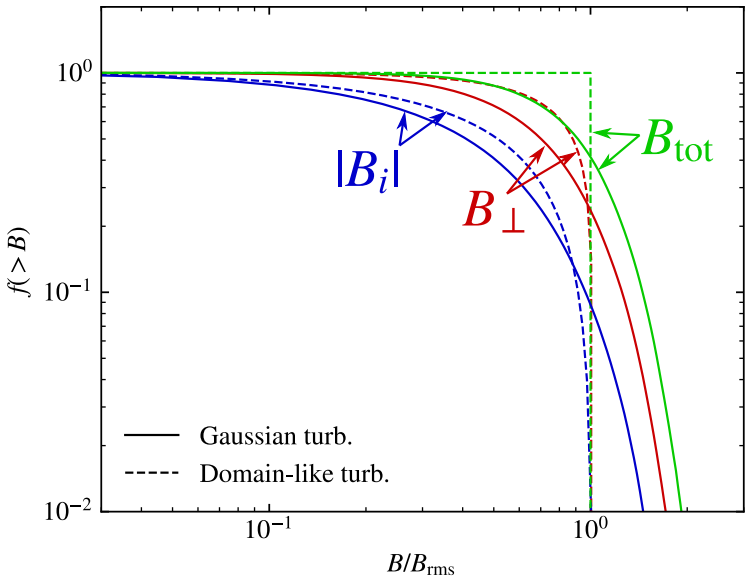

Figure 1. The cumulative distribution $f(B)$ of the magnetic field strengths for the turbulent (solid lines) and domain-like (dashed lines) cases are compared. The total magnetic field strength is shown in green, transverse strength in red and the strength in a given direction in blue.

contained mainly in its large-scale modes for $\gamma > 1$. However, also in this limit the large-scale fluctuations of the turbulent field will lead to important differences in the photon conversion relative to the domain-like case. To visualise these effects, the cumulative distribution of the magnetic field, i.e. the fraction $f(> B)$ of volume filled with a magnetic field stronger than B, is compared for the two models in figure 1.[4] Since the fluctuations of the turbulent magnetic field are spread over a large range of scales, the variance of the perpendicular field is greater and extends to larger field strengths than in the domain-like case. Considering single field realisations — as should be done for the study of single sources — in the domain-like case thus underestimates the expected "cosmic variance".

The effects discussed above are clearly visible in figure 2, where we plot the photon survival probability as a function of the oscillation length for a propagation distance equal to twelve coherence lengths choosing the parameters[5] of the extragalactic field as $B_{\rm rms} = B_{\rm tot} = 10^{-12}\,{\rm G}$ and $L_{\rm c} = 2\,{\rm Mpc}$, while the axion parameters were set to $m_a = 10^{-10}\,{\rm eV}$, $g_{a\gamma} = 10^{-16}\,{\rm eV}^{-1}$. The average photon survival probability from 100 realisations for a turbulent (blue solid) and a domain-like field (red solid) are shown. The opaqueness of the blue lines indicates the number of modes included; $n_k = \{2, 10, 20, 50, 100\}$ from the lightest to the darkest line. The result for a single realisation of the magnetic field is shown in dashed lines for comparison. The general energy dependence of the survival probability is similar for the two magnetic field models: below a given threshold energy determined by $\Delta_{\rm osc} \sim \Delta_{a\gamma}$, the

[4]Since the distribution of the magnetic fields for the Gaussian turbulent field and domain-like turbulence only depends on $B_{\rm rms}$, figure 1 remains unchanged if the coherence length L_c or the slope γ is changed.

[5]We set $L_{\rm min} = 0.01\,{\rm Mpc}$ and $L_{\rm max} = 5\,{\rm Mpc}$.

JCAP01(2022)025

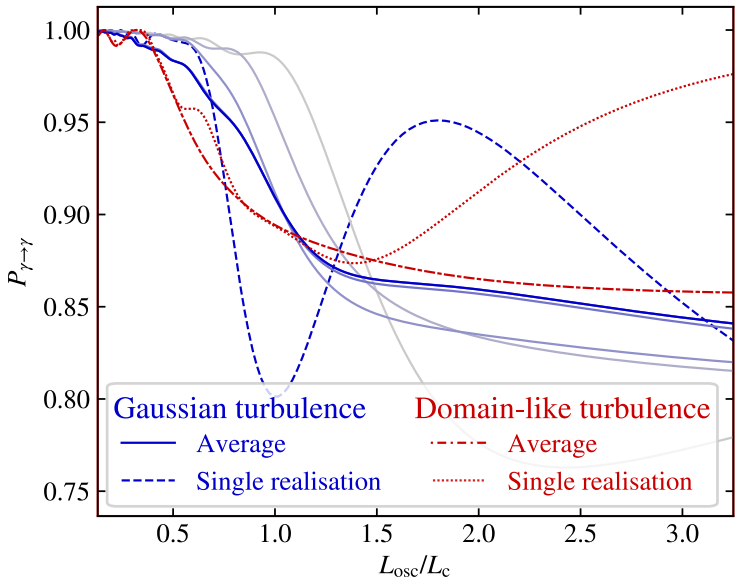

Figure 2. The average photon survival probability after 12 coherence lengths as a function of the oscillation length using 100 realisations is shown in for Gaussian (blue solid lines) and domain-like (red dashed dotted lines) turbulence. The oscillation length is computed by setting $B_\perp \simeq B$, and the parameters $m_a = 10^{-10}\,\mathrm{eV}$, $g_{a\gamma} = 10^{-16}\,\mathrm{eV}^{-1}$, $B_{\rm rms} = B_{\rm tot} = 10^{-12}\,\mathrm{G}$ and $L_{\rm c} = 2\,\mathrm{Mpc}$ are used. The results for a single realisation are shown in dashed lines and dotted lines. The opaqueness of the blue lines indicate the number of modes n_k included in the generation of the Gaussian turbulence as described in the text; $n_k = \{2, 10, 20, 50, 100\}$ from lightest to darkest.

survival probability is close to unity. Above the threshold energy, we are in the strong mixing regime. There are, however, clear differences in the detailed behaviour. Most notably, the oscillations for a turbulent field are smoothed out by the variation in the transverse magnetic field strength compared to the domain-like case. Furthermore, the survival probabilities predicted using the two magnetic field models differ even in the case when $L_{\rm c} > L_{\rm osc}$, as expected from the discussion in the previous paragraph. Meanwhile, the change induced by the increase of the number of modes[6] shows the importance of an accurate description of magnetic field also on small-scales. It is interesting to note that ref. [39] introduced a linear interpolation between the magnetic fields in the domain-like approach in order to resolve the discontinuities in the domain-like magnetic fields. While this approach leads to a slight smoothening of the peaks observed in figure 2 for the domain-like magnetic field, other effects like the variation for different realisations and the shift in the threshold energy are not reproduced in this approach.

[6]The normalisation is kept constant while additional modes are added towards smaller scales. Therefore, the total energy stored in the magnetic field increases slightly with increasing number of included modes in this example.

JCAP01(2022)025

4 Parameter space of photon-axion oscillations

Photon-axion oscillations are essentially determined by the axion parameters (m_a and $g_{a\gamma\gamma}$) and the refractive indices induced by the magnetic field, the medium and the EBL. In addition, the propagation distance and the photon energy enter the problem. The effect of the magnetic field via the QED vacuum polarisation, $\Delta_{\parallel,\perp}^{\rm QED}$, was already discussed in section 2. Among the medium effects, we neglect the Faraday contribution as the random direction of the turbulent magnetic field averages out its effect, as well as the Cotton-Mouton effect. Then the effective mass of the photon in a plasma,

$$m_{\rm pl} \simeq \omega_{\rm pl} = \sqrt{\frac{4\pi\alpha n_e}{m_e}} \simeq 0.0371 \left(\frac{n_e}{1\,{\rm cm}^{-3}}\right)^{1/2} {\rm neV}, \tag{4.1}$$

leads to the only additional contribution induced by the medium, $\Delta_{\parallel,\perp}^{\rm pl} = -m_{\rm pl}^2/(2E)$ [38]. In addition, the EBL and starlight may have profound effects on the refractive index at large energies, as first realised in ref. [51]. The isotropic EBL influences the two polarisation states equally, and its contribution is given by

$$\Delta_{\rm EBL} \simeq \Delta_{\rm CMB} \simeq 0.522 \cdot 10^{-42} E. \tag{4.2}$$

This approximation is valid below the pair creation threshold $E_{\rm th,CMB} \simeq 400\,{\rm TeV}$ on CMB photons, which are dominating the contribution of the EBL to the photon refractive index. In summary, we take into account the most important additional effects on the photon refractive index by using $\Delta_{\parallel,\perp} = \Delta_{\parallel,\perp}^{\rm QED} + \Delta_{\rm CMB} + \Delta_{\rm pl}$ in the mixing matrix (2.5).

For the ease of comparison and identification of scales in different astrophysical environments, we will consider in the following as numerical values for these free parameters

$$\begin{aligned}
\Delta_{\parallel}^{\rm QED} &= 1.5 \times 10^{-9}\,{\rm Mpc}^{-1} \left(\frac{E}{10^{11}\,{\rm eV}}\right) \left(\frac{B_\perp}{10^{-9}\,{\rm G}}\right)^2, \\
\Delta_{\parallel}^{\rm pl} &= -1.1 \times 10^{-10}\,{\rm Mpc}^{-1} \left(\frac{n_e}{10^{-7}\,{\rm cm}^{-3}}\right) \left(\frac{E}{10^{11}\,{\rm eV}}\right)^{-1}, \\
\Delta_{\parallel}^{\rm CMB} &= 8.2 \times 10^{-3}\,{\rm Mpc}^{-1} \left(\frac{E}{10^{11}\,{\rm eV}}\right), \\
\Delta_{a} &= -7.8 \times 10^{-3}\,{\rm Mpc}^{-1} \left(\frac{m_a}{10^{-10}\,{\rm eV}}\right)^2 \left(\frac{E}{10^{11}\,{\rm eV}}\right)^{-1}, \\
\Delta_{a\parallel} &= 1.5 \times 10^{-2}\,{\rm Mpc}^{-1} \left(\frac{B_\perp}{10^{-9}\,{\rm G}}\right) \left(\frac{g_{a\gamma}}{10^{-20}\,{\rm eV}^{-1}}\right).
\end{aligned} \tag{4.3}$$

We note that the value of the extragalactic magnetic field — which is often used in the literature — is close to the limits derived in refs. [52, 53].

In general, photon-axion oscillations depend both on the magnetic field strength and the plasma density. However, we can eliminate one of the two variables using the conservation of magnetic flux in a plasma. Then the magnetic field lines are frozen to the fluid elements and, neglecting dissipation and dynamo effects, we can employ the simple scaling relation

$$n_e \simeq n_{e,0} \left(\frac{B}{B_0}\right)^{\eta}, \tag{4.4}$$

JCAP01(2022)025

with $\eta = 3/2$ for isotropic volume changes. For concreteness, we set as reference $B_0 = \mu$G and $n_{e,0} = 0.02\,\mathrm{cm}^{-3}$ which is suitable for the Milky Way[7] [54]. Although this scaling should not be considered a general rule, it is sufficient for the purposes in this paper.

From the homogeneous solution (2.8), one can further conclude that the photon conversion probability will be governed by the relative ratios of $\Delta_{\rm osc}^{-1}$, $\Delta_{a\parallel}^{-1}$, $L_{\rm c}$ and the distance s travelled. That is, in order to have a significant conversion of photons, one must have a sizeable amount of oscillations ($s\Delta_{\rm osc} \gtrsim 1$) and a sizeable mixing ($\Delta_{a\parallel} \sim \Delta_{\rm osc}$). The coherence length, meanwhile, determines the intrinsic behaviour of the conversion probability: if $L_{\rm c} \gg 2\pi/\Delta_{\rm osc}$ the conversion probability "probes" the magnetic field with several oscillations per coherence length and the photon state parallel to the transverse magnetic field is completely mixed with the axion for each coherence length. If $L_{\rm c} \ll 2\pi/\Delta_{\rm osc}$, on the other hand, the magnetic field changes quickly so that the mixing slowly converges. Observationally, one can measure the energy spectrum of single gamma-ray sources, which means that one can probe the energy dependence of the photon-axion oscillation probability. The only energy dependence of the characteristic parameters lies in $\Delta_{\rm osc}$ and its generic behaviour is the same for all astrophysical environments (see also ref. [39] for a similar discussion):

1. $\Delta_{\rm osc} \sim E^{-1}$ at low energies. Here, the oscillation length is determined by the effective photon mass or the axion mass, depending on the magnetic field strength and the axion parameters.

2. $\Delta_{\rm osc} \sim E^{0}$ at intermediate energies. This is the strong mixing regime where the oscillation length is determined by the mixing term, $\Delta_{\parallel} \sim 2\Delta_{a\parallel}$.

3. $\Delta_{\rm osc} \sim E^{1}$ at large energies. The oscillation length is here determined by either the CMB or the vacuum polarisation depending on the magnetic field strength.

The transitions between these regimes occur around the energies $E_{\rm min}$ and $E_{\rm max}$ defined by $4\Delta_{a\parallel} = (\Delta_{\parallel} - \Delta_a)^2$. Depending on the treatment of the magnetic fields, the oscillation probability in the transition region vary. For instance, the larger variance in $B_\perp$ seen in figure 1 for a turbulent field will lead to a larger variance in the threshold energies $E_{\rm min}$ and $E_{\rm max}$. This will effectively reduce or even cancel oscillations close to the thresholds upon averaging and shift the threshold energies, as already seen in figure 2. In section 6, we will discuss how these generic energy dependence can be used as an observable in the search for axion-photon oscillations in astrophysical environments.

The discussions above can be summarised in the energy-magnetic field plane, as shown in figure 3 choosing the axion parameters[8] as in eq. (4.3). This plot is essentially a representation of $\Delta_{\rm osc}$ as function of energy and the transverse magnetic field strength. The red lines indicate the value of $\Delta_{\rm osc}$ in terms of $\Delta_{a\parallel}$, and the brown lines its value. The transverse magnetic field value and its 1σ distribution (from figure 1) is shown for three field strengths indicating the upper limit for extragalactic fields, a typical value for the Galactic magnetic field and for field close to sources. The three regions, $\Delta_{\rm osc} \sim E^{-1}$, $\Delta_{\rm osc} \sim E^{0}$ and $\Delta_{\rm osc} \sim E^{1}$, are indicated in the figure. Furthermore, the parameter space is divided into five regions

[7] Although we focus on extragalactic environments in this work, the galactic environment is put as reference since plasma effects are negligible for extragalactic propagation, as we soon will see. However, for magnetic fields $B \sim (10^{-9}$–$10^{-10})$ G one obtains $n_e \sim (6 \times 10^{-7}$–$2 \times 10^{-8})\,\mathrm{cm}^{-3}$, suitable for extragalactic space.

[8] Note that a change in the magnetic field strength is equivalent to the inverse change of the coupling strength (with the exception of the contribution from the plasma), since the product of these two quantities determines the oscillation amplitude.

JCAP01(2022)025

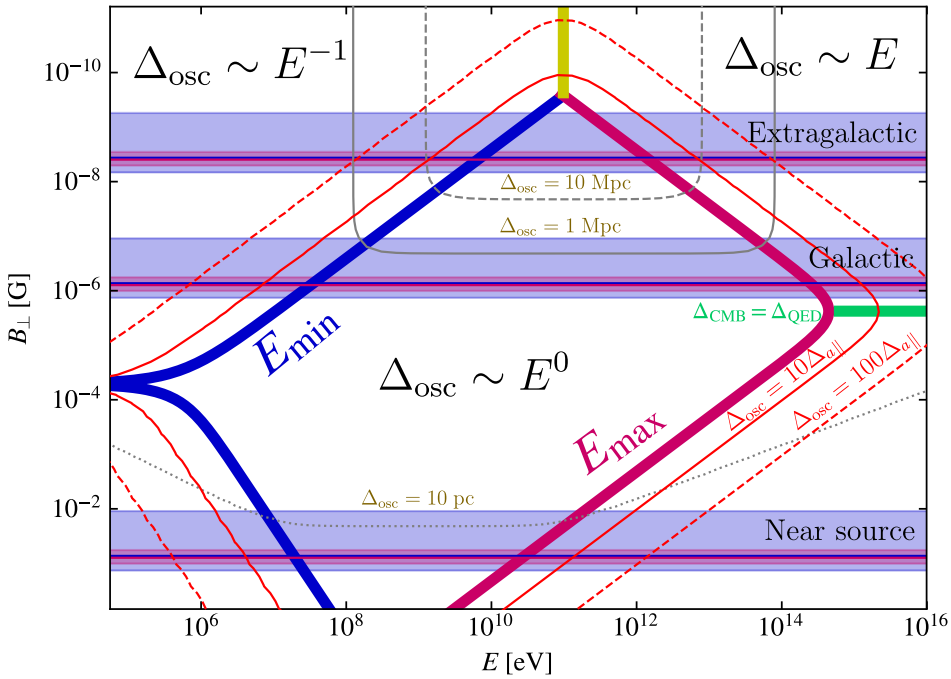

Figure 3. Visualisation of the photon-axion parameter space as explained in the text. The space is split into five main parts depending on the main contribution to the oscillation wave number $\Delta_{\rm osc}$: Δ_a (upper left), $\Delta_{\rm pl}$ (lower left), $\Delta_{a\parallel}$ (middle), $\Delta_{\rm CMB}$ (upper right) and $\Delta_{\rm QED}$ (lower right). The transition to the strong mixing regime $\Delta_{\rm osc} \sim \Delta_{\rm a\parallel}$ occurs at $E_{\rm min}$ and $E_{\rm max}$ as indicated in blue and red thick lines, respectively. The value of $\Delta_{\rm osc}$ is shown in brown lines for 10 pc, 1 Mpc and 10 Mpc, while its value in terms of $\Delta_{a\parallel}$ is shown in red lines. Furthermore, the magnetic field strength and variation for Gaussian and domain-like turbulences for extragalactic, galactic and "source near" environments are shown in shaded blue and red regions. For convenience, we have used $B \simeq B_\perp$ in this plot.

depending on the dominant contributions to $\Delta_{\rm osc}$: axion mass (upper left), plasma (lower left), mixing (middle), CMB (upper right) and QED (lower right). For very weak magnetic field strengths, there is no strong mixing regime and so the transition is marked in yellow. Likewise, the transition from a CMB to a QED dominated refractive index is shown in green. As an example of how this plot can be used, consider the extragalactic magnetic field: at low energies, the oscillations will be governed by the axion mass term Δ_a. In the energy range $E = 10^9$–10^{12} eV, we are in the strong mixing regime where there are no energy-dependent oscillations. The exact energy of this transition will vary by around an order of magnitude for different realisations of the Gaussian turbulence. The energy oscillations will occur close to, but outside, the strong mixing regime, and their strength depends on $\Delta_{\rm osc}/\Delta_{a\parallel}$. These features will be shown explicitly with an example in the next section. A short discussion on how figure 3 changes with m_a is given in the appendix.

An interesting region in parameter space is where the plasma contribution cancels (on average) the axion contribution, $|\Delta_a| = |\Delta_{\rm pl}|$. According to the previous discussions, the strong mixing regime will then extend to arbitrary low energies, potentially reaching the

JCAP01(2022)025

CMB. The homogeneity of the CMB can in principle thus be used to set stringent bounds on $g_{a\gamma}$ for specific m_a. Interestingly, from figure 3 one notes that this "resonance" transition will always occur in the passage from a typical gamma-ray source to its surrounding with weaker magnetic fields. It should be noted, however, that the resonance region should be comparable to the oscillation length in order to have detectable effects. Such a resonance transition in the early Universe has previously been discussed in ref. [55], where the homogeneity of the CMB was used to set limits on the axion parameters.

5 Characteristic axion signatures

In order to apply the concepts discussed in the previous sections, we consider now two concrete, albeit over-simplified, examples. A more realistic example will be considered in the next section, wherein we introduce a method of detecting the characteristic wiggles in the photon spectrum from a physical source.

We consider a photon source at a distance of 5 Mpc for the parameters given in eq. (4.3). The resulting photon survival probabilities using different models for the magnetic field are shown in figure 4 as a function of the photon energy. Averaging over 100 realisations, we see the same characteristics as before: at low and high energies, the photon survival probability is close to unity, while there is a strong mixing regime at intermediate energies. However, there are even after averaging clear differences in the results caused by the treatment of the magnetic field. Importantly, the variation in the survival probability between realisations is much larger using a turbulent field than in the domain-like treatment, in accordance to the variation in the magnetic field itself shown in figure 1. Looking at single realisations, one can clearly see the effect of the energy-dependent oscillation length. That is, the energy spectrum will have wiggles with a wave number scaling with $\Delta_{\rm osc}$, where the energy dependence of $\Delta_{\rm osc}$ at low energies is $\Delta_{\rm osc} \sim E^{-1}$, then $\Delta_{\rm osc} \sim$ const. and finally at high-energies $\Delta_{\rm osc} \sim E^{1}$. We note in particular that even though the oscillations on average cancel in a turbulent magnetic field, the oscillations in a single realisation — which is the relevant case for observations — may be huge.

Next, we consider in figure 5 the same set-up but for a fixed energy, $E = 10^{11}\,\text{eV}$, as function of the distance for 10^4 realisations of the magnetic field. The average photon conversion probability increases, as expected, slowly towards 1/3. Again, the relative variation for different realisations of the turbulent field is much larger than for the domain-like case, although the average values are similar. Interestingly, the survival probability for a single magnetic field realisation can vary almost over all the allowed range of values. This implies that the oscillation probability for a specific source can deviate strongly from the average, as already discussed in refs. [30, 56]. Moreover, the large "cosmic variance" prevents to define a characteristic signal which can be probed as function of the source distance.

An interesting observation is that the convergence time for the turbulent field is much larger than for the domain-like one at large distances. At short distances, the conversion probability is slightly larger for the turbulent field, cf. also figure 4. This can be understood by the following argument. The average conversion probability for a photon in a domain-like turbulence with *constant transverse magnetic field*, $B_\perp$, is [44, 57]

$$P_{\gamma\to a} = \frac{1}{3}\left(1 - \mathrm{e}^{-r/L_\tau}\right), \tag{5.1}$$

where $L_\tau = 2L_{\rm c}/3P$ and P is given by eq. (2.8). In figure 5, the strong mixing regime was considered, in which case P depends on the magnetic field as $P = \sin^2(B_\perp g_{a\gamma} L_{\rm c})/4 \sim$

JCAP01(2022)025

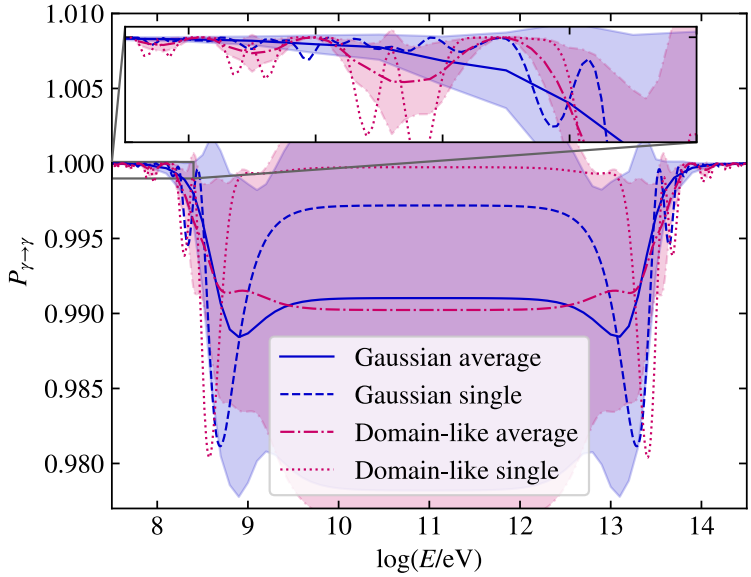

Figure 4. The photon survival probability for polarised photons propagating through five coherence lengths is plotted as a function of energy. The coherence length is set to $L_c = 1\,\mathrm{Mpc}$, and the axion parameters and extragalactic magnetic field parameters in eq. (4.3) are used. The average of 100 realisations of the magnetic field is plotted for Gaussian (blue solid) and domain-like turbulence (red dashed dotted), with their corresponding standard deviations indicated by the shaded regions. The results from a single realisation is shown in dashed and dotted lines, respectively. To better visualise the oscillations outside the strong mixing regime, a portion of the plot is enlarged.

$B_\perp^2 + \mathcal{O}(B_\perp^4)$. The decay rate will thus be dominated by $\langle B_\perp^2 \rangle$, which is larger for domain-like than for a turbulent field. For the domain-like turbulence we have $\langle B_\perp^2 \rangle = 0.67 B_{\mathrm{tot}}$. Because of the small variation in $B_\perp$, the analytical approximation (5.1) reproduces well the numerical results for the domain-like case. A turbulent field has, on the other hand, a larger variation in the transverse magnetic field. Moreover, the coherence length characterizes only on average the "typical" size of turbulent domains. Both effects lead to a distance dependence that differs significantly from eq. (5.1).

6 Direct detection of photon-axion oscillations

Although the wiggles after averaging over realisations of the turbulent field tend to disappear, the oscillatory behaviour in single realisations may be large. Moreover, the detection of these wiggles is made more difficult by the finite energy resolution of realistic experiments. Therefore, it is common to use either the increased photon survival probability at large energies (i.e. the opacity of the Universe) [21, 46–48, 58], the presence of large scale excesses in photon spectra [59–61] or the presence of irregularities in photon spectra (i.e. the variance in residuals) [45] to probe the existence of axion-photon oscillations.

Here we propose instead to use the energy-dependent frequency of the wiggles themselves as observable. A similar concept has previously been used to study the Earth-matter effect

JCAP01(2022)025

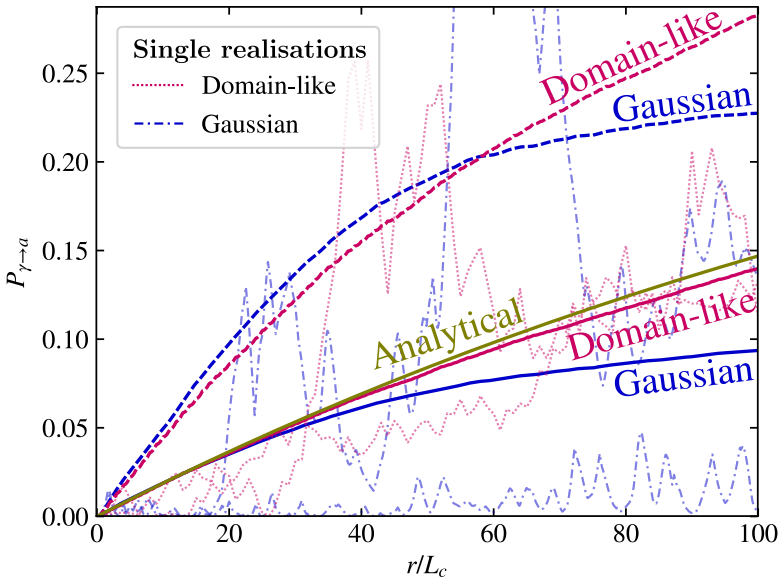

Figure 5. The average photon survival probability for polarised photons is plotted as a function of distance for 10^4 realisations of the magnetic fields and a fixed energy, $E = 10^{11}\,\mathrm{eV}$. The same parameters and color scheme as in figure 4 are used. The solid lines indicate the averaged results, while the dashed lines indicate their 1σ variation. Furthermore, the results from two single realisations are shown in dashed dotted (Gaussian) and dotted (domain-like) lines for visualisation. Finally, the analytical approximation (eq. (5.1)) is shown in yellow for comparison.

on neutrino oscillations [62–65] by considering the windowed power spectrum

$$G(k) = |g(k)|^2 = \left| \int_{\eta_{\min}}^{\eta_{\max}} \mathrm{d}\eta\, q(\eta) \mathrm{e}^{\mathrm{i}\eta k} \right|^2 , \tag{6.1}$$

where η is a function of energy and $q(\eta)$ is the observed neutrino flux from a hypothetical source. The oscillations are energy dependent and the strongest close to the strong-mixing regime. Thus, the window $(\eta_{\min}, \eta_{\max})$ should be chosen such that it includes the oscillations that can be resolved, while excluding the strong-mixing regime to remove noise. For large energies, the oscillation length $L_{\mathrm{osc}} \sim 2\pi/\Delta_{\mathrm{osc}}$ scales as E, while at low energies it scales with E^{-1}. Therefore, we expect clear peaks in the power spectrum with $\eta \sim E^{-1}$ or $\eta \sim E^{1}$. The windowing has unfortunately a major drawback that must be handled with care: it induces a low-frequency peak which may interfere with the signal peaks (see eq. (6.1) with $q = 1$),

$$G_{\mathrm{window}} = 2\,\frac{1 - \cos k\Delta\eta}{k^2}. \tag{6.2}$$

According to eq. (6.2), the power spectrum converges towards one as k^{-2}. This method shows the importance of a proper treatment of the magnetic field: as discussed in the previous sections, the characteristic signatures induced by photon-axion oscillations in more realistic magnetic field models are expected to have a larger cosmic variance and thus to be harder to detect than in simplified models.

JCAP01(2022)025

For practical purposes, it is more relevant to consider the discrete power spectrum

$$G_N(k) = N \left| \frac{1}{N} \sum_{\text{events}} \mathrm{e}^{\mathrm{i}\eta k} \right|^2 , \tag{6.3}$$

where the sum goes over detected events. Choosing the correct energy scale η and an optimal window $(\eta_{\min}, \eta_{\max})$, one may observe a peak that exceeds the expected background. The location of the signal peak depends on the periodicity of the wiggles and the chosen window. For example, in a homogeneous magnetic field the photon survival probability depends on the oscillation length via eq. (2.8). With $\eta = \Delta_{\text{osc}}(E)$ the signal peak will be located around the distance travelled, $k_{\text{peak}} = s$. We can, however, look for the generic features discussed in section 4: one expects peaks in two different window regions and having different energy dependencies, one at low energies with $\eta \sim E^{-1}$ and one with $\eta \sim E$ at larger energies. A similar concept was introduced in ref. [66]. There, the idea was to search for sinusoidal axion signatures in photon spectra by analysing the Fourier-transformed data or performing a sinusoidal fit.

To exemplify the suggestion of using the power spectrum to detect photon axion oscillations, we plot in figure 6 the photon distribution (first row) and the discrete power spectrum (second row) for two realisations of the turbulent magnetic field with the parameters given in eq. (4.3) for a source at redshift $z = 0.02$ and a turbulent field with $B_{\text{rms}} = 5\,\text{nG}$ and $L_{\max} = 10\,\text{Mpc}$. In addition, we plot in the last row the power spectrum multiplied by k^2 to better distinguish the peak from the background. The opaqueness of the lines indicates the number of photons used in the analysis. The signal peak is clearly visible by eye, and becomes visible already for $\mathcal{O}(1000)$ photons in these examples. A proper analysis may therefore yield a significant improvement in the sensitivity compared to previously suggested approaches. Furthermore, this problem may be a well-suited for machine learning that potentially can make the method even more sensitive.

Finally, we would like to comment on the interesting discussions recently given in ref. [67]. Here, it was shown that to first order in the coupling, eq. (2.3) can be solved in the interaction picture outside the strong mixing regime to obtain the polarised photon-conversion probability[9]

$$P_{\gamma_i \to a}(\eta) = \left| -\mathrm{i} \int_0^{s_{\max}} \mathrm{d}s' \, \Delta_{a\parallel}(s') \mathrm{e}^{-\mathrm{i}\eta s'} \right|^2 = \frac{g_{a\gamma}^2}{4} \left| \int_0^{\infty} \mathrm{d}s' \, B_i(s') \mathrm{e}^{\mathrm{i}\eta s'} \right|^2 \equiv \frac{g_{a\gamma}^2}{4} |\mathcal{F}[B(s)](\eta)|^2, \tag{6.4}$$

which in turn can be connected to the auto-correlation function of the magnetic field. Interestingly, photon-axion oscillations are therefore (within these assumptions) determined by the auto-correlation function. Since the autocorrelation function contains less information than the magnetic field, different magnetic fields may share the same autocorrelation function. This means that the framework introduced in ref. [67] allows for a more efficient scanning over magnetic field configurations in axion searches. There are, however, a few complications that must be considered: the description is not valid close to the strong mixing regime where the oscillations are the strongest, it does not apply to the full energy range, and one still need to make assumptions on the magnetic fields. Furthermore, the photon conversion probability predicted from the autocorrelation function is highly sensitive to small changes in the autocorrelation function (see e.g. figure 3 in ref. [67]). The most suitable

[9] The integration limit has been extended to infinity by assuming that B_i vanishes at $s_{\max}$.

JCAP01(2022)025

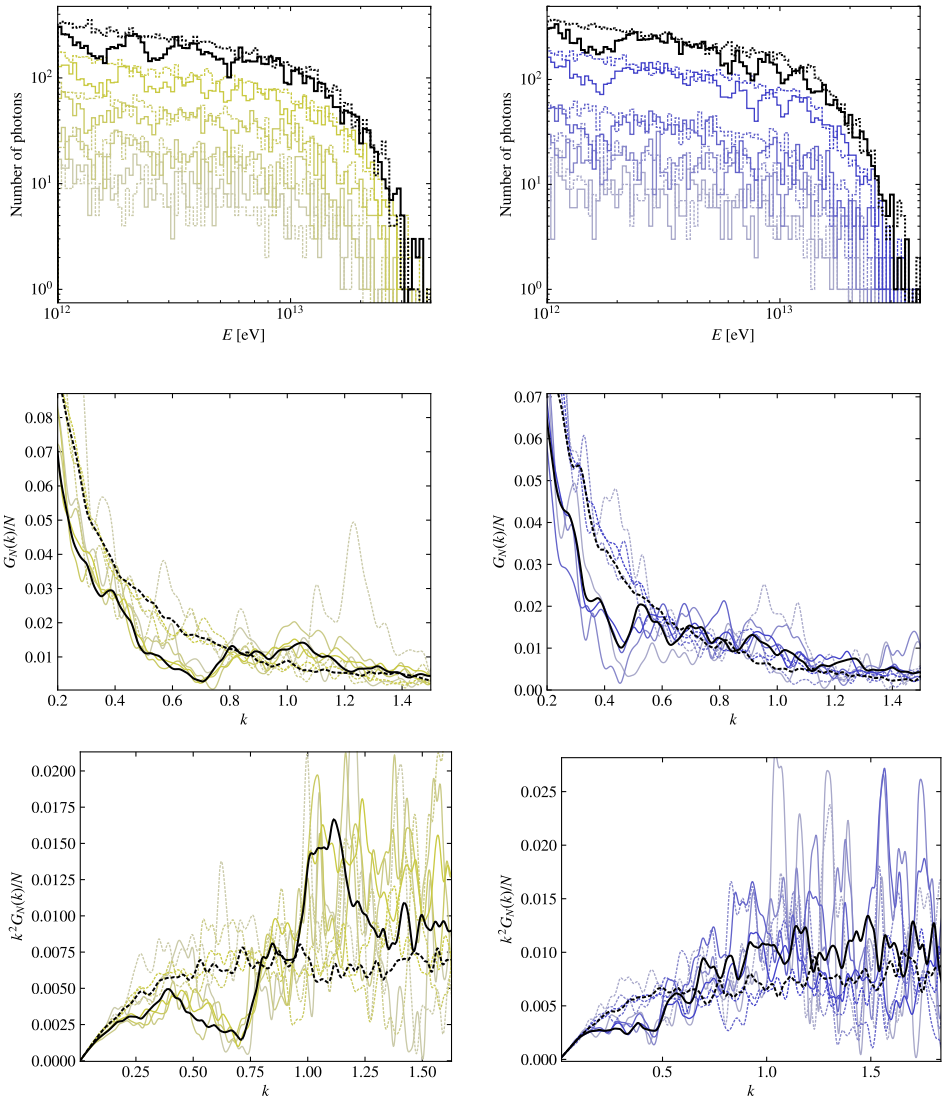

Figure 6. The photon spectrum with the number of photons per bin (first row), photon power spectrum (second row), and the photon spectrum multiplied by k^2 from a source at redshift $z = 0.02$ influenced by a Gaussian turbulence are shown for two realisations. The parameters in eq. (4.3) are used.

approach to photon-axion oscillations is therefore in our opinion to look for generic features of photon-axion oscillations in photon spectra without considering specific magnetic field environments, and from that infer information of the magnetic fields. In fact, computing the

JCAP01(2022)025

power spectrum of the conversion probability, it follows that

$$G(k) = \frac{g_{a\gamma}}{4} \int_0^{z_{\max}} \mathrm{d}z\, B(z) B^*(z-k) = \frac{g_{a\gamma}}{4} \int_{-\infty}^{\infty} \mathrm{d}k\, B(k) B^*(k) \mathrm{e}^{\mathrm{i}\eta k}, \tag{6.5}$$

which means that if axions are detected, one can in theory use the power spectrum of the oscillations, as shown e.g. in figure 6, to directly infer information about the magnetic field. One of the main advantages of using the discrete power spectrum compared to standard approaches of using fit residuals (such as mentioned in ref. [67]), is that no information on the microstructure of the axion wiggles is lost by the binning of the data.

7 Opacity of the universe

The focus in this work has been on the origin and the characterisation of axion wiggles in photon spectra, their detection and the effect of the magnetic fields. However, there is an additional important signature of photon-axion oscillations that can be used to probe the existence of axions: since axions propagate practically without any interactions, there will be an increased photon survival probability at large energies, thus decreasing the opacity of the Universe. In ref. [47], the difference in the apparent opacity using a turbulent and a domain-like magnetic field was already considered.

In order to strengthen our message that one should refrain from using domain-like turbulence in quantitative studies on axion oscillations, we plot in figure 7 the normalised flux from a source with the injection spectrum $\mathrm{d}N/\mathrm{d}E \propto E^{-1.2}$ at a distance $z = 1$ for the magnetic field and axion parameters given in eq. (4.3). The flux obtained averaged over many realisations of the magnetic field is shown as a solid (dashed) line for a Gaussian turbulent (domain-like) field, with the shaded regions corresponding to the 1σ variance between single realisations. In order to increase the statistics at high energies, we take into account the photon absorption by including a complex term $\mathrm{i}\lambda$ in the equation of motion that describes the mean free path length of the photon,[10] and update the mean free path length at redshift increments $\Delta z = 10^{-3}$. In other words, the photon attenuation is treated as a continuous change in the photon survival probability, in contrast to the Monte Carlo treatment of the electromagnetic cascade that is considered elsewhere in this work. As a basis for comparison and to check our numerical calculations, we plot also the spectrum obtained for a single realisation of the magnetic field using a Gaussian turbulent field with continuous attenuation (red squares) and the Monte Carlo treatment of the electromagnetic cascade (green circles). Furthermore, the spectrum obtained with the electromagnetic cascade without axions, i.e. using `ELMAG` without photon-axion oscillations, is shown (blue diamonds). The error bars are computed as the statistical 1σ Poisson uncertainty of the counts in a given bin, and reflect thus only the statistical uncertainty of the Monte Carlo run.[11]

It is clear from figure 7 that photon axion oscillations lead to a decreased opacity of the Universe. However, with the parameters considered here, the difference between the two treatments of the magnetic field leads to a significant difference in the predicted average flux which is increasing with energy: at $E \simeq 1\,\mathrm{TeV}$ the difference is around a factor 20. This

[10] This implies that only prompt photons are considered. However, the effect of cascade photons is negligible since the spectra are dominated by prompt photons.

[11] The number of injected photons in each energy bin is uniformly distributed. In the simulation with the continuous attenuation, all injected photons contribute to the statistics by a weight corresponding to the photon survival probability, making the error bars energy independent.

JCAP01(2022)025

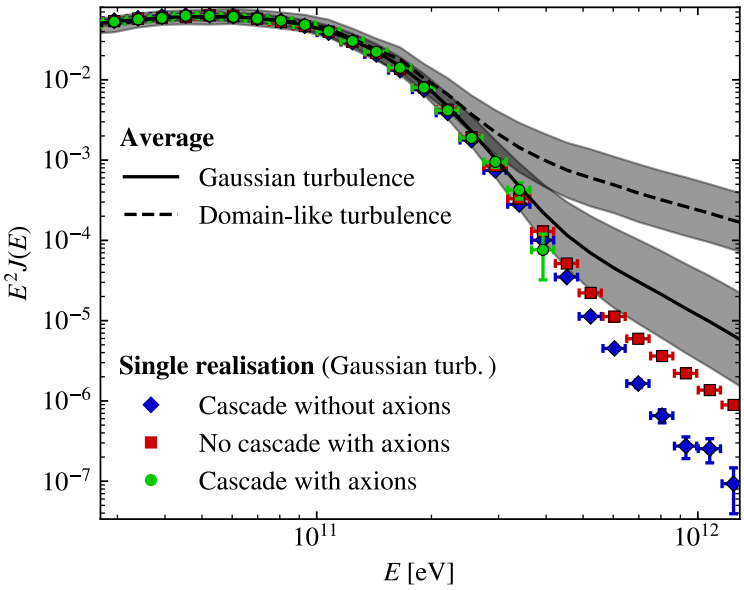

Figure 7. The normalised diffuse photon flux is plotted as a function of energy for a source with a power-law index $\alpha = -1.2$ at redshift $z = 1$. The magnetic field and axion parameters in eq. (4.3) are used. The average over many realisations of the magnetic field is shown for Gaussian (solid) and domain-like (dashed) as black lines. In order to increase the statistics at large energies, the photon absorption is taken into account by including an attenuation determined by the photon survival probability. Furthermore, the flux obtained for a single realisation is shown by red squares, while the flux obtained using the same magnetic field and the standard Monte Carlo treatment of the photon absorption as implemented in `ELMAG` is indicated by green circles. The errorbars indicate the 1σ Poisson uncertainty. Finally, the flux predicted by `ELMAG` without any axions is shown in blue diamonds to visualise the effect that the axions have on the flux.

result can be understood from figure 5: the conversion probability of photons into axions obtained using a domain-like field is on average larger than employing a Gaussian turbulent field at large distances.

The example considered in figure 7 further demonstrates the importance of a proper treatment of magnetic fields in the study of photon-axion oscillations. While the effect on the opacity on average is much less prominent for the Gaussian turbulence than for the domain-like approximation, there is still a significant variation between single realisations in both cases. The variation is however noticeably larger for the Gaussian turbulence than for the domain-like approximation.

8 Conclusion

In this work, we have studied photon-axion oscillations in a Monte-Carlo framework based on the `ELMAG` program. We have argued that the use of statistically averages over magnetic field configurations is misleading and should be abandoned in the search for signatures from axion-photon oscillation in the spectra of single sources. Moreover, we have shown that the

JCAP01(2022)025

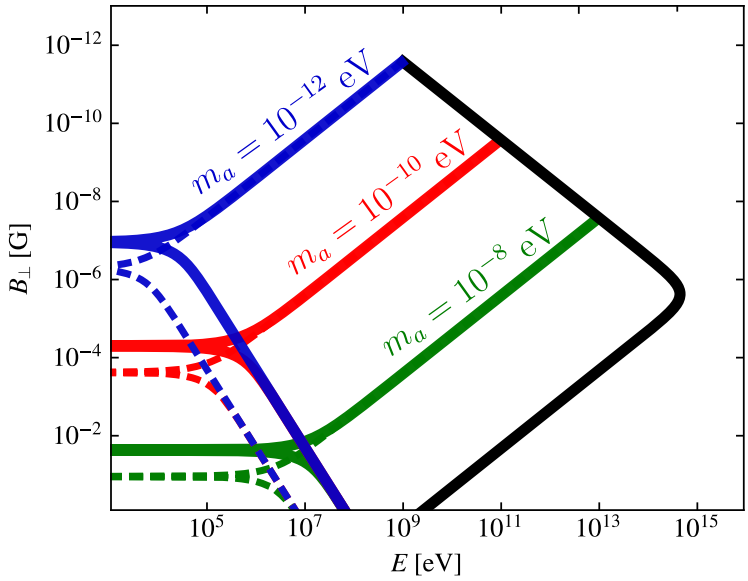

Figure 8. The transition energies in figure 3 is replotted for different axion masses. In addition, the effect of decreasing the reference electron density to $n_{e,0} = 0.002\,\mathrm{cm}^{-3}$ is shown by dashed lines.

predicted signatures — axion wiggles in photon spectra and the decreased opacity of the Universe — depend strongly on the chosen magnetic field models. Therefore, over-simplified magnetic field models as the domain-like field should be used with care for quantitative predictions.

We have discussed mainly those characteristic signatures of axion-photon oscillations which are independent of the concrete astrophysical environment. In particular, the oscillation length will scale as E^1 below the threshold energy E_{min} and as E^{-1} above the threshold energy E_{max}, while it will be constant at intermediate energies. We have proposed to use this energy dependence as an observable in the search for photon-axion oscillations using the discrete power spectrum. This method can in principle be also used to infer information about the magnetic field environment from the observation of axion wiggles.

Acknowledgments

We would like to thank Alessandro Mirizzi for providing valuable comments on the manuscript.

A Varying axion mass

For completeness, we plot in figure 8 the transition energies from figure 3 varying the axion mass and plasma density. The high energy transition to the strong mixing regime (black line) is independent of the axion mass and plasma density, while the low energy transition is decreasing for a decreasing axion mass and plasma density. Interestingly, this means that

JCAP01(2022)025

a weak magnetic field only will produce axion wiggles in photon spectra if the axion mass is sufficiently small. For example, if $m_a \sim 10^{-12}\,\mathrm{eV}$, the magnetic field strength must be stronger than $\sim 10^{-11}\,\mathrm{G}$ to produce wiggles. On the other hand, if $m_a \gtrsim 10^{-6}\,\mathrm{eV}$, the strong-mixing regime disappears and therefore no significant axion wiggles are produced.

References

[1] R.D. Peccei and H.R. Quinn, *CP Conservation in the Presence of Instantons*, *Phys. Rev. Lett.* **38** (1977) 1440 [INSPIRE].

[2] R.D. Peccei and H.R. Quinn, *Constraints Imposed by CP Conservation in the Presence of Instantons*, *Phys. Rev. D* **16** (1977) 1791 [INSPIRE].

[3] S. Weinberg, *A New Light Boson?*, *Phys. Rev. Lett.* **40** (1978) 223 [INSPIRE].

[4] F. Wilczek, *Problem of Strong P and T Invariance in the Presence of Instantons*, *Phys. Rev. Lett.* **40** (1978) 279 [INSPIRE].

[5] J. Preskill, M.B. Wise and F. Wilczek, *Cosmology of the Invisible Axion*, *Phys. Lett. B* **120** (1983) 127 [INSPIRE].

[6] L.F. Abbott and P. Sikivie, *A Cosmological Bound on the Invisible Axion*, *Phys. Lett. B* **120** (1983) 133 [INSPIRE].

[7] M. Dine and W. Fischler, *The Not So Harmless Axion*, *Phys. Lett. B* **120** (1983) 137 [INSPIRE].

[8] D.J.E. Marsh, *Axion Cosmology*, *Phys. Rept.* **643** (2016) 1 [arXiv:1510.07633] [INSPIRE].

[9] G. Grilli di Cortona, E. Hardy, J. Pardo Vega and G. Villadoro, *The QCD axion, precisely*, *JHEP* **01** (2016) 034 [arXiv:1511.02867] [INSPIRE].

[10] L. Di Luzio, M. Giannotti, E. Nardi and L. Visinelli, *The landscape of QCD axion models*, *Phys. Rept.* **870** (2020) 1 [arXiv:2003.01100] [INSPIRE].

[11] A. Arvanitaki, S. Dimopoulos, S. Dubovsky, N. Kaloper and J. March-Russell, *String Axiverse*, *Phys. Rev. D* **81** (2010) 123530 [arXiv:0905.4720] [INSPIRE].

[12] M. Cicoli, M. Goodsell and A. Ringwald, *The type IIB string axiverse and its low-energy phenomenology*, *JHEP* **10** (2012) 146 [arXiv:1206.0819] [INSPIRE].

[13] I.G. Irastorza and J. Redondo, *New experimental approaches in the search for axion-like particles*, *Prog. Part. Nucl. Phys.* **102** (2018) 89 [arXiv:1801.08127] [INSPIRE].

[14] K. Choi, S.H. Im and C.S. Shin, *Recent Progress in the Physics of Axions and Axion-Like Particles*, *Ann. Rev. Nucl. Part. Sci.* **71** (2021) 225 [arXiv:2012.05029] [INSPIRE].

[15] ADMX collaboration, *Extended Search for the Invisible Axion with the Axion Dark Matter Experiment*, *Phys. Rev. Lett.* **124** (2020) 101303 [arXiv:1910.08638] [INSPIRE].

[16] CAST collaboration, *New CAST Limit on the Axion-Photon Interaction*, *Nature Phys.* **13** (2017) 584 [arXiv:1705.02290] [INSPIRE].

[17] A. Ayala, I. Domínguez, M. Giannotti, A. Mirizzi and O. Straniero, *Revisiting the bound on axion-photon coupling from Globular Clusters*, *Phys. Rev. Lett.* **113** (2014) 191302 [arXiv:1406.6053] [INSPIRE].

[18] R. Bähre et al., *Any light particle search II — Technical Design Report*, 2013 *JINST* **8** T09001 [arXiv:1302.5647] [INSPIRE].

[19] IAXO collaboration, *Physics potential of the International Axion Observatory (IAXO)*, *JCAP* **06** (2019) 047 [arXiv:1904.09155] [INSPIRE].

[20] J.L. Ouellet et al., *First Results from ABRACADABRA-10 cm: A Search for Sub-μeV Axion Dark Matter*, *Phys. Rev. Lett.* **122** (2019) 121802 [arXiv:1810.12257] [INSPIRE].

JCAP01(2022)025

[21] A. De Angelis, M. Roncadelli and O. Mansutti, *Evidence for a new light spin-zero boson from cosmological gamma-ray propagation?*, *Phys. Rev. D* **76** (2007) 121301 [arXiv:0707.4312] [INSPIRE].

[22] H.E.S.S. collaboration, *Constraints on axionlike particles with H.E.S.S. from the irregularity of the PKS 2155-304 energy spectrum*, *Phys. Rev. D* **88** (2013) 102003 [arXiv:1311.3148] [INSPIRE].

[23] FERMI-LAT collaboration, *Search for Spectral Irregularities due to Photon-Axionlike-Particle Oscillations with the Fermi Large Area Telescope*, *Phys. Rev. Lett.* **116** (2016) 161101 [arXiv:1603.06978] [INSPIRE].

[24] A. Payez, C. Evoli, T. Fischer, M. Giannotti, A. Mirizzi and A. Ringwald, *Revisiting the SN1987A gamma-ray limit on ultralight axion-like particles*, *JCAP* **02** (2015) 006 [arXiv:1410.3747] [INSPIRE].

[25] M. Xiao et al., *Constraints on Axionlike Particles from a Hard X-Ray Observation of Betelgeuse*, *Phys. Rev. Lett.* **126** (2021) 031101 [arXiv:2009.09059] [INSPIRE].

[26] C.S. Reynolds et al., *Astrophysical limits on very light axion-like particles from Chandra grating spectroscopy of NGC 1275*, arXiv:1907.05475 [INSPIRE].

[27] J.S. Reynés, J.H. Matthews, C.S. Reynolds, H.R. Russell, R.N. Smith and M.C.D. Marsh, *New constraints on light Axion-Like Particles using Chandra Transmission Grating Spectroscopy of the powerful cluster-hosted quasar H1821+643*, arXiv:2109.03261 [INSPIRE].

[28] C. Dessert, J.W. Foster and B.R. Safdi, *X-ray Searches for Axions from Super Star Clusters*, *Phys. Rev. Lett.* **125** (2020) 261102 [arXiv:2008.03305] [INSPIRE].

[29] CTA collaboration, *Sensitivity of the Cherenkov Telescope Array for probing cosmology and fundamental physics with gamma-ray propagation*, *JCAP* **02** (2021) 048 [arXiv:2010.01349] [INSPIRE].

[30] A. Kartavtsev, G. Raffelt and H. Vogel, *Extragalactic photon-ALP conversion at CTA energies*, *JCAP* **01** (2017) 024 [arXiv:1611.04526] [INSPIRE].

[31] D. Montanino, F. Vazza, A. Mirizzi and M. Viel, *Enhancing the Spectral Hardening of Cosmic TeV Photons by Mixing with Axionlike Particles in the Magnetized Cosmic Web*, *Phys. Rev. Lett.* **119** (2017) 101101 [arXiv:1703.07314] [INSPIRE].

[32] M. Libanov and S. Troitsky, *On the impact of magnetic-field models in galaxy clusters on constraints on axion-like particles from the lack of irregularities in high-energy spectra of astrophysical sources*, *Phys. Lett. B* **802** (2020) 135252 [arXiv:1908.03084] [INSPIRE].

[33] P. Carenza, C. Evoli, M. Giannotti, A. Mirizzi and D. Montanino, *Turbulent axion-photon conversions in the Milky Way*, *Phys. Rev. D* **104** (2021) 023003 [arXiv:2104.13935] [INSPIRE].

[34] C. Wendel, J.B. González, A. Shukla, D. Paneque and K. Mannheim, *Gamma-ray signatures from pair cascades in recombination-line radiation fields*, *PoS* **ICRC2021** (2021) 911 [arXiv:2108.02649] [INSPIRE].

[35] T.A. Dzhatdoev, E.V. Khalikov, A.P. Kircheva and A.A. Lyukshin, *Electromagnetic cascade masquerade: a way to mimic γ-axion-like particle mixing effects in blazar spectra*, *Astron. Astrophys.* **603** (2017) A59 [arXiv:1609.01013] [INSPIRE].

[36] M. Kachelrieß, S. Ostapchenko and R. Tomas, *ELMAG: A Monte Carlo simulation of electromagnetic cascades on the extragalactic background light and in magnetic fields*, *Comput. Phys. Commun.* **183** (2012) 1036 [arXiv:1106.5508] [INSPIRE].

[37] M. Blytt, M. Kachelrieß and S. Ostapchenko, *ELMAG 3.01: A three-dimensional Monte Carlo simulation of electromagnetic cascades on the extragalactic background light and in magnetic fields*, arXiv:1909.09210 [INSPIRE].

JCAP01(2022)025

[38] G. Raffelt and L. Stodolsky, *Mixing of the Photon with Low Mass Particles*, *Phys. Rev. D* **37** (1988) 1237 [INSPIRE].

[39] G. Galanti and M. Roncadelli, *Behavior of axionlike particles in smoothed out domainlike magnetic fields*, *Phys. Rev. D* **98** (2018) 043018 [arXiv:1804.09443] [INSPIRE].

[40] M. Meyer, J. Davies and J. Kuhlmann, *gammaALPs: An open-source python package for computing photon-axion-like-particle oscillations in astrophysical environments*, *PoS* **ICRC2021** (2021) 557 [arXiv:2108.02061] [INSPIRE].

[41] R.A. Batista and A. Saveliev, *The Gamma-ray Window to Intergalactic Magnetism*, *Universe* **7** (2021) 223 [arXiv:2105.12020] [INSPIRE].

[42] J. Giacalone and J.R. Jokipii, *Charged-particle motion in multidimensional magnetic-field turbulence*, *Astrophys. J. Lett.* **430** (1994) L137.

[43] J. Giacalone and J.R. Jokipii, *The Transport of Cosmic Rays across a Turbulent Magnetic Field*, *Astrophys. J.* **520** (1999) 204.

[44] Y. Grossman, S. Roy and J. Zupan, *Effects of initial axion production and photon axion oscillation on type-IA supernova dimming*, *Phys. Lett. B* **543** (2002) 23 [hep-ph/0204216] [INSPIRE].

[45] D. Wouters and P. Brun, *Irregularity in gamma ray source spectra as a signature of axionlike particles*, *Phys. Rev. D* **86** (2012) 043005 [arXiv:1205.6428] [INSPIRE].

[46] A. De Angelis, G. Galanti and M. Roncadelli, *Relevance of axion-like particles for very-high-energy astrophysics*, *Phys. Rev. D* **84** (2011) 105030 [*Erratum ibid.* **87** (2013) 109903] [arXiv:1106.1132] [INSPIRE].

[47] M. Meyer, D. Montanino and J. Conrad, *On detecting oscillations of gamma rays into axion-like particles in turbulent and coherent magnetic fields*, *JCAP* **09** (2014) 003 [arXiv:1406.5972] [INSPIRE].

[48] G. Galanti and M. Roncadelli, *Extragalactic photon-axion-like particle oscillations up to* 1000 *TeV*, *J. High Energy Astrophys.* **20** (2018) 1 [arXiv:1805.12055] [INSPIRE].

[49] G. Galanti, F. Tavecchio, M. Roncadelli and C. Evoli, *Blazar VHE spectral alterations induced by photon-ALP oscillations*, *Mon. Not. Roy. Astron. Soc.* **487** (2019) 123 [arXiv:1811.03548] [INSPIRE].

[50] R. Buehler, G. Gallardo, G. Maier, A. Domínguez, M. López and M. Meyer, *Search for the imprint of axion-like particles in the highest-energy photons of hard γ-ray blazars*, *JCAP* **09** (2020) 027 [arXiv:2004.09396] [INSPIRE].

[51] A. Dobrynina, A. Kartavtsev and G. Raffelt, *Photon-photon dispersion of TeV gamma rays and its role for photon-ALP conversion*, *Phys. Rev. D* **91** (2015) 083003 [*Erratum ibid.* **95** (2017) 109905] [arXiv:1412.4777] [INSPIRE].

[52] M.S. Pshirkov, P.G. Tinyakov and F.R. Urban, *New limits on extragalactic magnetic fields from rotation measures*, *Phys. Rev. Lett.* **116** (2016) 191302 [arXiv:1504.06546] [INSPIRE].

[53] K. Jedamzik and A. Saveliev, *Stringent Limit on Primordial Magnetic Fields from the Cosmic Microwave Background Radiation*, *Phys. Rev. Lett.* **123** (2019) 021301 [arXiv:1804.06115] [INSPIRE].

[54] K.M. Ferriere, *The interstellar environment of our galaxy*, *Rev. Mod. Phys.* **73** (2001) 1031 [astro-ph/0106359] [INSPIRE].

[55] A. Mirizzi, J. Redondo and G. Sigl, *Constraining resonant photon-axion conversions in the Early Universe*, *JCAP* **08** (2009) 001 [arXiv:0905.4865] [INSPIRE].

[56] A. Mirizzi and D. Montanino, *Stochastic conversions of TeV photons into axion-like particles in extragalactic magnetic fields*, *JCAP* **12** (2009) 004 [arXiv:0911.0015] [INSPIRE].

[57] A. Mirizzi, G.G. Raffelt and P.D. Serpico, *Photon-axion conversion in intergalactic magnetic fields and cosmological consequences*, in *Lecture Notes in Physics* **741**, Springer (2008), pp. 115–134 [astro-ph/0607415] [INSPIRE].

[58] G. Long, S. Chen, S. Xu and H.-H. Zhang, *Probing μeV ALPs with future LHAASO observations of AGN γ-ray spectra*, *Phys. Rev. D* **104** (2021) 083014 [arXiv:2101.10270] [INSPIRE].

[59] C. Dessert, A.J. Long and B.R. Safdi, *No evidence for axions from Chandra observation of magnetic white dwarf*, arXiv:2104.12772 [INSPIRE].

[60] J. Zhou, Z. Wang, F. Huang and L. Chen, *A possible blazar spectral irregularity case caused by photon-axionlike-particle oscillations*, *JCAP* **08** (2021) 007 [arXiv:2102.05833] [INSPIRE].

[61] A. Mirizzi, G.G. Raffelt and P.D. Serpico, *Signatures of Axion-Like Particles in the Spectra of TeV Gamma-Ray Sources*, *Phys. Rev. D* **76** (2007) 023001 [arXiv:0704.3044] [INSPIRE].

[62] A.S. Dighe, M.T. Keil and G.G. Raffelt, *Identifying earth matter effects on supernova neutrinos at a single detector*, *JCAP* **06** (2003) 006 [hep-ph/0304150] [INSPIRE].

[63] A.S. Dighe, M. Kachelrieß, G.G. Raffelt and R. Tomas, *Signatures of supernova neutrino oscillations in the earth mantle and core*, *JCAP* **01** (2004) 004 [hep-ph/0311172] [INSPIRE].

[64] E. Borriello, S. Chakraborty, A. Mirizzi, P.D. Serpico and I. Tamborra, *(Down-to-)Earth matter effect in supernova neutrinos*, *Phys. Rev. D* **86** (2012) 083004 [arXiv:1207.5049] [INSPIRE].

[65] W. Liao, *Detecting supernovae neutrino with Earth matter effect*, *Phys. Rev. D* **94** (2016) 113016 [arXiv:1607.03334] [INSPIRE].

[66] J.P. Conlon and M. Rummel, *Improving Statistical Sensitivity of X-ray Searches for Axion-Like Particles*, *Mon. Not. Roy. Astron. Soc.* **484** (2019) 3573 [arXiv:1808.05916] [INSPIRE].

[67] M.C.D. Marsh, J.H. Matthews, C. Reynolds and P. Carenza, *The Fourier formalism for relativistic axion-photon conversion, with astrophysical applications*, arXiv:2107.08040 [INSPIRE].

JCAP01(2022)025

Paper IX – AAfrag 2.01: Interpolation routines for Monte Carlo results on secondary production including light antinuclei in hadronic interactions

Kachelrieß, M., Ostapchenko, S. & Tjemsland, J. "AAfrag 2.01: interpolation routines for Monte Carlo results on secondary production including light antinuclei in hadronic interactions". *Comput. Phys. Commun.* **287,** 108698. arXiv: 2206.00998 [hep-ph] (2023)

Abstract: Light antinuclei, like antideuteron and antihelium-3, are ideal probes for new, exotic physics because their astrophysical backgrounds are suppressed at low energies. In order to exploit fully the inherent discovery potential of light antinuclei, a reliable description of their production cross sections in cosmic ray interactions is crucial. We provide therefore the cross sections of antideuteron and antihelium-3 production in pp, pHe, Hep, HeHe, $\bar{p}p$ and $\bar{p}$He collisions at energies relevant for secondary production in the Milky Way, in a tabulated form which is convinient to use. These predictions are based on QGSJET-II-04m and the state of the art coalescence model WiFunC, which evaluates the coalesence probability on an event-by-event basis, including both momentum correlations and the dependence on the emission volume. In addition, we comment on the importance of a Monte Carlo description of the antideuteron production and on the use of event generators in general. In particular, we discuss the effect of two-particle momentum correlations provided by Monte Carlo event generators on antinuclei production.

This paper was written to make the cross sections computed for Paper II public as a part of `AAfrag`. In addition, motivated partly by discussions at the MIAPP workshop Feb. 2022, we commented on the importance of using Monte Carlo (MC) event generators in the study of cosmic ray antinuclei.

Computer Physics Communications 287 (2023) 108698

Contents lists available at ScienceDirect

Computer Physics Communications

journal homepage: www.elsevier.com/locate/cpc

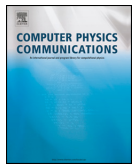

AAfrag 2.01: interpolation routines for Monte Carlo results on secondary production including light antinuclei in hadronic interactions ☆,☆☆

M. Kachelrieß [a], S. Ostapchenko [b,c], J. Tjemsland [a,*]

[a] Institutt for fysikk, NTNU, Trondheim, Norway
[b] II. Institute for Theoretical Physics, Hamburg University, Hamburg, Germany
[c] D.V. Skobeltsyn Institute of Nuclear Physics, Moscow State University, Moscow, Russia

ARTICLE INFO

Article history:
Received 12 June 2022
Received in revised form 26 January 2023
Accepted 11 February 2023
Available online 24 February 2023

Keywords:
Hadronic interactions
Production cross section
Secondary particles
Photon, neutrino, antiproton, positron, and antinuclei production
Coalescence

ABSTRACT

Light antinuclei, like antideuteron and antihelium-3, are ideal probes for new, exotic physics because their astrophysical backgrounds are suppressed at low energies. In order to exploit fully the inherent discovery potential of light antinuclei, a reliable description of their production cross sections in cosmic ray interactions is crucial. We provide therefore the cross sections of antideuteron and antihelium-3 production in pp, pHe, Hep, HeHe, $\bar{p}p$ and $\bar{p}$He collisions at energies relevant for secondary production in the Milky Way, in a tabulated form which is convinient to use. These predictions are based on QGSJET-II-04m and the state of the art coalescence model WiFunC, which evaluates the coalesence probability on an event-by-event basis, including both momentum correlations and the dependence on the emission volume. In addition, we comment on the importance of a Monte Carlo description of the antideuteron production and on the use of event generators in general. In particular, we discuss the effect of two-particle momentum correlations provided by Monte Carlo event generators on antinuclei production.

Program summary
Program Title: AAfrag 2.01
CPC Library link to program files: https://doi.org/10.17632/6f73jz6jx8.2
Developer's repository link: https://aafrag.sourceforge.io
Code Ocean capsule: https://codeocean.com/capsule/1159734
Licensing provisions: CC BY-NC 4.0
Programming language: The program exists both in a Python 3 and Fortran 90 version
Journal reference of previous version: Comp. Phys. Comm. 245, 106846 (2019)
Does the new version supersede the previous version?: Yes
Reasons for the new version: Inclusion of antinuclei tables, and a Python 3 version for the pedestrian.
Summary of revisions: Improved formatting of tables, inclusion of new secondaries, inclusion of Python version.
Nature of problem: Calculation of secondaries (photons, neutrinos, electrons, positrons, protons, antiprotons, antideuterons and antihelium-3) produced in hadronic interactions.
Solution method: Results from the Monte Carlo simulation QGSJET-II-04m are interpolated.

1. Introduction

A precise knowledge of the production cross section of secondaries in hadronic interactions is important in many applications in astrophysics and astroparticle physics, ranging from deducing the cosmic ray spectrum from the observation of secondary photons [1–3] to indirect dark matter searches using cosmic ray antinuclei [4,5]. Such studies are either based on convenient parametrisations tuned to available accelerator data, or on Monte Carlo gen-

☆ The review of this paper was arranged by Prof. Z. Was.
☆☆ This paper and its associated computer program are available via the Computer Physics Communications homepage on ScienceDirect (http://www.sciencedirect.com/science/journal/00104655).
* Corresponding author.
E-mail address: jonas.tjemsland@ntnu.no (J. Tjemsland).

https://doi.org/10.1016/j.cpc.2023.108698

erators. The former have to rely on empirical scaling laws, which are unreliable when extrapolated outside the measured kinematical range. Furthermore, such parametrisations are typically provided only for protons, and therefore a "nuclear enhancement factor" has to be used to describe the production cross sections in interactions involving nuclei. However, nuclear enhancement factors are, especially close to threshold, not able to capture the intricate dependence on the energy and the nuclear mass number of these cross sections [6–8]. Monte Carlo event generators, on the other hand, are generally less convenient for a user, but can describe consistently both hadron–hadron and hadron–nucleus collisions. In Ref. [9], the production cross sections for photons, neutrinos, electrons, positrons, (anti-) protons, and (anti-) neutrons in various interactions relevant for secondary production in the Milky Way were therefore derived from the event generator QGSJET-II-04m [10–12] and made publicly available in an easily usable form. In addition, Ref. [13] discussed the differences to other published parametrisations of the photon, neutrino, electron, and positron spectra and provided a python version of the interpolation subroutines.

The differences between parametrisations and event generators become even more pronounced in the case of antinuclei: The parametrisations rely on additional approximations like the neglect of two-particle correlations, while the Monte Carlo description is severely computationally demanding. This motivated us to extend the interpolation subroutines of `AAfrag` to include also our predictions for the production cross sections of antinuclei in pp, pHe, Hep, HeHe, $\bar{p}p$, and $\bar{p}$He interactions.

The production of (anti-) nuclei in small interacting systems is arguably best described using so-called coalescence models. In these models, final-state nucleons may merge to form a nucleus if they are sufficiently close in phase space [14,15]. Currently, the only model that is able to account (semi-classically) for nucleon momentum correlations in a Monte Carlo framework as well as the nucleon emission volume is the so-called WiFunC (short for Wigner Functions with Correlations) model introduced in Ref. [16] and discussed in more detail in Refs. [8,17]. In this model, the probability that a given (anti-) proton–(anti-) neutron pair coalesce is found by projecting the wave function describing the final-state nucleons onto the deuteron wave function. Using for the latter a two-Gaussian wave function, one obtains for the formation probability w of an (anti-) deuteron

$$w = 3\Delta\zeta_1 \mathrm{e}^{-d_1^2 q^2} + 3(1-\Delta)\zeta_2 \mathrm{e}^{-d_2^2 q^2}, \tag{1}$$

where q is the momentum of the nucleons in the pair rest frame and the parameters $\Delta = 0.581$, $d_1 = 3.979$ fm and $d_2 = 0.890$ fm are fixed such that $\phi(r=0)$ and the expectation value $\langle r \rangle$ of the two-Gaussian wave function have the same values as for the Hulthen wave function [18]. The resulting deuteron yield is then obtained by selecting proton-neutron pairs obtained in a particle collision in the event generator with probability w. The suppression factors ζ_i are given by

$$\zeta_i^2 = \frac{d_i^2}{d_i^2 + 4(\sigma m/m_T)^2} \frac{d_i^2}{d_i^2 + 4\sigma^2} \frac{d_i^2}{d_i^2 + 4\sigma^2}, \tag{2}$$

and depend on the coalescence parameter[1] σ which determines the size of the formation region of nucleons; Here, m and m_T are the nucleon mass and the nucleon transverse mass, respectively.

[1] The longitudinal spread is expected to be of the same size as the transverse spread. To minimize the number of free parameters of the model, we have therefore fixed $\sigma \equiv \sigma_\perp = \sigma_\parallel$. When more experimental data and improved event generators become available, the two spreads may have to be fitted separately.

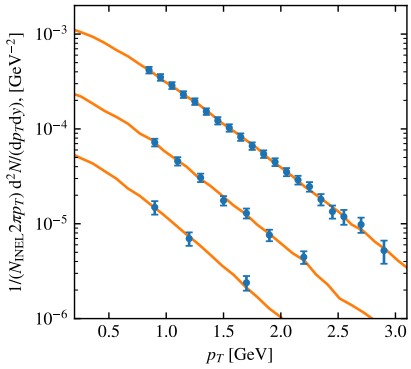

Fig. 1. Best fit of the WiFunC model, using QGSJET-II-04m, to the invariant differential yield of antideuterons, measured by the ALICE collaboration in pp collisions (blue data points) at 0.9, 2.76 and 7 TeV. The yields are multiplied by a constant factor to make the figure clearer. A re-weighting of the antinucleons was included as in Ref. [8].

The coalescence parameter is expected to be close to 1 fm and its process dependence can be approximated as described in Ref. [8]. Analytical expressions for the coalescence probability w of three nucleons into (anti-) helium-3 and (anti-) tritium have been derived in Ref. [8], thereby allowing for a consistent description of the production of light nuclei in various interactions relevant for astrophysical studies. It is important to note that this model contains basically no free parameters: The parameter σ can be fixed independently by femtoscopy experiments. Moreover, the numerical values derived for σ from femtoscopy experiments and from fits to various production channels of light antinuclei are consistent with each other and agree with its physical interpretation, $\sigma \simeq 1$ fm.

In this work, we provide the predictions for the production cross sections of antideuteron and antihelium-3 in pp, pHe, Hep, HeHe, $\bar{p}p$, and $\bar{p}$He interactions, based on the QGSJET-II-04m Monte Carlo generator and the WiFunC model. In addition, we comment on the importance of including momentum correlations when describing the production of astrophysical antinuclei, and on the interpretation of antideuteron and antihelium experiments at accelerators. Finally, we argue that the nuclear enhancement in the astrophysically interesting range is strongly energy dependent and can therefore not be approximated by a constant factor.

2. Selected results

In Fig. 1, we compare the invariant differential antideuteron yield measured by the ALICE collaboration in pp collisions at 0.9, 2.76 and 7 TeV [21] to that obtained using QGSJET-II-04m and the WiFunC model. This comparison clearly shows that the differential yields are well reproduced.

A compilation of fits of σ to various accelerator experiments on antideuteron and antihelium-3 production using QGSJET-II-04m and Pythia 8 is shown in Fig. 2 (see Refs. [8,16,17,19] and references therein for a discussion of the experimental data and the fitting procedures). It is clear that the numerical values of σ are consistent with being constant and equal to (1.0 ± 0.1) fm within the theoretical and experimental uncertainties. It should be emphasised that the triangular data point in Fig. 2 is obtained from a fit to the baryon source size and its m_T scaling measured by the ALICE collaboration in pp collisions [20]. Thus this data point represents an independent measurement of the coalesence parameter σ, using only data on baryon production. The agreement of this value with the one found applying the WiFunC model to anti-

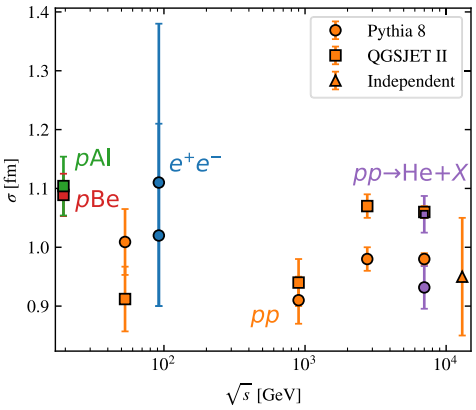

Fig. 2. A compilation of values of the coalescence parameter σ, obtained from fits to various experimental data on antideuteron and antihelium-3 production in pp [21,22], pN [23], and e^+e^- [24,25] collisions using Pythia 8 (circles) and QGSJET-II-04m (squares). The triangular data point is obtained from a femtoscopy experiment [20], and is thus independent on the event generator. The fitting is explained in Ref. [19] and references therein.

nuclei production supports the validity of the basic assumptions underlying this model. Note also that the free parameter σ in the WiFunC model can be fixed independently of the coalescence mechanism via baryon femtoscopy, see the last data point in Fig. 2.

3. Secondary production of antinuclei

3.1. Comparison with parametrisation methods

Traditionally, the production of a nucleus with mass number A has been parametrised by the proton spectrum as

$$E_A \frac{\mathrm{d}^3 N_A}{\mathrm{d}P_A^3} = B_A \left(E_N \frac{\mathrm{d}^3 N_p}{\mathrm{d}p_p^3} \right)^A , \tag{3}$$

where B_A is known as the coalescence factor. In the limit of isotropic nucleon yields, B_A is a constant that scales with the nucleon emission volume as $B_A \propto V^{A-1}$ if the coalescence condition is evaluated in position space, and with the coalescence momentum as $B_A \propto p_0^{3A-3}$ if evaluated in momentum space. In small interacting systems, such as pp, pN and e^+e^- collisions or dark matter annihilations, this approximation is not valid since the nucleon yield is highly non-isotropic. Even so, the approximation (3) is often used in astrophysical studies due to its simplicity.

Another reason for deviations from the simple relation (3) is the missing phase-space suppression close to the production threshold. Since the production channels with the minimal number of particles, compatible with baryon number conservation, will dominate close to the threshold, one can approximate the suppression at low collision energies and high secondary nucleus energies as a pure phase-space suppression, assuming an isotropic matrix element (see e.g. Refs. [26–28]). Thus, the approximation (3) can be improved if we include a phase-space suppression factor

$$R_N(x) \equiv \frac{\Phi_N(x; m_p)}{\Phi_N(x; 0)}, \tag{4}$$

where $x = \sqrt{s + A m_p^2 - 2\sqrt{s}\tilde{E}_A}$ describes the energy available in the centre of mass (CoM) frame, and $\tilde{E}_A$ is the nucleus energy in the CoM frame. One can compute the phase-space integrals,

$$\Phi_N(x; m_p) = \left[\prod_{i=1}^{N} \int \frac{\mathrm{d}^3 p_i}{(2\pi)^3 2E_i} \right] (2\pi)^4 \delta^{(3)} \left(\sum_{i=1}^{N} \boldsymbol{p}_i \right) \times \delta \left(\sum_{i=1}^{N} E_i - x \right), \tag{5}$$

with the integration volume being the full allowed phase-space, numerically using the method described in Ref. [29] (see Fig. 15 in Ref. [26] for a plot). This method has a major perk compared to a Monte Carlo treatment: It is significantly less computationally demanding. As in the case of the WiFunC model, the method contains no free parameters since the coalescence factor can be obtained from femtoscopy experiments [26,30,31]. However, the suppression factor is not exact and two-particle correlations are not taken into account, meaning that one may expect the method to give inaccurate results. For instance, at low energies near the threshold, the model is expected to overproduce nuclei since it does not take into account anti-correlations. Furthermore, the coalescence factor B_A is typically determined in a kinematical regime not relevant for cosmic ray studies. As such, results obtained within this approximation have to be interpreted with care.

In order to verify the importance of using a Monte Carlo description, we plot in Fig. 3 the antideuteron (left) and antihelium-3 (right) spectra $\mathrm{d}N/\mathrm{d}E = \sigma_{\mathrm{inel}}{}^{-1} \mathrm{d}\sigma_{\mathrm{inel}}/\mathrm{d}E$ obtained using Eqs. (3) and (4) (solid lines) and the WiFunC model (dashed lines) for various primary energies. The shaded areas correspond to the ranges $B_2 = (0.75, 2.4) \cdot 10^{-2}$ and $B_3 = (2, 20) \cdot 10^{-3}$ obtained from femtoscopy experiments [26]. Note that QGSJET-II-04m was used to obtain the antiproton spectrum, and that using instead a parametrisation of the antinucleon spectrum would lead to larger differences. While the phase-space suppression factor captures well the overall behaviour of the suppression for high secondary energies, there are large differences near the production threshold at low energies. These differences are much larger for helium-3 than for deuteron. A reason for these differences is that the parametrisation fails to account for the fact that certain processes are kinematically allowed but forbidden by conservation laws, e.g. for baryon number. In particular, antideuterons may be produced using parametrisations via the (forbidden) process $pp \to pp\bar{p}\bar{n}$. Furthermore, in high energy collisions and near the threshold, parametrisations fail to describe the momentum (anti-) correlations that may enhance or lower the antinuclei production [32]. Although the parametrisation (3) describes (within the experimental and theoretical uncertainties in B_A) the overall yield of antinuclei sufficiently well for order-of-magnitude estimates, an accurate Monte Carlo description is therefore needed if one aims to reduce the uncertainties in the theoretical predictions.

3.2. Nuclear enhancement

One of the major advantages of the WiFunC model and the use of a Monte Carlo generator is that one can describe the production of antideuteron and antihelium-3 in point-like and extended processes without any free parameters. In particular, one can avoid the use of a "nuclear enhancement factor", which is otherwise required if the primary and/or the target is a nucleus. Previous studies like those of Refs. [33,34] had to assume that the nuclear enhancement is constant and coincides with the one for antiproton production. In fact, these assumptions are invalid, as we shall demonstrate below.

To discuss the nuclear enhancement of secondary fluxes analytically, it is convenient to consider the case when the primary cosmic ray spectra can be approximated by power laws, $I_{A_i}(E_0) \propto E_0^{-\alpha_i}$, with α_i being the slope and E_0 the energy per nucleon. In such a case, the contribution $q_X^{A_i p}$ to the secondary flux of particles

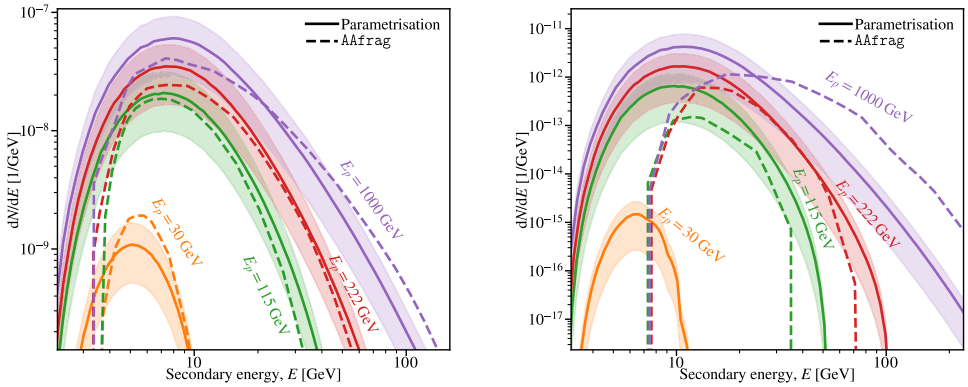

Fig. 3. The antideuteron (left) and antihelium-3 (right) spectra obtained using Eqs. (3) and (4) (solid lines) and the WiFunC model (dashed lines). The results are shown for primary energies of 21 GeV (blue), 30 GeV (orange), 115 GeV (green), 222 GeV (red) and 1000 GeV (purple).

X ($e^{\pm}$, γ, ν, or $\bar{p}$) from interactions of primary nuclei A_i with protons from the interstellar medium is proportional to the weighted moment of the corresponding production spectrum (see, e.g. [7]):

$$q_X^{A_i p}(E) \propto Z_X^{A_i p}(E, \alpha_i)\,, \tag{6}$$

with

$$Z_X^{A_i p}(E, \alpha_i) = \int_0^1 \mathrm{d}z\, z^{\alpha_i - 1}\, \frac{\mathrm{d}\sigma_{A_i p \to X}(E/z, z)}{\mathrm{d}z}\,. \tag{7}$$

Then the nuclear enhancement can be quantified by the ratio $Z_X^{A_i p}(E, \alpha_i)/Z_X^{pp}(E, \alpha_i)$ which would coincide with the ratio of the respective contributions to the secondary flux of interest, $q_X^{A_i p}/q_X^{pp}$, if the primary proton and nuclei flux would be the same. In the limit of very high energies, one obtains an A enhancement for that ratio [7,12],

$$\varepsilon_X^{A_i p}(E) \equiv Z_X^{A_i p}(E, \alpha_i)/Z_X^{pp}(E, \alpha_i) \to A_i\,. \tag{8}$$

This simple result follows from two important features of nucleus-proton (or, more generally, nucleus-nucleus) interactions. First, the forward (i.e. large z) spectrum for any secondary particle X in collisions of a nucleus A with protons can be approximated by the one for a superposition of $\langle n_A^{\mathrm{w}} \rangle$ independent pp collisions,

$$\left.\frac{dn_{A_i p \to X}(E_0, z)}{dz}\right|_{z\to 1} \simeq \langle n_A^{\mathrm{w}}(E_0)\rangle\, \frac{dn_{pp\to X}(E_0, z)}{dz}\,. \tag{9}$$

Here, the average number $\langle n_A^{\mathrm{w}} \rangle$ of interacting ("wounded") projectile nucleons satisfies [35]

$$\langle n_A^{\mathrm{w}}(E_0)\rangle \simeq \frac{A\,\sigma_{pp}^{\mathrm{inel}}(E_0)}{\sigma_{Ap}^{\mathrm{inel}}(E_0)}\,, \tag{10}$$

with $\sigma_{pp}^{\mathrm{inel}}$ and $\sigma_{Ap}^{\mathrm{inel}}$ as the inelastic cross sections of pp and Ap collisions, respectively. Inserting Eq. (10) into (9) and substituting the result in (7), one arrives at Eq. (8).

Let us consider now the production of light nuclei. For definiteness, we will discuss the case of antideuterons. The crucial difference to the picture described above is that this process proceeds via the coalescence mechanism and thus involves the double differential spectra of produced antiprotons and antineutrons, $\mathrm{d}^2\sigma_{Ap\to\bar{p}+\bar{n}}/\mathrm{d}z_{\bar{p}}\mathrm{d}z_{\bar{n}}$. In nucleus-proton collisions, the coalescing antiproton and antineutron are typically created in rescatterings of different projectile nucleons off the target proton [8]. Consequently, the forward-production spectra of antideutrons become proportional to the number of possible pair-wise nucleon-proton rescattering processes, $\propto n_A^{\mathrm{w}}(n_A^{\mathrm{w}} - 1)$. Thus, at sufficiently high energies and for large A, the nuclear enhancement for $\bar{d}$ production should satisfy

$$\varepsilon_{\bar{d}}^{Ap}(E) \propto \frac{A^2\sigma_{pp}^{\mathrm{inel}}(E)}{\sigma_{Ap}^{\mathrm{inel}}(E)} \simeq A^{4/3}\,, \tag{11}$$

with E as the energy per nucleon for $\bar{d}$. In the last step, we assumed for illustration a simple $A^{2/3}$ scaling for the Ap cross sections.

In Fig. 4, we plot the calculated energy dependence of the enhancement factors $\varepsilon_{\bar{d}}^{AB}(E) = q_X^{AB}/q_X^{pp}$, for $AB = \mathrm{He}p$, $p\mathrm{He}$, and HeHe and assuming the same primary proton and helium flux. At the highest energies, $\varepsilon_{\bar{d}}^{\mathrm{He}p}$ is larger than four and increasing towards the asymptotic limit, Eq. (11). In contrast, the behaviour of $\varepsilon_{\bar{d}}^{AB}(E)$ changes drastically in the low-energy limit. Such a trend has been previously observed and explained in Ref. [12], for the case of $\bar{p}$ production: Because of the relatively high proton mass, at low energies the integral in Eq. (7) is no longer dominated by forward (large z) $\bar{p}$ production. Instead, important contributions come from the central (in the centre of mass frame) and backward production, such that the reasoning which lead to Eq. (8) becomes inapplicable. The same considerations fully apply to the case of antideutron production. Moreover, regarding antideutron production in proton-helium collisions, the coalescing $\bar{p}$ and $\bar{n}$ are predominantly produced in inelastic rescatterings on different target nucleons. As a result, the energy threshold for $\bar{d}$ production is lower than in pp interactions, and gives rise to a large nuclear enhancement close to the production threshold.

3.3. The use of event generators and the interpretation of accelerator data

Currently, the best experimental data on antinuclei production, e.g. from the ALICE experiment, are obtained at energies and in kinematical regions that are not relevant for astrophysical studies. Fitting phenomenological coalescence models to such data leads to a biased model with a reduced predictive power. Therefore it is important to always assess the applicability of an event generator, e.g., by comparing with antiproton data obtained under the same conditions, when comparing the coalescence model to experimental data. For example, QGSJET does not reproduce well

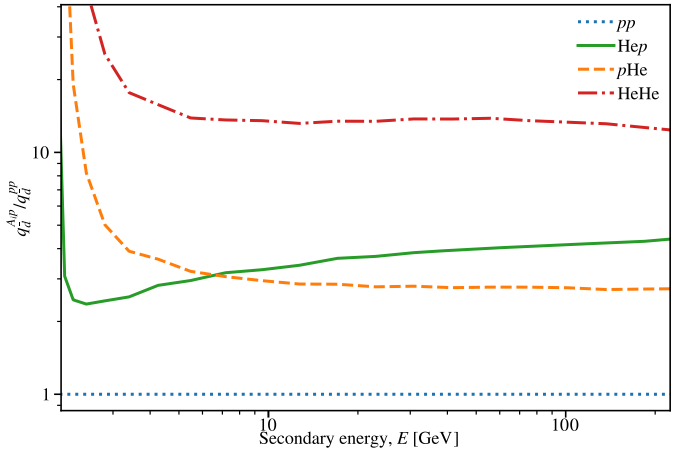

Fig. 4. The nuclear enhancement factors $\varepsilon_{\bar{d}}^{AB}(E) = q_X^{A_A B}/q_X^{pp}$ as function of the total energy for $AB = \mathrm{He}p$, $p\mathrm{He}$, and HeHe collisions.

the slope of the antiproton spectrum at 2.76 and 7 TeV measured by ALICE [8]. Therefore, a re-weighting[2] of the antiproton spectrum at these energies has been performed in order to obtain a more precise prediction for the coalescence factor [8] in Fig. 1. If QGSJET-II-04m is blindly applied to the 7 TeV ALICE data, the obtained value for the coalescence parameter σ is 1.4 fm, while adjusting the results to the antiproton data yields 1.1 fm [8,19].

4. Program structure and example output

For convenience of both the young generation and ancient users, the program `AAfrag 2` exists as both Python 3 and Fortran 90 versions.

4.1. Purpose and method

`Aafrag 2` is a tool that interpolates results relevant for secondary interactions in cosmic ray studies from the Monte Carlo simulation QGSJET-II-04m. The calculation of the production cross section of photons, neutrinos, electrons, positrons, (anti-) protons and (anti-) neutrons in pp, pHe, Hep, HeHe, Cp, Alp, Fep interactions, as well as production cross section of antideuteron and antihelium-3 in pp, pHe, Hep, HeHe, $\bar{p}p$ and $\bar{p}$He interactions, are included. The tool allows the users to benefit from the advantages of a Monte Carlo simulation, with minimal computational effort. The calculations of photons, neutrinos, electrons, positrons, (anti-) protons and (anti-) neutrons were discussed in Ref. [9], while the cases of antideuteron and antihelium were treated in this work.

The results from the Monte Carlo simulations were stored in tables, and the main purpose of `AAfrag 2` is to provide the user with convenient interpolation routines. The interpolation is performed using bilinear interpolation, with a fill value 0 outside the data range.

The Fortran 90 program includes its own interpolation routines and is thus self-consistent, while the Python 3 program depends on the `numpy`, `scipy` and `matplotlib` libraries.

[2] We emphasise that the re-weighting depends heavily on the collision energy and the kinematical region considered in the experiment. Therefore, it has no predictive power and is not used elsewhere in this work.

Table 1
The particle type determined by the parameter q.

Function	$q=1$	$q=2$	$q=3$	$q=4$
`spec_nu`	ν_e	$\bar{\nu}_e$	ν_μ	$\bar{\nu}_\mu$
`spec_elpos`	e^-	e^+	–	–
`spec_pap`	p	$\bar{p}$	–	–
`spec_nan`	n	$\bar{n}$	–	–
`spec_gam`	γ	–	–	–
`spec_ad`	$\bar{d}$	–	–	–
`spec_ah`	${}^3\bar{\mathrm{He}} + {}^3\bar{\mathrm{H}}$	–	–	–

4.2. Program structure

The Fortran 90 program consists of two Fortran files, `AAfrag2.f90` and `user.f90`, in addition to the numerical tables in the `Tables` folder. The file `AAfrag2.f90` contains the module `spectra` which is used to store physical parameters and the loaded tables, the main program, subroutines used to initialise and load the tables, and the interpolation functions. Meanwhile, the file `user.f90` contains an example calculation. For the normal user, only changes in `user.f90` are necessary. The main program calls `init` which loads all the tables and stores the data in the variables defined in the module `spectra`. Next, the subroutine `user_main` in `user.f90` is called. Users must adapt this subroutine to their specific needs.

The Python 3 program is contained in `AAfrag2.py`, in addition to the numerical tables in the `Tables` folder. The Python functions have the same names and input parameters as the Fortran subroutines and functions. The script contains an example calculation that is executed when the script is run as a standalone. The user can either change the example portion of the script, or import the file as a module.

4.3. Functions

The program includes five functions that are intended to be used by the user (`spec_gam`, `spec_nu`, `spec_elpos`, `spec_pap`, `spec_nan`, `spec_ad`, `spec_ah`) which interpolate the production spectra of secondaries $\{\gamma,\ \nu_i,\ e^-,\ e^+,\ p,\ \bar{p},\ n,\ \bar{n},\ \bar{d},\ {}^3\mathrm{He}+{}^3\bar{\mathrm{H}}\}$ in various cosmic ray interactions. The functions have the same input parameters: `(E_p, E_s, q, k)`. Here, `E_p` is the total energy of the primary nucleus in GeV, `E_s` is the kinetic energy of the produced secondary in GeV, `q` denotes the particle species as detailed in Table 1, and `k` denotes the interaction

Table 2
Reaction type determined by the parameter k. Reactions 5–7 are not implemented for antideuteron (`spec_ad`) and antihelium-3 (`spec_ah`), while reactions 8–9 are exclusively implemented for them.

	$k=1$	$k=2$	$k=3$	$k=4$	$k=5$	$k=6$	$k=7$	$k=8$	$k=9$
Beam–Target	p–p	p–He	He–p	He–He	C–p	Al–p	Fe–p	$\bar{p}$–p	$\bar{p}$–He
Mass number	1–1	1–4	4–1	4–4	12–1	26–1	56–1	1–1	1–4

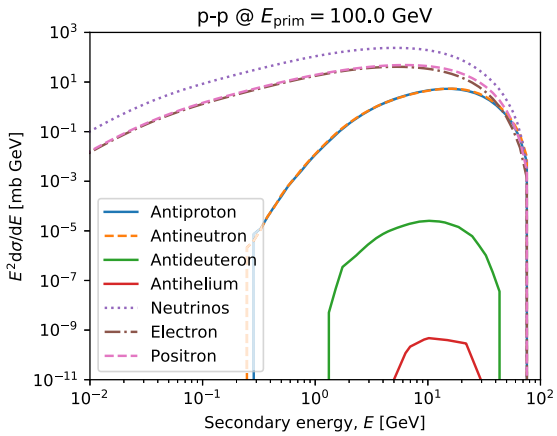

Fig. 5. Production spectrum of antiprotons, antineutrons, antideuterons, neutrinos, positrons and electrons in pp collisions with primary energy of 100 GeV. The figure is obtained by running the example programs included in `AAfrag2`.

type as detailed in Table 2. The output is the production spectrum $E_s^2 \mathrm{d}\sigma^k(E_p, E_s)/\mathrm{d}E_s$ in GeV mb. An example of their uses is given in the example programs.

4.4. Example output

The output of the example calculation are the files `spec_gam`, `spec_nu`, `spec_elpos`, `spec_aprot`, `spec_aneut`, `spec_adeut` and `spec_ahel`. They contain respectively the production spectra of photons, neutrinos, electrons and positrons, antiprotons, antineutrons, antideuterons, and antihelium-3. The result is plotted in Fig. 5 for pp collisions at 100 GeV.

5. Summary

Astrophysical antideuteron and antihelium-3 are ideal probes for new, exotic physics due to the suppressed background at low energies. Therefore, we made our predictions for the production cross sections of antideuteron and antihelium-3 in pp, pHe, Hep, HeHe, $\bar{p}p$ and $\bar{p}$He collisions at energies relevant for secondary production in the Galaxy publicly available through the interpolation subroutines `AAfrag`. The predictions are based on QGSJET-II-04m and the state of the art coalescence model evaluated on an event-by-event basis. Furthermore, we commented on the use of Monte Carlo generators to predict antinuclei fluxes, the use of a nuclear enhancement factor to predict secondary cosmic ray fluxes, and the effect of two-particle momentum correlations provided by a Monte Carlo.

Declaration of competing interest

The authors declare the following financial interests/personal relationships which may be considered as potential competing interests:

J. Tjemsland reports travel was provided by German Research Foundation. M. Kachelriess reports was provided by German Research Foundation. S. Ostapchenko reports financial support and travel were provided by German Research Foundation.

Data availability

Data will be made available on request.

Acknowledgements

This research was supported by the Munich Institute for Astro- and Particle Physics (MIAPP) which is funded by the Deutsche Forschungsgemeinschaft (DFG, German Research Foundation) under Germany's Excellence Strategy – EXC-2094 – 390783311. S.O. acknowledges support from the Deutsche Forschungsgemeinschaft (project number 465275045).

References

[1] A. Neronov, D.V. Semikoz, A.M. Taylor, Phys. Rev. Lett. 108 (2012) 051105, https://doi.org/10.1103/PhysRevLett.108.051105, arXiv:1112.5541.
[2] M. Ackermann, et al., Astrophys. J. 750 (2012) 3, https://doi.org/10.1088/0004-637X/750/1/3, arXiv:1202.4039.
[3] M. Kachelrieß, S. Ostapchenko, Phys. Rev. D 86 (2012) 043004, https://doi.org/10.1103/PhysRevD.86.043004, arXiv:1206.4705.
[4] F. Donato, N. Fornengo, P. Salati, Phys. Rev. D 62 (2000) 043003, https://doi.org/10.1103/PhysRevD.62.043003, arXiv:hep-ph/9904481.
[5] P. von Doetinchem, et al., J. Cosmol. Astropart. Phys. 08 (2020) 035, https://doi.org/10.1088/1475-7516/2020/08/035, arXiv:2002.04163.
[6] M. Kachelrieß, S. Ostapchenko, Phys. Rev. D 90 (8) (2014) 083002, https://doi.org/10.1103/PhysRevD.90.083002, arXiv:1405.3797.
[7] M. Kachelrieß, I.V. Moskalenko, S.S. Ostapchenko, Astrophys. J. 789 (2014) 136, https://doi.org/10.1088/0004-637X/789/2/136, arXiv:1406.0035.
[8] M. Kachelrieß, S. Ostapchenko, J. Tjemsland, J. Cosmol. Astropart. Phys. 08 (2020) 048, https://doi.org/10.1088/1475-7516/2020/08/048, arXiv:2002.10481.
[9] M. Kachelrieß, I.V. Moskalenko, S. Ostapchenko, Comput. Phys. Commun. 245 (2019) 106846, https://doi.org/10.1016/j.cpc.2019.08.001, arXiv:1904.05129.
[10] S. Ostapchenko, Phys. Rev. D 83 (2011) 014018, https://doi.org/10.1103/PhysRevD.83.014018, arXiv:1010.1869.
[11] S. Ostapchenko, EPJ Web Conf. 52 (2013) 02001, https://doi.org/10.1051/epjconf/20125202001.
[12] M. Kachelrieß, I.V. Moskalenko, S.S. Ostapchenko, Astrophys. J. 803 (2) (2015) 54, https://doi.org/10.1088/0004-637X/803/2/54, arXiv:1502.04158.
[13] S. Koldobskiy, M. Kachelrieß, A. Lskavyan, A. Neronov, S. Ostapchenko, D.V. Semikoz, Phys. Rev. D 104 (12) (2021) 123027, https://doi.org/10.1103/PhysRevD.104.123027, arXiv:2110.00496.
[14] A. Schwarzschild, C. Zupancic, Phys. Rev. 129 (1963) 854–862, https://doi.org/10.1103/PhysRev.129.854.
[15] S.T. Butler, C.A. Pearson, Phys. Rev. 129 (2) (1963) 836–842, https://doi.org/10.1103/PhysRev.129.836.
[16] M. Kachelrieß, S. Ostapchenko, J. Tjemsland, Eur. Phys. J. A 56 (1) (2020) 4, https://doi.org/10.1140/epja/s10050-019-00007-9, arXiv:1905.01192.
[17] M. Kachelrieß, S. Ostapchenko, J. Tjemsland, Eur. Phys. J. A 57 (5) (2021) 167, https://doi.org/10.1140/epja/s10050-021-00469-w, arXiv:2012.04352.
[18] V.I. Zhaba, APS Phys. 42 (2017) 191–195, https://doi.org/10.24144/2415-8038.2017.42.191-195, arXiv:1802.02778.
[19] J. Tjemsland, PoS TOOLS2020 (2021) 006, https://doi.org/10.22323/1.392.0006, arXiv:2012.12252.
[20] S. Acharya, et al., Phys. Lett. B 811 (2020) 135849, https://doi.org/10.1016/j.physletb.2020.135849, arXiv:2004.08018.
[21] S. Acharya, et al., Phys. Rev. C 97 (2) (2018) 024615, https://doi.org/10.1103/PhysRevC.97.024615, arXiv:1709.08522.
[22] S. Henning, et al., Lett. Nuovo Cimento 21 (1978) 189, https://doi.org/10.1007/BF02822248.
[23] W. Bozzoli, A. Bussiere, G. Giacomelli, E. Lesquoy, R. Meunier, L. Moscoso, A. Muller, D.E. Plane, F. Rimondi, S. Zylberajch, Nucl. Phys. B 159 (1979) 363–382, https://doi.org/10.1016/0550-3213(79)90340-7.

[24] S. Schael, et al., Phys. Lett. B 639 (2006) 192–201, https://doi.org/10.1016/j.physletb.2006.06.043, arXiv:hep-ex/0604023.
[25] R. Akers, et al., Z. Phys. C 67 (1995) 203–212, https://doi.org/10.1007/BF01571281.
[26] K. Blum, K.C.Y. Ng, R. Sato, M. Takimoto, Phys. Rev. D 96 (10) (2017) 103021, https://doi.org/10.1103/PhysRevD.96.103021, arXiv:1704.05431.
[27] R.P. Duperray, K.V. Protasov, A.Y. Voronin, Eur. Phys. J. A 16 (2003) 27–34, https://doi.org/10.1140/epja/i2002-10074-0, arXiv:nucl-th/0209078.
[28] R.P. Duperray, K.V. Protasov, L. Derome, M. Buenerd, Eur. Phys. J. A 18 (2003) 597–604, https://doi.org/10.1140/epja/i2003-10099-9, arXiv:nucl-th/0301103.
[29] F.E. James, Monte Carlo Phase Space, CERN, Geneva, 1968, p. 41, [numerical implementation given in the GENBOD subroutine (W515) in the CERNLIB Fortran libraries] https://doi.org/10.5170/CERN-1968-015.
[30] K. Blum, M. Takimoto, Phys. Rev. C 99 (4) (2019) 044913, https://doi.org/10.1103/PhysRevC.99.044913, arXiv:1901.07088.
[31] F. Bellini, K. Blum, A.P. Kalweit, M. Puccio, Phys. Rev. C 103 (1) (2021) 014907, https://doi.org/10.1103/PhysRevC.103.014907, arXiv:2007.01750.
[32] L.A. Dal, M. Kachelrieß, Phys. Rev. D 86 (2012) 103536, https://doi.org/10.1103/PhysRevD.86.103536, arXiv:1207.4560.
[33] S.-J. Lin, X.-J. Bi, P.-F. Yin, Expectations of the cosmic antideuteron flux, arXiv:1801.00997, 2018.
[34] A. Ibarra, S. Wild, Phys. Rev. D 88 (2013) 023014, https://doi.org/10.1103/PhysRevD.88.023014, arXiv:1301.3820.
[35] A. Białas, M. Bleszynski, W. Czyz, Nucl. Phys. B 111 (1976) 461.

Paper X – The effect of non-equal emission times and space-time correlations on (anti-) nuclei production

Kachelrieß, M., Ostapchenko, S. & Tjemsland, J. "The effect of non-equal emission times and space-time correlations on (anti-) nuclei production". *Submitted to Phys. Rev. C.* arXiv: 2303.08437 [hep-ph] (Mar. 2023)

Abstract: Light (anti-) nuclei are a powerful tool both in collider physics and astrophysics. In searches for new and exotic physics, the expected small astrophysical backgrounds at low energies make these antinuclei ideal probes for, e.g., dark matter. At the same time, their composite structure and small binding energies imply that they can be used in collider experiments to probe the hadronisation process and two-particle correlations. For the proper interpretation of such experimental studies, an improved theoretical understanding of (anti-) nuclei production in specific kinematic regions and detector setups is needed. In this work, we develop a coalescence framework for (anti-) deuteron production which accounts for both the emission volume and momentum correlations on an event-by-event basis. This framework goes beyond the equal-time approximation, which has been commonly assumed in femtoscopy experiments and (anti-) nucleus production models until now. Using PYTHIA 8 as an event generator, we find that the equal-time approximation leads to an error of $\mathcal{O}(10\%)$ in low-energy processes like Υ decays, while the errors are negligible at LHC energies. The framework introduced in this work paves the way for tuning event generators to (anti-) nuclei measurements.

In this paper, we discussed the effect of non-equal emission times and space-time correlations on the antideuteron production in the WiFunC model. In other words, we went beyond the equal-time approximation and considered the use of the space-time coordinates provided by the event generator instead of the Gaussian emission ansätze used in Papers I, II, IV and V. We had the idea that one can use the space-time coordinates provided by an event-generator in Paper IV already. However, we did not immediately see the importance of exploring it further and it was not clear how we could consistently go beyond the equal-time approximation. However, during the MIAPP workshop in Feb. 2022, it became clear that there was an interest and a need for a discussion of these topics.

The effect of non-equal emission times and space-time correlations on (anti-) nuclei production

M. Kachelrieß[1], S. Ostapchenko[2,3], and J. Tjemsland[1]
[1] *Institutt for fysikk, NTNU, Trondheim, Norway*
[2] *II. Institute for Theoretical Physics, Hamburg University, Hamburg, Germany and*
[3] *D.V. Skobeltsyn Institute of Nuclear Physics, Moscow State University, Moscow, Russia*
(Dated: 15. March 2023)

Light (anti-) nuclei are a powerful tool both in collider physics and astrophysics. In searches for new and exotic physics, the expected small astrophysical backgrounds at low energies make these antinuclei ideal probes for, e.g., dark matter. At the same time, their composite structure and small binding energies imply that they can be used in collider experiments to probe the hadronisation process and two-particle correlations. For the proper interpretation of such experimental studies, an improved theoretical understanding of (anti-) nuclei production in specific kinematic regions and detector setups is needed. In this work, we develop a coalescence framework for (anti-) deuteron production which accounts for both the emission volume and momentum correlations on an event-by-event basis. This framework goes beyond the equal-time approximation, which has been commonly assumed in femtoscopy experiments and (anti-) nucleus production models until now. Using PYTHIA 8 as an event generator, we find that the equal-time approximation leads to an error of $\mathcal{O}(10\%)$ in low-energy processes like Υ decays, while the errors are negligible at LHC energies. The framework introduced in this work paves the way for tuning event generators to (anti-) nuclei measurements.

PACS numbers:

I. INTRODUCTION

Light (anti-) nuclei are interesting particles due to their composite structure and small binding energies. This makes them ideal probes for, e.g., two-particle correlations and the QCD phase diagram in heavy ion collisions [1]. In particle collisions and decays, (anti-) nuclei can provide valuable information on the hadronisation process and momentum correlations that can be used to tune QCD inspired event generators. For the astroparticle community, the production of antinuclei is of immense interest since it is an ideal tool to search for new and exotic physics, such as dark matter annihilations or decays in the Milky Way [2–4]. In order to correctly interpret astrophysical and collider data, a description of the formation process as precise as possible is desirable.

The best motivated production model for light nuclei[59] in particle collisions—especially for small interacting systems—is arguably the coalescence model. In this model, final-state nucleons may merge if they are close in phase space. In heavy-ion collisions, the coalescence probability is often assumed to be mainly determined by the nucleon emission volume, while momentum correlations are neglected or treated as a collective effect [5, 6]. In small interacting systems, on the other hand, the coalescence condition is typically only evaluated in momentum space: For instance, in the simplest phenomenological coalescence model two nucleons merge if the momentum difference Δp in their pair rest frame is smaller than the coalescence momentum p_0 [7, 8]. However, two-particle correlations should not be neglected in small systems because of the low multiplicities and large anti-correlations of produced nucleons [9]. It was therefore suggested in Refs. [10, 11] that the coalescence condition $\Delta p < p_0$ should be evaluated on an event-by-event basis using a Monte Carlo event generator. Moreover, the expected nucleon emission length in small interacting systems, $\sigma \simeq 1$ fm, is of the same order as the size of the wave function of the deuteron, $r^d_{\rm rms} \simeq 2$ fm, even in point-like interactions [12] (see also Ref. [9] for an early discussion of the decay of Υ mesons). Thus, one should consider both the size of the formation region and momentum correlations simultaneously on an event-by-event basis. This is currently only achieved by the WiFunC model (Wigner Function with Correlations) introduced in Ref. [12], and further developed and discussed in Refs. [13–15]. This model is especially suitable for production processes relevant to cosmic ray interactions [13, 16, 17].

The WiFunC model, as most other sophisticated coalescence models [18–24], relies on the Wigner function approach, in which the coalescence probability is found by projecting the nucleon Wigner function onto the Wigner function of the light nucleus [25]. One of the key advantages of this approach is the fact that the coalescence probability depends on the hadronic emission region, a quantity which can be measured in femtoscopy experiments [18]. This allows one to determine independently the free parameter of these models [14, 26, 27]. Moreover, femtoscopy experiments can be used to distinguish between the coalescence hypothesis and other formation processes like thermal freeze-out [28–34]. For instance, it was argued in Ref. [35] that the current success of the framework is a strong indication that coalescence is a major antinuclei production mechanism.

This work is structured as follows: In section II, we review the basis of the Wigner function approach to coalescence, focusing on small interacting systems. In par-

ticular, we extend the framework to allow for non-equal emission times of the nucleons. That is, we go beyond the equal-time approximation which underlies both the experimental and theoretical framework of femtoscopy, and is expected to give up to $\mathcal{O}(30\,\%)$ uncertainties [35]. In section III, we review the WiFunC model and give an in-depth discussion of the choice of the nucleus wave function. Furthermore, we discuss the possibility of using the semi-classical space-time picture in QCD inspired event generators to describe the nucleon emission volume, thus allowing one to take into account space-time correlations on an event-by-event basis. Finally, in section IV, the discussions are exemplified using Pythia 8.3 [36, 37], with a focus on the equal-time approximation and the space-time picture provided by Pythia. Concretely, we consider the size of the hadronic emission region [38] (in IV A), the antideuteron spectrum [39] (in IV B), and the coalescence probability in jets [40, 41] (in IV C) measured by the ALICE collaboration. Furthermore, we compute the energy dependence of the emission volume, predicted by Pythia in section IV D and the antideuteron production in Υ decays [42, 43] in section IV E. The examples indicate that the equal-time approximation leads to an error of $\sim 10\%$ at low energies, while the error is neglible at LHC energies. The main uncertainties of the WiFunC model and of its predictions are currently related to the accuracy of the underlying event generators for high energy collisions. Conversely, the framework allows one to use femtoscopy and antideuteron measurements to tune such event generators.

II. THE WIGNER FUNCTION APPROACH TO COALESCENCE

A. General frame-work

In femtoscopy experiments, the correlations of pairs of particles with small relative momenta are measured. Since the final-state interactions that give rise to the correlations even from an initially uncorrelated source decrease rapidly with increasing distance in phase space, we only consider the contribution from the dominant pair[60]. The double energy spectrum can in this case be written as

$$(2\pi)^8\gamma_1\frac{\mathrm{d}^6N}{\mathrm{d}^3p_1\,\mathrm{d}^3p_2}=\sum_S\int \mathrm{d}^4x_1\,\mathrm{d}^4x_2\,\mathrm{d}^4x_1'\,\mathrm{d}^4x_2'\,\rho(x_1,x_2;x_1',x_2')\Psi^{S(-)}_{d,P}(x_1,x_2)\Psi^{S(-)\,\dagger}_{d,P}(x_1,x_2), \tag{1}$$

where ρ is the two-particle density matrix of the source and $\Psi^{S(-)}_{d,P_d}(x_1,x_2)=[\Psi^{S(+)}_{d,P_d}(x_1,x_2)]^\dagger$ is the Bethe-Salpeter wave function accounting for the final-state interactions [44]. In the case of weakly bound systems such as the deuteron, helion and triton, we can connect Eq. (1) with the coalesence formalism based on generalised or relativistic Wigner functions: Neglecting the binding energy and employing the sudden approximation, the Bethe-Salpeter wave function reduces to the wave function of the static bound state. The deuteron energy spectrum can then be approximated as

$$(2\pi)^8\gamma_d\frac{\mathrm{d}^3N_d}{\mathrm{d}P_d^3}=S\int \mathrm{d}^4x_1\,\mathrm{d}^4x_2\,\mathrm{d}^4x_1'\,\mathrm{d}^4x_2'\,\rho(x_1,x_2;x_1',x_2')\Psi^{(-)}_{d,P_d}(x_1,x_2)\Psi^{(-)\,\dagger}_{d,P_d}(x_1,x_2), \tag{2}$$

where the factor $S=3/8$ is obtained by averaging over all spin and isospin states. Factoring out then the center-of-mass motion, $\Psi^{S(-)}_{d,P_d}(x_1,x_2)=\mathrm{e}^{\mathrm{i}P_dX}\Psi^{S(-)}_d(x)$, one can re-write Eq. (1) as (see, e.g., Ref. [18] for details),

$$(2\pi)^8\gamma_d\frac{\mathrm{d}^3N_d}{\mathrm{d}P_d^3}=S\int \mathrm{d}^4r\,\mathrm{d}^4r_d\,\mathrm{d}^4q\,\mathcal{D}^{(4)}(q,r)W_{np}(P_d/2+q,P_d/2-q,r,r_d), \tag{3}$$

where

$$\mathcal{D}^{(4)}(q,r)=\int \mathrm{d}^4\xi\,\mathrm{e}^{-\mathrm{i}q\xi}\Psi^{(-)}_d(r+\xi/2)\Psi^{(-)*}_d(r-\xi/2) \tag{4}$$

is the (generalised or off-shell) deuteron Wigner function and W_{np} the two-nucleon Wigner function of the source. Here, r denotes the space-time distance between the nucleons, r_d the space-time position and $P_d=p_1+p_2$ the four-momentum of the nucleus, while $q=(p_1-p_2)/2$ is the four-momentum of the nucleons in the nucleus frame. The main difference between Eq. (3) and the expression usually used in the literature (e.g. in Refs. [12, 18, 35]) is its time and energy dependence: The variable r_d^0 describes the "freeze-out" time of the nucleus, and does not affect the emission volume[61]. Meanwhile, the variable $r^0=t$ describes the time difference in the production of the nucleons, which clearly may impact the measured emission volume. Finally, q^0 describes the off-shell structure of the two-particle system.

To proceed, it is normally assumed that the particles are produced at the same time (equal-time approximation) and/or that the source is independent of q (smoothness-approximation) [45]. However, as argued in Ref. [35], the equal-time approximation is not expected to be accurate in the case of small interacting systems. In order to check the reliability of this approximation, one should therefore go beyond the equal time approximation. As we will see, it is sufficient to assume that the particles are (approximately) on-shell when they coalesce, $W_{np} \simeq W_{np}(q^0 = 0)$. This assumption is well motivated due to the low binding energy of the antinuclei. We are in this case left with[62]

$$(2\pi)^7 \gamma_d \frac{\mathrm{d}^3 N_d}{\mathrm{d}P_d^3} = S \int \mathrm{d}^4 r \, \mathrm{d}^3 q \, \mathcal{D}_t^{(3)}(\boldsymbol{q}, \boldsymbol{r}) W_{np}^{(4)}(\boldsymbol{P}_d/2 + \boldsymbol{q}, \boldsymbol{P}_d/2 - \boldsymbol{q}, r), \tag{5}$$

where

$$\mathcal{D}_t^{(3)}(\boldsymbol{q}, \boldsymbol{r}) = \int \mathrm{d}^3 \xi \, \mathrm{e}^{-\mathrm{i}\boldsymbol{q}\cdot\boldsymbol{\xi}} \Psi_d^{(-)}(\boldsymbol{r} + \boldsymbol{\xi}/2, t) \Psi_d^{(-)*}(\boldsymbol{r} - \boldsymbol{\xi}/2, t) \tag{6}$$

is the time dependence of the static deuteron Wigner function. In the nucleus frame, this reduces to

$$\frac{\mathrm{d}^3 N_d}{\mathrm{d}P_d^3} = \frac{S}{(2\pi)^7} \int \mathrm{d}t \, \mathrm{d}^3 r \, \mathrm{d}^3 q \, \mathcal{D}_t^{(3)}(\boldsymbol{q}, \boldsymbol{r}) W_{np}^{(4)}(\boldsymbol{q}, \boldsymbol{r}, t). \tag{7}$$

In order to evaluate the deuteron yield using Eq. (5), the deuteron Wigner function and the two-nucleon Wigner function have to be modelled. A key observation is that, in the classical limit, the nucleon Wigner function will reduce to the phase-space distribution. In section III, we discuss the WiFunC approach, in which the momentum correlations are provided by an event generator, while the emission volume is either assumed to be Gaussian or taken also from an event generator.

B. The effect of non-equal emission times

The framework underlying the Wigner function approaches to coalescence and femtoscopy experiments relies on the equal-time approximation [35, 45], i.e., it is assumed that the particles are produced at the same time, $t = 0$. More concretely, it is assumed that $q \ll m\sigma/t \simeq 1\,\mathrm{GeV}$ [44], where σ is the linear size of the emission volume. Since the bulk of nuclei are produced by nucleons with $q \sim \mathcal{O}(0.1)\,\mathrm{GeV}$, this condition is expected to yield an uncertainty of $\mathcal{O}(10\%)$ [35].

The effect of non-equal emission times on femtoscopy experiments is discussed in detail in Ref. [44], where it is shown that the relation between the Bethe-Salpeter amplitude and the corresponding non-relativistic wave function can be expressed as

$$\Psi(r) = \Psi(\boldsymbol{r}, t) = \int \mathrm{d}^3 r' \, \delta_q(\boldsymbol{r} - \boldsymbol{r}', t) \psi(\boldsymbol{r}') \tag{8}$$

under the condition $q^2 \ll m^2$, which clearly is the case we are interested in. The function $\delta_q(\boldsymbol{r}, t)$ reduces to the ordinary Dirac delta function for $t = 0$, and for $t > 0$ it is given by [44]

$$\delta_q(\boldsymbol{r}, t) = \left(\frac{m}{2\pi \mathrm{i} t}\right)^{3/2} \exp\left(\frac{\mathrm{i} q^2 t}{2m} + \frac{\mathrm{i}\boldsymbol{r}^2 m}{2t}\right). \tag{9}$$

Inserting Eq. (8) into Eq. (6) leads to

$$\mathcal{D}_t^{(3)}(\boldsymbol{q}, \boldsymbol{r}) = \mathcal{D}^{(3)}(\boldsymbol{q}, \boldsymbol{r} + \boldsymbol{q}t/m) \tag{10}$$

with

$$\mathcal{D}^{(3)}(\boldsymbol{q}, \boldsymbol{r}) = \int \mathrm{d}^3 \xi \mathrm{e}^{-\mathrm{i}\boldsymbol{\xi}\cdot\boldsymbol{q}} \psi(\boldsymbol{r} + \boldsymbol{\xi}/2) \psi^*(\boldsymbol{r} - \boldsymbol{\xi}/2). \tag{11}$$

Therefore, the deuteron yield can be expressed as

$$\frac{\mathrm{d}^3 N_d}{\mathrm{d}P_d^3} = \frac{S}{(2\pi)^7} \int \mathrm{d}t \, \mathrm{d}^3 r \, \mathrm{d}^3 q \, \mathcal{D}^{(3)}(\boldsymbol{q}, \boldsymbol{r} + \boldsymbol{q}t/m) W_{np}^{(4)}(\boldsymbol{q}, \boldsymbol{r}, t) \tag{12}$$

in the pair rest frame. This is one of the main results of this paper: By comparing with, e.g., Refs. [12, 18, 35], one can see that non-equal emission times of the nucleons change r by the classical distance the first particle propagates before the second particle is produced. If the equal-time approximation ($t \to 0$) is applied to Eq. (12), one re-obtains, as expected, the same equation as in Refs. [12, 18, 35].

Note that four assumptions are needed to obtain Eq. (12): (1) The coalescing particles are non-relativistic in the pair rest frame ($q^2 \ll m^2$) and (2) approximately on-shell. Moreover, (3) the wave function describing the initial and final states changes slowly compared to the interaction time (i.e., the sudden approximation) and (4) the interaction between a single pair of nucleons is dominant. All these assumptions are well motivated, and always used in the coalescence model. For example, due to the small binding energy of the deuteron, one will expect that the nucleons have to be close in phase space and approximately on-shell to coalesce.

C. Relation to femtoscopy experiments

Since the measured source function is strongly linked to the Wigner function, any coalescence model arising from Eq. (5) can be directly and independently tested and tuned by baryonic correlation experiments. Under

the smoothness approximation (i.e. $W_{np}(r, r_d, P_d, q) \simeq W_{np}(r, r_d, P_d, 0)$), Eq. (5) can be written as

$$\frac{\mathrm{d}^3 N_d}{\mathrm{d}P_d^3} \propto \int \mathrm{d}^3 r\, \mathrm{d}t\, W_{np}^{(4)}(\boldsymbol{r}, t) \int \mathrm{d}^3 q\, \mathcal{D}_t^{(3)}(\boldsymbol{q}, \boldsymbol{r}) = \int \mathrm{d}^3 r\, |\phi(\boldsymbol{r})|^2 \mathcal{S}(\boldsymbol{r}), \tag{13}$$

where $\mathcal{S}(\boldsymbol{r}) = W_{np}^{(3)}(\boldsymbol{r})$ is the emission source defined in the pair rest frame. The last equality follows directly if one in addition uses the equal-time approximation [45], $W_{np} \propto \delta(t)$. In a femtoscopy experiment, the source size $\mathcal{S}(\boldsymbol{r})$ can be measured via the final-state interactions encoded into the wave function $\psi(r)$ [45]. Thus, a femtoscopy experiment can be interpreted as an indirect measurement of the Wigner function. Recently, the ALICE collaboration measured the size of the baryonic emission source in pp collisions at 13 TeV, assuming an isotropic Gaussian source [38]. This measurement can be used to fix the free parameter of a coalescence model, allowing one to test and tune the coalescence models like the WiFunC model [14].

Femtoscopy experiments include often a cut in the momentum q [38]. It is thus interesting to note that it is sufficient to assume that $qt/m \ll r$ to derive Eq. (13), thereby removing the need to invoke the equal-time and smoothness approximations.

III. THE WIFUNC MODEL

In the classical limit, the nucleon Wigner function [see Eq. (12)] will describe the phase space distribution of the nucleons [46]. The main idea behind the WiFunC model is to include particle momentum correlations provided by a Monte Carlo event generator. At the same time, the nucleon emission volume can be described either by a simple ansatz or by the event generator. In this section, we give a short review of the model and at the same time a deeper discussion of the choice of the nucleus wave function as well as the use of the space-time picture provided by an event generator to describe the nucleon emission volume. In particular, we comment on the consequences of the equal-time approximation [cf. Eq. (12)].

A. Deuteron wave function

In the WiFunC model, the deuteron Wigner function $\mathcal{D}$ is an essential ingredient in the calculation of the coalescence probability. For a specific choice of the deuteron wave function ϕ, the corresponding Wigner function $\mathcal{D}$ can be evaluated using Eq. (11). The deuteron is in a pure state, and can be well approximated by the Hulthen wave function [47]. However, it is known that the Wigner function of a pure state is strictly positive if and only if the wave function is a Gaussian [48, 49]. An interpretation of the deuteron Wigner function as a probability distribution, as it is required for the evaluation of the coalescence probability, requires therefore at first sight to use a simple Gaussian wave function, $\phi(r) \propto \exp\left(-r^2/2d^2\right)$. In this case, the Wigner function becomes

$$\mathcal{D}(r, q) = 8\mathrm{e}^{-r^2/d^2 - d^2 q^2}. \tag{14}$$

where the choice $d = 3.2$ fm reproduces the deuteron charge radius. However, the Gaussian wave function is neither a good representation of the Hulthen wave function nor does it lead to a Wigner function which is similar to that obtained using the Hulthen wave function, cf. with Fig. 1. Thus, one should aim for a better description of the deuteron wave function.

In order to find such an improved wave function, consider now the more general pure state $\phi(r) = (\phi_r(r) + \mathrm{i}\phi_i(r))/\sqrt{2}$, where ϕ_r and ϕ_i are real wave-functions. In this case, the Wigner function can be split into a symmetric and an antisymmetric part, $\mathcal{D}(q, r) = \mathcal{D}_r(q, r) + \mathcal{D}_i(q, r) - A(q, r)$, where $\mathcal{D}_r$ and $\mathcal{D}_i$ are the Wigner functions of ϕ_r and ϕ_i, respectively. The antisymmetric interference term A vanishes upon performing the integrations in Eq. (12) and will therefore not contribute to the coalescence probability. This implies that the sum of two Wigner functions from pure states can be re-cast into a Wigner function from a mixed state,

$$\mathcal{D}_r(\boldsymbol{q}, \boldsymbol{r}) + \mathcal{D}_i(\boldsymbol{q}, \boldsymbol{r}) = \int \mathrm{d}^3\xi\, \mathrm{e}^{-\mathrm{i}\boldsymbol{q}\cdot\boldsymbol{\xi}} \times \langle \boldsymbol{r} - \boldsymbol{\xi}/2| \left(\frac{1}{2} |\phi_r\rangle \langle\phi_r| + \frac{1}{2} |\phi_i\rangle \langle\phi_i| \right) |\boldsymbol{r} + \boldsymbol{\xi}/2\rangle\,. \tag{15}$$

A particular choice is the "ϕ_0-fit" of Ref. [12], where the deuteron Wigner function is given by

$$\mathcal{D}(\boldsymbol{q}, \boldsymbol{r}) = 8\Delta \mathrm{e}^{-d_1^2 q^2 - r^2 d_1^2} + 8(1-\Delta)\mathrm{e}^{-d_2^2 q^2 - r^2 d_2^2} - \mathcal{A}(\boldsymbol{q}, \boldsymbol{r}) \tag{16}$$

with $\Delta = 0.581$, $d_1 = 3.979$ fm, $d_2 = 0.890$ fm and $\mathcal{A}$ is antisymmetric in $\boldsymbol{q}$ and $\boldsymbol{r}$.

If one describes the deuteron—incorrectly—as a mixed state, one can approximate its wave function, e.g., the Hulthen wave function, arbitrarily accurately by a sum of Gaussian states. In the fourth panel of Fig. 1, we show a one-dimensional example[63] using 12 Gaussians whose centers are distributed evenly between $x = -5$ and $x = 5$. Since we are considering a mixed state of Gaussians, the deuteron Wigner function is itself a sum of Gaussians and strictly positive. This approach presents a clear method for handling the negative parts of the phase space distribution. However, the mixed state neglects the "quantum correlations" encoded in the Wigner function.

The negative parts of the Wigner function should vanish in the classical limit. This leads to another method of getting around the problem of a negative Wigner function: If one uses the equal-time approximation and assumes that the space and momentum distributions are uncorrelated, $W_{np} = G(\boldsymbol{q})H(\boldsymbol{r}_p, \boldsymbol{r}_n)$, the deuteron yield

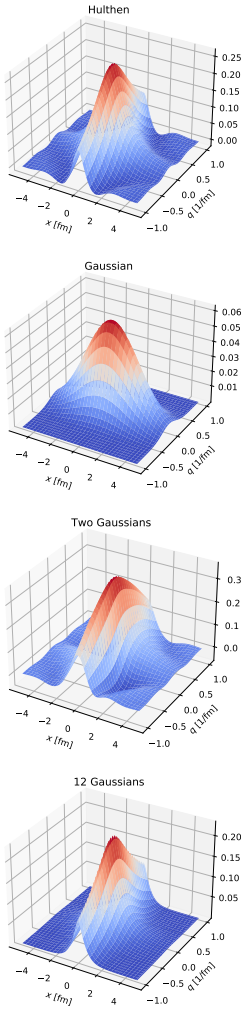

FIG. 1: The Wigner function in the (x, q_x) plane obtained numerically using (from top to bottom) the Hulthen wave function, a single Gaussian wave function, the sum of two Gaussians with a phase shift π, and the sum of 12 Gaussians. The wave functions are discussed in more detail in the text and in Ref. [12]. While it is difficult to see in the plot, the Hulthen Wigner function is symmetric, while the negative parts of the two-Gaussian Wigner function are antisymmetric.

can be written as

$$\frac{\mathrm{d}^3N_d}{\mathrm{d}P_d^3} = \frac{S}{(2\pi)^6}\int \mathrm{d}^3q\, G_{np}^{(3)}(\boldsymbol{q})\int \mathrm{d}^3r_p\,\mathrm{d}^3r_n \times \mathcal{D}^{(3)}(\boldsymbol{q},\boldsymbol{r})H_{np}(\boldsymbol{r}_n,\boldsymbol{r}_p) \tag{17}$$

where the last integral can be interpreted at the probability density for coalescence and G_{np} is the momentum distribution provided by the event generator [12]. These are the same assumptions used in the next subsection, where H_{np} is approximated as a Gaussian. If H_{np} is sufficiently wide and well-behaved, the "probability density" will be strictly positive[64]. Thus, this may allow one to use *any* wave function and evaluate numerically the coalescence probability event-by-event. While this may work well for, e.g., high multiplicity pp collisions, the method should not be applied if position–momentum correlations are included, or the multiplicity of the interaction is small, such as in Υ decays.

In conclusion, if the deuteron wave function in the WiFunC model is represented by *any* $\phi(\boldsymbol{r}) = \phi_r(\boldsymbol{r}) + \mathrm{i}\phi_i(\boldsymbol{r})$, where ϕ_r and ϕ_i are Gaussians centered at $r = 0$, the coalescence probability is well defined for all interactions; we suggest, with the current theoretical uncertainties, using the Wigner function in Eq. (16).

B. Nucleon distribution

Current QCD inspired event generators evaluate the parton cascade in momentum space using a probabilistic scheme. While this is sufficient to provide two-particle momentum correlations, an extraction of the two-nucleon Wigner function W_{np} is not possible. Therefore, a semi-classical ansatz has to be made before one can evaluate the coalescence equation (12) on an event-by-event basis. In Ref. [12], the equal-time approximation was used and it was assumed that the space and momentum distributions are uncorrelated, $W_{np}(\boldsymbol{q}, \boldsymbol{P}_d, \boldsymbol{r}_p, \boldsymbol{r}_n) = G(\boldsymbol{q})H(\boldsymbol{r}_p, \boldsymbol{r}_n)$. In turn, the ansatz

$$H(\boldsymbol{r}_p, \boldsymbol{r}_n) = h(\boldsymbol{r_p})h(\boldsymbol{r_n}) \tag{18}$$

with

$$h(\boldsymbol{r}) = \left(2\pi\sigma^2\right)^{-3/2}\exp\left(-\frac{r_\perp^2}{2\sigma_\perp^2} - \frac{r_\parallel^2}{2\sigma_\parallel^2}\right) \tag{19}$$

was used for the nucleon distributions in the laboratory (lab) frame. In particle collisions, e.g., pp, e^+e^- and pN, the longitudinal and transverse directions are defined relative to the beam direction. In annihilation and decay processes, e.g., dark matter annihilations, one should define the coordinate system relative to the initial quark–antiquark pair. With a one-Gaussian wave function, the deuteron spectrum can be written as

$$\frac{\mathrm{d}^3N_d}{\mathrm{d}P_d^3} = \frac{3\zeta(d)}{(2\pi)^3}\int \mathrm{d}^3q\,\mathrm{e}^{-q^2d^2}G(\boldsymbol{q}), \tag{20}$$

where

$$\zeta(d) = \left[\left(\frac{d^2}{d^2+4\sigma_\perp^2 m_T^2/m^2}\right)\left(\frac{d^2}{d^2+4\sigma_\perp^2}\right)\left(\frac{d^2}{d^2+4\sigma_\parallel^2}\right)\right]^{1/2}. \tag{21}$$

The m_T dependence arises due to the Lorentz boost of the transverse spread from the lab frame to the pair rest frame, see Ref. [12] for details. The model can be added as an afterburner to any Monte Carlo event generator by applying the weight

$$w = 3\Delta\zeta(d_1)\mathrm{e}^{-d_1^2 q^2} + 3(1-\Delta)\zeta(d_2)\mathrm{e}^{-d_2^2 q^2}, \qquad (22)$$

to each nuleon pair. Here, the numerical values of the parameters are $\Delta = 0.581$, $d_1 = 3.979\,\mathrm{fm}$ and $d_2 = 0.890\,\mathrm{fm}$, while m_T and q are determined event-by-event from the Monte Carlo data.

The two parameters σ_i describe the average emission length of nucleons, $\sigma_{\parallel/\perp} \simeq 1\,\mathrm{fm}$. In point-like processes, like e^+e^- collisions, the longitudinal spread is dominated by the hadronisation length, $\sigma_\parallel \sim L_{\mathrm{had}} \simeq 1\,\mathrm{fm}$, while the transverse spread is related to Λ_{QCD}. Since they are of the same order of magnitude, it is convenient to set $\sigma = \sigma_\perp = \sigma_\parallel$. In collisions involving hadrons and nuclei, the spread will also obtain a geometrical contribution due to multiple parton–parton scatterings. In the particular case of pp collisions, the spread in the transverse and longitudinal directions are of the same size as the point-like spread [12]. Thus, one will expect $\sigma \equiv \sigma_{e^+e^-} = \sigma_{pp}/\sqrt{2}$.

The numerical value $\sigma = (1.0 \pm 0.1)\,\mathrm{fm}$ has been shown to reproduce a wide range of experimental data on pp, e^+e^- and pN collisions, as well as baryonic femtoscopy, within experimental and theoretical uncertainties [15]. This value is also in agreement with the physical interpretation of the model, being thus a strong indication of the validity of the underlying model assumptions. The spread should in principle vary between events; in particular, it should depend on the impact parameter and multiplicity. Moreover, $\sigma_\perp \lesssim \sigma_\parallel$. With improved experimental data and improved event generators, one may have therefore to tune $\sigma_\perp$ and $\sigma_\parallel$ independently and vary them as a function of multiplicity.

C. Spatial correlations in event generators

Some event generators, like Pythia [36, 37] and EPOS [50, 51], include a semi-classical description of the space-time evolution of the cascade. If one employs the space-time treatment of an event generator, the coalescence weight becomes

$$w = \mathcal{D}(\boldsymbol{q}, \boldsymbol{r}) = 3\exp\left\{-\frac{1}{d^2}\left(\boldsymbol{r} + \frac{\boldsymbol{q}t}{m}\right)^2 - q^2 d^2\right\}, \qquad (23)$$

and can be extended to a two-Gaussian wave function as Eq. (2). Heisenberg's uncertainty relation limits the precision of the space-time information a specific event can contain. As a result, the space-time evolution predicted by these generators can be only an approximation to the expected probability distributions. Thus, this approach is merely a change of the semi-classical description of the nucleon distribution from that discussed in the previous subsection to that supplied by the event generator. It has, however, some advantages: First, the non-trivial Lorentz transformation of the emission volume can be taken into account in a straight-forward manner. For example, one does not have to assume that the momenta of the quark pair initiating the cascade are directed along the beam direction. Thus, more complicated processes, like $\Upsilon \to ggg$, are trivial to consider, provided that the event generator describes the process accurately. Second, the emission volume is expected to be strongly correlated with the centrality of the collision in pN and NN collisions, and thus the multiplicity. These effects can in principle be described by an event generator. Third, a weak energy dependence of the emission volume is expected. Note that these effects will likely only be visible in accelerator data, when narrow parts of the phase space are considered. In cosmic ray physics, however, it is more appropriate to use an event generator which is specialised to such applications, e.g., QGSJET [52, 53].

IV. EXAMPLES

In this section, we will be considering a few examples of antinuclei production in small interacting systems, using Pythia 8 as event generator. One should note that the space-time treatment of parton–parton interactions in Pythia is not yet complete and there exist yet no official tunes [37]. In particular, the geometrical contribution to the longitudinal spread is not implemented, i.e., all parton–parton interactions occur at $z = 0$. As such, we cannot expect at this time Pythia to perfectly reproduce the experimental data. Nevertheless, the examples we are considering can be used to tune and develop Pythia's space-time picture. Moreover, they will highlight some of the important features of the WiFunC model.

A. Emission volume in pp collisions at LHC

The ALICE collaboration measured recently the source radius of the baryon emission at 13 TeV in pp collisions by assuming an isotropic Gaussian source profile in the femtoscopy framework [38]. As discussed in section II C, the source radius is directly connected to the Wigner function in the coalescence model via Eq. (12). Although a simplified description of the source was used, the treatment of W_{np} in the coalescence model should reproduce this measurement. It allows us thereby to tune the coalescence model completely independently of antideuteron measurements. A caveat is that the measurement is conducted in the lab frame, while the source is defined in the pair rest frame. Therefore, the measured source size is the Euclidean distance in the lab frame at "freeze-out" boosted into the pair rest frame. This naturally explains the m_{T} scaling observed in Ref. [38].

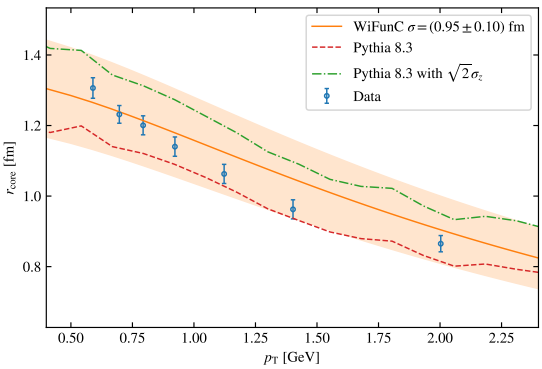

FIG. 2: The Gaussian emission size of pp and $\bar{p}\bar{p}$, $r_{\rm core}$, measured by the ALICE collaboration [38] (blue circles) is compared to the prediction of the WiFunC model using the space-time picture of Pythia 8 (red dashed line) and the Gaussian ansatz for the emission volume [14] (orange solid line). Since the longitudinal geometrical spread is not yet included in Pythia, we show the results with a longitudinal spread added by hand (green dashed dotted) for visualisation.

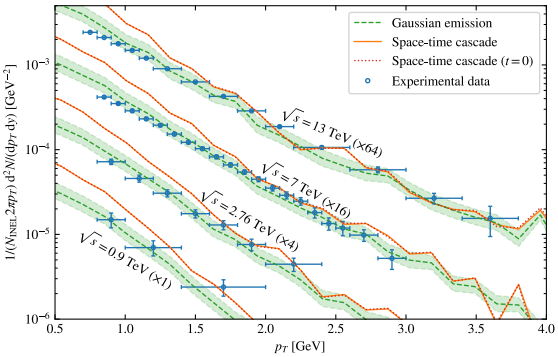

FIG. 3: The antideuteron spectrum in pp collisions at $\sqrt{s} = 0.9$, 2.7, 7 and 13 TeV, predicted by Pythia 8 using a Gaussian ansatz with $\sigma = (1.0 \pm 0.1)$ fm (green dashed line) and the space-time approach of Pythia (orange line), is compared to the experimental data of the ALICE collaboration [39, 54] (the data at 13 TeV is multiplied by a factor 0.79 to normalise the spectrum to the total number of inelastic events). The result without the equal-time approximation (red dotted line) is shown for completeness.

In Fig. 2, we compare the $pp \otimes \bar{p}\bar{p}$ source radius measured by ALICE to that predicted by the Gaussian ansatz in the WiFunC model (see Ref. [14]) and by the space-time picture implemented in Pythia. It is clear that the qualitative behaviour of the m_T scaling is well reproduced by Pythia, while the overall source size is underestimated. The latter is expected as the longitudinal geometrical spread is not yet included in Pythia. For illustration, we have added an additional line where σ_z was increased by a factor $\sqrt{2}$; the resulting agreement indicates that the space-time picture in Pythia has the potential to reproduce the experimental data. In turn, these data can be used to tune the space-time approach of Pythia.

B. Deuteron spectrum at LHC

In Fig. 3, the deuteron spectrum in pp collisions at 0.9, 2.76, 7 and 13 TeV, as predicted by the WiFunC model with the Gaussian emission volume and with the space-time picture implemented in Pythia, is compared to the experimental data measured by the ALICE collaboration [39, 54]. It is clear that the space-time approach of Pythia is overproducing antinuclei, as expected from the under-estimated longitudinal size discussed in the previous subsection. We note again that these measurements can be used to tune Pythia's space-time picture. Due to the composite structure of the deuteron, one can also use antinuclei experiments to tune the event generator to two-particle correlations.

The lines with and without the equal-time approximation completely overlap. That is, Pythia predicts that the inaccuracy of the equal-time approximation is neglegible at LHC energies: Although the uncertainty in the emission volume in single events is of order 10%, the effect is suppressed since the coalescence condition requires the pairs of nucleons to be close-by in phase space.

C. Enhanced coalescence probability in jets

The ALICE collaboration has measured an enhanced (anti-) deuteron coalescence probability in jets [40, 41], compared to the underlying events for pp collisions at 13 TeV. More concretely, the measured coalescence factor

$$B_2 = \left(\frac{1}{2\pi p_T^{\rm deut}} \frac{{\rm d}^2 N_{\rm deut}}{{\rm d}y \, {\rm d}p_T^{\rm deut}} \right) / \left(\frac{1}{2\pi p_T^{p}} \frac{{\rm d}^2 N_{p}}{{\rm d}y \, {\rm d}p_T^{p}} \right)^2 \qquad (24)$$

for $p_T^p = p_T^d/2$ and $|y| < 0.5$ is a factor ≈ 10 larger in a jet than in the underlying event. In the coalescence model, this is naturally explained by the larger phase space density of nucleons in the jet, and is therefore a strong indication that coalescence is a major production mechanism for deuterons. Moreover, this experiment may prove useful for understanding the exact nature of the coalescence mechanism.

In Fig. 4, we compare the coalescence factor (24) predicted by the WiFunC model with a simple Gaussian ansatz (blue) and using the space-time picture in Pythia (orange). The results were obtained simulating inelastic

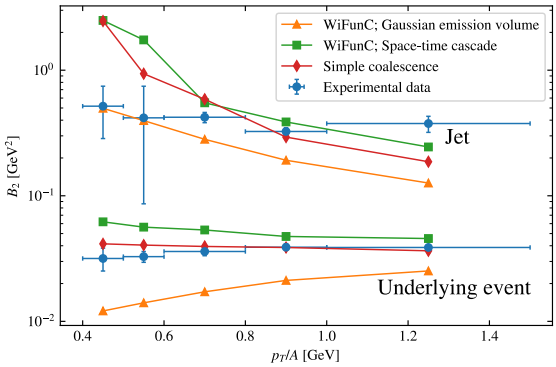

FIG. 4: The measured coalescence factor B_2 in pp collisions at $\sqrt{s} = 13\,\text{TeV}$ (blue circles) is compared to the predictions of Pythia 8.3 combined with the WiFunC model using a simple Gaussian ansatz (orange triangles) or based on the space-time treatment of Pythia (green squares). In addition, the results using the simple coalescence model (red diamonds) are shown for comparison.

pp collisions at 13 TeV, using Pythia 8.3 and enforcing the experimental triggers and cuts used in the event selection [40, 41]. The jet axis was approximated as the region with an azimuthal angle $|\Delta\phi| < 60°$ around the so-called leading particle, as explained in Ref. [41]. Any charged particle at midrapidity ($|y| < 0.5$) and high transverse momentum ($p_T > 5$ GeV) is considered a leading particle. In the same manner, the underlying event was approximated by the region $60° < |\Delta\phi| < 120°$.

The overall results shown in Fig. 4 are consistent with those of Ref. [40]: There is an enhancement of a factor ~ 10 in the coalescence probability (i.e., the coalescence factor B_2) in the jet, compared to the underlying event. For comparison, we also use the simple coalescence model [40] (green) with a hard cutoff in momentum space, $p < 0.285\,\text{GeV}$, and a statistical weight 3/8. We emphasise that no fitting was performed, and the result from the WiFunC model (orange and blue) should be considered as a prediction. In accordance with Fig. 2, the space-time treatment overpredicts the coalescence probability. One should further note that the emission volume used in the simple Gaussian ansatz includes a Lorentz transformation relative to the beam axis, which is expected to be a valid approximation for a typical pp interaction. However, in Fig. 4, we are only considering events within a clear jet, in which case the boost should be done relative to the initial parton in the parton cascades. This is one of the main perks in using the space-time treatment in Pythia, since more complicated geometries are automatically taken into account.

D. Energy dependence of the emission volume

The emission volume is expected to have a weak energy dependence [12]. Within the current experimental and theoretical uncertainties, the emission volume is consistent with being constant [15]. The expected energy dependence and its relevance to coalescence is however not trivial: At high energies, the source size measured via femtoscopy experiments will increase and be much larger than 1 fm. For instance, the average Γ factor of nucleons in their pair rest-frame increases with the center-of-mass energy $\sqrt{s}$ of the collision. As a result, the hadronisation length $\ell \simeq \Gamma/m_N$ increases with $\sqrt{s}$. This growth will affect mainly the longitudinal emission length. Moreover, multiple scattering in hadronic collisions enlarges the source volume additionally. While the first effect is strongly suppressed in the production of light nuclei because of the coalesence weight w, it is also suppressed in femtospectroscopy measurements because of experimental cuts. For instance, the ALICE collaboration used $q < 0.375\,\text{GeV}$, in addition to the trigger condition and the rapidity cut.

In order to test this expectation and at the same time to highlight some differences between the Gaussian ansatz for the emission volume and the space-time picture of the event generator, we plot in Fig. 5 the predicted energy dependence of σ by Pythia 8.3 in pp collisions. A weight $\exp\left(-d^2q^2\right)$ was included (q being the nucleon momentum in the pair rest frame) to highlight the "coalescence relevant" source size. Pythia predicts, as expected [12], a weak energy dependence of the emission volume and $\sigma_\parallel > \sigma_\perp$. The energy dependence can be explained by correlations between the position and momentum: Initially, the spread σ increases due to the increased energy available to the nucleons; the increase is dominated by nucleons produced back-to-back. At some point, the cut in momentum space suppresses the emission volume, making σ approximately constant.

Furthermore, there is a significant difference in the energy evolution of the spread in the longitudinal and transverse direction. In the Gaussian ansatz of the source volume [cf. with Eq. (21)], the longitudinal spread will be constant while the transverse spread will effectively be Lorentz contracted for large transverse momenta: $\sigma_\perp = \sigma m/m_T$. Meanwhile, using Pythia, the Lorentz boost is performed on a pair-by-pair basis and is thus not defined relative to the initial particle beam. Therefore, the expected transverse contraction in Pythia will occur both for $\sigma_\perp$ and $\sigma_\parallel$.

Cosmic ray antiuclei are mainly produced by primary protons colliding with the interstellar medium at energies 10–20 GeV in the center-of-mass frame. According to the results in Fig. 5, Pythia predicts a decrease of σ by ~ 0.1 fm, when moving from LHC to such low energies. Closer to the threshold, outside the validity range of Pythia, anti-correlations can increase the baryon emission volume but will have little impact on the final deuteron spectrum since the nuclei are already sup-

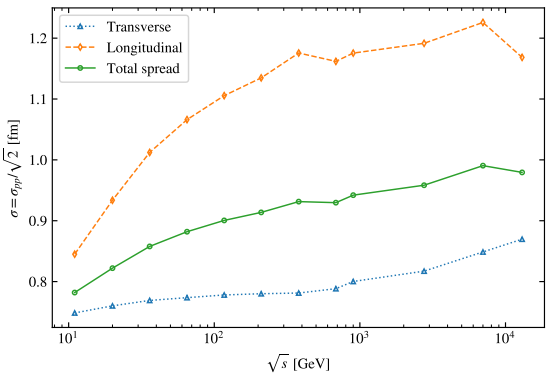

FIG. 5: The spread σ predicted by Pythia is computed as the rms value of the size of the nucleon emission region, while using the weight $\exp(-d^2q^2)$. The transverse (blue triangles), longitudinal (orange diamonds) and total (green circles) spreads are plotted as a function of the center of mass energy in pp collisions.

pressed by the anti-correlations in momentum. This will in any case have negligible effects on cosmic ray studies.

E. Υ decays

The decay of Υ is interesting because one can learn about the hadronisation and coalescence process at low energies. Recently, Ref. [55] systematically tested phase-space Monte Carlo models on Υ decay data. Using the WiFunC model, it was found that the emission size $\sigma \simeq 1.6\,\text{fm}$—greatly larger than the expected $\simeq 1\,\text{fm}$—is needed to reproduce the measured antideuteron yield. This may have three explanations [16]: (1) the WiFunC model fails, or (2) the event generator over-predicts the nucleon yield or nucleon correlations. (3) the nucleon emission volume is larger than expected in this process,

To test the first explanations, we simulate the decay of 10^7 Υ using Pythia 8.3, turning off the decay of strong resonances. In the WiFunC model with the Gaussian ansatz, we obtain[65] $B(\Upsilon \to \bar{d}X) = 6.7^{+0.1}_{-0.2} \times 10^{-5}$ with $\sigma = (1.0 \pm 0.1)$ fm. In agreement with Ref. [55], we need $\sigma \simeq 1.5\,\text{fm}$ to reproduce the value measured by BaBar [42], $2.81 \pm 0.49^{+0.2}_{-0.24}$. Using the space-time treatment of Pythia, we obtain $B(\Upsilon \to \bar{d}X) = 18.0 \times 10^{-5}$, and an effective size $\sigma = 0.83\,\text{fm}$. Without the equal time approximation, the result is $B(\Upsilon \to \bar{d}X) = 17.2 \times 10^{-5}$ with an effective size $\sigma = 0.93\,\text{fm}$. This is a change of 4.5%. Even if the estimated emission volume in Pythia is similar to the one used in the Gaussian ansatz, the branching ratio is a factor 2–3 larger, indicating a substantial enhancement due to position and momentum correlations. In all cases, the WiFunC model over-predicts the measurement, which may well be due to uncertainties in the event generator.

In order to test the hypothesis that Pythia over-predicts the nucleon yield in the meson-to-three-gluon decay[66], we simulate the decay of J/ψ and compare the measured branching ratio [56] of common decays into nucleons and pions[67]. The result is shown in Tab. I. As readily seen from the table, Pythia has a tendency to under-estimate the branching ratio into pions, and to over-estimate the branching into nucleons. This is a strong indication that Pythia over-predicts the nucleon production in J/ψ, and thus Υ decays. The nucleon yield is overproduced by a factor 2–3, implying that the deuteron yield may be overestimated by a factor 4–9.

In Pythia, the Υ meson decays mainly into three gluons, which may initiate parton showers and hadronise. In a different line of thought, the three gluons expand a triangular Lund string, and so the hadronic emission length might be substantially larger than in other processes, ~ 3 fm [9].

In conclusion, the theoretical uncertainties prevent at present a conclusion about the size of the emission volume in Υ decays. The baryonic production and baryon–baryon femtoscopy measurements in Υ decays are therefore highly warranted. This will allow one, in tandem with the antideuteron data, to learn about hadronic meson decays, the hadronisation process and the coalescence process. Moreover, it may increase significantly the predictive power for some exotic antinuclei production mechanisms, such as dark matter decays or annihilation.

V. SUMMARY AND CONCLUSIONS

We have discussed the WiFunC model, a coalescence model that allows one to include momentum and spatial correlations on an event-by-event basis. Two choices for the nucleon emission volume were discussed: (1) a Gaussian ansatz, and (2) using the emission volume provided by an event generator. In the latter case, one can go beyond the equal-time approximation which until now has been invariably assumed. We have shown that this approximation leads to a $\mathcal{O}(10\,\%)$ uncertainty in the coalescence probability in processes close to the production threshold, such as Υ decays. The error is strongly reduced at high energies, implying that non-equal production times can be neglected for hadronic collisions at LHC.

As concrete examples, we considered pp collisions and Υ decays, using Pythia 8. The Gaussian ansatz for the emission volume leads to a satisfactory description of the baryon emission volume and the antideuteron spectrum measured by the ALICE collaboration at LHC, while overpredicting the antideuteron production in Υ decays. We have argued, based on experimental data on nucleon production in J/ψ decays, that Pythia likely overpredicts the nucleon production in Υ decays. The space-time ap-

Decay	Measured value [56]	Pythia
$2(\pi^+\pi^-)\pi^0$	$(3.71 \pm 0.28) \times 10^{-2}$	2.50×10^{-3}
$3(\pi^+\pi^-)\pi^0$	$(2.9 \pm 0.6) \times 10^{-2}$	0
$\pi^+\pi^-3\pi^0$	$(1.9 \pm 0.9) \times 10^{-2}$	1.36×10^{-3}
$\pi^+\pi^-4\pi^0$	$(6.1 \pm 1.3) \times 10^{-3}$	6.5×10^{-5}
$\pi^+\pi^-\pi^0$	$(2.10 \pm 0.08) \times 10^{-2}$	1.51×10^{-2}
$2(\pi^+\pi^-\pi^0)$	$(1.61 \pm 0.20) \times 10^{-2}$	2.50×10^{-4}
$\pi^+\pi^-\pi^0K^+K^-$	$(1.20 \pm 0.30) \times 10^{-2}$	6.06×10^{-3}
$\pi^+\pi^-$	$(1.47 \pm 0.14) \times 10^{-4}$	7.68×10^{-3}
$2(\pi^+\pi^-)$	$(3.57 \pm 0.30) \times 10^{-3}$	5.31×10^{-3}
$\gamma 2\pi^+2\pi^-$	$(2.8 \pm 0.5) \times 10^{-3}$	–
$3(\pi^+\pi^-)$	$(4.3 \pm 0.4) \times 10^{-3}$	5.90×10^{-5}
$2(\pi^+\pi^-)3\pi^0$	$(6.2 \pm 0.9) \times 10^{-2}$	7.30×10^{-6}
$4(\pi^+\pi^-)\pi^0$	$(9.0 \pm 3.0) \times 10^{-3}$	0
Total	0.222 ± 0.015	0.057
$p\bar{p}$	$(2.120 \pm 0.029) \times 10^{-3}$	1.36×10^{-2}
$p\bar{p}\pi^0$	$(1.19 \pm 0.08) \times 10^{-3}$	4.31×10^{-3}
$p\bar{p}\pi^+\pi^-$	$(6.0 \pm 0.5) \times 10^{-3}$	9.07×10^{-4}
$p\bar{p}\pi^+\pi^-\pi^0$	$(2.3 \pm 0.9) \times 10^{-3}$	1.02×10^{-4}
$p\bar{n}\pi^-$	$(2.12 \pm 0.09) \times 10^{-3}$	7.47×10^{-3}
$n\bar{n}$	$(2.09 \pm 0.16) \times 10^{-3}$	1.36×10^{-2}
Total	$(1.58 \pm 0.01) \times 10^{-2}$	4.10×10^{-2}

TABLE I: Branching ratios of common J/ψ decays into pions and nucleons.

proach of Pythia 8, on the other hand, underpredicts the nucleon emission volume and fails to accurately describe the antideuteron spectrum. However, these deficiencies are most likely explained by the fact that the space-time treatment is not yet complete and has not yet been tuned to experimental data. Importantly, this implies that the coalescence framework introduced in this work can be used to tune the space-time treatments and momentum correlations in event generators, when comparing them to antideuteron and femtoscopy data. Once nucleon production in Υ decays is measured, one can use also antinuclei to probe the hadronisation process. In addition, we predicted the energy dependence of the emission volume using Pythia 8. This resulted, as expected, in a weak energy dependence, consistent with a constant (1.0 ± 0.1) fm within experimental and theoretical uncertainties.

This work has been motivated by an increasing amount of high-precision data on antinuclei production in small interacting systems, obtained by, e.g., the ALICE, NA61/SHINE and BELLE-II experiments. Our framework paves the way for using these antinuclei measurements to tune the space-time picture and momentum correlations in event generators used to describe these data. Improving thereby the accuracy of such generators, regarding the description of antinuclei production, may furthermore have an important impact on predictions of antinuclei production by cosmic rays and dark matter.

Note added: While finalising this manuscript, the related work [57] appeared on the arxiv. The authors of that work employ the equal-time approximation together with Eq. (17) and a Gaussian ansatz for H_{np}. The width of the Gaussian was however treated as a variable, $\sigma \to \sigma(\boldsymbol{r}, t)$, what is inconsistent with the assumptions needed to derive the deuteron yield in Eq. (17). We also note that our results for the emission volume, based on Pythia 8, are in disagreement with theirs: We obtain with Pythia a source size which decreases with transverse mass—in agreement with the experimental data—while the source size derived in Ref. [57] increases. This discrepency is likely mainly caused by a different interpretation of the effect of the equal-time approximation in a femtoscopy experiment: In deriving the core size shown in Fig. 2, we enforce $t = 0$ in the lab frame. Meanwhile, Ref. [57] enlarges the emission volume by propagating the produced particles until $t = 0$.

VI. ACKNOWLEDGEMENTS

This work benefited from discussions at the workshop "Antinuclei in the Universe" at the Munich Institute for Astro- and Particle Physics (MIAPP) which is funded by the Deutsche Forschungsgemeinschaft (DFG, German Research Foundation) under Germany's Excellence Strategy – EXC-2094 – 390783311. S.O. acknowledges support from the Deutsche Forschungsgemeinschaft (project number 465275045).

[1] H. Caines, The Search for Critical Behavior and Other Features of the QCD Phase Diagram – Current Status and Future Prospects, Nucl. Phys. A967 (2017) 121–128. doi:10.1016/j.nuclphysa.2017.05.116.

[2] P. Chardonnet, J. Orloff, P. Salati, The production of antimatter in our galaxy, Phys. Lett. B409 (1997) 313–320. arXiv:astro-ph/9705110, doi:10.1016/S0370-2693(97)00870-8.

[3] F. Donato, N. Fornengo, P. Salati, Anti-deuterons as a signature of supersymmetric dark matter, Phys. Rev. D62 (2000) 043003. arXiv:hep-ph/9904481, doi:10.1103/PhysRevD.62.043003.

[4] P. von Doetinchem, et al., Cosmic-ray Antinuclei as Messengers of New Physics: Status and Outlook for the New Decade, JCAP 08 (2020) 035. arXiv:2002.04163, doi:10.1088/1475-7516/2020/08/035.

[5] L. Csernai, J. I. Kapusta, Entropy and Cluster Production in Nuclear Collisions, Phys. Rept. 131 (1986) 223–318. doi:10.1016/0370-1573(86)90031-1.

[6] J. Nagle, B. Kumar, D. Kusnezov, H. Sorge, R. Mattiello,

Coalescence of deuterons in relativistic heavy ion collisions, Phys. Rev. C 53 (1996) 367–376. doi:10.1103/PhysRevC.53.367.

[7] A. Schwarzschild, C. Zupancic, Production of Tritons, Deuterons, Nucleons, and Mesons by 30-GeV Protons on A-1, Be, and Fe Targets, Phys. Rev. 129 (1963) 854–862. doi:10.1103/PhysRev.129.854.

[8] S. T. Butler, C. A. Pearson, Deuterons from high-energy proton bombardment of matter, Phys. Rev. 129 (2) (1963) 836–842. doi:10.1103/PhysRev.129.836.

[9] G. Gustafson, J. Hakkinen, Deuteron production in e+ e- annihilation, Z. Phys. C 61 (1994) 683–688. doi:10.1007/BF01552635.

[10] L. A. Dal, Antideuterons as signature for dark matter, Master's thesis, NTNU Trondheim, available at http://hdl.handle.net/11250/246403 (2011).
URL http://hdl.handle.net/11250/246403

[11] M. Kadastik, M. Raidal, A. Strumia, Enhanced anti-deuteron dark matter signal and the implications of PAMELA, Phys. Lett. B683 (2010) 248–254. arXiv:0908.1578, doi:10.1016/j.physletb.2009.12.005.

[12] M. Kachelrieß, S. Ostapchenko, J. Tjemsland, Alternative coalescence model for deuteron, tritium, helium-3 and their antinuclei, Eur. Phys. J. A56 (1) (2020) 4. arXiv:1905.01192, doi:10.1140/epja/s10050-019-00007-9.

[13] M. Kachelrieß, S. Ostapchenko, J. Tjemsland, Revisiting cosmic ray antinuclei fluxes with a new coalescence model, JCAP 08 (2020) 048. arXiv:2002.10481, doi:10.1088/1475-7516/2020/08/048.

[14] M. Kachelrieß, S. Ostapchenko, J. Tjemsland, On nuclear coalescence in small interacting systems, Eur. Phys. J. A 57 (5) (2021) 167. arXiv:2012.04352, doi:10.1140/epja/s10050-021-00469-w.

[15] J. Tjemsland, Formation of light (anti)nuclei, PoS TOOLS2020 (2021) 006. arXiv:2012.12252, doi:10.22323/1.392.0006.

[16] M. Kachelriess, S. Ostapchenko, J. Tjemsland, AAfrag 2.01: Interpolation routines for Monte Carlo results on secondary production including light antinuclei in hadronic interactionsarXiv:2206.00998.

[17] L. Šerkšnytė, et al., Reevaluation of the cosmic antideuteron flux from cosmic-ray interactions and from exotic sources, Phys. Rev. D 105 (8) (2022) 083021. arXiv:2201.00925, doi:10.1103/PhysRevD.105.083021.

[18] R. Scheibl, U. W. Heinz, Coalescence and flow in ultrarelativistic heavy ion collisions, Phys. Rev. C59 (1999) 1585–1602. arXiv:nucl-th/9809092, doi:10.1103/PhysRevC.59.1585.

[19] K.-J. Sun, L.-W. Chen, C. M. Ko, J. Pu, Z. Xu, Light nuclei production as a probe of the QCD phase diagram, Phys. Lett. B 781 (2018) 499–504. arXiv:1801.09382, doi:10.1016/j.physletb.2018.04.035.

[20] K.-J. Sun, L.-W. Chen, C. M. Ko, Z. Xu, Probing QCD critical fluctuations from light nuclei production in relativistic heavy-ion collisions, Phys. Lett. B 774 (2017) 103–107. arXiv:1702.07620, doi:10.1016/j.physletb.2017.09.056.

[21] T. Shao, J. Chen, C. M. Ko, K.-J. Sun, Probing QCD critical fluctuations from the yield ratio of strange hadrons in relativistic heavy-ion collisions, Phys. Lett. B 801 (2020) 135177. arXiv:1910.14281, doi:10.1016/j.physletb.2019.135177.

[22] K.-J. Sun, C. M. Ko, Light nuclei production in a multi-phase transport model for relativistic heavy ion collisions, Phys. Rev. C 103 (6) (2021) 064909. arXiv:2005.00182, doi:10.1103/PhysRevC.103.064909.

[23] W. Zhao, K.-j. Sun, C. M. Ko, X. Luo, Multiplicity scaling of light nuclei production in relativistic heavy-ion collisions, Phys. Lett. B 820 (2021) 136571. arXiv:2105.14204, doi:10.1016/j.physletb.2021.136571.

[24] T. Shao, J. Chen, Y.-G. Ma, Z. Xu, Production of light antinuclei in pp collisions by dynamical coalescence and their fluxes in cosmic rays near earth, Phys. Rev. C 105 (6) (2022) 065801. arXiv:2205.13626, doi:10.1103/PhysRevC.105.065801.

[25] P. Danielewicz, G. Bertsch, Production of deuterons and pions in a transport model of energetic heavy ion reactions, Nucl. Phys. A 533 (1991) 712–748. doi:10.1016/0375-9474(91)90541-D.

[26] K. Blum, K. C. Y. Ng, R. Sato, M. Takimoto, Cosmic rays, antihelium, and an old navy spotlight, Phys. Rev. D96 (10) (2017) 103021. arXiv:1704.05431, doi:10.1103/PhysRevD.96.103021.

[27] K. Blum, M. Takimoto, Nuclear coalescence from correlation functions, Phys. Rev. C 99 (4) (2019) 044913. arXiv:1901.07088, doi:10.1103/PhysRevC.99.044913.

[28] S. Acharya, et al., Production of ^{4}He and $^4\overline{\mathrm{He}}$ in Pb-Pb collisions at $\sqrt{s_{\mathrm{NN}}} = 2.76$ TeV at the LHC, Nucl. Phys. A 971 (2018) 1–20. arXiv:1710.07531, doi:10.1016/j.nuclphysa.2017.12.004.

[29] A. Andronic, P. Braun-Munzinger, K. Redlich, J. Stachel, Decoding the phase structure of QCD via particle production at high energy, Nature 561 (7723) (2018) 321–330. arXiv:1710.09425, doi:10.1038/s41586-018-0491-6.

[30] V. Vovchenko, B. Dönigus, H. Stoecker, Multiplicity dependence of light nuclei production at LHC energies in the canonical statistical model, Phys. Lett. B 785 (2018) 171–174. arXiv:1808.05245, doi:10.1016/j.physletb.2018.08.041.

[31] F. Bellini, A. P. Kalweit, Testing production scenarios for (anti-)(hyper-)nuclei and exotica at energies available at the CERN Large Hadron Collider, Phys. Rev. C 99 (5) (2019) 054905. arXiv:1807.05894, doi:10.1103/PhysRevC.99.054905.

[32] J. Chen, D. Keane, Y.-G. Ma, A. Tang, Z. Xu, Antinuclei in Heavy-Ion Collisions, Phys. Rept. 760 (2018) 1–39. arXiv:1808.09619, doi:10.1016/j.physrep.2018.07.002.

[33] X. Xu, R. Rapp, Production of Light Nuclei at Thermal Freezeout in Heavy-Ion Collisions, Eur. Phys. J. A 55 (5) (2019) 68. arXiv:1809.04024, doi:10.1140/epja/i2019-12757-7.

[34] D. Oliinychenko, L.-G. Pang, H. Elfner, V. Koch, Microscopic study of deuteron production in PbPb collisions at $\sqrt{s} = 2.76TeV$ via hydrodynamics and a hadronic afterburner, Phys. Rev. C 99 (4) (2019) 044907. arXiv:1809.03071, doi:10.1103/PhysRevC.99.044907.

[35] F. Bellini, K. Blum, A. P. Kalweit, M. Puccio, Examination of coalescence as the origin of nuclei in hadronic collisions, Phys. Rev. C 103 (1) (2021) 014907. arXiv:2007.01750, doi:10.1103/PhysRevC.103.014907.

[36] C. Bierlich, et al., A comprehensive guide to the physics and usage of PYTHIA 8.3arXiv:2203.11601.

[37] S. Ferreres-Solé, T. Sjöstrand, The space–time structure of hadronization in the Lund model, Eur. Phys. J. C 78 (11) (2018) 983. arXiv:1808.04619, doi:10.1140/

epjc/s10052-018-6459-8.
[38] S. Acharya, et al., Search for a common baryon source in high-multiplicity pp collisions at the LHC, Phys. Lett. B 811 (2020) 135849. arXiv:2004.08018, doi:10.1016/j.physletb.2020.135849.
[39] S. Acharya, et al., Production of deuterons, tritons, ^{3}He nuclei and their antinuclei in pp collisions at $\sqrt{s} = 0.9$, 2.76 and 7 TeV, Phys. Rev. C 97 (2) (2018) 024615. arXiv:1709.08522, doi:10.1103/PhysRevC.97.024615.
[40] Enhanced deuteron coalescence probability in jetsarXiv:2211.15204.
[41] S. Acharya, et al., Jet-associated deuteron production in pp collisions at $\sqrt{s} = 13$ TeV, Phys. Lett. B 819 (2021) 136440. arXiv:2011.05898, doi:10.1016/j.physletb.2021.136440.
[42] J. P. Lees, et al., Antideuteron production in $\Upsilon(nS)$ decays and in $e^+e^- \to q\bar{q}$ at $\sqrt{s} \approx 10.58$ GeV, Phys. Rev. D 89 (11) (2014) 111102. arXiv:1403.4409, doi:10.1103/PhysRevD.89.111102.
[43] D. M. Asner, et al., Anti-deuteron production in Upsilon(nS) decays and the nearby continuum, Phys. Rev. D 75 (2007) 012009. arXiv:hep-ex/0612019, doi:10.1103/PhysRevD.75.012009.
[44] R. Lednicky, Finite-size effects on two-particle production in continuous and discrete spectrum, Phys. Part. Nucl. 40 (2009) 307–352. arXiv:nucl-th/0501065, doi:10.1134/S1063779609030034.
[45] M. A. Lisa, S. Pratt, R. Soltz, U. Wiedemann, Femtoscopy in relativistic heavy ion collisions, Ann. Rev. Nucl. Part. Sci. 55 (2005) 357–402. arXiv:nucl-ex/0505014, doi:10.1146/annurev.nucl.55.090704.151533.
[46] W. B. Case, Wigner functions and weyl transforms for pedestrians, American Journal of Physics 76 (10) (2008) 937–946. arXiv:https://doi.org/10.1119/1.2957889, doi:10.1119/1.2957889.
URL https://doi.org/10.1119/1.2957889
[47] V. I. Zhaba, Deuteron: properties and analytical forms of wave function in coordinate spacearXiv:1706.08306.
[48] R. Hudson, When is the wigner quasi-probability density non-negative?, Reports on Mathematical Physics 6 (2) (1974) 249–252. doi:https://doi.org/10.1016/0034-4877(74)90007-X.
URL https://www.sciencedirect.com/science/article/pii/003448777490007X
[49] F. Soto, P. Claverie, When is the wigner function of multidimensional systems nonnegative?, Journal of Mathematical Physics 24 (1) (1983) 97–100. arXiv:https://doi.org/10.1063/1.525607, doi:10.1063/1.525607.
URL https://doi.org/10.1063/1.525607
[50] K. Werner, F.-M. Liu, T. Pierog, Parton ladder splitting and the rapidity dependence of transverse momentum spectra in deuteron-gold collisions at RHIC, Phys. Rev. C 74 (2006) 044902. arXiv:hep-ph/0506232, doi:10.1103/PhysRevC.74.044902.
[51] T. Pierog, I. Karpenko, J. M. Katzy, E. Yatsenko, K. Werner, EPOS LHC: Test of collective hadronization with data measured at the CERN Large Hadron Collider, Phys. Rev. C 92 (3) (2015) 034906. arXiv:1306.0121, doi:10.1103/PhysRevC.92.034906.
[52] S. Ostapchenko, Monte Carlo treatment of hadronic interactions in enhanced Pomeron scheme: I. QGSJET-II model, Phys. Rev. D83 (2011) 014018. arXiv:1010.1869, doi:10.1103/PhysRevD.83.014018.
[53] S. Ostapchenko, QGSJET-II: physics, recent improvements, and results for air showers, EPJ Web Conf. 52 (2013) 02001. doi:10.1051/epjconf/20125202001.
[54] S. Acharya, et al., (Anti-)deuteron production in pp collisions at $\sqrt{s} = 13$ TeV, Eur. Phys. J. C 80 (9) (2020) 889. arXiv:2003.03184, doi:10.1140/epjc/s10052-020-8256-4.
[55] D. Marietti, A. Pilloni, U. Tamponi, Production of loosely-bound hadron molecules from bottomonium decaysarXiv:2208.14185.
[56] R. L. Workman, et al., Review of Particle Physics, PTEP 2022 (2022) 083C01. doi:10.1093/ptep/ptac097.
[57] M. Horst, L. Barioglio, F. Bellini, L. Fabbietti, C. Pinto, B. Singh, S. Tripathy, Novel parameter-free coalescence model for deuteron productionarXiv:2302.12696.
[58] R. Mattiello, H. Sorge, H. Stoecker, W. Greiner, Nuclear clusters as a probe for expansion flow in heavy ion reactions at 10-A/GeV - 15-A/GeV, Phys. Rev. C 55 (1997) 1443–1454. arXiv:nucl-th/9607003, doi:10.1103/PhysRevC.55.1443.
[59] In the following, we denote with nuclei both nuclei and anti-nuclei.
[60] This was checked explicitly in Ref. [12] for coalescing nucleons in small interacting systems.
[61] We emphasise that we are referring to the emission volume as a function of r, which is what one measures experimentally.
[62] We define $W^{(4)}(\boldsymbol{P}_d/2 + \boldsymbol{q}, \boldsymbol{P}_d/2 - \boldsymbol{q}, r) = \int \mathrm{d}^4 r_d \, W^{(4)}_{np}(\boldsymbol{P}_d/2 + \boldsymbol{q}, \boldsymbol{P}_d/2 - \boldsymbol{q}, r, r_d)$
[63] See, e.g., Ref. [58] for an example in 3D.
[64] The positivity condition depends on the shape of H_{np} and the wave function.
[65] Due to the lack of a preferred direction, we neglect the Lorentz boost in the transverse direction.
[66] In the decay tables in Pythia, the J/ψ meson decays mainly into two gluons, even though the dominant decay channel is $J/\psi \to ggg$ [56]. We therefore change this decay channel to three gluons, like for Υ, in the simuations.
[67] We neglect the contributions from resonances, as well as final state photons since Pythia includes Bremstralung photons in the decays.

Paper XI – Detecting ALP wiggles at TeV energies

Kachelrieß, M. & Tjemsland, J. "Detecting ALP wiggles at TeV energies". *Sumbitted to JCAP*. arXiv: 2305.03604 [hep-ph] (May 2023)

Abstract: Axions and axion-like-particles (ALPs) are characterised by their two-photon coupling, which entails so-called photon-ALP oscillations as photons propagate through a magnetic field. These oscillations lead to distinctive signatures in the energy spectrum of high-energy photons from astrophysical sources, allowing one to probe the existence of ALPs. In particular, photon-ALP oscillations will induce energy dependent oscillatory features, or "ALP wiggles", in the photon spectra. We propose to use the discrete power spectrum to search for ALP wiggles and present a model-independent statistical test. By using PKS 2155-304 as an example, we show that the method has the potential to significantly improve the experimental sensitivities for ALP wiggles. Moreover, we discuss how these sensitivities depend on the modelling of the magnetic field. We find that the use of realistic magnetic field models, due to their larger cosmic variance, substantially enhances detection prospects compared to the use of simplified models.

In Paper VIII, we suggested using the discrete power spectrum to directly probe ALP wiggles in photon spectra. However, a proof of concept with examples was still missing. In this paper, we therefore further discussed and exemplified the concept. In particular, we introduced a statistical procedure and showed that it has the potential to significantly improve current detection prospects for ALP wiggles.

Prepared for submission to JCAP

Detecting ALP wiggles at TeV energies

M. Kachelrieß and J. Tjemsland

Institutt for fysikk, NTNU, Trondheim, Norway

Abstract. Axions and axion-like-particles (ALPs) are characterised by their two-photon coupling, which entails so-called photon-ALP oscillations as photons propagate through a magnetic field. These oscillations lead to distinctive signatures in the energy spectrum of high-energy photons from astrophysical sources, allowing one to probe the existence of ALPs. In particular, photon-ALP oscillations will induce energy dependent oscillatory features, or "ALP wiggles", in the photon spectra. We propose to use the discrete power spectrum to search for ALP wiggles and present a model-independent statistical test. By using PKS 2155-304 as an example, we show that the method has the potential to significantly improve the experimental sensitivities for ALP wiggles. Moreover, we discuss how these sensitivities depend on the modelling of the magnetic field. We find that the use of realistic magnetic field models, due to their larger cosmic variance, substantially enhances detection prospects compared to the use of simplified models.

Keywords: axion, axion-like particles, photon-ALP oscillation, turbulent magnetic fields

Contents

1 Introduction

Axions are well motivated beyond the standard model particles that can explain a variety of unsolved problems in physics, such as the strong CP problem [1, 2] and the nature of dark matter [3–5]. These particles are mainly characterised by their two-photon coupling $g_{a\gamma}$ from the interaction term $\mathcal{L} = \frac{1}{4} g_{a\gamma} a F_{\mu\nu} \tilde{F}^{\mu\nu} = g_{a\gamma} a \boldsymbol{E} \cdot \boldsymbol{B}$, and by their small mass m_a obtained through pion mixing [6, 7]. The relationship between $g_{a\gamma}$ and m_a is thus fixed as $g_{a\gamma}\,\mathrm{GeV} \sim 10^{-16} m_a / \mu\mathrm{eV}$ up to a $\mathcal{O}(1)$ factor [8, 9]. A more general class of light pseudoscalar particles which share the same two-photon coupling as the axion but have an arbitrary mass m_a, is known as axion-like particles (ALPs). Although ALPs do not solve the strong CP problem, they are nevertheless interesting as they, e.g., arise naturally in string theories and other extensions of the standard model [10, 11].

The majority of ALP searches are based on photon-ALP mixing in a magnetic field (see Refs. [12, 13] for two recent reviews): Due to the characteristic two-photon–ALP vertex, a photon/ALP may interact with a virtual photon provided by the magnetic field and convert into an ALP/photon. Currently, the most solid and extensive exclusions at sub-eV masses, $g_{a\gamma} < 6.6 \times 10^{-11}\,\mathrm{GeV}^{-1}$, are set by the CAST helioscope ($m_a \lesssim$ eV) [14] by attempting to convert solar ALPs into photons on Earth. A comparable limit is found for $m_a \lesssim$ keV by studying the lifetime of horizontal branch stars [15, 16]. The planned "shining light through a wall" experiment ALPS-II [17] and the solar helioscope IAXO [18] are expected to improve upon these limits immensely. Significantly stronger limits around $m_{a\gamma} \sim 10^{-6}\,\mathrm{eV}$ are obtained for ALP dark matter

in haloscope experiments, such as ADMX [19] and the upcoming ABRACADABRA experiment [20], or by conversion near neutron stars [21, 22].

The strongest limits ($g_{a\gamma} \lesssim 10^{-11}$–$10^{-13}\,\mathrm{eV}^{-1}$) at low masses ($m_a \lesssim 10^{-6}$) are set by observations of astrophysical photon sources using the signatures that photon-ALP oscillations will imprint on photon spectra: First, photon-ALP oscillations will induce "irregularities". The non-detection of such spectral irregularities has been used to constrain the parameter space using, e.g., gamma-ray observations by HESS [23] and Fermi-LAT [24], observations of the Galactic diffuse gamma-rays by Tibet ASγ and HAWC [25], and using X-ray observations from Chandra [26–28]. The Cherenkov Telescope Array (CTA) is expected to improve the limits from HESS and Fermi-LAT [29]. Second, ALPs that are produced near or in the source can convert back into photons in, e.g., the Galactic magnetic field, thus inducing an additional gamma- or X-ray flux which has been searched for in SN1987A [30], Betelgeuse [31], and super star clusters [32]. Moreover, ALPs that are sourced near the polar caps in pulsars and resonantly converted to photons have recently been used to set leading limits [33]. Third, photon-ALP oscillations will increase the linear polarisation of photons, which can be used to set limits using e.g. optical photons or X-rays[1] from magnetic white dwarfs and neutron stars [35, 36]. In Ref. [37], it was shown that the measurement of linear polarisation in white dwarf spectra excludes $g_{a\gamma} \gtrsim 5.4 \times 10^{-12}\,\mathrm{GeV}^{-1}$ for $m_a \lesssim 3 \times 10^{-7}\,\mathrm{eV}$, which is the strongest existing limit for ALP masses between $\sim 10^{-9}$ and $\sim 10^{-6}\,\mathrm{eV}$. At masses $m_a \lesssim 10^{-11}\,\mathrm{eV}$, the best limit is set by the non-detection of spectral irregularities in X-ray data from Chandra [26]. Finally, photon-ALP oscillations will effectively increase the mean-free path of photons at TeV energies since ALPs travel practically without any interactions with the extragalactic background light (EBL) [38]. This effect has been recently used to set strong limits with HAWC [39]. Moreover, this effect is important in combining fit analyses, such as in the recent limit set using FERMI flat radio quasars [40].

All the limits discussed in the previous paragraph are, however, strongly dependent on the treatment of the magnetic fields [41–44]. Therefore, one either needs a reliable description of the magnetic fields, or knowledge of how uncertainties in the magnetic fields affect the results (see e.g. the discussions in Refs. [27, 45, 46]). This is particularly important for the turbulent component of the magnetic fields, since oversimplified models are often used to describe these fields.

In Ref. [46] we introduced the idea of using the discrete power spectrum to probe photon-ALP oscillations in photon spectra. In this work, we further discuss and exemplify this concept. In particular, we introduce a statistical procedure that has the potential to significantly improve current detection prospects for irregularities induced by photon-ALP oscillations, which we name "ALP wiggles". The statistical method has two main applications: First, it can be used to search for ALP wiggles without specifying the EBL distribution and the magnetic field model. Second, the method is a convenient way to analyse the effect of various magnetic field models on the expected ALP wiggles. We find that this method is more robust than a standard χ^2 comparison

[1]The same phenomenon occurs naturally also for gamma-rays, but the measurement of the polarisation is with current and planned detectors not possible [34].

with data. In order to stay as concrete as possible, the examples focus on gamma-rays at TeV energies, of relevance for the upcoming CTA experiment.

2 Photon-ALP oscillations in astrophysical magnetic fields

2.1 Equation of motion

Physically, one can interpret the photon-ALP oscillation as a mixing between two mass eigenstates, similar to neutrino oscillations. The mixing strength and oscillation length depend on the effective mass of the photon which in turn is determined by the propagation environment (i.e. the surrounding magnetic field, plasma, photon bath, etc.) and photon energy. A photon and an ALP with energy E propagating in z direction can be described by the linearised equation of motion [47],

$$(E + \mathcal{M} - \mathrm{i}\partial_z)\phi(z) = 0, \tag{2.1}$$

where $\phi = (A_\perp, A_\parallel, a)^\mathrm{T}$ is the wave function describing the photon and ALP state. The mixing matrix can be written as

$$\mathcal{M} = \begin{pmatrix} \Delta_\perp & 0 & 0 \\ 0 & \Delta_\parallel & \Delta_{a\parallel} \\ 0 & \Delta_{a\parallel} & \Delta_a \end{pmatrix}, \tag{2.2}$$

where $\Delta_{\perp/\parallel} = (n_{\perp/\parallel} - 1)E$, $\Delta_a = -m_a^2/(2E)$ and $\Delta_{a\gamma} = g_{a\gamma}B_\mathrm{T}/2$. The transverse magnetic field $\boldsymbol{B}_\mathrm{T}$ is the component of the magnetic field perpendicular to the propagation direction, and the index $\perp$ ($\parallel$) refers to the direction perpendicular (parallel) to $\boldsymbol{B}_\mathrm{T}$.

In this work, we consider only photons in the sensitivity range of CTA ($\sim 10^{11}$–$10^{14}\,\mathrm{eV}$) and low ALP mass ($m_a \lesssim 10^{-10}\,\mathrm{eV}$). Then the dominant contribution to the photon refractive index is the one from the EBL [46], given by [48]

$$\Delta_\mathrm{EBL} \simeq \Delta_\mathrm{CMB} \simeq 0.5 \times 10^{-42} E. \tag{2.3}$$

All turbulent magnetic fields lead to similar dependencies on the oscillation parameters [46], and the discussions in this paper can therefore be applied to other energy ranges and magnetic field strengths.

2.2 `ELMAG`

We simulate the propagation of photons using `ELMAG` [49, 50] which is a Monte Carlo program that simulates electromagnetic cascades of high-energy photons, electrons and positrons created by their interactions with the EBL. We have implemented ALPs into `ELMAG` [46], thereby allowing for a consistent treatment of cascading and oscillations. This advantage is however at the cost of being significantly more computationally demanding than the alternative Python packages GammaALP [51] and ALPro [27], which are based on transfer matrices.

Compared to Ref. [46] we have added the following features to ELMAG[2]: Gaussian turbulent fields with a broken power-law as power spectrum [see Eq. (2.4)] can be modelled, the magnetic field strength can be distributed as a top-hat function with a given filling factor, and the computation time is significantly reduced.

2.3 Magnetic field models

High-energy photons will encounter a variety of turbulent magnetic fields on their path towards Earth, with strengths varying from $B \sim 1\,\mathrm{G}$ near jets of AGNe, fields on galactic scales with $\sim \mu$G, within galaxy clusters ($\sim$ 0.1–10 nG) and finally the intergalactic magnetic field, see e.g. Refs. [52, 53] for recent reviews. The energy in the turbulent magnetic fields in galaxies and galaxy clusters are believed to be generated at large scales 0.1–10 kpc through, e.g., "mechanical stirring", large- and small-scale dynamos, and compression. The energy is in turn transported to smaller length scales through an energy cascade, leading to a power-law spectrum of the turbulent magnetic field. It is common to assume that the magnetic field either has a Kolmogorov ($\gamma = -5/3$) or Kraichnan ($\gamma = -2/3$) spectrum. At small k, a Batchelor spectrum ($\beta = 5$) is expected, but other spectral indices have been suggested too.

In order to take into account the stochastic nature of the turbulence, we will describe it as a divergence-free Gaussian turbulent field with zero mean and RMS-value $B_{\mathrm{rms}}^2 = \langle B^2 \rangle$. Following the approach of Refs. [54, 55], we describe the magnetic field as a superposition of n left- and right-circular polarised Fourier modes. The modes will be distributed according to the power-law spectrum

$$B_j = B_{\mathrm{min}} \left(\frac{k_j}{k_0}\right)^{\beta/2} \left[1 + \left(\frac{k_j}{k_0}\right)^{\gamma+\beta}\right]^{-1/2} \tag{2.4}$$

between k_{min} and k_{max}. The parameter k_0 determines the break in the power law which is visible in the magnetic field spectra shown in Fig. 1. In the case of astrophysical magnetic fields, $L_0 = 2\pi/k_0$ corresponds to the injection scale. The field modes extend down to the dissipation scale $L_{\mathrm{min}} = 2\pi/k_{\mathrm{max}}$ which is below any astrophysical scale of interest. In practise, one cuts off therefore the spectrum at a value of L_{min} which is much smaller than the smallest relevant scale of the problem in question[3]. We use $k_{\mathrm{max}} = 100 k_0$, fix k_{min} by the condition $B(k_{\mathrm{min}}) = B(k_{\mathrm{max}})$ and use 33 modes per decade. The field is normalised such that $B_{\mathrm{rms}}^2/2$ coincides with the energy density stored in the field. We define the coherence length L_{c} of the turbulent fields as

$$L_{\mathrm{c}} = \frac{\pi}{B_{\mathrm{rms}}^2} \int \frac{\mathrm{d}k}{k} \boldsymbol{B}^2(k). \tag{2.5}$$

For comparison, we will also consider a simple domain-like field which is often used in the literature due to its simplicity [26, 28, 56, 56–60]. In this approach, the magnetic field is split into patches with a size equal to the coherence length L_{c}. Within each

[2]The code will be made publicly available in a future release of ELMAG.

[3]Here, the largest relevant wave number is $k_{\mathrm{osc}} = \Delta_{\mathrm{CMB}}(10^{14}\,\mathrm{eV}) \sim 8\,\mathrm{Mpc}^{-1}$.

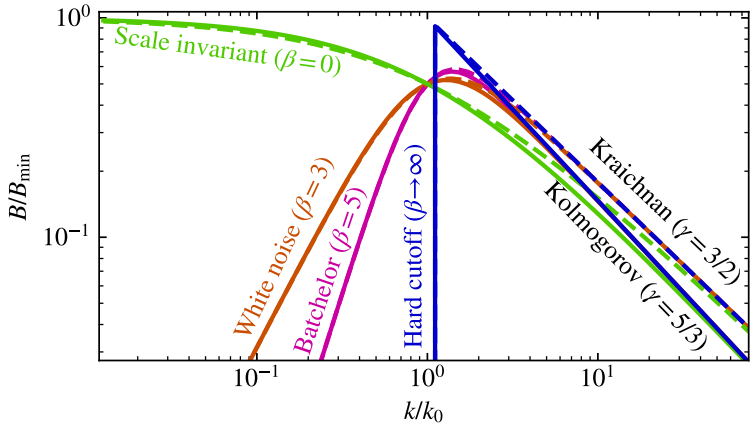

Figure 1. Visualisation of different magnetic field spectra that can be modelled in `ELMAG`.

patch, the magnetic field is homogeneous with a randomly chosen direction. This model is unphysical and may lead to a bias in the strength of the ALP signatures deduced [42, 45, 46].

As already mentioned, we will focus on the effect of the intergalactic magnetic field. From the non-detection of electromagnetic cascades from blazars, it was concluded that the extragalactic space must be filled with an turbulent magnetic field with a strength of $B \gtrsim 10^{-15}\,\mathrm{G}$ with a large filling factor [61, 62], while an upper limit of $B \lesssim 10^{-9}\,\mathrm{G}$ is derived from Faraday rotation measurements [63]. The nature and the production of the extragalactic magnetic field remain however unknown: A large range of magnetic field strengths, spectral index at small k (i.e. β) and coherence lengths are made possible by the many conceivable production mechanisms. For example, if produced during inflation, the initial magnetic spectrum will be scale invariant ($\beta = 0$). Its coherence length is currently limited by hydrodynamical turbulence decay from below ($\sim$ kpc) and the Hubble radius from above. Meanwhile, the range of allowed magnetic field strengths is slowly closing, and it has been argued that the remaining parameter space can be completely eliminated by the non-detection of magnetic halos from misaligned blazars [64]. As a solution, Ref. [64] proposed that the electromagnetic cascades are quenched by plasma instabilities, what, if confirmed, would re-open large parts of the parameter space for intergalactic magnetic fields.

In the remaining of this work, we will focus on the effect of a primordial intergalactic magnetic field with a field strength $B \sim 10^{-9}\,\mathrm{G}$. This value is chosen to highlight the signatures and the effect of the statistical method introduced in section 3.3. Although this value is arguably over-optimistic for primordial fields, similar field strengths can easily be obtained in filaments between clusters of galaxies, or in Galactic magnetic fields which we for concreteness do not include. Although we consider only TeV photons, all of the discussions and considerations made in this paper can be applied to other energies and astrophysical environments [46], taking into ac-

count that the energy dependence of the refractive index scales as E^{-1} at low energies and as E^{1} at high energies. Due to the many uncertainties, and since the expected signal depends strongly on the treatment of the magnetic fields, we will in this work advocate for an experimental approach independent of the modelling of the magnetic fields and the source spectrum.

2.4 Parameter space

Photon-ALP oscillations will lead to two important signatures on high-energy photon spectra at $E \sim$ TeV. First, they will perturb the photon spectrum by energy dependent oscillations with $k \sim \Delta_{\rm osc}$ [see Eq. (2.6)], even for a turbulent magnetic field [46]. Second, the mean free path length of photon will increase since ALPs will propagate without interacting with the EBL. In this work, we focus on the former effect. In this subsection, we will estimate the ALP and magnetic field properties needed to observe ALP wiggles with CTA, and motivate our focus on intergalactic magnetic fields. The conditions discussed here can be deduced graphically from Fig. 3 in Ref. [46].

For a homogeneous magnetic field, the oscillation probability is given by

$$P_s(\gamma \to a) = \left(\frac{2\Delta_{a\gamma}}{\Delta_{\rm osc}}\right)^2 \sin^2\left(\Delta_{\rm osc} s/2\right) \tag{2.6}$$

with $\Delta_{\rm osc}^2 = (\Delta_{\parallel} - \Delta_a)^2 + 4\Delta_{a\parallel}^2$. The oscillation length is then defined as $L_{\rm osc} = 2\pi/\Delta_{\rm osc}$. The oscillatory features—which we name "ALP wiggles"—described by the solution in Eq. (2.6) are present also in turbulent magnetic fields provided that the coherence length is on the same order of magnitude or larger than the oscillation length. At TeV energies, this happens when $2\pi/\Delta_{\rm CMB} \lesssim L_{\rm c}$, or

$$E \gtrsim 8 \times 10^{12}\,{\rm eV} \left(\frac{L_{\rm c}}{10\,{\rm Mpc}}\right)^{-1}. \tag{2.7}$$

The coherence length of the intergalactic magnetic field is practically unconstrained from above, for concreteness we will use $L_{\rm c} \sim 5\,{\rm Mpc}$ as default value. Meanwhile, the Galactic magnetic field has a turbulent component which coherence length is usually assumed to be around 20 pc, and the regular component should be comparable to the size of the Galaxy, $\sim 10\,{\rm kpc}$. Thus, the turbulent component of the Galactic magnetic field is expected to contribute little to the ALP wiggles at CTA energies.

The ALP wiggles are most prominent around the transition from the strong mixing regime, occurring when $\Delta_{\rm CMB} \sim \Delta_{a\gamma}$ or

$$E^{\rm crit} \simeq 2 \times 10^{11}\,{\rm eV} \times \frac{g_{a\gamma} B}{10^{-11}\,{\rm GeV}^{-1}\,{\rm nG}}. \tag{2.8}$$

Since CTA is most sensitive in the range between 10^{11} and $10^{14}\,{\rm eV}$, one should ideally have $10^{11}\,{\rm eV} \lesssim E^{\rm crit}$. This yields

$$\frac{g_{a\gamma} B_{\rm T}}{10^{-11}\,{\rm GeV\,nG}} \lesssim 1/2. \tag{2.9}$$

Furthermore, the ALP mass should be small enough that there exists a strong mixing regime for the given magnetic field strength. This leads to the condition $m_a \lesssim 10^{-10} B_{\rm T}/{\rm nG}$. Since the onset of the wiggles is determined by the weakest magnetic field and photon spectra are usually steeply falling, the intergalactic magnetic field may prove to lead to the strongest wiggles

3 Statistical tests for ALP wiggles

3.1 The χ^2 test for irregularities

The ALP wiggles induced by photon-ALP oscillations will be perceived as "irregularities" in the photon spectrum. Thus, one can use as a probe the χ^2 test,

$$\chi^2 = \frac{1}{N_{\rm bins} - 1} \frac{[f_{\rm data}(E) - f(E)]^2}{\sigma^2_{\rm data}}, \tag{3.1}$$

where $f_{\rm data}(E)$ is the measured binned energy spectrum (with photon-ALP oscillations if they exist) and $f(E)$ is the modelled spectrum (without ALP oscillations) [58]. However, even though this method is statistically sound, it can only measure whether the photon spectrum is more irregular than statistically expected. In the simulated examples in this work we 'model' instead the spectrum by fitting the function

$$f(E) \propto E^{-b} \exp\left\{-\tau(E)\right\}, \quad \text{with} \quad \tau = \alpha \exp\{\beta(\log(E))\} \tag{3.2}$$

where $\beta(x)$ is a fifth order polynomial, to the unbinned spectra by minimising the maximum likelihood estimate (MLE) in order to isolate the effect of the wiggles in a model independent way.

3.2 The discrete power spectrum

The photon-ALP oscillations will perturb the photon spectrum by energy dependent oscillations, $k \sim \Delta_{\rm osc}$, even for a turbulent magnetic field. At energies above the strong mixing regime, the ALPs with thus lead to wiggles with $k \sim E$ in the observed photon spectra. Likewise, below the strong mixing regime, the wiggles have the wavenumber $k \sim E^{-1}$. In Ref. [46], we suggested therefore to use the windowed discrete power spectrum,

$$G_N(k) = \left| \frac{1}{N} \sum_{\rm events} {\rm e}^{{\rm i}\eta k} \right|, \tag{3.3}$$

to extract information on the wiggles. Only photons with energies between $E_{\rm min}$ and $E_{\rm max}$ are included, and we use $\eta = E/E_{\rm min}$ to resemble the expected energy dependence of the wiggles above the strong mixing regime. A similar concept was introduced in Ref. [65]. Importantly, one can use the discrete power spectrum to search for ALPs without specifying the magnetic field. However, for a turbulent magnetic field, the ALP signal is a broadened peak whose location and width is a priori unknown. While this makes a detection more challenging, it enables the extraction of information on the magnetic field.

Note that the signal strength depend on the choice of $E_{\rm min}$: It should be chosen close to the transition from the strong mixing regime, which a priori is unknown. This means, on the other hand, that the conditions (2.7) and (2.9) can in principle be used to deduce the ALP parameters from a detected photon-ALP oscillation signal: The combination $g_{a\gamma}B_\perp$ will for most astrophysical environments determine the onset of the oscillations $\Delta_{\rm CMB} = 2\Delta_{a\parallel}$ (see Fig. 3 in Ref. [46]). This means that $g_{a\gamma}B_\perp$ can be fixed by finding the value of $E_{\rm min}$ that optimises the observed oscillations. The mass m_a can likewise be determined by X-ray measurements.

We consider the test statistic (TS) given by the goodness-of-fit measure compared to an estimated background,

$$\mathrm{TS} = \frac{1}{\Delta k}\int_0^{\Delta k} \frac{[G_N(k) - G_N^B(k)]^2}{\sigma_N^B(k)^2}\,\mathrm{d}k\ . \tag{3.4}$$

We choose $\Delta k = 6$ to reduce the contributions from random fluctuations at large k. While Eq. (3.4) shares similarities with the χ^2 statistics, one should emphasise that one expects a longer tail in this test statistics since we are integrating over a range in which there statistically is expected to be random peaks, i.e. the probability that there is a random peak at any k is larger than the probability that there is a peak at a fixed k. The TS can in principle be improved if the shape, position and width is taken into account, using for example machine learning.

3.3 Statistical procedure and examples

In this section, the use of the discrete power spectrum to detect ALP wiggles will be exemplified. We will focus on the effect of the magnetic field modelling on the ALP wiggles, thereby illustrating the importance of a proper treatment of the magnetic fields in modelling photon-ALP oscillations. Based on the discussions above, we define the following statistical procedure:

1. Photons are sampled according to the chosen source spectrum using `ELMAG`. The simulations are stopped when a given number N of photons has reached the detector within the considered energy range. The energy of the simulated photons that reached the detector is used to compute the discrete power spectrum G.

2. The "measured spectrum" is modelled by minimising the maximum-likelihood-estimate (MLE) of the fit function (3.2) to the simulated data.

3. The background power spectrum and its statistical variation is in turn found by drawing $N \times 10^3$ energies using the fitted spectrum as a probability distribution.

4. The TS is computed using (3.4).

In all the scenarios considered in this section, we repeat this procedure for 10^3 realisations of the magnetic field in order to obtain the distribution of TS values.

For concreteness, we will consider $N = 10^4$ detected photons and in the energy range $E \in (10^{12}, 10^{14})\,\mathrm{eV}$ with the injection spectrum $\mathrm{d}N/\mathrm{d}E \propto E^{-1.2}$. Moreover,

we fix $g_{a\gamma} = 10^{-20}\,\mathrm{GeV}^{-2}$ and use a turbulent magnetic field with $B_{\mathrm{rms}} = 5\,\mathrm{nG}$. The power spectrum using a Gaussian turbulent field with $\gamma = 5/3$, $\beta \to \infty$ and $L_{\mathrm{c}} = 5\,\mathrm{Mpc}$ (default parameters) is shown in the left pane of Fig. 2. In all plots in this section, the various scenarios will be labelled using the parameters that differs from the default parameters. The results for 50 realisations with photon-ALP oscillations are shown in orange lines, those without photon-ALP oscillations in blue. The averages and the 1σ statistical variance (black lines) were computed using the full set of 10^3 realisations. For comparison, the results using a domain-like field are shown in the right pane of Fig. 2.

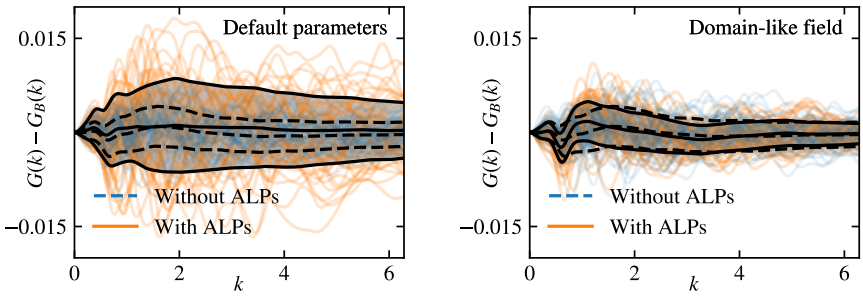

Figure 2. The power spectrum with the estimated background subtracted is plotted using a Gaussian turbulent field (left) and a domain-like field (right). The results for 50 realisation of the magnetic field with (orange) and without (blue) photon-ALP oscillations is shown, and the averages and the statistical standard deviations from a sample of 10^3 realisations are shown in black lines. The parameters used in the simulations are discussed in the main text.

The results in Fig. 2 show the power of the statistical procedure: There are clear peaks in the power spectrum including photon-ALP oscillations compared to the case without photon-ALP oscillations[4]. Interestingly, due to the lack of cosmic variance in the simple domain-like field, there is a lack of variance in the photon spectra which represents itself as a clear signal in the discrete power spectrum, even after averaging over many realisations of the magnetic field. This becomes even clearer for larger coherence lengths, as shown in Fig. 3 for $L_{\mathrm{c}} = 10\,\mathrm{Mpc}$. As such, the use of simplified magnetic field models, such as the domain-like field, may lead to a bias in searches for ALP wiggles and impact the estimated limits on $g_{a\gamma}$. However, the larger variance in more realistic magnetic field models—in these examples represented by Gaussian turbulent fields—increases the rate of random encounters of regions of magnetic fields that may enhance the wiggles (see also the discussion in, e.g., Ref. [66]). Thus, a more realistic modelling of the magnetic fields may, in fact, improve the detection prospects

[4]Note that there is a minor bump, still comparable with flat, in the power spectrum without any photon-ALP oscillations. This indicates that our fit function does not perfectly describe the optical depth of the used EBL model. For the purposes of this paper, where the fitting procedure is made automatic using $\mathcal{O}(10^4)$ spectra, the quality of the fit is sufficient.

by such random encounters. The detection prospects could be further improved choosing more suitable fitting functions. Moreover, a constant windowing function was used. By varying the minimal energy, $E_{\rm min}$, one may hope to further increase the detection sensitivity

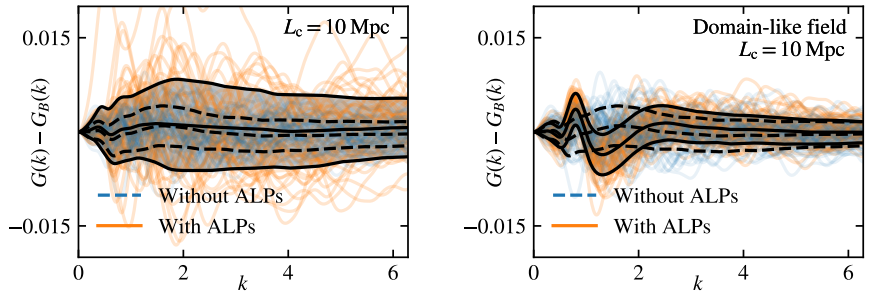

Figure 3. Same as Fig. 2, but with $L_c = 10\,\mathrm{Mpc}$.

For visualisation and to better understand the essence of the method, we plot in Fig. 4 the binned energy spectrum (green errorbars) and the fitted[5] spectrum (blue dashed line) for one random realisation of the magnetic field, both with and without photon-ALP oscillations. In addition, the spectrum averaged over all simulations and its standard deviation is shown (orange region). It is clear that photon-ALP oscillations increase the variation in the energy spectrum. The task of the generic fitting function (3.2) is to reduce the effect of unknown features in the source spectrum, such as uncertainties in the modelling of the EBL or unresolved features in the source spectrum. This leads to a caveat of this approach, well visualised in Fig. 4 with the spectrum that yielded the highest TS value in this analysis: The spectrum may be "over-fitted", i.e. part of the signal will be incorporated into the fit function, weakening thereby the signal. This applies especially for the wiggles extending over a larger energy range. Since the true injection spectrum of the source is not known, a detailed modelling of the source would be required in such cases to distinguish between intrinsic and ALP induced features in the energy spectrum.

In Fig. 5, we plot the distribution of the TS (3.4), for the default parameters, $L_c = 1\,\mathrm{Mpc}$, $L_c = 10\,\mathrm{Mpc}$, and a domain-like field. With the chosen TS, the domain-like field is difficult to distinguish from the non-ALP scenario. The Gaussian turbulent field, however, has a clear tail in the TS distribution, which distinguishes the ALP from the non-ALP scenario. While increasing the coherence length improves the detection prospects, details of the magnetic field like the values of γ and β have only a minor influence on the TS distribution and we therefore do not vary them in the figure. The reason for the weak dependence on these parameters is that the integrated magnetic field distributions, or the filling factor, is independent of the magnetic field spectrum

[5]We emphasise that un-binned data are used in the fit.

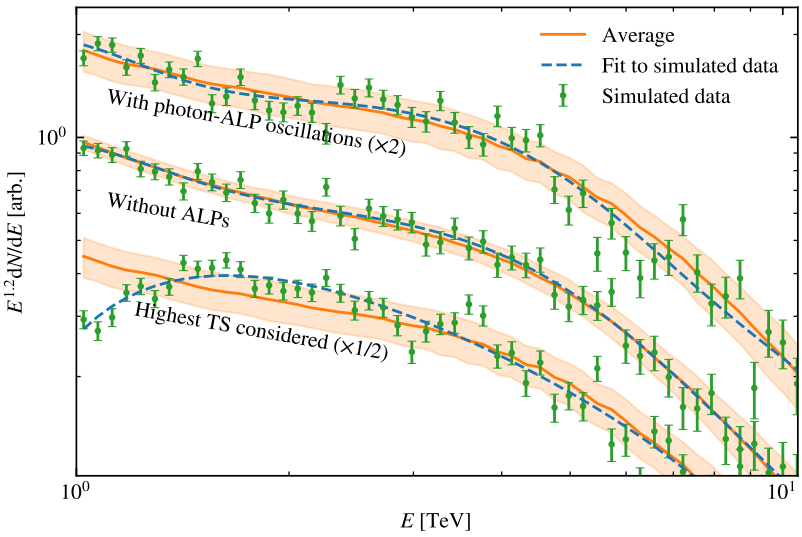

Figure 4. The simulated data (green errorbars) for one random realisation of the magnetic field are plotted with and without photon-ALP oscillations. The spectra are multiplied by a constant to improve visibility. Furthermore, the function (3.2) fitted to the (un-binned) data is shown as a blue dashed line together with the average obtained from the complete sample of 1000 realisations is shown. In addition, the spectrum from the simulation that yielded the highest TS is shown.

for a Gaussian turbulent field with the same $B_{\rm rms}$ and $L_{\rm c}$. In order to more clearly quantify the differences, we list in Tab. 1 the probability that a signal is detected with a confidence level of 2σ, denoted as C_{95}, and the 99 % quantile for the various magnetic field scenarios considered. Although there are only minor differences in the C_{95} value, there are noticeable differences in the tails of the distributions, registered in the 99 % quantiles.

Note that the results of our examples are in agreement with the conclusions made in, e.g., Ref. [42]: The experimental sensitivities depend on whether a realistic magnetic field model or a domain-like model is used. Importantly, the use of realistic magnetic field models may increase significantly the detection prospects.

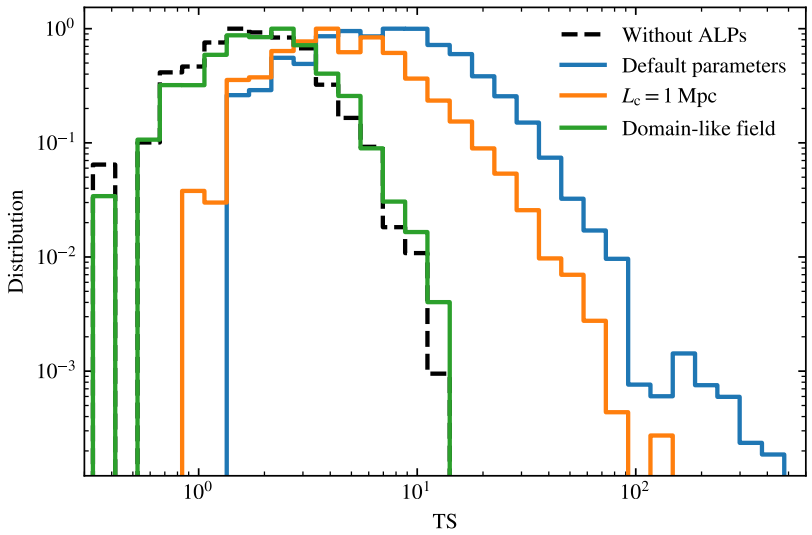

Figure 5. Histograms of the TS (3.4) obtained using the statistical method described in subsection 3.3. The various colored lines are obtained using different parameters for the magnetic field; the labels indicate the parameter changed compared to the default parameters (see the main text for a description). The results in the no-ALP scenario is plotted as a dashed black line.

4 Detecting ALP wiggles from PKS 2155-304 with CTA

In this section, we will consider PKS 2155-304 [67] at redshift $z = 0.116$ as a concrete example. Its photon spectrum can be approximated by [68]

$$\frac{\mathrm{d}N}{\mathrm{d}E} = N_0 \left(\frac{E}{E_b}\right)^{-\alpha-\beta\log(E/E_b)}, \tag{4.1}$$

with $N_0 = 15.4 \times 10^{-12}\,\mathrm{cm}^{-2}\mathrm{s}^{-1}\mathrm{MeV}^{-1}$, $E_b = 1136\,\mathrm{MeV}$, $\alpha = 1.77$ and $\beta = 0.035$. Since CTA [69] is not yet operational and its sensitivities are preliminary, we assume conservatively an energy-independent effective collection area $A = 10^5\,\mathrm{m}^2$. We take, however, into account the energy resolution of the detector by scrambling the detected energies using a normal deviate with an energy dependent half-width given by the preliminary energy resolution of CTA. Furthermore, we consider an energy range $E \in [10^{12}, 10^{14}]\,\mathrm{eV}$, for which the energy resolution $\Delta E/E$ is approximately energy independent[6]. The expected number of photons detected by CTA in this energy range

[6]If the larger energy range $E \in [10^{11}, 10^{14}]\,\mathrm{eV}$ is used, one should convolve a parametrisation of the energy resolution with the fit function.

Parameter	C_{95}	99 % quantile
Default	0.984	98.3
$\gamma = 4/3$	0.989	135
$\gamma = 2$	0.989	101
$\beta = 2$	0.988	183
$\beta = 4$	0.991	183
$f = 0.1$	0.988	69.9
$L_\mathrm{c} = 1\,\mathrm{Mpc}$	0.955	50.2
$L_\mathrm{c} = 10\,\mathrm{Mpc}$	0.972	140
Domain-like field	0.628	9
Domain-like $L_\mathrm{c} = 10\,\mathrm{Mpc}$	0.660	10

Table 1. The probability that a signal is detected with a confidence level of 2σ, denoted as C_{95}, for the various magnetic field scenarios considered with Eq. (3.4) as TS.

from PKS 2155-304 can then be approximated as

$$N = A\Delta t \int \mathrm{d}E \, \frac{\mathrm{d}N}{\mathrm{d}E} \approx 2.6 \times 10^3 \left(\frac{\Delta t}{50\,\mathrm{h}}\right) \left(\frac{A}{10^5\,\mathrm{m}^2}\right). \tag{4.2}$$

In Fig. 6, we plot the spectrum obtained from one simulation of PKS 2155-304 for an observation time $\Delta t = 50\,\mathrm{h}$ and a Gaussian turbulent field with $L_\mathrm{c} = 5\,\mathrm{Mpc}$.

To get an idea of the detectability of ALP wiggles from PKS 2155-304, we follow the statistical procedure from section 3.3. The result is shown in Fig. 7 for observation times $\Delta t = \{50, 100, 400\}\,\mathrm{h}$. As expected, increasing the observation time increases the detection prospects. As a basis for comparison, we consider in Fig. 8 the TS distribution using Eq. (3.1) with the same binning as in Fig. 6.

In order to more clearly quantify the differences between the statistical methods used in Figs. 7 and 8, we list in Tab. 2 the probability that a signal is detected with a confidence level of 2σ, denoted as C_{95}, for the various magnetic field scenarios considered. From these values, we conclude that the use of the discrete power spectrum leads to better detection prospects compared to a standard irregularity search in the energy spectrum, especially for low observation times. Note, however, that the search for irregularities will depend on the binning, and can thus be improved. On the flip side, the optimal windowing function for the power spectrum will depend on the ALP coupling and the magnetic field strength. There is, in any case, a clear advantage of using the discrete power spectrum compared to a standard search for residual: While a high χ^2 value merely indicates that the data are more irregular than expected, a signal in the discrete power spectrum is a clear indication that the data have wiggles with the same energy dependence as expected for photon-ALP oscillations.

In this work, we have thus far considered an optimistic value for the intergalactic magnetic field, $B_\mathrm{rms} = 5 \times 10^{-9}\,\mathrm{G}$, and a coupling which is on the verge of be-

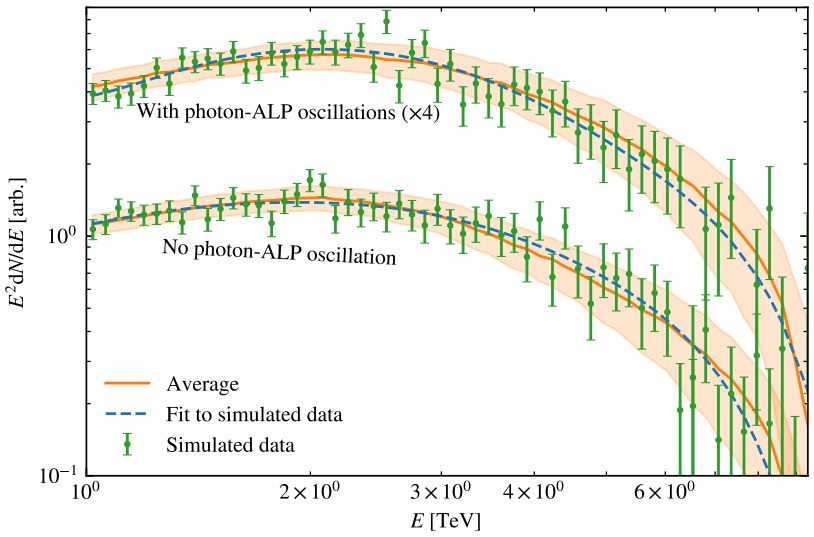

Figure 6. Same as Fig. 4, but with $N = 2.6 \times 10^3$ photons and the parameters used for PKS 2155-304.

	$\Delta t = 50\,\mathrm{h}$	$\Delta t = 100\,\mathrm{h}$	$\Delta t = 200\,\mathrm{h}$	$\Delta t = 400\,\mathrm{h}$
Power spec.	0.218	0.469	0.591	0.644
Spec.	0.094	0.228	0.478	0.597

Table 2. The table indicates the probability that ALPs are detected in an observation of PKS 2155-304 using CTA with a confidence level larger than 2σ, denoted as C_{95}, using the power spectrum [Eq. (3.4)] and a standard χ^2 search [Eq. (3.1)]. The columns corresponds to the detection times used in Fig. 7.

ing excluded for $m_a \gtrsim 10^{-11}\,\mathrm{eV}$, $g_{a\gamma} = 10^{-20}\,\mathrm{GeV}^{-2}$. It is thus useful to check to what extent the detectability worsens when the magnetic field strength is decreased[7]. Therefore, we plot in Fig. 9 the histograms of the TS obtained for varying magnetic field strength, $B_{\mathrm{rms}} = \{5, 1, 0.5\}\,\mathrm{nG}$. The corresponding detection probabilities are $C_{95} = \{0.947, 0.547, 0.521\}$. Two effects lead to the quick reduction in C_{95} with decreasing magnetic field strength: First, the wiggles are strongest close to the strong mixing regime, and decreasing the magnetic field strength shifts the strong mixing regime to lower energies. From the condition in Eq. (2.9), it it expected that our choice of default parameters leads to the strongest wiggles. This reduction in sensitiv-

[7]Since the oscillation depend on the magnetic field and the coupling strength via the combination $g_{a\gamma}B$, this is equivalent to reducing the coupling.

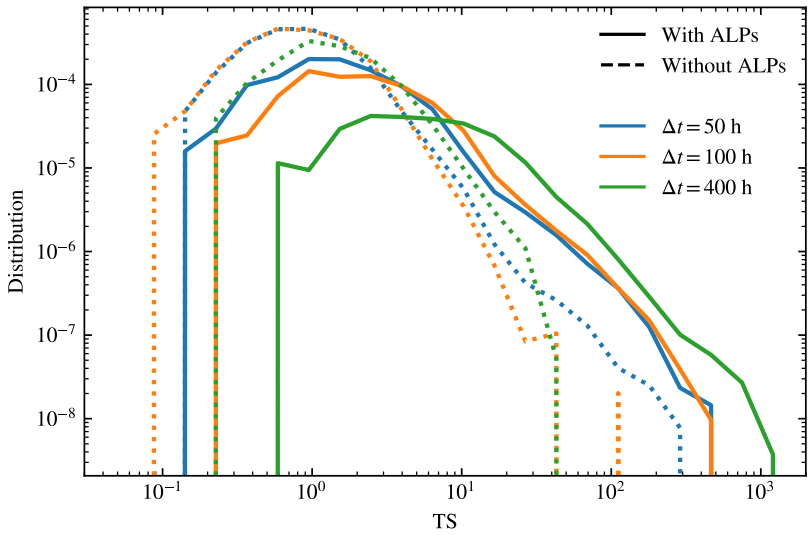

Figure 7. Histograms of the TS (3.4) obtained using the statistical method described in subsection 3.3 on the simulated data from PKS 2155-304 for the observation times $\Delta t = 50\,\mathrm{h}$ (blue), 100 h (orange) and 400 h (green). The corresponding no-ALP cases are shown with dashed lines.

ity may be partly compensated for by changing the lowest energy considered. Second, the mixing strength is proportional to the magnetic field strength, which can only be compensated for by increasing the observation time.

5 Summary and conclusion

Photon-ALP oscillations will imprint energy-dependent oscillatory features, which we name "ALP wiggles", on photon spectra from distant high-energy sources. We have therefore proposed to use the discrete power spectrum (3.3) to directly probe such wiggles in experimental data. Such a search will be independent of the modelling of magnetic fields and theoretical uncertainties in, e.g., the EBL. This work serves as a first proof of principle, and there is room for improvement: We only considered the simple test statistic (3.4) which only measures the residual of the measured discrete power spectrum compared to the estimated background. Furthermore, in order to stay as concrete as possible, and since the onset of the ALP wiggles at TeV energies is determined by the weakest magnetic field that contribute to the oscillations, we considered only an intergalactic magnetic field. In a complete analysis, one should furthermore consider photon-ALP oscillations in, e.g., the Milky Way and the host

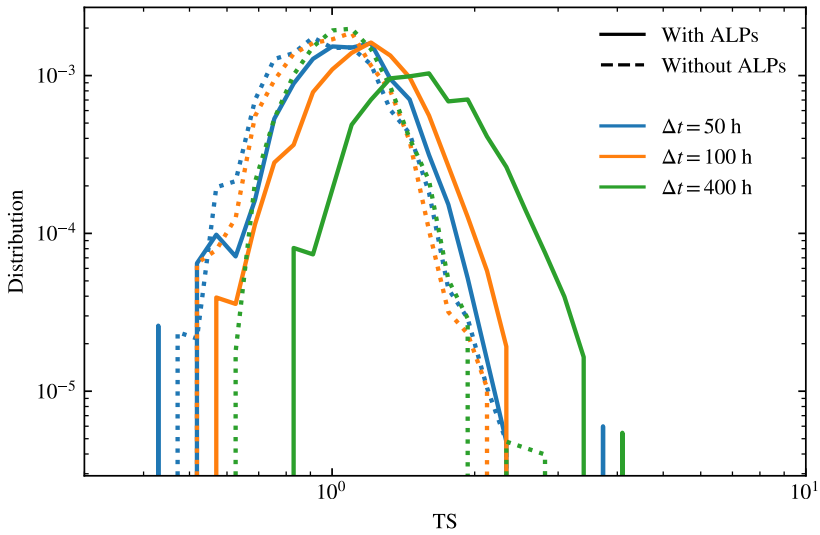

Figure 8. Same as Fig. 7, but with the χ^2 value [Eq. (3.1)] as TS.

galaxy, and in the source itself. As a second step, the discrete power spectrum can be used to extract information about the magnetic field, more specifically, it can be related to the two-point correlation function of the magnetic field [46, 70].

We have compared two different treatments of the magnetic field: a Gaussian turbulent field, and a simple and unphysical domain-like field. We found that the increased cosmic variance of the Gaussian turbulent field may significantly improve the detection prospects. Varying the shape of its power spectrum, we did not observe a strong dependence on the resulting axion wiggles, as long as the effective coherence length remained constant.

As a concrete example, we considered the detection of ALP wiggles in the energy spectrum from PKS 2155-304 using conservative estimates of the Cherenkov Telescope Array (CTA) sensitivity. Our analysis indicates that ALP wiggles can be detected by CTA for optimistic values of the magnetic field and photon-ALP coupling. Importantly, the method is an improvement compared to a standard search for "irregularities" in photon spectra. The statistical method can furthermore be optimised choosing an appropriate windowing function: Since the extragalactic magnetic field strength currently is only weakly constrained, one cannot know at which energy the first ALP wiggle occur. Thus, the signal can be enhanced by choosing an appropriate windowing function. Moreover, the simple test statistic considered does not take into account the size, shape and location of the peak.

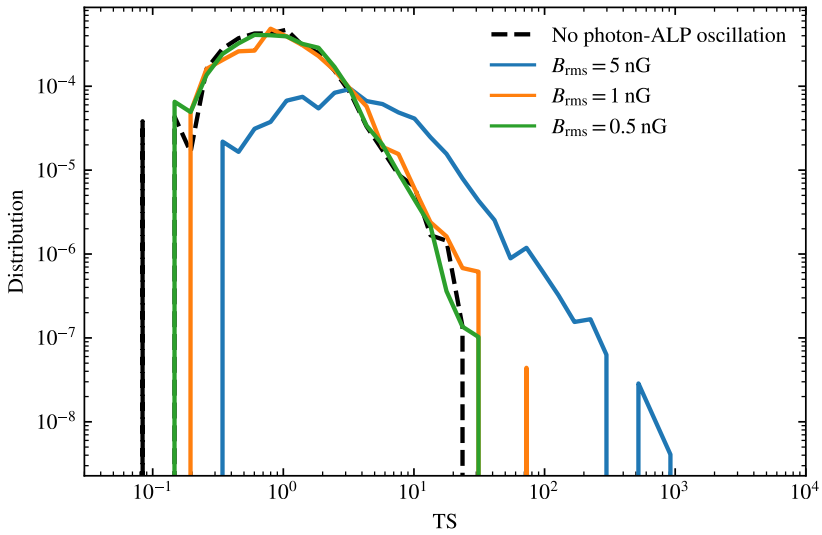

Figure 9. Histograms of the TS (3.4) obtained using the statistical method described in subsection 3.3 on the simulated data from PKS 2155-304 for an obervation time $\Delta t = 200\,\mathrm{h}$. The results obtained with magnetic field strengths $B_{\rm rms} = 5\,\mathrm{nG}$ (blue), $B_{\rm rms} = 1\,\mathrm{nG}$ (orange) and $B_{\rm rms} = 0.5\,\mathrm{nG}$ (green) are shown. The no-ALP scenario is shown in dashed line.

Acknowledgements

We would like to thank M. Unger for valuable discussions that helped to improve the computational time for generating the Gaussian turbulent fields. JT would like to thank M. Meyer for interesting discussions and hospitality at the University of Hamburg.

References

[1] R. D. Peccei and H. R. Quinn, *CP Conservation in the Presence of Instantons*, *Phys. Rev. Lett.* **38** (1977) 1440.

[2] R. D. Peccei and H. R. Quinn, *Constraints Imposed by CP Conservation in the Presence of Instantons*, *Phys. Rev. D* **16** (1977) 1791.

[3] J. Preskill, M. B. Wise and F. Wilczek, *Cosmology of the Invisible Axion*, *Phys. Lett. B* **120** (1983) 127.

[4] L. F. Abbott and P. Sikivie, *A Cosmological Bound on the Invisible Axion*, *Phys. Lett. B* **120** (1983) 133.

[5] M. Dine and W. Fischler, *The Not So Harmless Axion*, *Phys. Lett. B* **120** (1983) 137.

[6] S. Weinberg, *A New Light Boson?*, *Phys. Rev. Lett.* **40** (1978) 223.

[7] F. Wilczek, *Problem of Strong P and T Invariance in the Presence of Instantons*, *Phys. Rev. Lett.* **40** (1978) 279.

[8] G. Grilli di Cortona, E. Hardy, J. Pardo Vega and G. Villadoro, *The QCD axion, precisely*, *JHEP* **01** (2016) 034 [1511.02867].

[9] L. Di Luzio, M. Giannotti, E. Nardi and L. Visinelli, *The landscape of QCD axion models*, *Phys. Rept.* **870** (2020) 1 [2003.01100].

[10] A. Arvanitaki, S. Dimopoulos, S. Dubovsky, N. Kaloper and J. March-Russell, *String Axiverse*, *Phys. Rev. D* **81** (2010) 123530 [0905.4720].

[11] M. Cicoli, M. Goodsell and A. Ringwald, *The type IIB string axiverse and its low-energy phenomenology*, *JHEP* **10** (2012) 146 [1206.0819].

[12] P. W. Graham, I. G. Irastorza, S. K. Lamoreaux, A. Lindner and K. A. van Bibber, *Experimental Searches for the Axion and Axion-Like Particles*, *Ann. Rev. Nucl. Part. Sci.* **65** (2015) 485 [1602.00039].

[13] I. G. Irastorza and J. Redondo, *New experimental approaches in the search for axion-like particles*, *Prog. Part. Nucl. Phys.* **102** (2018) 89 [1801.08127].

[14] CAST collaboration, *New CAST Limit on the Axion-Photon Interaction*, *Nature Phys.* **13** (2017) 584 [1705.02290].

[15] A. Ayala, I. Domínguez, M. Giannotti, A. Mirizzi and O. Straniero, *Revisiting the bound on axion-photon coupling from Globular Clusters*, *Phys. Rev. Lett.* **113** (2014) 191302 [1406.6053].

[16] M. J. Dolan, F. J. Hiskens and R. R. Volkas, *Advancing globular cluster constraints on the axion-photon coupling*, *JCAP* **10** (2022) 096 [2207.03102].

[17] R. Bähre et al., *Any light particle search II —Technical Design Report*, *JINST* **8** (2013) T09001 [1302.5647].

[18] IAXO collaboration, *Physics potential of the International Axion Observatory (IAXO)*, *JCAP* **06** (2019) 047 [1904.09155].

[19] ADMX collaboration, *Extended Search for the Invisible Axion with the Axion Dark Matter Experiment*, *Phys. Rev. Lett.* **124** (2020) 101303 [1910.08638].

[20] J. L. Ouellet et al., *First Results from ABRACADABRA-10 cm: A Search for Sub-μeV Axion Dark Matter*, *Phys. Rev. Lett.* **122** (2019) 121802 [1810.12257].

[21] J. W. Foster, S. J. Witte, M. Lawson, T. Linden, V. Gajjar, C. Weniger et al., *Extraterrestrial Axion Search with the Breakthrough Listen Galactic Center Survey*, *Phys. Rev. Lett.* **129** (2022) 251102 [2202.08274].

[22] R. A. Battye, M. J. Keith, J. I. McDonald, S. Srinivasan, B. W. Stappers and P. Weltevrede, *Searching for Time-Dependent Axion Dark Matter Signals in Pulsars*, 2303.11792.

[23] H.E.S.S. collaboration, *Constraints on axionlike particles with H.E.S.S. from the irregularity of the PKS 2155-304 energy spectrum*, *Phys. Rev. D* **88** (2013) 102003 [1311.3148].

[24] Fermi-LAT collaboration, *Search for Spectral Irregularities due to Photon–Axionlike-Particle Oscillations with the Fermi Large Area Telescope*, *Phys. Rev. Lett.* **116** (2016) 161101 [1603.06978].

[25] C. Eckner and F. Calore, *First constraints on axionlike particles from Galactic sub-PeV gamma rays*, *Phys. Rev. D* **106** (2022) 083020 [2204.12487].

[26] J. S. Reynés, J. H. Matthews, C. S. Reynolds, H. R. Russell, R. N. Smith and M. C. D. Marsh, *New constraints on light axion-like particles using Chandra transmission grating spectroscopy of the powerful cluster-hosted quasar H1821+643*, *Mon. Not. Roy. Astron. Soc.* **510** (2021) 1264 [2109.03261].

[27] J. H. Matthews, C. S. Reynolds, M. C. D. Marsh, J. Sisk-Reynés and P. E. Rodman, *How Do Magnetic Field Models Affect Astrophysical Limits on Light Axion-like Particles? An X-Ray Case Study with NGC 1275*, *Astrophys. J.* **930** (2022) 90 [2202.08875].

[28] C. S. Reynolds, M. C. D. Marsh, H. R. Russell, A. C. Fabian, R. Smith, F. Tombesi et al., *Astrophysical limits on very light axion-like particles from Chandra grating spectroscopy of NGC 1275*, *Astrophys. J.* **890** (2020) 59 [1907.05475].

[29] CTA collaboration, *Sensitivity of the Cherenkov Telescope Array for probing cosmology and fundamental physics with gamma-ray propagation*, *JCAP* **02** (2021) 048 [2010.01349].

[30] A. Payez, C. Evoli, T. Fischer, M. Giannotti, A. Mirizzi and A. Ringwald, *Revisiting the SN1987A gamma-ray limit on ultralight axion-like particles*, *JCAP* **02** (2015) 006 [1410.3747].

[31] M. Xiao, K. M. Perez, M. Giannotti, O. Straniero, A. Mirizzi, B. W. Grefenstette et al., *Constraints on Axionlike Particles from a Hard X-Ray Observation of Betelgeuse*, *Phys. Rev. Lett.* **126** (2021) 031101 [2009.09059].

[32] C. Dessert, J. W. Foster and B. R. Safdi, *X-ray Searches for Axions from Super Star Clusters*, *Phys. Rev. Lett.* **125** (2020) 261102 [2008.03305].

[33] D. Noordhuis, A. Prabhu, S. J. Witte, A. Y. Chen, F. Cruz and C. Weniger, *Novel Constraints on Axions Produced in Pulsar Polar Cap Cascades*, 2209.09917.

[34] G. Galanti, *Photon-ALP oscillations inducing modifications to photon polarization*, *Phys. Rev. D* **107** (2023) 043006 [2202.11675].

[35] D. Lai and J. Heyl, *Probing Axions with Radiation from Magnetic Stars*, *Phys. Rev. D* **74** (2006) 123003 [astro-ph/0609775].

[36] R. Gill and J. S. Heyl, *Constraining the photon-axion coupling constant with magnetic white dwarfs*, *Phys. Rev. D* **84** (2011) 085001 [1105.2083].

[37] C. Dessert, D. Dunsky and B. R. Safdi, *Upper limit on the axion-photon coupling from magnetic white dwarf polarization*, *Phys. Rev. D* **105** (2022) 103034 [2203.04319].

[38] A. De Angelis, M. Roncadelli and O. Mansutti, *Evidence for a new light spin-zero boson from cosmological gamma-ray propagation?*, *Phys. Rev. D* **76** (2007) 121301 [0707.4312].

[39] S. Jacobsen, T. Linden and K. Freese, *Constraining Axion-Like Particles with HAWC*

Observations of TeV Blazars, 2203.04332.

[40] J. Davies, M. Meyer and G. Cotter, *Constraints on axionlike particles from a combined analysis of three flaring Fermi flat-spectrum radio quasars*, *Phys. Rev. D* **107** (2023) 083027 [2211.03414].

[41] A. Kartavtsev, G. Raffelt and H. Vogel, *Extragalactic photon-ALP conversion at CTA energies*, *JCAP* **01** (2017) 024 [1611.04526].

[42] D. Montanino, F. Vazza, A. Mirizzi and M. Viel, *Enhancing the Spectral Hardening of Cosmic TeV Photons by Mixing with Axionlike Particles in the Magnetized Cosmic Web*, *Phys. Rev. Lett.* **119** (2017) 101101 [1703.07314].

[43] M. Libanov and S. Troitsky, *On the impact of magnetic-field models in galaxy clusters on constraints on axion-like particles from the lack of irregularities in high-energy spectra of astrophysical sources*, *Phys. Lett. B* **802** (2020) 135252 [1908.03084].

[44] P. Carenza, C. Evoli, M. Giannotti, A. Mirizzi and D. Montanino, *Turbulent axion-photon conversions in the Milky Way*, *Phys. Rev. D* **104** (2021) 023003 [2104.13935].

[45] M. Meyer, D. Montanino and J. Conrad, *On detecting oscillations of gamma rays into axion-like particles in turbulent and coherent magnetic fields*, *JCAP* **09** (2014) 003 [1406.5972].

[46] M. Kachelriess and J. Tjemsland, *On the origin and the detection of characteristic axion wiggles in photon spectra*, *JCAP* **01** (2022) 025 [2111.08303].

[47] G. Raffelt and L. Stodolsky, *Mixing of the Photon with Low Mass Particles*, *Phys. Rev. D* **37** (1988) 1237.

[48] A. Dobrynina, A. Kartavtsev and G. Raffelt, *Photon-photon dispersion of TeV gamma rays and its role for photon-ALP conversion*, *Phys. Rev. D* **91** (2015) 083003 [1412.4777].

[49] M. Kachelrieß, S. Ostapchenko and R. Tomàs, *ELMAG: A Monte Carlo simulation of electromagnetic cascades on the extragalactic background light and in magnetic fields*, *Comput. Phys. Commun.* **183** (2012) 1036 [1106.5508].

[50] M. Blytt, M. Kachelrieß and S. Ostapchenko, *ELMAG 3.01: A three-dimensional Monte Carlo simulation of electromagnetic cascades on the extragalactic background light and in magnetic fields*, 1909.09210.

[51] M. Meyer, J. Davies and J. Kuhlmann, *gammaALPs: An open-source python package for computing photon-axion-like-particle oscillations in astrophysical environments*, *PoS* **ICRC2021** (2021) 557 [2108.02061].

[52] R. Alves Batista and A. Saveliev, *The Gamma-ray Window to Intergalactic Magnetism*, *Universe* **7** (2021) 223 [2105.12020].

[53] R. Durrer and A. Neronov, *Cosmological Magnetic Fields: Their Generation, Evolution and Observation*, *Astron. Astrophys. Rev.* **21** (2013) 62 [1303.7121].

[54] J. Giacalone and J. R. Jokipii, *Charged-particle motion in multidimensional magnetic-field turbulence*, *Astrophys. J. Lett.* **430** (1994) L137.

[55] J. Giacalone and J. R. Jokipii, *The Transport of Cosmic Rays across a Turbulent*

Magnetic Field, *Astrophys. J.* **520** (1999) 204.

[56] G. Galanti and M. Roncadelli, *Behavior of axionlike particles in smoothed out domainlike magnetic fields*, *Phys. Rev. D* **98** (2018) 043018 [1804.09443].

[57] G. Galanti and M. Roncadelli, *Extragalactic photon–axion-like particle oscillations up to 1000 TeV*, *JHEAp* **20** (2018) 1 [1805.12055].

[58] D. Wouters and P. Brun, *Irregularity in gamma ray source spectra as a signature of axionlike particles*, *Phys. Rev. D* **86** (2012) 043005 [1205.6428].

[59] A. De Angelis, G. Galanti and M. Roncadelli, *Relevance of axion-like particles for very-high-energy astrophysics*, *Phys. Rev. D* **84** (2011) 105030 [1106.1132].

[60] G. Galanti, F. Tavecchio, M. Roncadelli and C. Evoli, *Blazar VHE spectral alterations induced by photon–ALP oscillations*, *Mon. Not. Roy. Astron. Soc.* **487** (2019) 123 [1811.03548].

[61] A. Neronov and I. Vovk, *Evidence for strong extragalactic magnetic fields from Fermi observations of TeV blazars*, *Science* **328** (2010) 73 [1006.3504].

[62] K. Dolag, M. Kachelriess, S. Ostapchenko and R. Tomas, *Lower limit on the strength and filling factor of extragalactic magnetic fields*, *Astrophys. J. Lett.* **727** (2011) L4 [1009.1782].

[63] M. S. Pshirkov, P. G. Tinyakov and F. R. Urban, *New limits on extragalactic magnetic fields from rotation measures*, *Phys. Rev. Lett.* **116** (2016) 191302 [1504.06546].

[64] A. E. Broderick, P. Tiede, P. Chang, A. Lamberts, C. Pfrommer, E. Puchwein et al., *Missing Gamma-ray Halos and the Need for New Physics in the Gamma-ray Sky*, *Astrophys. J.* **868** (2018) 87 [1808.02959].

[65] J. P. Conlon and M. Rummel, *Improving Statistical Sensitivity of X-ray Searches for Axion-Like Particles*, *Mon. Not. Roy. Astron. Soc.* **484** (2019) 3573 [1808.05916].

[66] P. Carenza, R. Sharma, M. C. D. Marsh, A. Brandenburg and E. Müller, *Magnetohydrodynamics predicts heavy-tailed distributions of axion-photon conversion*, 2208.04333.

[67] F. Aharonian et al., *An Exceptional Very High Energy Gamma-Ray Flare of PKS 2155-304*, *Astrophys. J. Lett.* **664** (2007) L71 [0706.0797].

[68] Q. Yu and D. Horns, *Searching for photon-ALPs mixing effects in AGN gamma-ray energy spectra*, 2208.00079.

[69] CTA Consortium collaboration, *Performance of the Cherenkov Telescope Array*, *PoS* **ICRC2019** (2020) 733 [1907.08171].

[70] M. C. D. Marsh, J. H. Matthews, C. Reynolds and P. Carenza, *Fourier formalism for relativistic axion-photon conversion with astrophysical applications*, *Phys. Rev. D* **105** (2022) 016013 [2107.08040].

ISBN 978-82-326-7180-9 (printed ver.)
ISBN 978-82-326-7179-3 (electronic ver.)
ISSN 1503-8181 (printed ver.)
ISSN 2703-8084 (online ver.)

NTNU

Norwegian University of
Science and Technology